DEVELOPMENT AND NON-LINEAR CONTROL OF A NOVEL ROTARY SERIES ELASTIC ACTUATOR

A THESIS SUBMITTED TO
GRADUATE SCHOOL OF NATURAL AND APPLIED SCIENCES
OF
KOCAELİ UNIVERSITY

BY

MOHAMMAD JAVAD FOTUHI

IN PARTIAL FULFILLMENT OF THE REQUIREMENTS
FOR
THE DEGREE OF DOCTOR OF PHILOSOPHY
IN
MECHATRONICS ENGINEERING

KOCAELİ 2021

DEVELOPMENT AND NON-LINEAR CONTROL OF A NOVEL ROTARY SERIES ELASTIC ACTUATOR

A THESIS SUBMITTED TO
GRADUATE SCHOOL OF NATURAL AND APPLIED SCIENCES
OF
KOCAELİ UNIVERSITY

BY

MOHAMMAD JAVAD FOTUHI

IN PARTIAL FULFILLMENT OF THE REQUIREMENTS
FOR
THE DEGREE OF DOCTOR OF PHILOSOPHY
IN
MECHATRONIC ENGINEERING

Prof.Dr. Zafer BİNGÜL		
Supervisor,	**Kocaeli University**	**.....**
Prof.Dr. Serdar KÜÇÜK		
Jury member,	**Kocaeli University**	**.....**
Assist.Prof.Dr. Oğuzhan KARAHAN		
Jury member,	**Kocaeli University**	**.....**
Prof.Dr. Ahmet YAZICI		
Jury member,	**Eskişehir Osmangazi University**	**.....**
Assoc.Prof.Dr. Metin TOZ		
Jury member,	**Karamanoğlu Mehmetbey University**	**.....**

Thesis Defense Date: 24.06.2021

ACKNOWLEDGEMENTS

I would like to thank my supervisor Prof. Dr. ZAFER BİNGÜL, for his support and encouragement throughout my PhD and express deep gratitude for having provided me with an excellent search environment. At many stages in this research project, I benefited from his advice, particularly so when exploring new ideas. His positive outlook and confidence in my research inspired me and gave me confidence. His careful editing contributed enormously to the production of this thesis. Also, for his essential corrections while I was writing the scientific papers.

I would like to thank the Mechatronics Engineering Department at Kocaeli University. I would like to express my gratitude and deep respect for all my professors for their high educational qualities and teaching competence. Moreover, I would like to thank the Automation and Robotics Research Laboratory (ARRL) research assistants in the Mechatronics Engineering Department at Kocaeli University for their help and encouragement during my PhD.

I would like to thank The Presidency for Turks Abroad and Related Communities, Turkey for the PhD scholarship.

I would like to thank the Scientific Research Projects Coordination Unit (SRPCU) of Kocaeli University for the experimental setup support (Project Number: 389).

I would like to many thanks my wife, Ms. Nasim Aminzadeh, for their social support during the Ph.D. Also, thanks to my laboratory partner, the Tunisian friend Dr. Zied Ben Hazem for his theoretical support.

Finally, I would like to say a big thank to my family, who supported me from afar, but they always felt near in my heart. Thank you very much for your kind support, love and patience. I would especially like to thank my father and my mother, Mohammad Hosein Fotuhi and Ehteram Beygi, who always supported me and they made me feel much healthier after talking to them. Many thanks to my parents for teaching us that hard work and love for what we do are the ingredients for success. Also thank you both for your encouragement to try always for better things. Finally, I would like to thank my father-in-law and mother-in-law, Mohammad Reza Aminzadeh and Nazanin Ghelich, for their unwavering support, which made this way easy for me.

June – 2021 Mohammad javad FOTUHI

TABLE OF CONTENTS

LIST OF FIGURES

LIST OF TABLES

LIST OF SYMBOLS AND ABBREVIATIONS

θ_m	:	motor joint angle (worm gear angle) in the X plane (rad, °)
θ_w	:	worm gear angle in the Y plane (rad, °)
θ_s	:	worm gear angle in the Y plane (rad, °)
θ_l	:	load joint angle in the Y plane (rad, °)
J_{tot}	:	total of rotational inertias in the RSEA (Kg m^2)
J_X, J_Y	:	rotational inertias relative to the X axis and Y axis (Kg m^2)
J_{Xm}, J_{Xw}	:	rotational inertias of the motor and worm gear to the X axis (Kg m^2)
J_{Ys}, J_{Yw}	:	rotational inertias of the spring and worm gear to the Y axis (Kg m^2)
B_{tot}	:	total of damping coefficient in the RSEA
B_X, B_Y	:	coefficient of damping to the X and Y axis
B_{Xm}	:	motor's damping coefficient to the X axis
B_{Ym}	:	damping coefficient of the worm gear to the Y axis
N	:	transmission ratio
τ_X	:	the torque applied to the X axis (Nm)
τ_Y	:	the torque applied to the Y axis (Nm)
τ_m	:	the torque generated by the motor (Nm)
τ_l	:	the torque applied to the load (Nm)
m_l	:	load mass, (Kg)
d_l	:	link distance, (m)
θ_i	:	The angle of the i-th link, (rad, °)
$\dot{\theta}_i$	:	The angular velocity of the i-th link, (rad/s, °/s)
$\ddot{\theta}_i$	:	The angular acceleration of the i-th link, (rad/s^2, °/s^2)
τ_i	:	Torque of the i-th link, (Nm)
I_i	:	Inertia tensor of i-th link, (Kg m^2)
I_{zzi}	:	Z-component of the inertia tensor of i-th link, (Kg m^2)
m_i	:	Mass of the i-th link, (Kg)
m_B	:	Mass of balance mass, (Kg)
L_i	:	Length of the i-th link, (m)
b_i	:	Viscous damping coefficient of i-th link, (N-m-s/rad)
g	:	Gravity, (N kg^{-1})
C_p	:	Viscous friction coefficient of the NCFM, (N-m-s/rad)
B_i	:	Viscous friction coefficient of the LFM, (N-m-s/rad)
C_i	:	Coulomb friction coefficient of the LFM, (Nm)
f_o	:	Zero-drift error of friction torque of the NLFM, (Nm)
f_c	:	Coulomb friction coefficient of the NLFM, (Nm)
f_v	:	Viscous friction coefficient of the NLFM, (N-m-s/rad)
f_a	:	Experimental friction coefficient of the NLFM, (Nm)
f_b	:	Experimental friction coefficient of the NLFM, (Nm)
G_m	:	Gain margin, (dB)
P_m	:	Phase margin, (°)
G_{ff}	:	Fedforward function, (dB)
G_c	:	Controller, (dB)

U	:	Control signal, (V)
T_s	:	Settling time, (s)
MO	:	Maximum overshoot, (%)
MP	:	Maximum peak, (°)
S_{PSO}	:	Soft-PSO algorithm
M_{PSO}	:	Medium-PSO algorithm
H_{PSO}	:	Hard-PSO algorithm
E_{ss}	:	Steady-state error, (°)
Δ_{h_i}	:	Center of gravity vectors of the i-th link
h_i	:	The coordinate vector in the mass center of the i-th link
${}^{i}_{i+1}R$	:	Rotation matrix from a coordinate i-th link to a coordinate *i+1-th* link
J_i	:	Jacobian matrix of the i-th link
$D(\theta)$	:	Mass matrix
$C(\theta, \dot{\theta})$	:	Coriolis and Centripetal force vector
$G(\theta)$	:	Gravity vector
$\tau_f\ (\theta, \dot{\theta})$	:	Friction torque vector
${}^{i-1}_{i}T$	:	Homogeneous transformation matrix from a coordinate attached to an $i\ th$ link to a coordinate attached to *i-1-th*.

Abbreviations

ACE	:	Automation and Control Engineering
ADC	:	Analog-to-Digital Converter
AFHIC	:	Adaptive Fractional Hybrid Impedance Control
AFLC	:	Adaptive Fuzzy Logic Controller
ARRL	:	Automation and Robotics Research Laboratory
AJS-RSEA	:	Ankle joint system driven by a rotational series elastic actuator
BR	:	Bayesian Regularization
DAC	:	Digital -to- Analog Converter
DC	:	Direct Current
DFTFS	:	Double Fibonacci Torsional Flat Spring Design
DH	:	Denavit Hartenberg
DOF	:	Degree of Freedom
EA	:	Elastic Acuator
EAS	:	Elastic Acuator System
EATA	:	Experimental angular torque analysis
FEM	:	Finite element methods
FHIC	:	Fractional Hybrid Impedance Control
FLC	:	Fuzzy Logic Controller
FOC	:	Fractional-Order Controller
FTC-FC	:	Fuzzy Torque Controller with Friction Compensation
FL-FFC	:	Fuzzy Logic Feedforward Controller
IC	:	Impedance Control
HC	:	Hybrid Control
HIC	:	Hybrid Impedance Control
IRR	:	Infinite Impulse Response
LQR	:	Linear Quadratic Regulator
LQG	:	Linear Quadratic Gaussian

LFM	:	Linear Friction Model
MSE	:	Means Squared Error
NCFM	:	Non-Conservative Friction Model
NLCT	:	Non-Linear Control Theory
NLFM	:	Non-Linear Friction Model
PD	:	Proportional Derivative
PID	:	Proportional Integral Derivative
PID-FFC	:	Proportional Integral Derivative – Feedforward Controller
PSO	:	Particle Swarm Optimization
PWM	:	Pulse Width Modulation
RMSEs	:	Root Mean Squared Errors
RMS-PE	:	Root Mean Squared -Position Errors
RMS-FE	:	Root Mean Squared -Force Errors
RSEA	:	Rotary- Series Elastic Actuator
SEA	:	Series Elastic Actuator
SEM-TA	:	Series Elastic Muscle-Tendon Actuator
SFC	:	State Feedback Control
SMC	:	Sliding Mode Control

DEVELOPMENT AND NON-LINEAR CONTROL OF A NOVEL ROTARY SERIES ELASTIC ACTUATOR

ABSTRACT

RSEA (rotary series elastic actuator) is one of the fundamental problems in the control theory field. To verify the modern control theory, RSEA may be considered as a better example in control engineering. The RSEA is a highly non-linear and open-loop unstable system that makes the control more challenging. It is an intriguing subject from the control point of view due to its intrinsic nonlinearity. The RSEA include a nonlinearity due to the frictions in the joints. Common control approaches require a good knowledge of the frictions in the joints of the system and accurate friction estimation to obtain the desired performances of feedback controllers. However, the frictions have high non-linear values, which result in steady-state errors, limit cycles, and poor performance of the system. It has an influence on the system's response, and it should be considered seriously. Therefore, friction estimation has the potential to ameliorate the quality and dynamic behavior of the system. For humanoid/memetic robots, modeling and accurate torque trajectory control of a rotary series elastic actuator (RSEA) is of great importance. In this study, the fuzzy logic torque controller with nonlinear friction compensation (NLFC) is used to improve the deteriorating trajectory tracking performance caused by these nonlinear elements in RSEA systems. In order to demonstrate the power efficiency and performance of the proposed control system, several experiments have been performed on the experimental setup, including a torque motor with worm gear and torsional flat-double spiral spring (TFDSS). The proposed novel RSEA is designed and tested using different controllers, including PID feedforward controller (PID-FFC), fuzzy logic feedforward controller (FL-FFC), and fuzzy torque controller with friction compensation (FTC-FC). A comparative study among controllers is conducted to show the robustness of FTC-FC against a step and ramp-type disturbances. The simulation and experimental results here strongly confirm that the proposed control method produces better control performance.

Another aim of this thesis is to develop non-linear controllers for the impedance control problems. In this paper, a new fuzzy adaptive fractional hybrid Impedance (FAFHI) control approach is developed for high-sensitive contact stress force tracking control of the rotary series elastic actuators (RSEAs) in rugged terrains. The aim of this study is to obtain an adaptive hybrid impedance control model (AHICM) which depends on both position and torque in a large range of motion trajectory that involves difficult and sudden large changes. In three different cases, the fractional parameters of the FAFHI control were optimized with the particle swarm optimization algorithm (PSO). Its adaptability to the pressure of the sole of the foot on real environments such as grass (soft), carpet (medium), and solid floors (hard) is far superior to traditional impedance control. Hence, the torque error triggered by the time-varying stiffness environment can be compensated by using our fuzzy adaptive algorithm. Simulations are tested on an RSEA, in order to verify the torque control accuracy as well as its robustness in terms of a time-varying stiffness environment. Both the simulation and the experiment show that our proposed control scheme has a better performance on

maintaining the desired contact force than hybrid impedance (HI) control and fractional hybrid impedance (FHI) control.

Keywords: Rotary Series Elastic Actuator System (RSEA), Fuzzy Torque Controller with Friction Compensation (FTC-FC), Nonlinear Friction Estimation Model (NLFEM), Fractional Hybrid Impedance Control (FHIC), Adaptive Fractional Hybrid Impedance Control (AFHIC).

YENİ BİR DÖNER SERİSİ ELASTİK AKTÜATÖRÜN GELİŞTİRİLMESİ VE DOĞRUSAL OLMAYAN KONTROLÜ

ÖZET

RSEA (döner seri elastik aktüatör), kontrol teorisi alanındaki temel problemlerden biridir. Modern kontrol teorisinde doğrulama yöntemi olarak kullanılabilecek iyi bir sistem örneği olarak düşünülebilir. RSEA, kontrolü daha zor hale getiren, doğrusal olmayan ve açık döngü kararsız bir sistemdir. Doğrusal olmaması nedeniyle kontrol teorisi açısından ilgi çekici bir konudur. RSEA, eklemlerdeki sürtünmelerden kaynaklanan doğrusal olmama durumunu içermektedir. Genel kontrol yaklaşımları, geri besleme kontrolörlerinin istenen performanslarını elde etmek için sistemin bağlantı noktalarındaki sürtünmeler hakkında bilgi ve doğru sürtünme tahmini gerektirmektedir. Bununla birlikte, sürtünmeler yüksek doğrusal olmayan değerlere sahiptir, bu da kararlı durum hatalarına, limit döngülere ve sistemin zayıf performansına neden olmaktadır. Bu nedenle sürtünme tahmini, sistemin kalitesini ve dinamik davranışını iyileştirme potansiyeline sahiptir.

İnsansı/memetik robotlar için, döner seri elastik aktüatörün (RSEA) modellenmesi ve doğru tork yörünge kontrolü büyük önem taşımaktadır. Bu çalışmada, RSEA sistemlerinde bu doğrusal olmayan elemanların neden olduğu bozulan yörünge izleme performansını iyileştirmek için doğrusal olmayan sürtünme kompanzasyonuna (NLFC) sahip bulanık mantık tork kontrolörü kullanılmıştır. Önerilen kontrol sisteminin güç verimliliğini ve performansını göstermek için, deney düzeneği üzerinde sonsuz dişli ve burulma düz-çift spiral yaylı (TFDSS) bir tork motoru da dahil olmak üzere çeşitli deneyler yapılmıştır. Önerilen yeni RSEA, PID ileri beslemeli kontrolör (PID-FFC), bulanık mantık ileri beslemeli kontrolör (FL-FFC) ve sürtünme dengelemeli bulanık tork kontrolörü (FTC-FC) dahil olmak üzere farklı kontrolörler kullanılarak tasarlanmış ve test edilmiştir. FTC-FC'nin adım ve rampa tipi bozulmalara karşı sağlamlığını göstermek için kontrolörler arasında karşılaştırmalı bir çalışma yapılmıştır. Buradaki simülasyon ve deneysel sonuçlar, önerilen kontrol yönteminin daha iyi kontrol performansı ürettiğini kuvvetle doğrulamaktadır.

Bu tezin bir diğer amacı, empedans kontrol problemleri için doğrusal olmayan kontrolör geliştirmektir. Bu yazıda, engebeli arazilerde döner seri elastik aktüatörlerin (RSEA'lar) yüksek hassasiyetli temas stres kuvveti izleme kontrolü için yeni bir bulanık uyarlamalı kesirli hibrit empedans (FAFHI) kontrol yaklaşımı geliştirilmiştir. Bu çalışmanın amacı, zor ve ani büyük değişimler içeren geniş bir hareket yörüngesinde hem pozisyona hem de torka bağlı olan adaptif bir hibrit empedans kontrol modeli (AHICM) elde etmektir. Üç farklı durumda, FAFHI kontrolünün kesirli parametreleri parçacık sürüsü optimizasyon algoritması (PSO) ile optimize edilmiştir. Yumuşak (çim), orta (halı) ve sert zemine sahip gerçek ortamlarda ayak tabanının basıncına uyarlanabilirliği, geleneksel empedans kontrolünden çok daha üstündür. Bu nedenle, zamanla değişen sertlik ortamı tarafından tetiklenen tork hatası, bulanık uyarlamalı algoritmamız kullanılarak telafi edilebilmektedir. Simülasyon sonuçları, zamanla değişen bir sertlik ortamı açısından tork kontrol doğruluğunu ve sağlamlığını

doğrulamak için bir RSEA üzerinde test edilmiştir. Hem simülasyon hem de gerçek zamanlı deney sonuçları, önerilen kontrol şemasının, istenen temas kuvvetini koruma konusunda hibrit empedans (HI) kontrolü ve kesirli hibrit empedans (FHI) kontrolüne göre daha iyi bir performansa sahip olduğunu göstermektedir.

Anahtar Kelimeler: Döner Seri Elastik Aktüatör Sistemi (RSEA), Sürtünme Dengelemeli Bulanık Tork Kontrolörü (FTC-FC), Doğrusal Olmayan Sürtünme Tahmin Modeli (NLFEM), Kesirli Hibrit Empedans Kontrolü (FHIC), Uyarlanabilir Kesirli Hibrit Empedans Kontrolü (AFHIC).

INTRODUCTION

In recent years, many researchers have focused on developing humanoid/memetic robots that have grown dramatically [1]. These robots are used to perform dangerous and difficult tasks for human life in various projects in real life [2]. Their joints must be capable of absorbing high impact force, producing maximum force/torque, and reasonable acceleration. The limitations of these physical parameters can be enhanced with a usage of elastic actuator systems used in many robotic applications. Compliant manipulation [3], rehabilitation systems [4,5], exoskeletons [6], humanoid robots [7,8], haptic devices, interaction systems of human-robot, and active human orthosis, and prosthesis are examples of applications using serial actuators. The joints driven by a series elastic actuator system (SEAs) have compatible behavior, which tends to reduce the impedance of mechanical output [9]. In addition, the control performance of the serial actuator systems differs from rigid systems. Also, the output force is easier to control, though control of position is a challenge. There are two main methods of closed-loop SEA force control systems [10]. The first one is the use of strain gauge force sensors, and the second one is measuring the amount of elastic component deflection and applying Hooke's law [11]. Although the use of force sensors may increase measurement accuracy, these sensors are expensive, and installing and reading these devices is further complicated. Therefore, a simple position sensor should be employed for measuring the deviation of the elastic part in SEA systems.

SEAs have been used frequently in many areas such as bio-mechatronic, humanoid, and memetic robotics. Brooks et al. [12,13] developed firstly the COG robot employing with the SEA. In [14], the design of the SEA was examined through the elastic element in the propulsion. The advantages of the elastic element in terms of greater shock tolerance, accurate and stable force output, and energy storage ability were presented in [15]. Due to the elasticity behaviors of the SEAs, the torque, position, and stiffness of the SEA are changing time dependently. Therefore, the interaction control with SEA is very important in the field of robot-robot, robot-

human, and robot-machine interaction [16,17]. In order to study the dynamics of the robot's legs in the literature, different pendulum systems have been used as an analogy.

The trajectory tracking error is dependent on the effects of the nonlinear elements such as backlash, friction, and quantization in the control loop. The increase of these effects causes deterioration of the accuracy and control bandwidth of the RSEA force control. In the legged locomotion system, the control of the torque is essentially required in an unstructured environment. If only position control is applied in RSEA, the robot may not be able to maintain the desired force applied to the environment. High performance torque control is needed for complex structured robotic applications in uncertain environments [18].

Series Elastic Actuator (SEA) has been widely used for legged robots, haptics, and rehabilitation robots. SEA is often preferred for these properties: robustness, high power density, and high-bandwidth control performance which allows the implementation of impedance control. The impedance control of Rotary Series Elastic Actuators (RSEA) has been an interesting research area in the last few years. In the literature, many novel approaches for impedance control have been developed [19, 20]. Nowadays, the torque control approaches are classified as either Impedance Control (IC) or Hybrid Control (HC). The approaches classified as impedance control [21] do not attempt to explicitly control torque but to control the relationship between the force and position at the end of the ankle in contact with the environment [22]. Hence, position control leads to applied force control. Alternatively, HC separates the robotic force task into two subspaces, the first one is the force control subspace and the second one is the position control subspace [23]. Two independent controllers are required for each subspace. In [24], they developed a novel method to combine the two algorithms into a one control algorithm strategy. This approach can be called the hybrid impedance controller (HIC) which combines HC and IC strategies and can be reduced to either approach. HIC can separate the task space into two subspaces, an impedance-controlled, position subspace and an explicit force-controlled subspace [25, 26] The fractional-order dynamic systems and controllers have been a part of different science/engineering disciplines for many years. Fractional-Order Controllers (FOC) is defined by the fractional-order

differential equations. Using the derivatives and integrals operations in fractional orders may be adjusted for the frequency response of the control system directly and continuously (Oh and Kong, 2016). The controllers based on fractional-order derivatives and integrals are usually used in industrial applications and other various fields such as system identification, haptic, power electronics, robotic arms, and magnetic levitation system control [27, 28]. It should be noted that the behavior of many physical systems can be determined using FOC theory and can be controlled with FHIC even if the system has unstable or time delay behaviors. [29, 30]. The FOC for a HIC extends the controller to the fractional hybrid impedance controller, in order to yield a robust and stable force control system. Moreover, many aspects needed to be taken into account when designing these controllers. Controller parameters optimization in linear and nonlinear systems is quite difficult. There is a need for an effective and efficient global approach to optimize these parameters automatically. The particle swarm optimization (PSO) algorithm was used to estimate the optimal parameters of the FHI controller [31]. PSO is an evolutionary algorithm that can be used to find the optimal solutions in a large search space. PSO algorithm is particularly used for parameter optimization in a continuous and multi-dimensional search space. The PSO technique converges faster than other optimization techniques and generates a high-quality solution in a short time [32]. Furthermore, the implementation of PSO is easily comparable to other metaheuristic optimization algorithms.

In this study, the RSEA's torque control based on the nonlinear model was developed to establish a stable and robust performance. Firstly, a dynamic model of the RSEA was derived considering frictional forces, uncertainties, and disturbances. Then, the friction estimator model for the nonlinear frictions in RSEA was added to the control structure. A novel fuzzy torque controller with friction compensation (FTC-FC) was developed and tested in RSEA.

In summary, the main contributions of this work are: (i) obtaining less trajectory tracking error by nonlinear estimation of the frictions that occur in joint bearings and worm gear of the legged mechanism. (ii) providing high accuracy trajectory control by using fuzzy logic control (FLC) structure when actuators are subjected to nonlinear loads/effects in legged robots.

In this work, a novel FHIC approach is developed with a fractional order controller for the SEM-TA. The FHIC parameters are tuned with the PSO algorithm. This work proposed fractional hybrid impedance control (FHIC) for high-sensitive contact stress force tracking in uncertain environments [33]. The main goal of such a controller is to avoid the force overshoots in the contact stage while keeping stress force error in the high-sensitive tracking stage, where traditional control algorithms are not competent. Moreover, the FHIC is presented here mainly in order to cater to a sensitive fractional behavior. Its adaptability to the pressure of the sole of the foot on real environments such as grass (soft), carpet (medium), and solid floors (hard) is far superior to traditional impedance control [34]. It allows precise force (or torque) mode control. Using this control method, the design of higher-level controls for human-robot interaction can be achieved easily [35]. The proposed control model consists of an outer concept position control loop that generates the reference acceleration to an inner force control loop. The performance of the controllers is examined according to these parameters: MO, E_{ss}, T_s, and RMSE of the positions. Moreover, robustness analysis of the controllers here are compared for three different cases. The simulation and an experimental works are developed to validate the performance of the proposed controller. According to the comparative study results, the responses of controllers in simulation and experimental cases are very similar.

In this work, three different friction estimation models such as Non-Conservative, Linear and Nonlinear friction models are compared to estimate the joint frictions of the RSEA developed in our laboratory [36]. NCFM considers only viscous frictions. LFM is dependent on Coulomb and viscous frictions. The NLFM is the sum of five types of frictions: the zero drift error of friction, the Coulomb friction, the viscous friction, and two experimental frictions[37]. Based on comparative experimental friction analysis, the joint frictions of the RSEA are estimated more effectively using an NLFM. Moreover, In order to determine the estimation performance of the friction models, RMSEs between position simulation results obtained from each joint friction model and encoders in the experimental setup are computed. Based on the RMSEs' position, the NLFM produce better estimation results than the LFM. Among NLFM, the LFM gives the best results.

The first chapter deals with the overview of the EA: working principles, types, classification and application of the EAS are described. A detailed literature survey of EAS is provided, and the structure of the RSEA is investigated. Definition and contributions of the thesis are presented.

The second chapter design and modeling of RSEA are introduced, the DFTFS and the investigates kinematic model, nonlinear dynamic model, and dynamic simulation of the RSEA systems. The kinematic model of system is derived based on the DH convention. Rotation and homogeneous transformation matrices between coordinates are calculated. The nonlinear dynamic equations of system is obtained by the Newton-Euler method and explained in details. The nonlinear dynamic equations are obtained based on the calculated rotation and homogeneous transformation matrices. Dynamic comparison between the obtained results from both nonlinear mathematical and the Matlab/SimMechanics models is described. Finally, inertia analysis of the vertical arms of the RSEA is given.

In the third chapter, approaches to estimate the joint friction coefficients of joint link rotary is explained in detailed. Three NCFM, LFM, NLFM are compared to estimate the joint frictions of the RSEA developed in our laboratory.

In the fourth chapter, torque and impedance control problems of the RSEA, systems are explained. PID-FFC, FL-FFC, and FTC-FC torque-based HI, FHI, AFHI controllers are developed for impedance control problem of the RSEA. Furthermore, FL-FFC and FTC-FC controllers are developed using fuzzy logic to torque control of RSEA. The robust control structure, including the fuzzy feedforward, is designed to provide an efficient torque controller. Then the efforts of the torque controller and estimated nonlinear frictions from the velocity of the joint are computed. Furthermore, the proposed control structure is compared with other complicated torque controllers. AFHI controller is developed using fuzzy logic to impedance control of RSEA. Presents the hybrid impedance controller. Analysis of the steady-state error and tuning of the FHIC using PSO algorithm are explained. The dynamic responses of the controllers were compared based on robustness analysis such as under noises, internal and external disturbances.

The last chapter focuses on experimental studies. The torque control of a RSEA with NLFM and impedance controls are verified in real experimental setups. The results obtained experimentally are compared with simulation results.

1. ELASTIC ACTUATOR SYSTEM

1.1. Introduction

The reviews existing in literature are undertaken as a part of the RSEA project. It is focused to understand: the background and the principal application of the EAS, the nonlinear analytic mathematical model, numerical mechanical simulation model, mechanical design aspects, friction models, control algorithms, and other successful projects of the similar nature. The EAS is a classic model of the nonlinear control topic. It is used frequently to study the design, implementation and control development for nonlinear systems. The EAS appears in the undergraduate control textbooks, for example, it is used as an example to describe the physical systems mathematically by Dorf and Bishop [38]. The physical analysis of the EAS has been an important consideration in the modern control theory studies [39]. The control of the EAS, for which different configurations exist, is a very complicated task. it has provided the best demonstration of the capabilities of the scientific and engineering area [40]. In the past years, motion control has focused on a fast and a precision positioning of motors or manipulators since robot mission was rapid manufacturing or improving product quality in automated producing processes. Recently, service robots such as human assistive robots or rehabilitation robots are receiving attention from many researchers [41, 42]. However, there are still a large number of challenging problems. Service robots, unlike the industrial robots, has interaction with uncertain environments such as human body, and thus should be able to observe the external force and also absorb the impact for safety not only of humans but also of the robot itself. From this requirement, compliant actuation using elastic actuators has received much attention in this filed. One of the most widely-used elastic actuator is series elastic actuator (SEA). SEA, firstly introduced by Pratt [43] in 1995, contains series elasticity between the motor and the load. By using two position sensors (e.g., encoder) to measure deformation of the elastic component and the control of the deformation, force control can be achieved without using any force sensors.

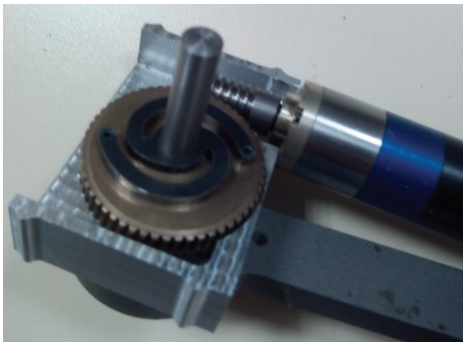	
Torsional spring Worm gear	Torsional spring Timing belt
	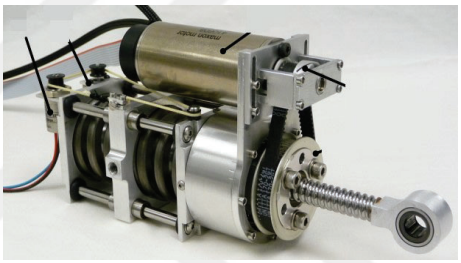
Compression spring Cable driven	Compression spring Ball screw

Figure 1.1. Various Type of SEAs in robotic application

In the past 20 years, many researchers have come up with various mechanisms to realize high performance compliant actuators proposing various configuration for SEA [44, 45]. As a result (see Figure. 1.2), various configurations of SEAs are world widely developed to satisfy their application requirements. Figure 1.1 shows some representative SEA mechanisms including University of Texas - Series Elastic Actuator (UT-SEA) [46], compact Rotary Series Elastic Actuator(cRSEA) [47], Bowdencable-based series elastic actuator [48] and Valkyrie's series elastic actuators [49].

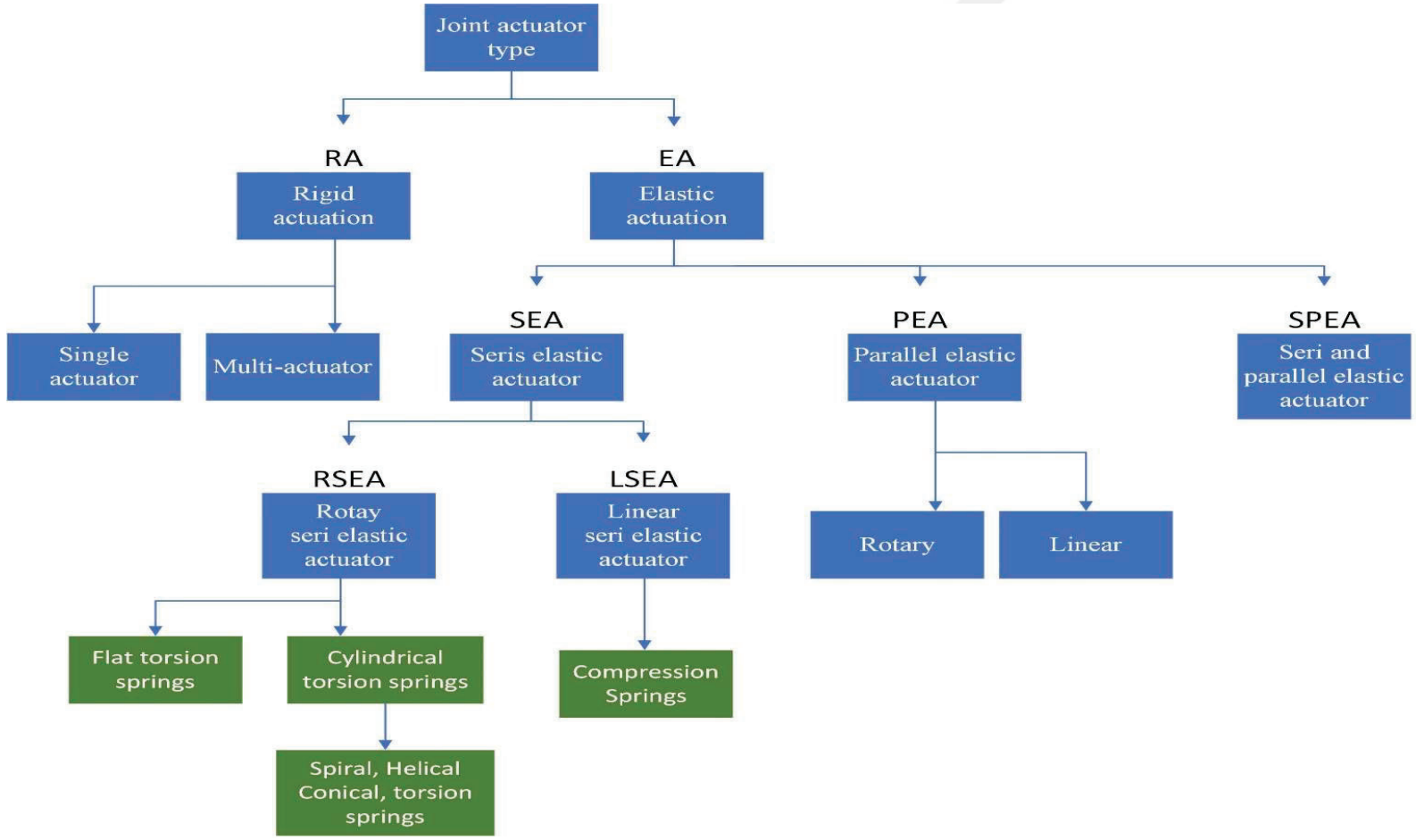

Figure 1.2. Classification of the SEA according to the actuator configuration

These mechanisms have their own drawbacks: UT-SEA chose the ball-screw as drive-train [50], so it converts the rotary motion of the motor to the linear motion of the load. Since the spring in RFSEA is designed to have very high stiffness, it needs high resolution encoders for precision force sensing. cRSEA consists of the small torsional spring with worm gear, and this leads to compactness of whole-body size. However, the small rotary spring in cRSEA can cause some attachment issues which can end up with large backlash. This backlash leads to large dead zone in the spring deformation and significantly deteriorates the precision force/position control of cRSEA.

Table 1.1. A comparison of major actuation technologies

Actuation type	Maximum force	Maximium speed	Low force ability	Position controllability	Back-driveability
Pneumatic	Medium	Meduim	Fair, stiction	Poor	Fair
Hydraulic	High	Medium	Poor, stiction	Good	Poor
Direct drive electric	Low	High	Excellent	Good	Excellent
Electric gear motor	Medium/ high	High	Poor, friction	Good	Poor
Electric series elastic actuator	Medium/ high	High	Excellent	Good	Excellent
Hydraulic series elastic actuator	High	Medium	Excellent	Good	Excellent

In Table 1.1 the series elastic actuators are compared with traditional actuation methods. Series elasticity improves the force fidelity of gear motors and hydraulics so they are comparable to direct drive motors without sacrificing high force/torque capabilities [51]. In this research, a novel mechanism for SEA is developed to provide high control performance while keeping the size compact. To achieve better performance and versatility of SEA, the following features are particularly taken into account in this research:

1) Minimized backlash of gear train

2) Spring linearity

3) Compactness of actuator

1.2. Series elasticity

Series Elastic Actuator (SEA), a variable impedance actuator (VIA), is an actuator that is highly regarded as the next-generation actuator [51]. Since SEA was first introduced in 1995, SEA is now recognized in the robotics field as an actuator system for high-performance torque control [52].

Table 1.2. Classification of SEAs in terms of types of transmission and types of movements

SEA classification		Transmission type	
		Gear	Wire
Output movement type	Linear	(a) SEA of MIT	(e) RSEA
		(b) UT-SEA	(f) CDSEA
	Rotary	(c) cRSEA	(g) BCDSEA
		(d) cPEA	(h) MARIONET

Table 1.2 shows various types of SEAs, that can be categorized in terms of the transmission type and movement type. The SEAs which are categorized in terms of the types of transmission and the types of motion. (a) Series Elastic Actuator [45], (b) University of Texas-Series Elastic Actuator [46], (c) compact Rotary Series Elastic Actuator [48], (d) compact Planetary-geared Elastic Actuator [49], (e) Rotary Series Elastic Actuator [50], (f) Cable Driven Series Elastic Actuator [51], (g) Bowden Cable Driven Series Elastic Actuator [18] and (h) Series elastic actuator of MARIONET [52]. This classification is more of a kinematic classification than a dynamic classification, which can be used to display and compare SEA output motion. SEA dynamic performance cannot be compared or categorized using this standard. This dynamic classification of SEAs needs to provide some insights and criteria for the dynamic characteristics of SEAs that can be reflected in the design of SEA mechanisms and controllers.

The SEA is classified into three types according to the relative position of the spring with regard to the gear: Force-sensing Series Elastic Actuator (FSEA) which locates the spring after the transmission gear, Reaction Force-sensing Series Elastic Actuator (RFSEA) which locates the spring before the transmission gear and Transmitted Force-sensing Series Elastic Actuator (TFSEA) which locates the spring inside the transmission gear.

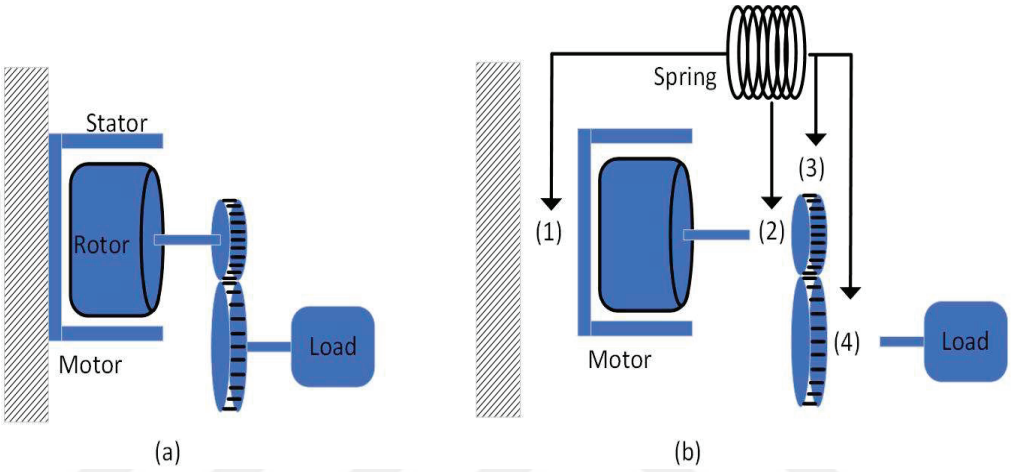

Figure 1.3. (a) Rigid Actuator; (b) Series Elastic Actuator

This work categorizes SEA configuration into three types based on the position of the spring as follows. Reaction Force-sensing Series Elastic Actuator (RFSEA) spring located at (1) or (2), before the transmission Transmitted Force-sensing Series Elastic Actuator (TFSEA) spring located at (3), inside the transmission Force-sensing Series Elastic Actuator (FSEA) spring located at (4), after the transmission.

Since most of actuator system consists of the motor (see Figure. 1.3), the load and the transmission (gear box) as in Figure. 1.4, the overall motions of this actuation system consist of two angles: θ_m , the motor angle and $\theta_l$the load angle [52]. These two angles are kinetically coupled by the gear train as

$$\theta_l = N_m^{-1}\theta_m \,, \tag{1.1}$$

where N_m is the gear ratio of the gear train. This kinematic chain constrains the movement between $\theta_m$with θ_l , and thus the motion of θ_l is coupled by the motion of θ_m , which determines the degree of freedom of the system down to 1.

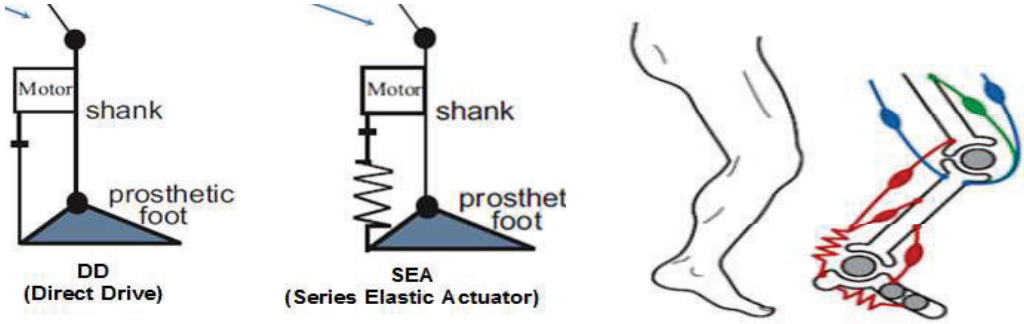

Figure 1.4. Direct drive and series elastic actuator

Whereas, the general way to achieve elastic actuation which is to place the elasticity between the load and the motor (see Figure. 1.5, and Figure. 1.6), which was proposed by Pratt as the basic configuration of SEA [52].

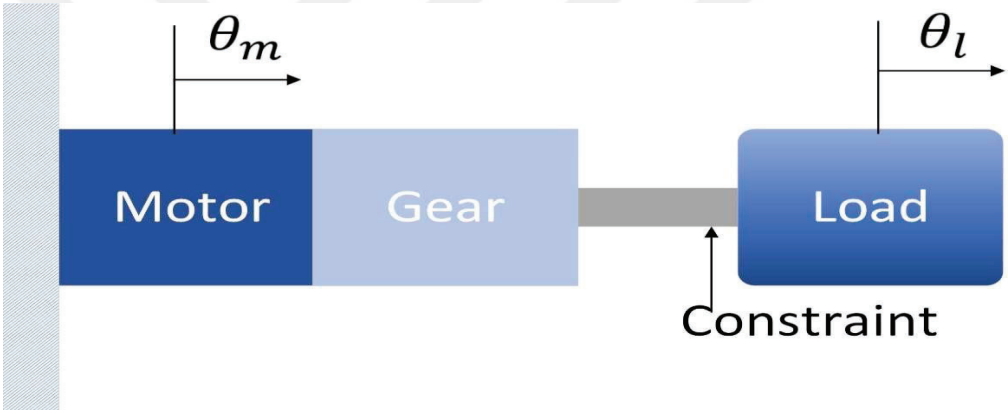

Figure 1.5. Rigid actuation with directly connected load

In the configuration of SEA, there are three degrees of freedom in its motion, which is represented by the motion ofθ_m , θ_l and θ_s .

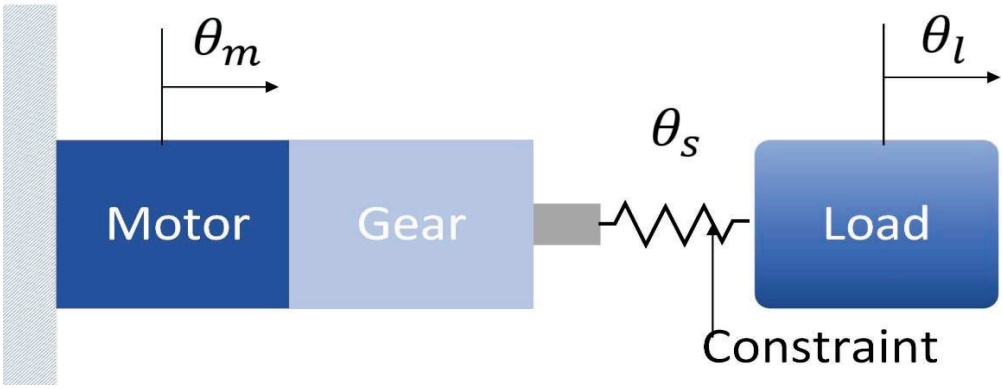

Figure 1.6. Series elastic actuation with the spring placed between the gearbox and the load

These motions have the following kinematic constraint.

$$\theta_s = N_m^{-1}\theta_m - \theta_l \tag{1.2}$$

In other words, SEA originally has three degrees of freedom and one kinematic constraint in its motion, which can be considered as the differential mechanism.

1.2.1. Force-Sensing Series Elastic Actuator (FSEA)

FSEA, is a SEA which combines a motor, a reduction gear, a spring and a load in this order so that the spring can directly measure the force from the load. This structure, which was proposed as the structure of the initial SEA, has been adopted as the configuration of many SEA designs. In the Figure 1.7 to Figure 1.12, the detail of FSEA configuration is illustrated, where the motor stator is attached to ground to provide absolute force to the transmission, and the amplified force by the transmission drives the spring deformation to generate spring force/torque. In other words, the force/torque output of SEA is the spring torque, which can be controlled by the motor torque. Notice that the external force from the load side can directly affect the spring deformation too. The proposed generalized dynamic model of SEA is derived and validated through the following process.

The following three different SEAs are selected as representatives of the proposed three SEA configurations, and dynamic model of each SEA is examined.

FSEA—Compact Rotary SEA (cRSEA) proposed in [46]

RFSEA—UT-SEA (RFSEA) proposed in [49]

TFSEA—Compact Planetary-geared Elastic Actuator (cPEA) proposed in [52]

A generalized dynamic model is proposed, and it is shown that all the SEAs with the different SEA configurations can be modeled using the generalized dynamic model.

Transfer functions of SEA (from the motor torque to the load angle, from the motor torque to the spring deformation and so on) are derived using the derived dynamic model.

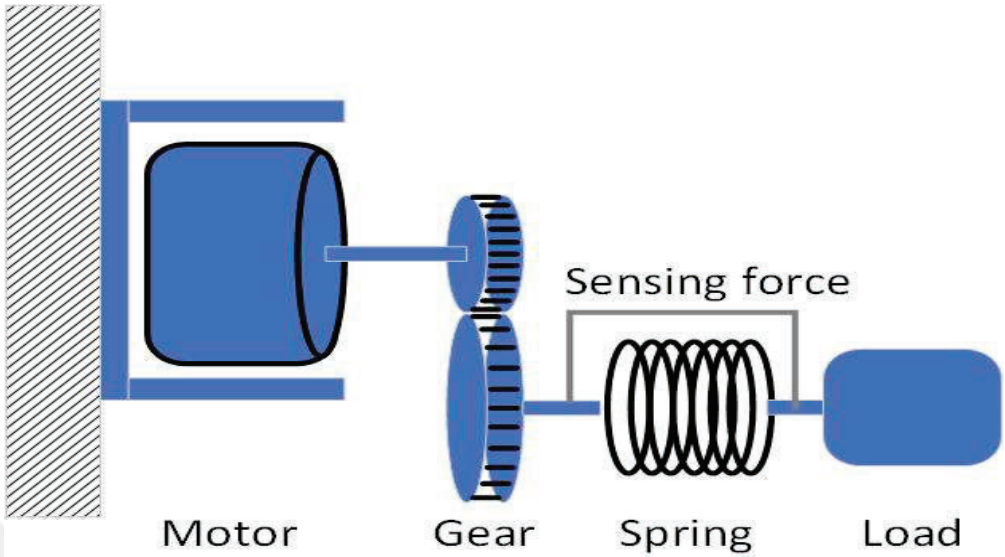

Figure 1.7. Configuration of Force-sensing Series Elastic Actuator (FSEA)

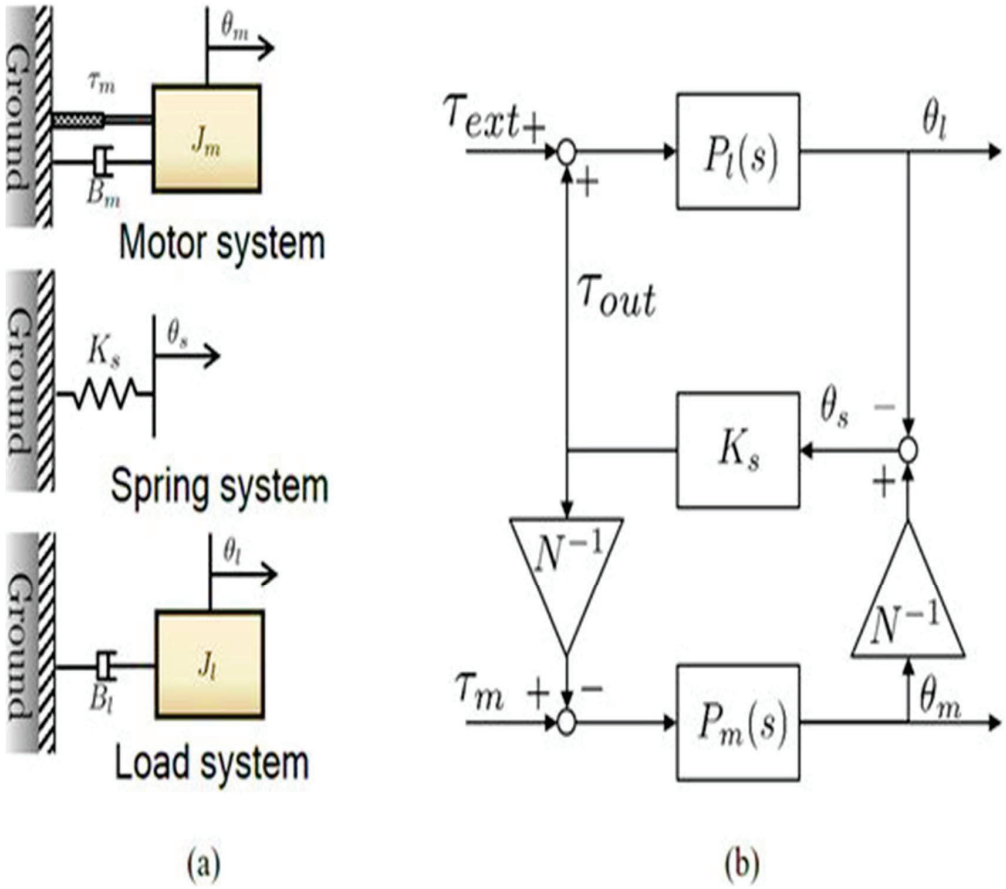

(a) (b)

Figure 1.8. Dynamic modelling of FSEA. (a) Free-body diagrams of FSEA and (b) block diagram representation of FSEA dynamics.

1.2.2. Reaction Force-Sensing Series Elastic Actuator (RFSEA)

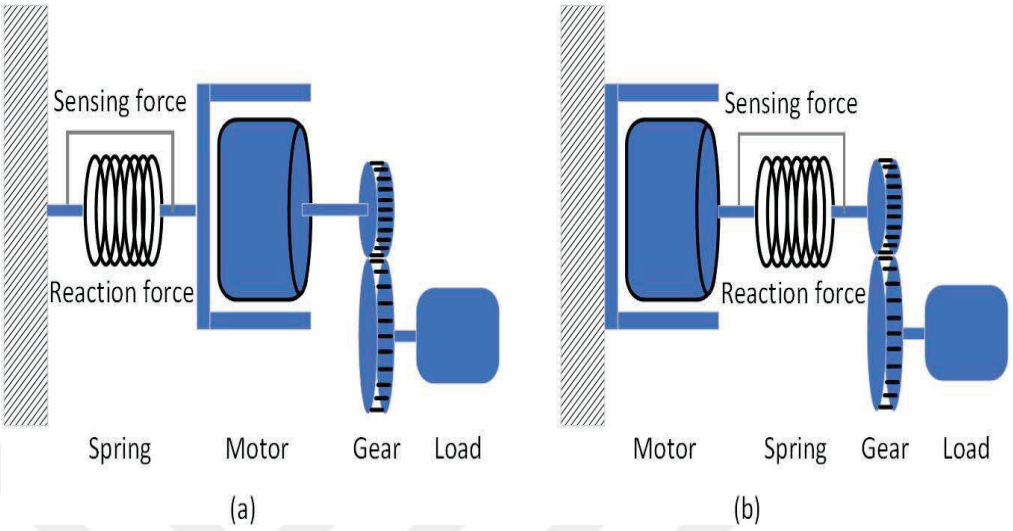

Figure 1.9. Configurations of Reaction Force-sensing Series Elastic Actuator (RFSEA). (a) "motor reaction force" sensing type and (b) "gear reaction force" sensing type.

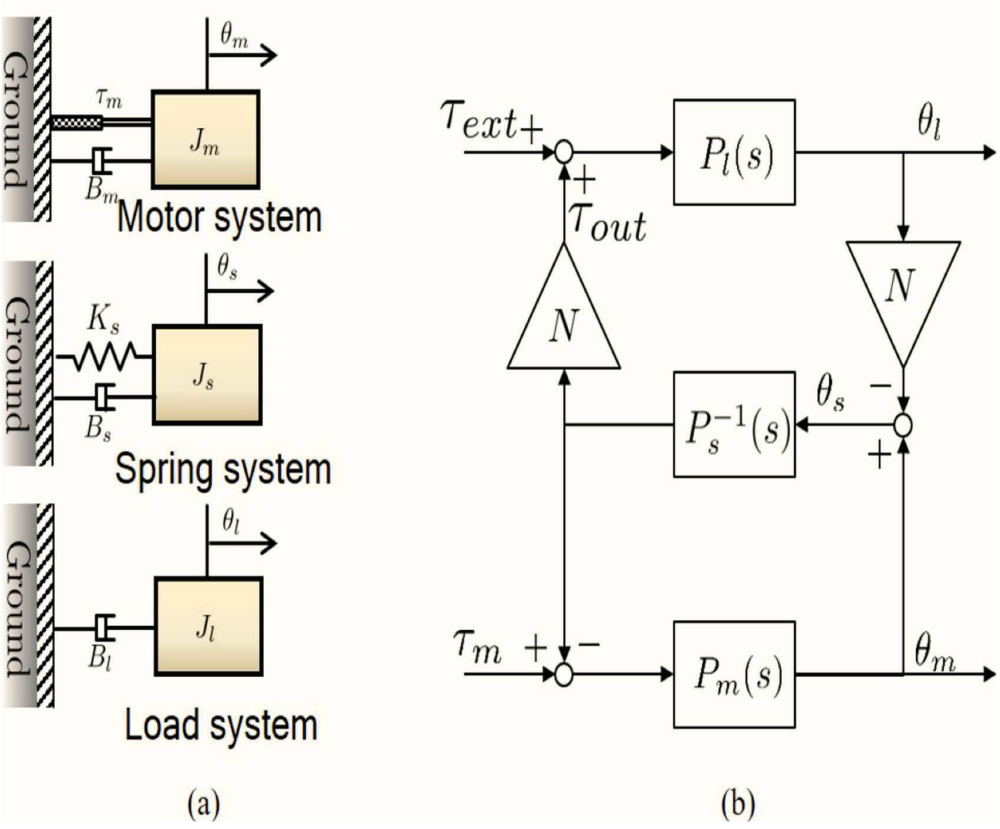

Figure 1.10. Dynamic modelling of RFSEA. (a) free-body diagrams of RFSEA and (b) block diagram representation of RFSEA dynamics.

1.2.3. Transmitted Force-Sensing Series Elastic Actuator (TFSEA)

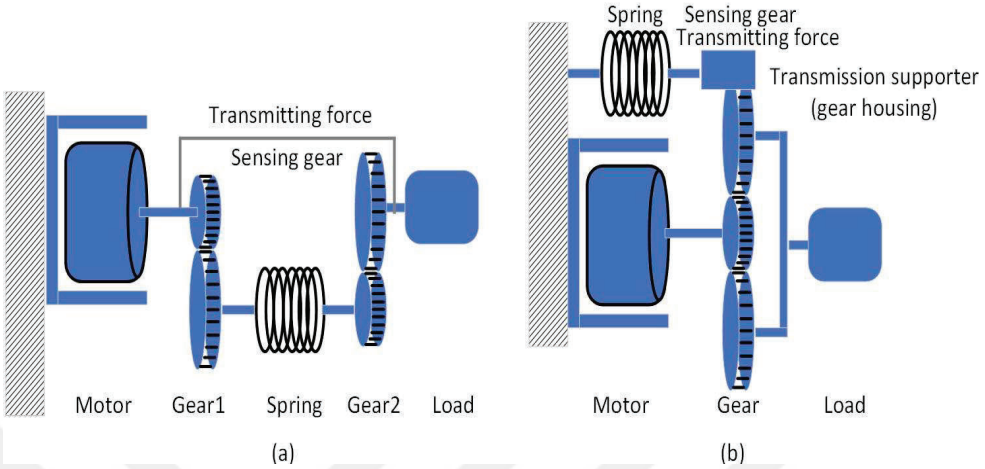

Figure 1.11. Configurations of Transmitted Force-sensing Series Elastic Actuator (TFSEA). (a) "internal transmitted force of gear" Sensing type and (b) "external transmitted force of gear" Sensing type.

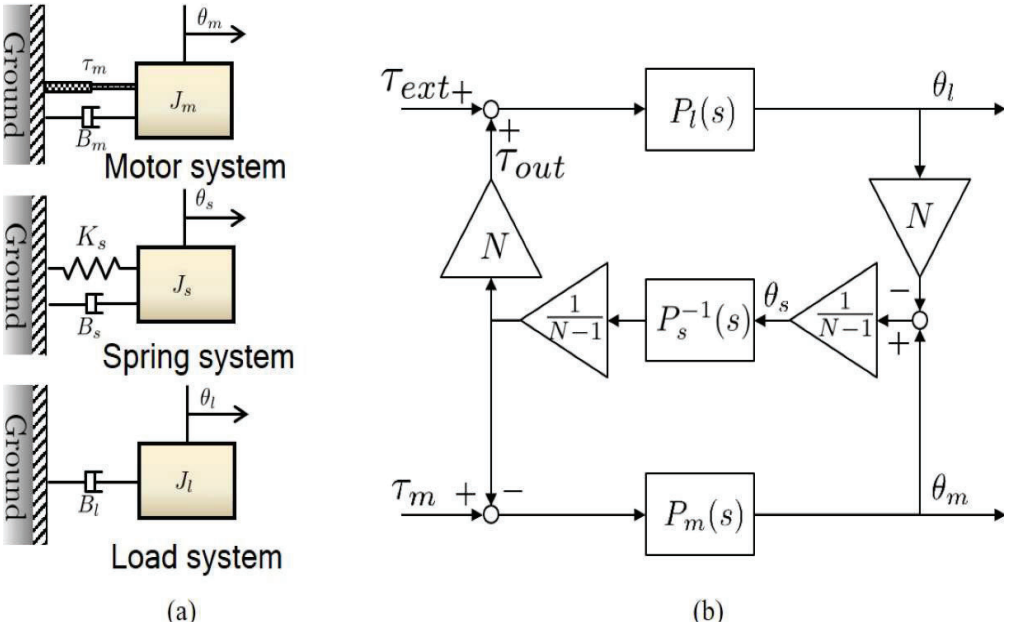

Figure 1.12. Dynamic modelling of cPEA. (**a**) free-body diagrams of cPEA and (**b**) block diagram representation of cPEA dynamics

Several studies to consider had sought to evaluate the performance of the compliant actuator. Tagliamonte et al. [53] attempted to numerically compare the performance of a double actuated VIA with the concept of "power/mass" or "power/volume" depending on the position of the spring. Robinson et al. [54] proposed a criterion of

the Large Rorque Bandwidth (LTB) that can evaluate the performance under the large force command by using simple model of force-controlled SEA. In a similar study, Maximum Torque Transmissibility (MTT), which is the criterion for defining the maximum force generation performance from the viewpoint of velocity limitation, is presented by using the dynamics of FSEA under force control [55].

In this section, three criteria to represent the characteristics and performance of SEA are proposed using the proposed generalized dynamic model. The three SEA configurations are compared based on the proposed assessment criteria. An actuator system as an ideal force source is supposed to deliver accurate force to the load while it can react to any type of external forces sensitively and safely. This defines the requirements for SEA as: (1) the generation of accurate and efficient forces, and (2) the sensitive and safe response to external forces. One of the advantages of SEA, energy storing, is an important factor that should be considered as a criterion. However, by considering the governing equation of the spring potential energy, the energy storing characteristic depends on the behavior of the spring itself, not on the structural differences of SEA. Therefore, energy storage is not considered in this paper which mainly deals with the performance differences caused by the relative placement among the spring, the gearbox and the motor.

1.3. Objectives and Contributions of the Thesis

The main purpose of this research is to design an RSEA with a special flat spring made of titanium and to develop a hybrid impedance control and torque control of a RSEA with nonlinear friction models. RSEA system has been developed in the ARRL, in the Mechatronics Engineering Department part of the Faculty of Engineering at Kocaeli University. In reality, the control of RSEA attached to a rotary elastic link seems to be impossible. But nowadays, according to computer control power, can give the ability to torque and impedance control. The system can be used in rehabilitation systems ans robotic legs. Physically, the system must be robust enough to permit people to attempt balancing the joint manually to give them a better idea about the degree of difficulty applied in the control method phase. The system is a highly nonlinear and open-loop unstable system that makes control more challenging. It is an intriguing subject from the control point of view due to its

intrinsic nonlinearity. On the other hand, the system includes a nonlinearity caused by the existing frictions in the joints. Common control approaches require a good knowledge of the frictions in the system's joints and accurate friction estimation to obtain desired performances of feedback controllers. However, the frictions have high nonlinear values resulting in steady-state errors, limit cycles, and poor performance of the system [56]. It has an influence on the system's response that must be taken seriously. Moreover, friction estimation ameliorates the system's quality and dynamic. In this project, NFFEMs are developed to estimate the joint friction coefficients in our system. The main contributions of this work are: (i) obtaining less trajectory tracking error by nonlinear estimation of the frictions that occur in joint bearings and worm gear of the legged mechanism. (ii) providing high accuracy trajectory control by using fuzzy logic control (FLC) structure when actuators are subjected to nonlinear loads/effects in legged robots. The main goal of such a controller is to avoid the force overshoots in the contact stage while keeping stress force error in the high-sensitive tracking stage, where traditional control algorithms are not competent. Moreover, the FHIC is presented here mainly in order to cater to a sensitive fractional behavior. Its adaptability to the pressure of the sole of the foot on real environments such as grass (soft), carpet (medium), and solid floors (hard) is far superior to traditional impedance control.

2. SYSTEM MODELING AND DYNAMIC SIMULATION

In this chapter, kinematic, nonlinear dynamic models of RSEA model is explained in details. The kinematic parameters of each model are described corresponding to its design. The kinematics model was derived using an adaptation of the DH convention. The nonlinear dynamics model was derived based on the Euler-Lagrange formulation. Furthermore, rotation and transformation matrices of the kinematics model are used to determine the dynamic model. To verify the mathematical model of a system, a numeric model is developed using the Matlab/SimMechanics toolbox. A comparison of the RSEA joint positions obtained from the mathematical and Matlab/SimMechanics model of each system are explained. Finally, in order to examine the effects of the inertia of the RSEA links, the dynamic equations of the RSEA were solved and simulated in three different inertia cases.

2.1. Design and Modeling of the RSEA

The ankle joint system driven by a rotational series elastic actuator (RSEA) is depicted in Figure 2.1. AJS-RSEA is an experimental training setup for the Human ankle model. The design specifications of the RSEA based on the ankle of AJS-RSEA are summarized in Table 2.1.

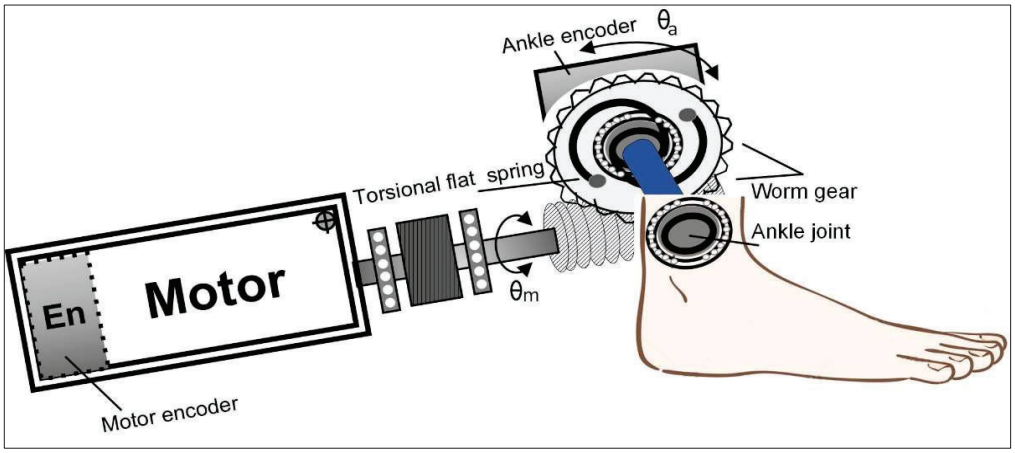

Figure 2.1. The ankle joint system driven by a rotational series elastic actuator (RSEA)

Table 2.1. Design goals and properties of RSEA (as low as possible)

Design value	Goal	Unit
Peak torque	20	Nm
Actuator output speed	1.2	rad/s
Maximal mass	3.5	Kg
Large torque bandwidth for 45 Nm	5	Hz
Torque resolution	0.1	Nm
Zero-impedance torque limit (Peak to peak)	0.3	Nm
Zero-impedance bandwidth,	15	Hz
Spring stiffness Ks	65	Nm/rad

In this part, a mechanical design of the DFTFS, dynamic modeling of RSEA, and the proposed torque estimation method based on the nonlinear friction model of the RSEA are described in detail

2.1.1. Double Fibonacci Torsional Flat Spring Design (DFTFS)

This section is very crucial in the design and construction of the RSEA. In designing a spring, the maximum and minimum torque range and force determine its dimensions. In order to create a compact and rather stiff spring, it has been decided to rely on the double flat spring design (see Figure. 2.2) proposed by [57]. The spring is adapted to the needs of the new RSEA. A maximal torque of 15.2 Nm is built up before the spring windings will block each other [58]. Beyond 15.2 Nm the actuator output stiffness is rapidly increased. The double spiral design has the advantage to cancel out undesired radial forces acting on the spring center when the spring is wrapping or unwrapping. The proposed Double Fibonacci Torsional Flat Spring (DFTFS) is composed of two preloaded spiral springs in opposite directions. Springs made of three materials: aluminum, steel, and titanium are analyzed and made.

In double Fibonacci torsional flat spring design, since the geometrical properties of a spring greatly affect the spring performance, the geometric equations of the spring must be considered very well before anything else.

2.1.2 Placement of Spring and Encoders

Figure. 2.2 shows a schematic of our rotary SEA with possible locations for the encoders. According to [59, 60], there can be multiple possible locations to place the series spring. To minimize the effect of gearbox friction and motor inertia on the output torque measurement, the spring should be placed as close to the load as possible. Hence, we choose to place the spring between the gearbox and the load.

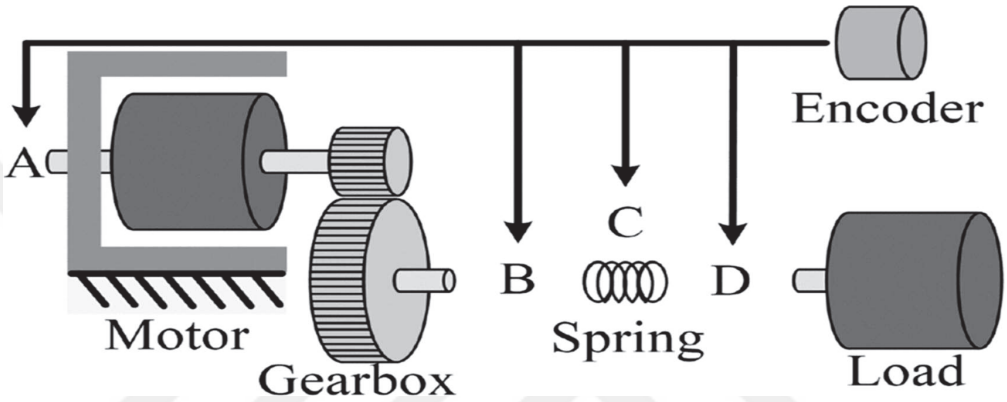

Figure. 2.2. Possible locations for the encoders

Two encoders are required for each SEA to measure the spring deformation and output angle simultaneously. As indicated in Figure. 2.2, placing an encoder on position C would provide direct measurement of the spring deformation. Because the spring is soft and would rotate with the output of the gearbox, placing an encoder next to the rotating spring would be more challenging due to the complexity of encoder fixture and wire routing. It would be more convenient to place the two encoders on the two sides of the spring and measure the angle difference to obtain the spring deformation. Two types of settings have been used. The first type places encoders on locations A and D. This type has been adopted in [61, 62]. The second type places encoders on locations B and D. This type has been adopted in [63, 64]. Compared with location B, placing an encoder on location A can reduce the demand on the resolution of the encoder because the gear ratio can be used to magnify the resolution for the measure of angle on location B. Besides, placing an encoder on location A can increase the compactness between A and D. For size considerations, locations A and D will be used in this paper to place the two encoders.

2.1.3 Geometry design method of spring

There are many different types of involutes in response to different geometrical figures. Among them, the involute of circle is widely used and also the most convenient one that can be described and machined. So, in this report, the involute of circle has been analyzed. The involute of a circle is the path traced out by a point on a straight line that Ys around a circle. The pedal of the involute of a circle, with the center as pedal point, is a Spiral of Archimedes. Parametric Polar equation in the Polar coordinate is:

$$c_r = 1.61803, \theta = (0\ , 2\pi), r_s(\theta) = c_r\sqrt{\theta_s}, s_1 = (\theta, r_s), s_2 = ((\theta - \pi), r_s)$$

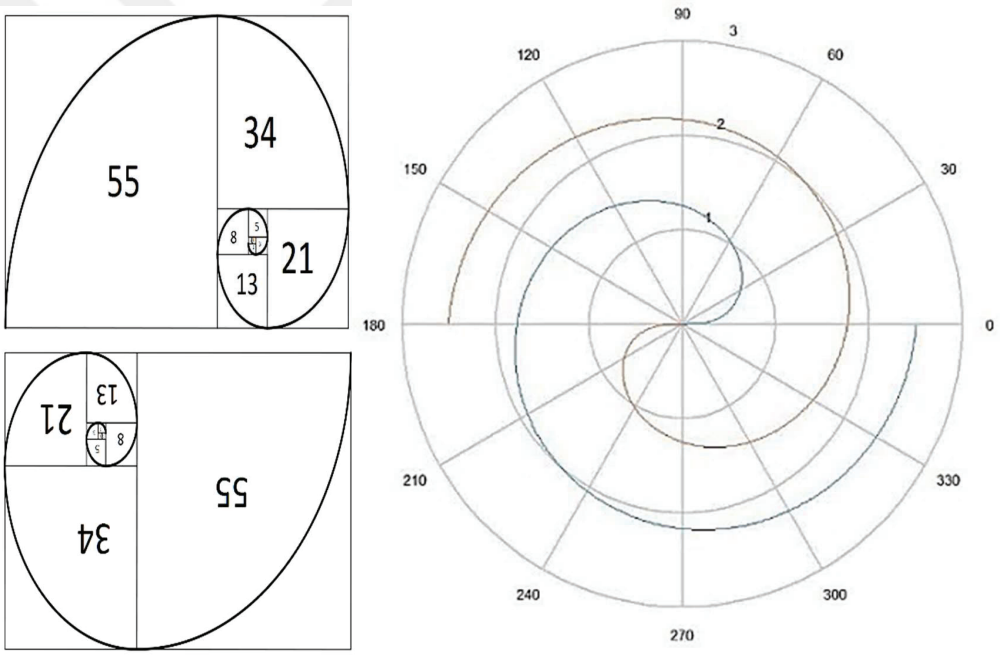

Figure 2.3. Double Fibonacci Torsional Spring profile

The proposed DTFS is included of two spiral springs in contrary directions using three different materials (Figure 2.3). When the shaft's torque is applied through the DFTFS, the worm of the gearbox is rotated by the motor that connects to the worm wheel directly. The DFTFS is rotated using a worm wheel connected to the joint of the load directly and rotates the load [65]. An encoder with 2048 pulses is employed to measure the angle of the joint load. The difference between the motor and the joint load angle is the torsion angle of the DFTFS.

Table 2.2. Elastic and Shear Moduli and Poisson's Ratio for Various Metal Alloys in Room-Temperature (Source Wiley Plus)

Metal Alloy	Modulus of Elasticity		Shear Modulus		Poisson's Ratio
	GPa	10^6 Psi	GPa	10^6 Psi	
Aluminum	69	10	25	3.6	0.33
Titanium	107	15.5	45	6.5	0.34
Steel	207	30	83	12	0.3
Copper	110	16	46	6.7	0.34
Nickel	207	30	76	11	0.31
Brass	97	14	37	5.4	0.34
Magnesium	45	6.5	17	2.5	0.29
Tungsten	407	59	160	23.2	0.28
ABS plastics	40	6.1	14	2.1	0.29

The spring design method requires the maximum torque and the stiffness parameters of DFTFS. Since the DFTFS has two springs in contrary directions, the required stiffness is twice the stiffness of one spring [66, 67]. The maximum torque of the DFTFS can be calculated once the deflection angle is selected. It is expressed as follows. Once the specifications on the stiffness and maximum torque of the DFTFS are determined (see Figure 2.3), the parameters can be obtained using (equation 2.1) given the material. Since there are more parameters to be determined than the number of equations, the dimension can be selected in terms of (2.2) and (2.3) to satisfy the size specifications. Torsion springs exert a torque when they are twisted or deflected. The spring torque and the length of the legs together create a force.

$$k_s = \frac{E * {w_1}^3 * w_2}{12 * L} \tag{2.1}$$

$$\Delta\theta = \frac{12 * \tau * L}{E * {w_1}^3 * w_2} \tag{2.2}$$

$$L = \pi * n * (R_o + R_i) = \frac{\pi * (R_o + R_i)}{a + w_1} \tag{2.3}$$

Maximum length of the DFTFS is given below

$$L_{max} = \frac{4({R_o}^2 - {R_i}^2)}{2.55 * w_1} \tag{2.4}$$

$$\sigma = K_b \frac{6 * \tau}{{w_1}^2 * w_2} \tag{2.5}$$

$$K_b = f(\beta), \quad \beta = \frac{R_i}{w_1} \tag{2.6}$$

$$15 < \frac{d}{t} < 25 \quad , \quad \frac{L}{t} > 1000 \tag{2.7}$$

The dimension parameters of the DFTFS are given in Table 2.3.

Series spring design and weight minimization springs made of a single piece of material requires no preload and could be more lightweight. we designed and produced a DFTFS (Figure 2.4), the torsional flat spring consists of two Fibonacci spirals. the edges of the DFTFS are two curves equally offset a certain distance (W1/2) from the Fibonacci spirals (centerline). this new design aims to improve in torque density, and the accuracy of spring stiffness estimation, and to eliminate connection backlash.

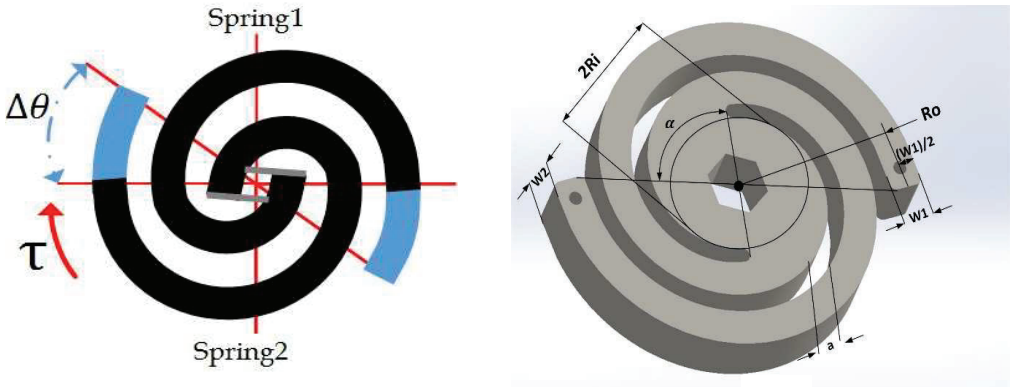

(a) (b)

Figure 2.4. (a) conceptual model of spring and (b) solid model of spring for configuration and parameters of DFTFS

Table 2.3. DFTFS parameters

Symbol	Parameter	Value1 of Aluminum	Value2 of Aluminum	Value of steel	Value of titanium	Unit
a	space between coils	2	2	2	2	mm
$\boldsymbol{\tau}$	Maximum torque loading of spring	25	25	25	25	Nm
E	modulus of elasticity in tension (Young's Modulus)	68	68	76	83	Gpa
$\boldsymbol{k_s}$	Stiffness of spring	64.251	60	70	78	Nm/rad
L	functional spring length	115.13	115.13	115.13	115.13	mm
n	number of active coils	2	2	2	2	-
$\boldsymbol{w_1}$	thickness of spring strip	5.13	5.13	5.13	5.13	mm
$\boldsymbol{w_2}$	width of spring strip	9.87	15	15	15	mm
$\boldsymbol{R_o}$	outer radius of spring	63.35	63.35	63.35	63.35	mm
$\boldsymbol{R_i}$	inner radius of spring	12.42	12.42	12.42	12.42	mm
$\boldsymbol{\Delta\theta}$	Maximum angular deflection	0.35	0.31	0.28	0.27	rad

Correction coefficient represents the spring additional stress resulting from its curvature. Its value can be found in the graph:

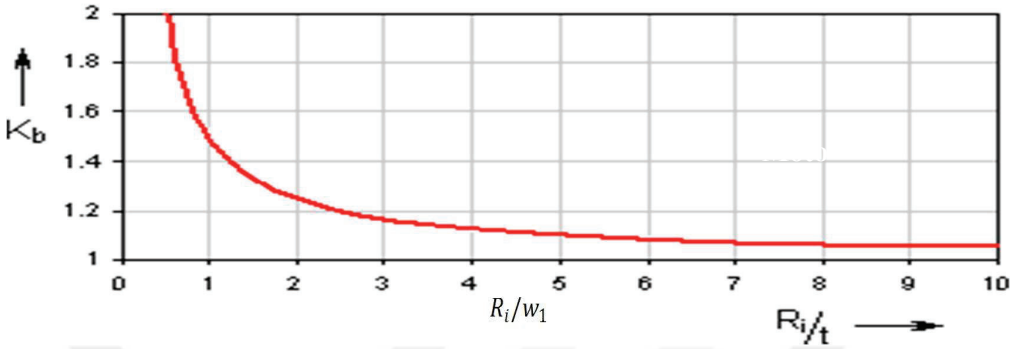

Figure 2.5. Curvature correction factor

Table 2.4. Recommended spring dimensions

ratio R_i/w_1	Min 0. 8
ratio w_2/w_1	1 - 5
number of active coils n_0	Min 0. 2

The controls located in this paragraph serve for starting the design (optimization) functions of the calculation. Spring design for the given ratios R_i/w_1, w_2/w_1, $a_0/w_1$is started by moving one of the scroll bars (see Figure 2.5, and Figure 2.6). When designing the spring the calculation is trying to optimize the dimensions so that the strip thickness is as small as possible while keeping the required safety [68].

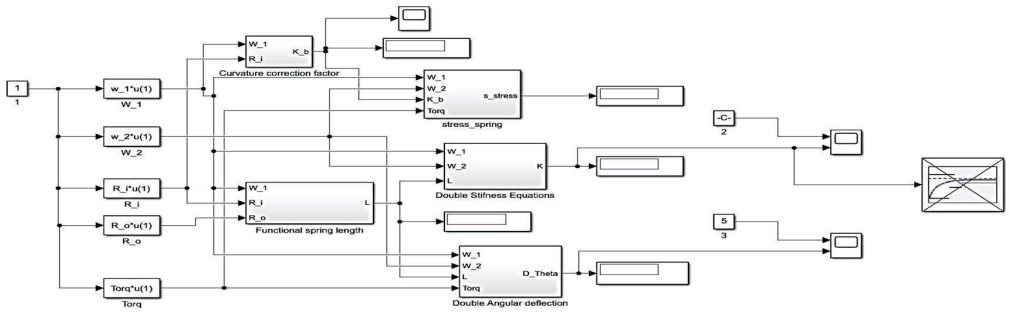

Figure 2.6. Optimization model in MATLAB

2.1.4 Finite element analysis and experiment verification

FEM static stress-strain analyses have been performed to evaluate alternative designs. Static large displacement FEM analysis (Abaqus) was performed with the clamped inner ring and outer ring loaded by a tangential distributed force equivalent to a pure torque (see Figure.2.8). The FEA method had been proved to be an effective way to analyze the performance of spring [69]. Here geometrically non-linear static structural analysis has been conducted with personal computer based on advanced FE code. The mesh is successively refined and convergence study is conducted to decide on the adequacy of the final mesh. The details of the final refined mesh used in the model shown in Figure.2.7, are as follows, element type: brick eight-node elements, number of nodes: 1500, number of elements: 600, in the Table 2.5. Optimization spring geometry for each parameter, based on the upper and lower bound and minimum increment adopted in the optimization process. R_i, R_o, W1 and W2 are in (mm), a is in (rad).

Table 2.5. Optimized Spring Parameter

Parameter		Min	Max	Min. increment	Optimized Aluminum	Optimized S- Steel	Optimized Titanium
w_1		4	19	0.1	7.7	7.7	7.7
w_2		4	20	0.1	7.34	5.1	4.2
R_i		16	23.5	0.05	18.38	18.38	18.38
R_o		60	80	0.1	75.07	75	75
a		90	90	0	90	90	90

(a) (b)

(c) (d)

Figure 2.7. Different DFTFS springs used in the system (a)-ABS Plastic (b)-Aluminum (c) - Stainless steel (d) - Titanium.

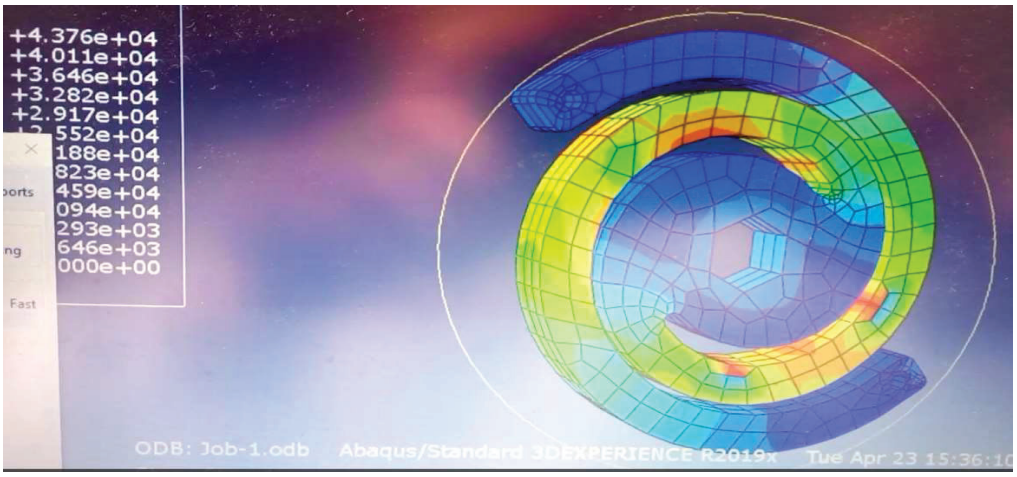

Figure 2.8. Model simulation in the Abaqus

2.1.5 Validation of the spring stiffness in RSEA

In this section, the DFTFS parameters obtained using finite element methods (FEM) and experimental angular torque analysis (EATA) are used to validate the DFTFS stiffness of the RSEA system with torsional elastic properties.

The force transducer (Gamma SI-65-5) is used to find the force applied by the RSEA [70]. The angle of rotation of the motor and the link is obtained by encoders connected to the system. Using the spring force equation, the stiffness of the DFTFS is obtained. As shown in Figure 2.8 and Figure 2.9, the force transducer is located below the end of the link connected to the RSEA.

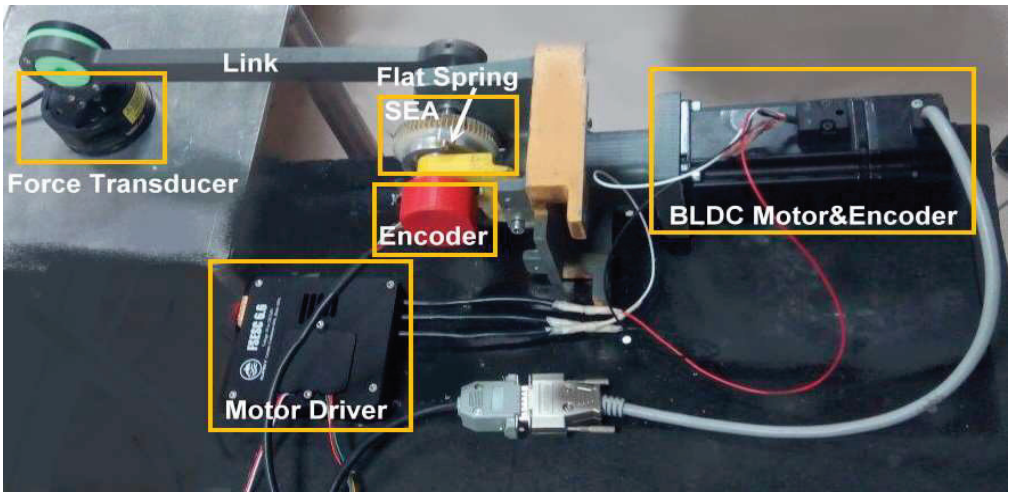

Figure 2.9. Experimental Setup for validation of the flat spring stiffness in RSEA.

The system is given a duty-cycle input and reads the angle difference encoders created by the spring, and on the other hand, the force is read from the end of the link. The duty-cycle has given to the system and reads the encoders angle changes can be seen in Figure 2.10, max angle= 12.5765 (Deg) and max Force = 48.2652 (N).

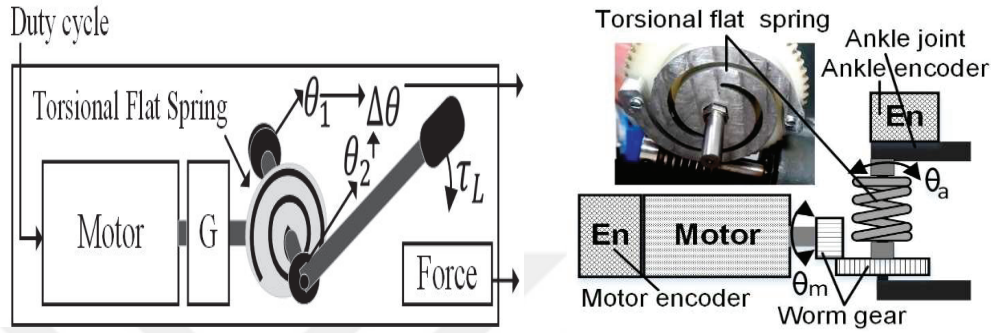

Figure. 2.10. DFTFS validation test system

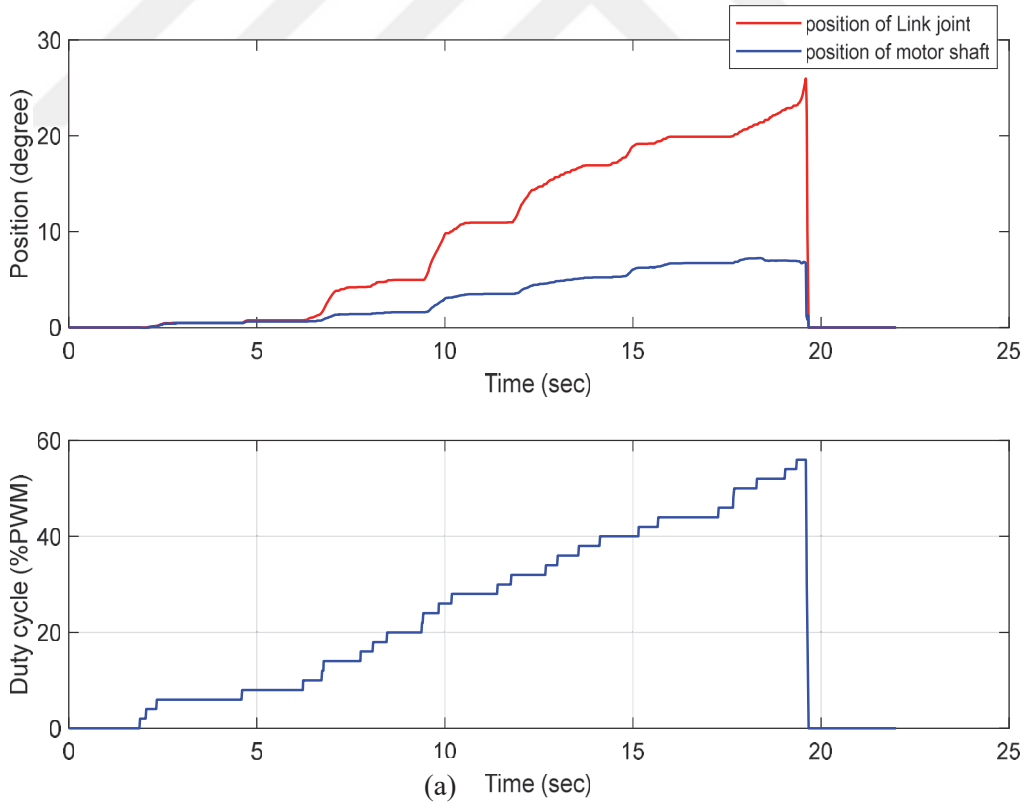

Figure. 2.11. Encoders angle changes and Motor Duty cycle (a) without frequency and (b) in a period with 0.1 Hz frequency

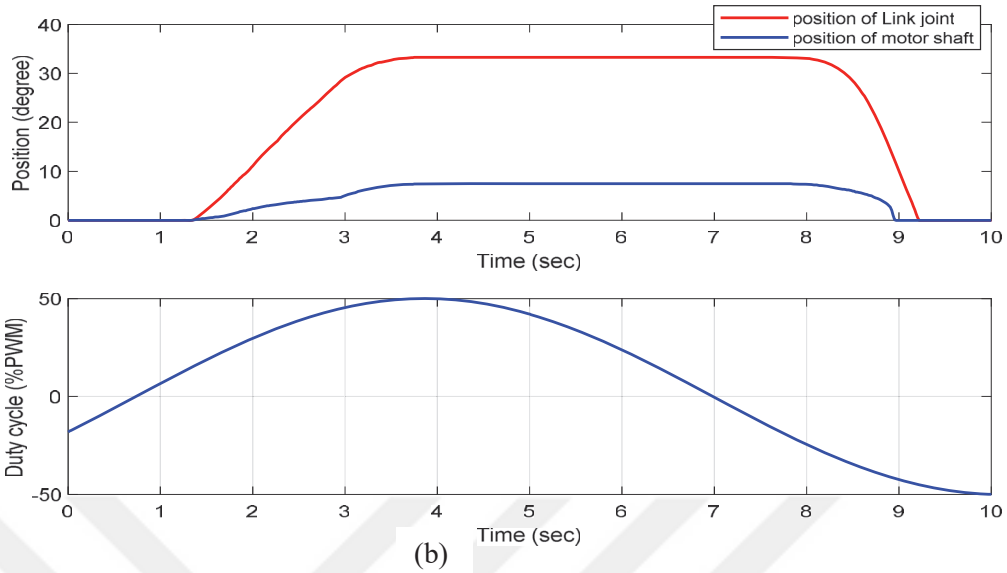

(b)

Figure 2.11.(Cont.) Encoders angle changes and Motor Duty cycle (a) without frequency and (b) in a period with 0.1 Hz frequency

Finding the difference between angles (θ_m, θ_l) created by the spring and the force applied by motor at the same time, the spring stiffness is calculated by Equation 2.8, The graph of the force changes relative to the changes in angle is shown in Figure 2.11 and Figure 2.12. It can be seen that the changes are almost linear.

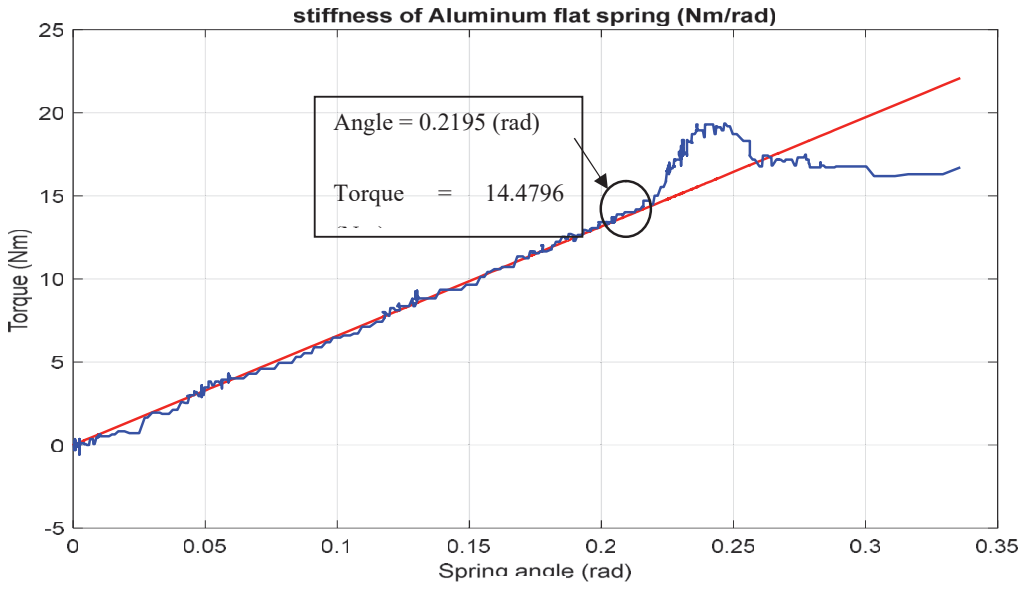

(a)

Figure. 2.12. Mechanical torsion test experimental data. (a) plot of torque against angular displacement on the left and (b) combined plot of torque and angular displacement against time on the right (spring stiffness: 65.771 Nm/rad)

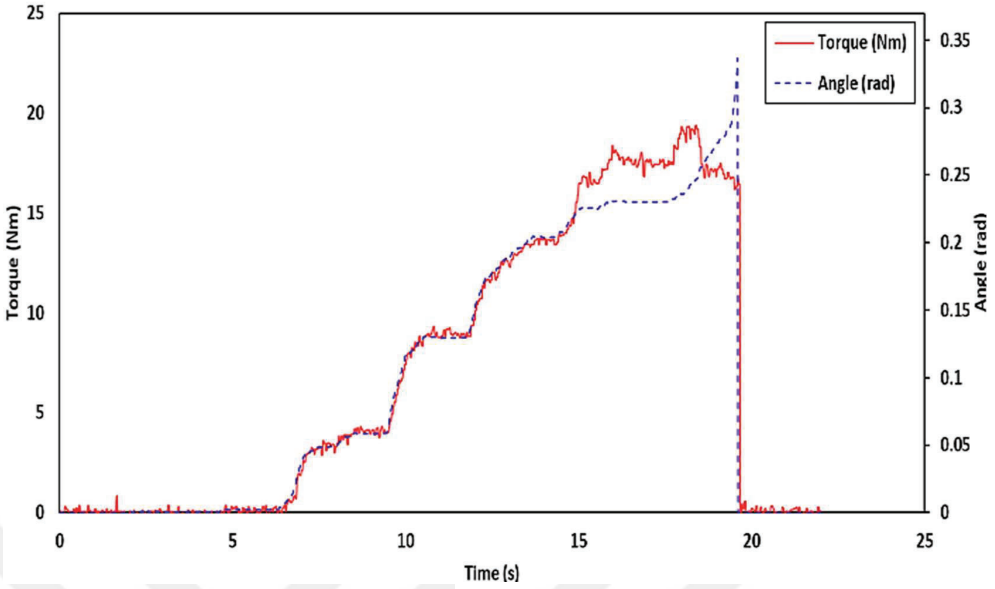

(b)

Figure. 2.12. (Cont.) Mechanical torsion test experimental data. (a) plot of torque against angular displacement on the left and (b) combined plot of torque and angular displacement against time on the right (spring stiffness: 65.771 Nm/rad).

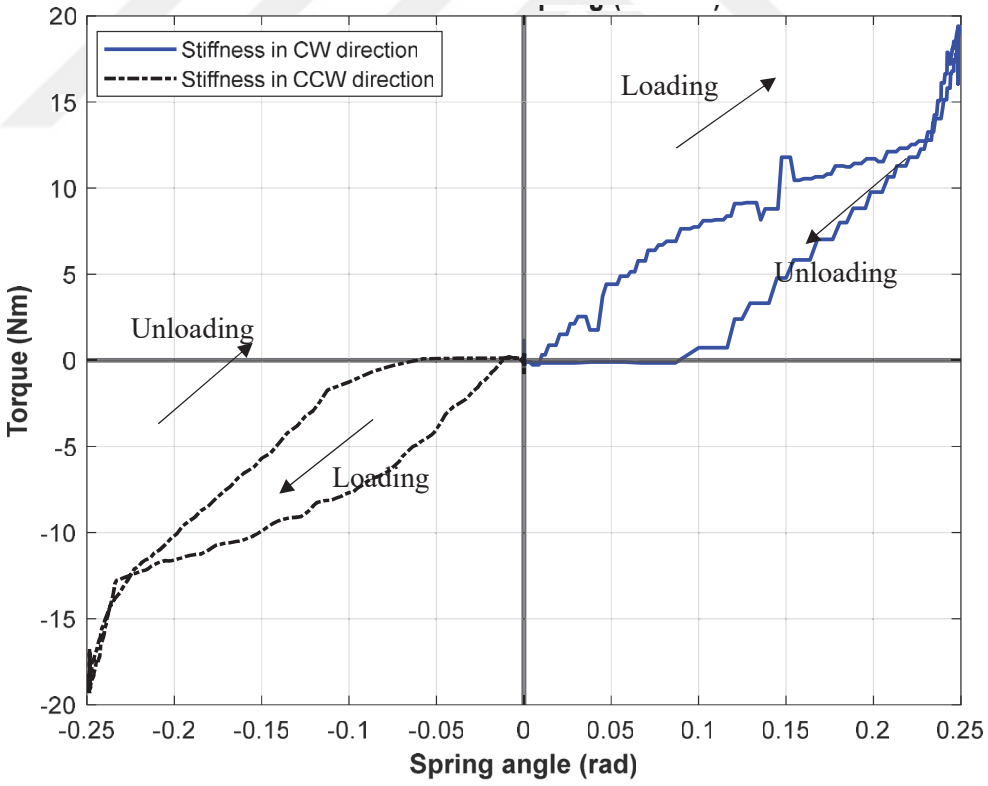

Figure 2.13. Experimental relationship between torque and angular deflection for aluminum spring (DFTFS-AL1). (w2=7.34mm, Ks= 65.771 Nm/rad). Notice the hysteresis

High output torque resolution results from the combination of incremental encoders and an elastic element. As expected, the spring stiffness is quite linear until the windings start touching each other.

Under loading conditions without frequency, the spring stiffness is nearly linear (see Figure 2.13) until it reaches the point where the windings touch each other. The spring stiffness differs Slightly from what has been calculated and simulated. The measured spring stiffness is only 57 Nm/rad instead of the calculated and simulated 53 Nm/rad. Moreover, the windings start touching each other around 13 Nm instead of 15 Nm in each direction of rotation. During unloading hysteresis is observed.

$$K_s = \frac{\tau_L}{\Delta\theta_s} \tag{2.8}$$

where τ_L is the Torque/Load applied (Nm), $\Delta\theta_s$ is the Spring angle change, K_s is the spring stiffness (Nm/rad) of the SEA system, Figure 2.14 shows the diagram of the aluminum spring stiffness changes, which is about 66 (Ks =65.771 Nm/rad).

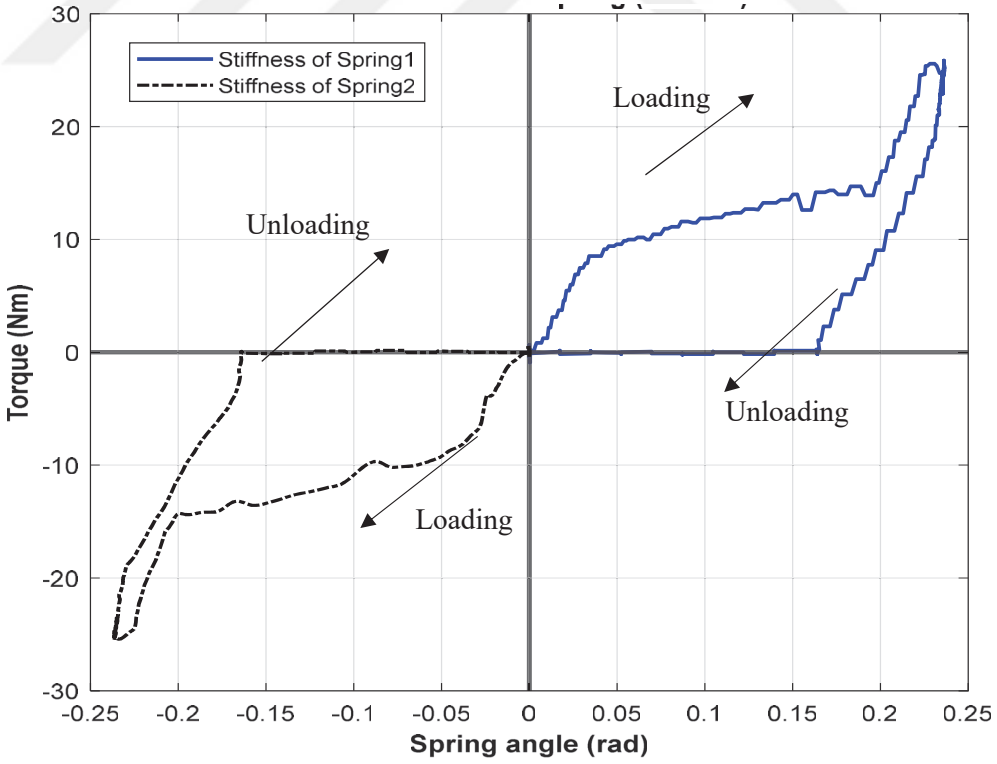

Figure. 2.14 Experimental relationship between torque and angular deflection for aluminum spring (DFTFS-AL1). (w2=10mm Ks= 80 Nm/rad). Notice the hysteresis

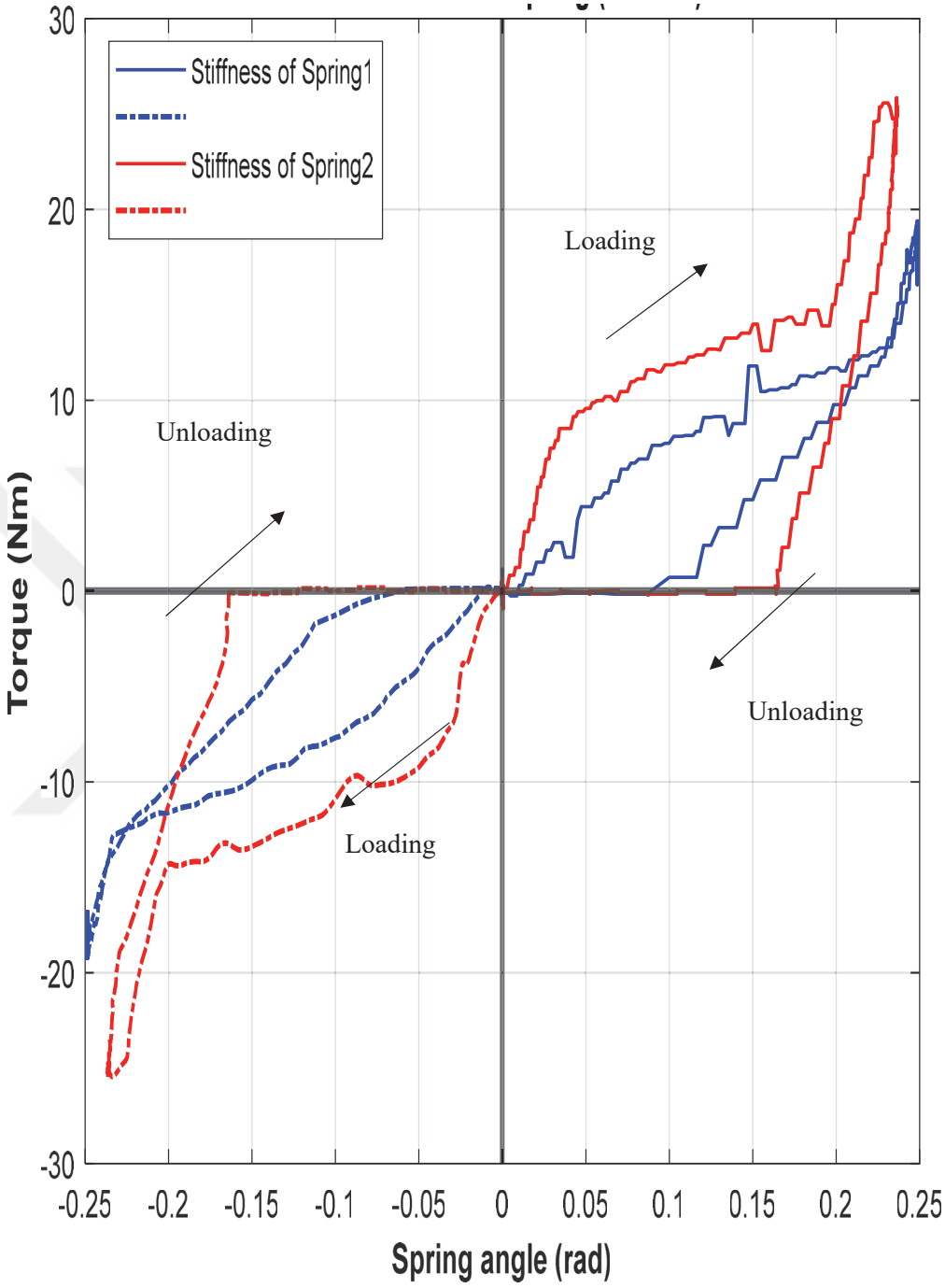

Figure. 2.15. Experimental 2 Aluminum spring stiffness. Spring1: W2=7.34mm and Spring2: W2=10mm, Notice the hysteresis

Aluminum flat springs have been tested at different frequencies. Depending on the frequency of the spring stiffness changes. The spring stiffness without frequency is 66 Nm/rad and the spring stiffness at a frequency (1Hz) is 60 Nm/rad.

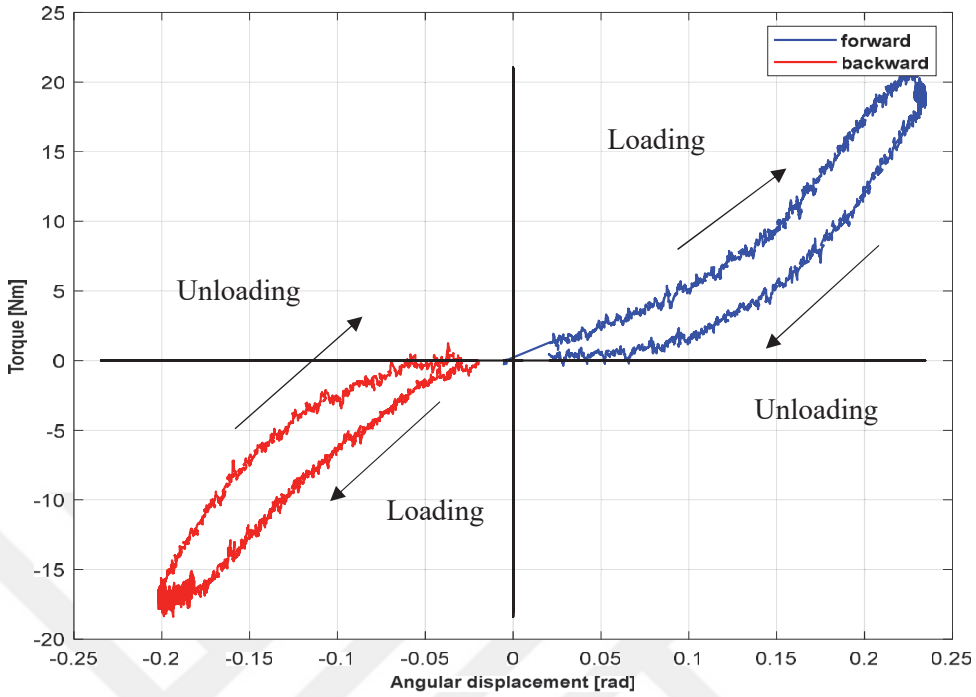

Figure. 2.16 Experimental relationship between torque and angular deflection for stainless steel spring (DFTFS-SS). (W2=5.1mm, Ks=64), Notice the hysteresis

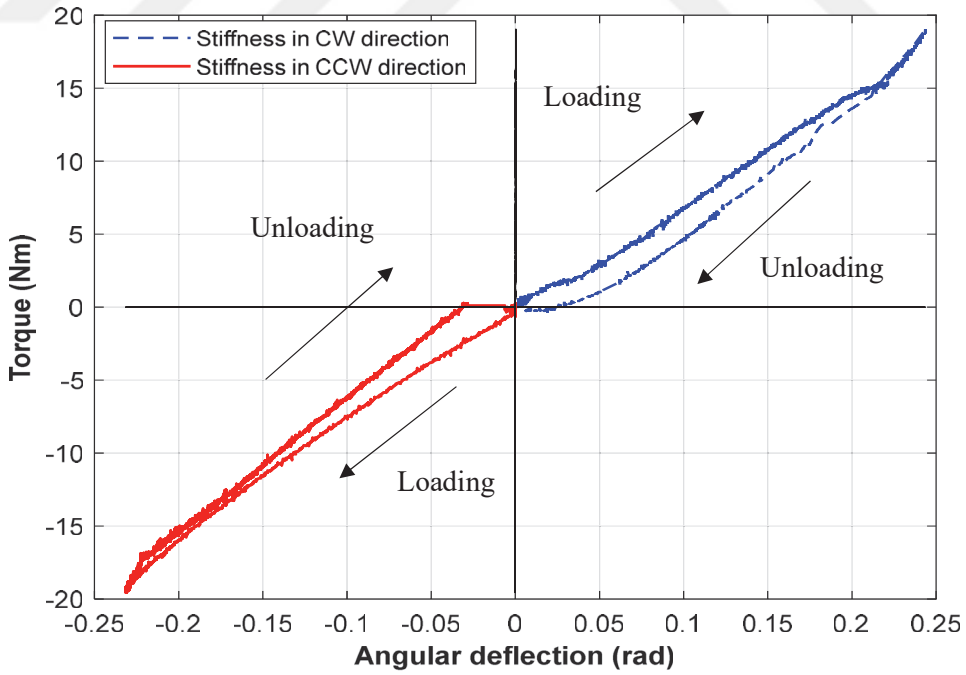

Figure. 2.17. Experimental relationship between torque and angular deflection for Titanium spring (DFTFS-TI). (W2=4.2mm, Ks=76.305 Nm/rad), Notice the hysteresis

Table 2.6. Experimental and analytical stiffness of spring with different materials

Spring type	Material of spring	Width of spring strip (w2) mm	Ks (analytical) (Nm/rad)	Ks (Experimental) (Nm/rad)
DFTFS-AL1	Aluminum	7.34	66.102	65.771
DFTFS-AL2	Aluminum	10	82.31	80.46
DFTFS-SS	Stainless Steel	5.1	71.1	71.1
DFTFS-TI	Titanium	4.2	85.2	88.305

In the DFTFS-TI, Titanium (Ti-Grade 2) was used as the spring material. Under loading conditions, the spring stiffness is nearly linear (see Figure 2.15 to Figure 2.17) until it reaches the point where the windings touch each other. The stiffness constant of the spring is 76.305Nm/rad

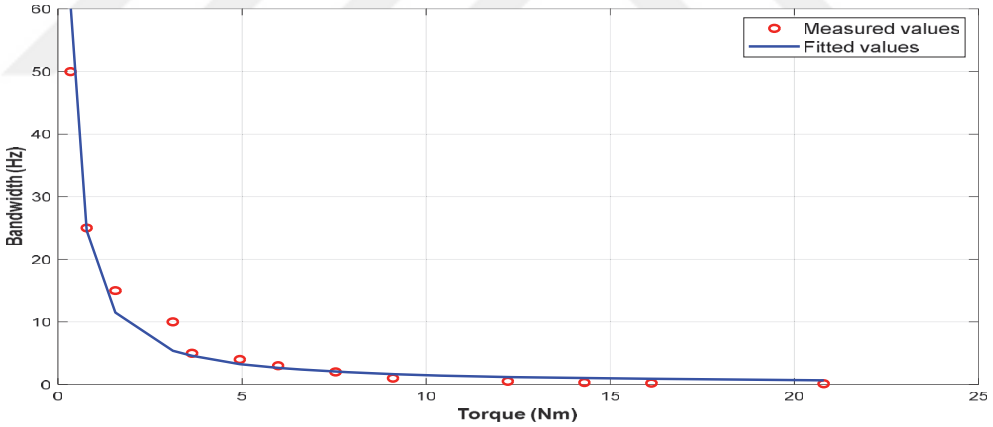

Figure. 2.18. Plot of the large torque bandwidth limitation due to saturation of the aluminum spring actuator. At 20.8 Nm the bandwidth is 0.1 Hz. Values are fitted with cubic spline data interpolation (y = *(x^(- 1.093)) $y = 18.7149x$.

The large torque bandwidth limit for 20 Nm output torque (40 Nm peak to peak) is 0.1 Hz when reaching motor saturation. In the titanium spring actuator favorable torque tracking with a bandwidth of 15 Hz was achieved while peak-to-peak torque input was 7 Nm. This result was achieved by generating sine sweep signals with different torque amplitudes ranging from 1 to 20 Nm (see Figure. 2.18). A spectral / - frequency analysis of each response signal was performed to generate a full Bode.

For the data points in Figure. 2.19 the large torque bandwidth values at -3 dB were used. The torque resolution is estimated to be at least 0.05 Nm.

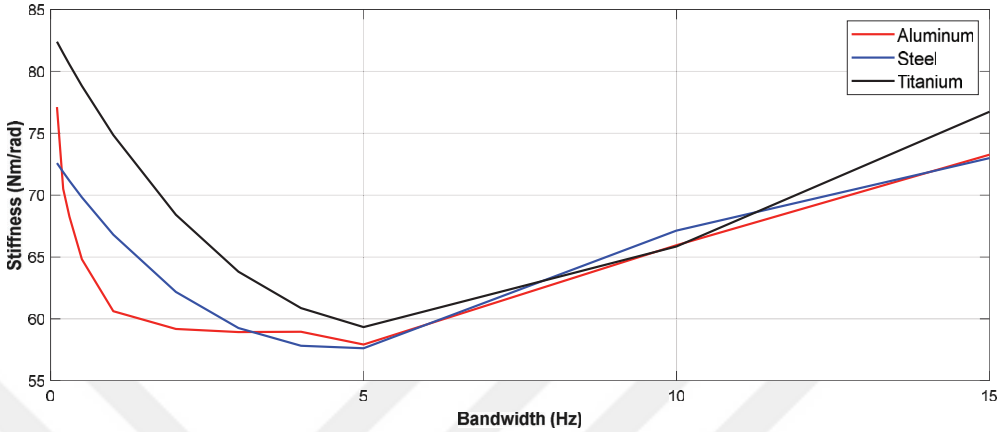

Figure. 2.19. Spring stiffness-frequency diagram

The DFTFS actuation system utilizes the characteristics of the large deformation and compliance while overcoming the directional properties of the spiral spring.

In particular, deformation during axial loading tests after fatigue, it was observed that the line of refraction of the DFTFS line is always close to the inner ring (Figure 2.20). Recent studies have evaluated the flexural stiffness of various spring designs and materials.

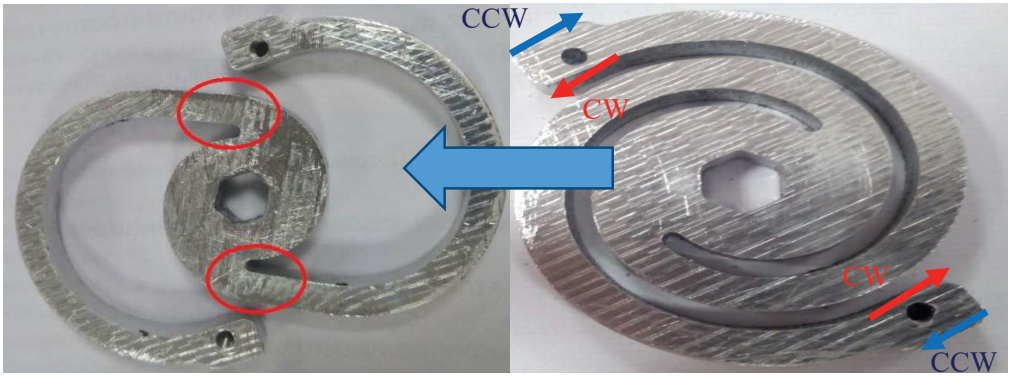

Figure. 2.20. DFTFS permanent deformation line close to the inner ring, during post-fatigue axial loading tests.

This work proposes a test categorization of SEA in terms of the type of the spring and the motor gearbox in SEA.

SEA is classified into six types according to the type of the spring with regard to the motor gearbox:

Table 2.7. Comparison of physical parameters between the different series elastic actuators

Actuator - type	Motion range(deg)	Stiffness range (Nm/rad)	Weight (kg)	Size (cm)	Power (watt)	Speed (rpm)
MDCM-AL	±8.5	(0 – 98.2)	1.560	28*12*8	5 – 95	12
MDCM-SS	±7	(0 – 86)	1.585	28*12*8	11 – 106	12
MDCM-TI	±7.2	(0 – 108.5)	1.575	28*12*8	16 – 112	12
MTBM-AL	±15	(0 – 80.46)	3.250	36*18*15	12 – 115	18
MTBM-SS	±13	(0 – 71)	3.320	36*18*15	20 – 123	18
MTBM-TI	±14	(0 – 88.305)	3.300	36*18*15	22 – 130	18

Maxon DC Motor - Aluminum spring (MDCM-AS), Maxon DC Motor - Stainless steel spring (MDCM-SS), Maxon DC Motor - Titanium spring (MDCM-TS) which Maxon DC motor is used and locates the spring (aluminum, stainless steel, and titanium respectively) after the transmission worm gear, MDS Brushless Torque Motor - Aluminum Spring (MBTM-AS), MDS Brushless Torque Motor - Stainless steel Spring (MBTM-SS), MDS Brushless Torque Motor - Titanium (MBTM-TS) which MDS Brushless Torque Motor is used and locates the spring (aluminum, stainless steel, and titanium respectively) after the transmission worm gear (Figure 2.21).

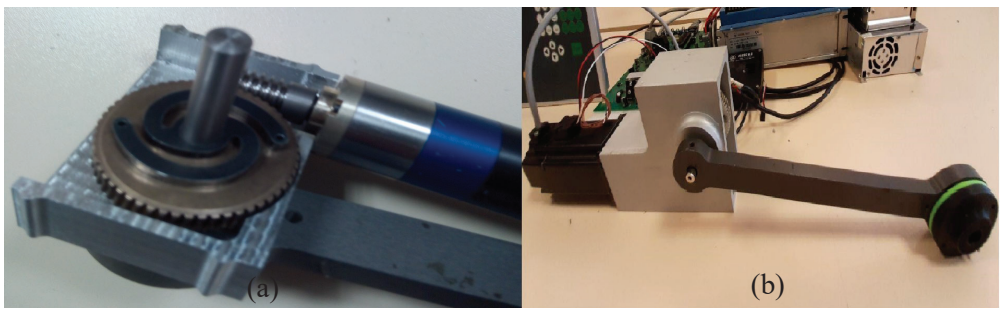

Figure. 2.21. Test models with different configurations (a) Maxon motor (b) MDS motor

2.2. Modeling of the RSEA

2.2.1 Kinematic model of the RSEA

Solid 3D model and kinematics parameters of the RSEA are shown in the Figure 2.22. The RSEA comprises a horizontal rotary link and one pendulum link. A direct drive brushless DC torque motor servo system is mounted to provide torque to the link to control the system. The rotary arm rotates in the horizontal plane. The pendulum link is connected to the extremity of the rotary link.

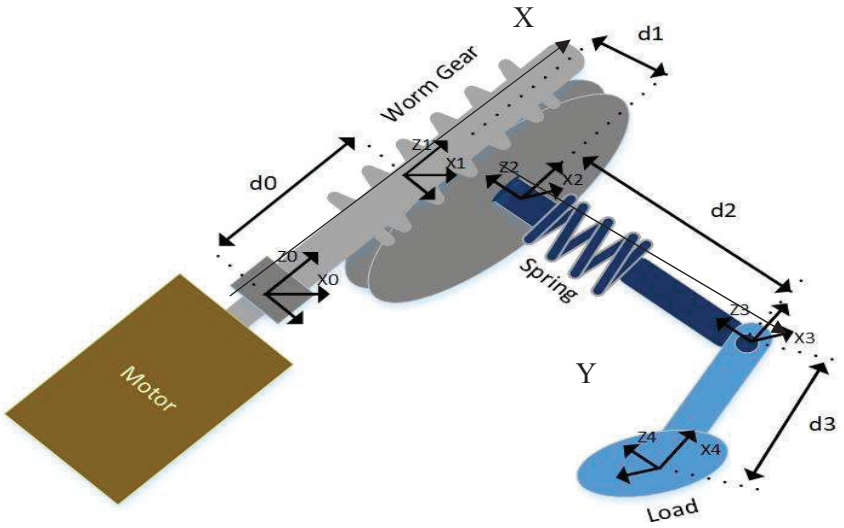

Figure 2.22. Model and kinematic parameters of the RSEA

The mechanical implementation of the RSEA is shown in Figure. 2.22. the whole system can be regarded as a kinematic chain in series, and the whole kinematic system's mathematical equation can be expressed as:

Table 2.8. DH-Parameters of the RSEA

Coordinate	α_{i-1}	a_{i-1}	d_i	Variable (θ_i)
1	0	0	d_0	$\theta_1 = \theta$
2	$\pi/2$	d_1	0	$\theta_2 = \phi_w = N^{-1}\theta$
3	0	0	d_2	$\theta_3 = \phi_l$
4	0	d_3	0	

$$ {}^{i-1}_{i}\mathrm{T} = \begin{bmatrix} \cos\theta_i & -\sin\theta_i & 0 & a_{i-1} \\ \sin\theta_i \cos a_{i-1} & \cos\theta_i \cos a_{i-1} & -\sin a_{i-1} & -\sin a_{i-1}\, d_i \\ \sin\theta_i \sin a_{i-1} & \cos\theta_i \sin a_{i-1} & \cos a_{i-1} & \cos a_{i-1}\, d_i \\ 0 & 0 & 0 & 1 \end{bmatrix} \tag{2.9} $$

The homogeneous transformation matrix of the RSEA is derived in equation (2.10) using the DH-parameters in Table 2.3.

$$ {}^{0}_{4}\mathrm{T} = {}^{0}_{1}\mathrm{T}\,{}^{1}_{2}\mathrm{T}\,{}^{2}_{3}\mathrm{T}\,{}^{3}_{4}\mathrm{T} \tag{2.10} $$

Where

$$ {}^{0}_{1}\mathrm{T} = \begin{bmatrix} \cos\theta_1 & -\sin\theta_1 & 0 & 0 \\ \sin\theta_1 & \cos\theta_1 & 0 & 0 \\ 0 & 0 & 1 & d_0 \\ 0 & 0 & 0 & 1 \end{bmatrix} {}^{1}_{2}\mathrm{T} = \begin{bmatrix} \cos\theta_2 & -\sin\theta_2 & 0 & d_1 \\ 0 & 0 & -1 & 0 \\ \sin\theta_4 & \cos\theta_4 & 0 & 0 \\ 0 & 0 & 0 & 1 \end{bmatrix} \tag{2.11} $$

$$ {}^{2}_{3}T = \begin{bmatrix} \cos\theta_3 & -\sin\theta_3 & 0 & 0 \\ \sin\theta_3 & \cos\theta_3 & 0 & 0 \\ 0 & 0 & 1 & d_2 \\ 0 & 0 & 0 & 1 \end{bmatrix} {}^{2}_{3}\mathrm{T} = \begin{bmatrix} 1 & 0 & 0 & \mathrm{L}_2 \\ 0 & 1 & 0 & 0 \\ 0 & 0 & 1 & 0 \\ 0 & 0 & 0 & 1 \end{bmatrix} \tag{2.12} $$

$$ {}^{0}_{4}\mathrm{T} = \tag{2.13} $$

$\cos\theta_1 \cos\theta_2 \sin\theta_3 + \cos\theta_1 \cos\theta_3 \sin\theta_2$	$\cos\theta_1 \cos\theta_2 \cos\theta_3 - \cos\theta_1 \sin\theta_2 \sin\theta_3$	$-\cos\theta_1 \cos\theta_2 \sin\theta_3 - \cos\theta_1 \cos\theta_3 \sin\theta_2$	$d_1 \cos\theta_1 + d_2 \sin\theta_1 + d_3(\cos\theta_1 \cos\theta_2 \cos\theta_3 - \cos\theta_1 \sin\theta_2 \sin\theta_3)$
$\cos\theta_2 \sin\theta_1 \sin\theta_3 + \cos\theta_3 \sin\theta_1 \sin\theta_2$	$\cos\theta_2 \cos\theta_3 \sin\theta_1 - \sin\theta_1 \sin\theta_2 \sin\theta_3$	$-\cos\theta_2 \sin\theta_1 \sin\theta_3 - \cos\theta_3 \sin\theta_1 \sin\theta_2$	$d_1 \sin\theta_1 - d_2 \cos\theta_1 + d_3(\cos\theta_2 \cos\theta_3 \sin\theta_1 - \sin\theta_1 \sin\theta_2 \sin\theta_3)$
$\sin\theta_2 \sin\theta_3 - \cos\theta_2 \cos\theta_3$	$\cos\theta_2 \sin\theta_3 + \cos\theta_3 \sin\theta_2$	$\cos\theta_2 \cos\theta_3 - \sin\theta_2 \sin\theta_3$	$d_0 + d_3(\cos\theta_2 \sin\theta_3 + \cos\theta_3 \sin\theta_2)$
0	0	0	1

The position vector is given from the calculated homogeneous transformation matrix ${}^{0}_{3}\mathrm{T}$, as follows:

$$\begin{bmatrix} P_x \\ P_y \\ P_z \end{bmatrix} = \begin{bmatrix} d_1 \cos\theta_1 + d_2 \sin\theta_1 + d_3(\cos\theta_1 \cos\theta_2 \cos\theta_3 - \cos\theta_1 \sin\theta_2 \sin\theta_3) \\ d_1 \sin\theta_1 - d_2 \cos\theta_1 + d_3(\cos\theta_2 \cos\theta_3 \sin\theta_1 - \sin\theta_1 \sin\theta_2 \sin\theta_3) \\ d_0 + d_3(\cos\theta_2 \sin\theta_3 + \cos\theta_3 \sin\theta_2) \end{bmatrix} \quad (2.14)$$

2.2.2 Dynamic model of the RSEA

The RSEA dynamic model is shown in Figure 2.23. At RSEA, a torque motor with a worm gearbox is connected to the DFTFS to apply for a moment in the spring. Furthermore, two encoders are employed to measure the motor's angular position θ_m (worm gear angle), position in the X plane, and the load position θ_l load joint angle position in the Y plane. The RSEA mathematical model is enhanced based on Hooke's and Newton's law formula [71, 72]. The series elastic element can function both as an actuator and a force transducer in the control loop. The stiffness of the series elastic element (k_s) can be chosen as the constant coefficient of DFTFS.

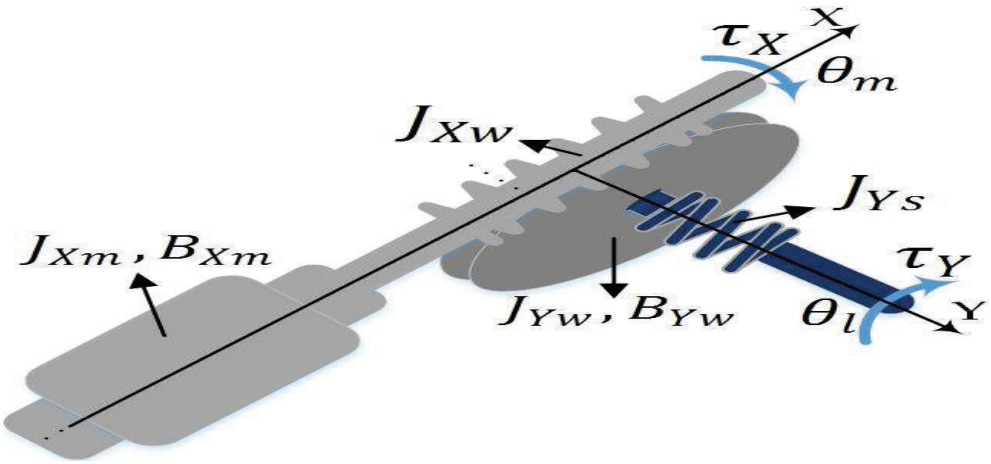

Figure 2.23. Schematic diagram of RSEA

Depending on the rigidity of the spring, the stiffness can be changed. Figure 2.23 shows the relationship between the applied torque and angular deflection of the developed spring. As seen in Figure 2.23, the relationship in both movement directions (clockwise and anti-clockwise) is almost linear in the range of 0 and 0.3 rad. A slight hysteresis behavior occurs in this case. Therefore, the linear relationship is used instead of hysteresis. The dynamic torque equation will be as follows.

$$\theta_w = N^{-1}\theta_m \,,\ \tau_Y = N\tau_X \quad (2.15)$$

$$\tau_X = \tau_m - (J_{Xm}\ddot{\theta}_m + J_{Xw}\ddot{\theta}_m + B_{Xm}\dot{\theta}_m) \quad (2.16)$$

$$\tau_Y = \tau_l + J_{Ys}\ddot{\theta_w} + J_{Yw}\ddot{\theta_w} + B_{Yw}\dot{\theta_w} \quad (2.17)$$

then substituting with equation (2.15) and (2.16) in equation (2.17), the following equation is obtained as

$$\tau_l + J_{Ys}\ddot{\theta_w} + J_{Yw}\ddot{\theta_w} + B_{Yw}\dot{\theta_w} = N(\tau_m - (J_{Xm}\ddot{\theta_m} + J_{Xw}\ddot{\theta_m} + B_{Xm}\dot{\theta_m})) \quad (2.18)$$

Then from equation (2.18), the following equation is obtained

$$N\tau_m - \tau_l = J_{Ys}\ddot{\theta_w} + J_{Yw}\ddot{\theta_w} + B_{Yw}\dot{\theta_w} + NJ_{Xm}\ddot{\theta_m} + NJ_{Xw}\ddot{\theta_m} + NB_{Xm}\dot{\theta_m} \quad (2.19)$$

The following equation is the Laplace transform equation (2.19)

$$\begin{aligned} N\tau_m(s) - \tau_l(s) \\ &= \theta_w(s)s^2(J_{Ys} + J_{Yw}) + \theta_w(s)s^2N^2(J_{Xm} + J_{Xw}) \\ &+ s\theta_w(s)(B_{Yw} + N^2B_{Xm}) \end{aligned} \quad (2.20)$$

It follows from Equation (2.15) and (2.20)

$$\theta_m(s) = N\,\theta_w(s) \quad (2.21)$$

$$\begin{aligned} &N\tau_m(s) - \tau_l(s) \\ &= \theta_w(s)s^2(J_{Ys} + J_{Yw}) + \theta_w(s)s^2N^2(J_{Xm} + J_{Xw}) + s\theta_w(s)(B_{Yw} \\ &+ N^2B_{Xm}) \end{aligned} \quad (2.22)$$

$$J_X = (J_{Xm} + J_{Xw}),\quad J_Y = (J_{Ys} + J_{Yw}),\ J_{tot} = J_Y + N^2J_X \quad (2.23)$$

$$B_X = B_{Xm},\quad B_Y = B_{Yw},\qquad B_{tot} = B_Y + N^2B_X \quad (2.24)$$

Then, according to Equations 2.20, 2.23, and 2.24, the following equations are obtained

$$N\tau_m(s) - \tau_l(s) = s^2\theta_w(s)J_{tot} + s\theta_w(s)\,B_{tot} \quad (2.25)$$

$$\tau_m + k_s(\theta_w - \theta_m) = \ddot{\theta_m}J_{tot} + \dot{\theta_m}B_{tot} \quad (2.26)$$

$$\tau_l = -k_s(\theta_l - \theta_w) \;=>\; \theta_w = \frac{\tau_l}{k_s} + \theta_l \quad (2.27)$$

Then, according to Equations 2.26 and 2.27 the following equations are obtained

$$\tau_m + k_s\left(\theta_l - \frac{\tau_l}{k_s} - \theta_l\right) = J_{tot}\left(\frac{\ddot{\tau_l}}{k_s} + \ddot{\theta_l}\right) + B_{tot}\left(\frac{\dot{\tau_l}}{k_s} + \dot{\theta_l}\right) \quad (2.28)$$

$$\tau_m - \tau_l = J_{tot}\frac{\ddot{\tau_l}}{k_s} + J_{tot}\,\ddot{\theta_l} + B_{tot}\frac{\dot{\tau_l}}{k_s} + B_{tot}\,\dot{\theta_l} \quad (2.29)$$

The following equation is the Laplace transform equation (2.30)

$$\tau_m(s) = \frac{\tau_l(s)}{k_s}(s^2 J_{tot} + sB_{tot} + k_s) + \theta_l(s)(s^2 J_{tot} + sB_{tot}) \tag{2.30}$$

If $(\ddot{\theta}_l = 0)$ Let's assume (Speed constant) the following equation is obtained

$$\frac{\tau_l}{\tau_m}(s) = \frac{k_s}{(s^2 J_{tot} + sB_{tot} + k_s)} \tag{2.31}$$

and (Natural frequency)

$$\omega = \sqrt{\frac{k_s}{J_x}} \tag{2.32}$$

$\tau_l(s)$ is defined as a function of $\tau_m(s)$ and $\theta_l(s)$

$$\tau_l(s) = \frac{1}{s^2\frac{J_{tot}}{k_s} + s\frac{B_{tot}}{k_s} + 1}\tau_m(s) + \frac{(s^2 J_{tot} + sB_{tot})}{s^2\frac{J_{tot}}{k_s} + s\frac{B_{tot}}{k_s} + 1}\theta_l(s) \tag{2.33}$$

In the RSEA torque model, parameters such as the position of load and the position of the motor can be directly measured. However, the friction coefficients on the system load joint should be experimentally determined to have an accurate RSEA model of torque.

Figure 2.24 shows the non-linear mathematical model of the RSEA in Matlab/Simulink. In order to verify the mathematical model, a mechanical dynamic model of the RSEA was developed by using the MATLAB/SimMechanics toolbox.

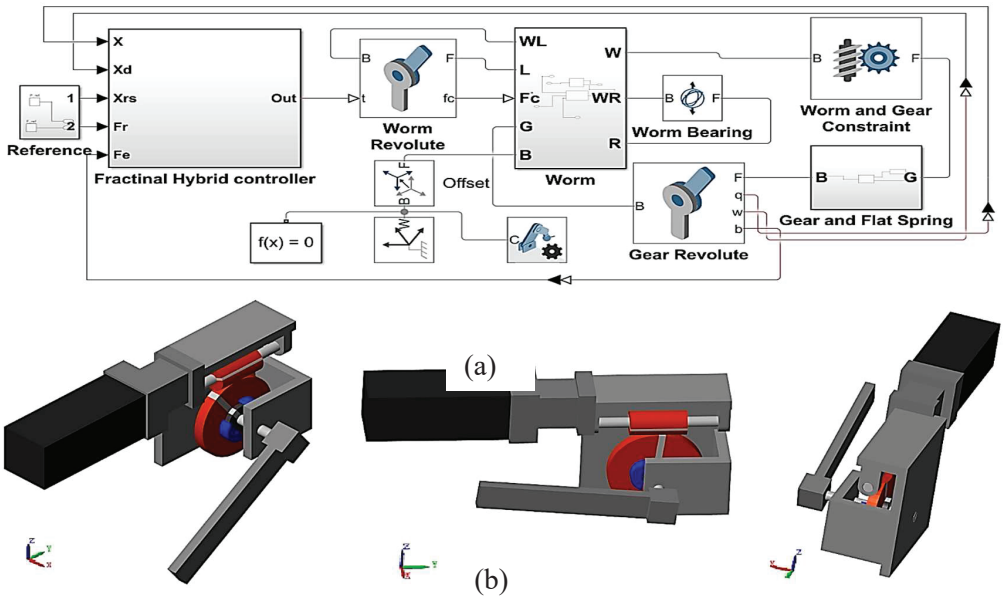

Figure 2.24. (a) Mathematical model of the RSEA in Matlab/Simulink, (b) Different views from Solid model of RSEA in Matlab Simulink

MATLAB/SimMechanics model of the RSEA is shown in Figure 2.24. Different views from virtual reality model of the RSEA in Matlab Simulink is shown in Figure 2.24. Furthermore, for both model, the initial conditions of RSEA joint positions are chosen as follows $\theta = 0°$ The obtained results from MATLAB/SimMechanics and the mathematical models match exactly. Figure 2.24 illustrates a comparison of the two joint positions obtained from simulation mathematical and the SimMechanics models without frictions. The simulations are performed by 1ms of the sampling time and 10s of the simulation time. A numerical method Bogacki-Shampine solver is selected with fixed-step.

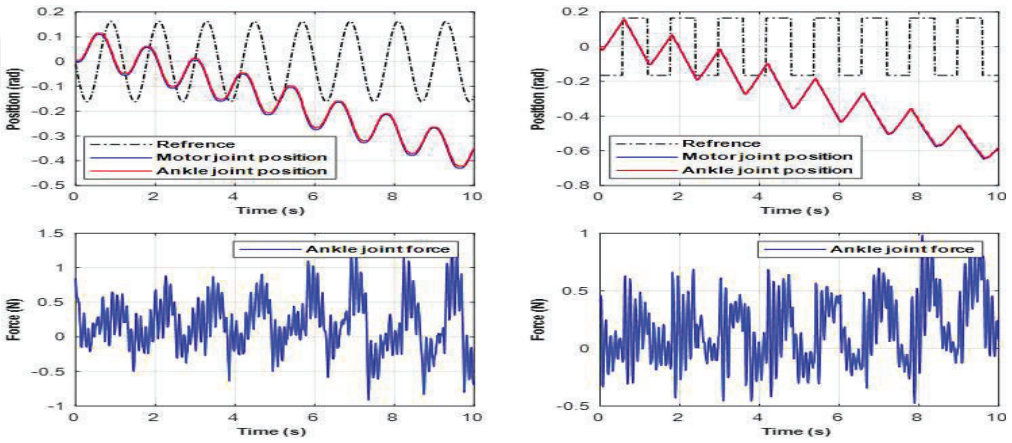

Figure 2.25. SEM-TA open-loop control : (a) position output and force output with sinusoidal signal input. (b) position output and force output with square signal input (Not : Motor joint position = $N^{-1}\theta_m$, Ankle joint position = θ_a)

A numeric dynamic model of the SEM-TA is developed using Matlab/Simscape toolbox for comparing the analytic mathematical model. Matlab/Simscape model of the SEM-TA is shown in Figure 2.25. According to the ankle position conditions and ankle force, the system was tested as an open-loop before applying control to the system. As shown in Figure 2.25, (a) the sinusoidal signal input and (b) the square signal input was performed at one stage, which decreased due to the weight of the ankle and the position of the ankle was out of control, and the ankle force changed without feedback control and was variable with changes in gravitational force. The controller cannot track the desired trajectory properly. In real situations, if the DFTFS stiffness is set too low, the torque of the motor is saturated, and the bandwidth of the open-loop force is reduced.

2.3. RSEA efficiency

In biomechatronics and robotic leg, where portability and weight are important issues, a DC power source such as a battery pack is usually the most convenient solution. when a motor is operated at variable load and/or varying speed, its efficiency can drop far below the datasheet value. By comparing the input power (electrical power) and output power (mechanical power) of the RSEA system, we can calculate the practical efficiency of the system (see Figure 2.26).

The motor's electrical power consumption is calculated with the following DC motor model [72]:

$$\begin{cases} \tau_m + v_m \dot{\theta}_m \\ U = l\dfrac{di}{dt} + Ri + k_b \dot{\theta}_m \end{cases} \tag{2.34}$$

Which gives the relationship between motor torque τ_m and motor speed $\dot{\theta}_m$ and current i and voltage U. From the above motor model, the electrical power consumption can be calculated as:

$$P_{elec} = i.U \tag{2.35}$$

The power of a lossless motor can be found by setting R; L and mm to zero:

$$P_{elec} = i.U = \frac{\tau_m}{k_t}.k_b \dot{\theta}_m \tag{2.36}$$

and, since the motor's speed constant k_b is equivalent to the torque constant k_t,

$$P_{mech} = \tau_m.\dot{\theta}_m \tag{2.37}$$

Efficiency is the ratio of total output power to input power, expressed as a percentage. This is typically specified at full load and nominal input voltage. System efficiency is the amount of actual power delivered to the output over the electrical power taken from the input.

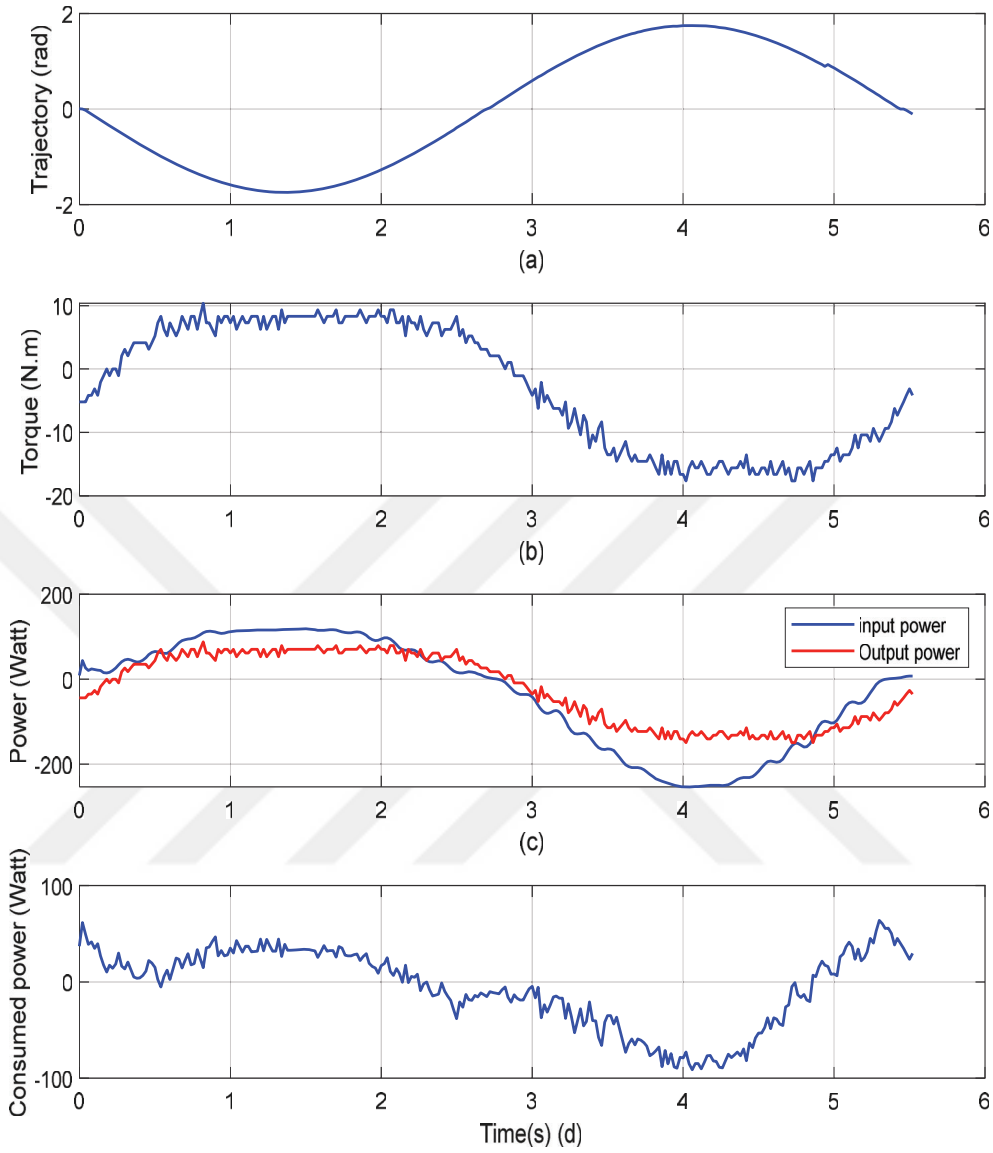

Figure 2.26. Power input and generated by the RSEA system : (a) The trajectory given to the system. (b) power output and power input. (c) Power consumed by gear, motor, and link element.

The RSEA system efficiency gm can be found by dividing the system's mechanical output power by the electrical power input or vice versa, depending on the direction of power flow:

$$\eta_{RSEA} = \frac{\tau_m . \dot{\theta}_m}{P_{elec}} \tag{2.38}$$

The average efficiency for a typical sinusoidal cycle trajectory is 58.94%.

3. JOINT FRICTION ESTIMATION OF THE RSEA

3.1. Introduction

Frictions are very important in AS, such as in pneumatic-hydraulic systems, anti-lock brakes for cars and robotic systems. Frictions are highly nonlinear, and they can result in steady-state errors, limit cycles, and poor performance in different systems [73]. It is, therefore, important for control engineers to understand friction phenomena and to estimate the ideal frictions for each system. Today, using the computational power available, it is possible to deal effectively with frictions. Frictions estimation has the potential to ameliorate the quality, economy, and safety of any system. Moreover, due to the gravitational forces and the coupling arising from the Coriolis and centripetal forces, the RSEA is underactuated, unstable and extremely nonlinear. The RSEA include a nonlinearity due to the frictions in the joints. RSEA is the most convenient example to understand the influence of the joint frictions on the design and performance of feedback controllers that aim to stabilize the pendulum in the upright position. The frictions have an influence on the system's response that should be considered seriously [74]. Therefore, friction estimation has the potential to ameliorate the quality and dynamic behavior of the system [75]. In this chapter, friction estimation models are developed to estimate the frictions in the joints of RSEA. The parameters of frictions models are described with details. The following approach was used to estimate the joint friction of pendulum, Comparison of Friction Estimation Models (FEMs) for RSEA based on three friction models existing in the literature: NCFM, LFM, and NLFM.

3.2. Friction Estimation Models (FEMs)

The joint frictions are dependent on many physical parameters, such as position, velocity and acceleration of the joints [76]. The changes in the positions, velocities and the accelerations of the robotic legs can change the friction’s characteristics in a complex manner [77]. The dynamic behavior of the joints’ frictions is simulated with the different models in the existing literature. Most of these models are defined by

friction coefficients. Therefore, it is necessary to develop an accurate friction model to estimate the friction's coefficients in the joints in accordance with the dynamic behavior of positions, velocities and accelerations. NCFM, LFM, and NLFM estimation models were given in this chapter [78], [79], [100-104]. To estimate the constant friction coefficients in the pendulum's joints of the RSEA, different friction estimation models (NCFM, LFM, and NLFM) were examined. These friction models consist of different important components. Each component takes care of certain aspects of the friction force in the joints [80-82]. Mostly used friction model in the literature is the generalized static friction model which depends only on the velocity (v). It describes only the steady-state behavior of the friction force F_f in the sliding regime, and it is given the equation below [83]:

$$\mathrm{F_f} = \sigma_2 \mathrm{v} + \mathrm{sign(v)} \left(\mathrm{F_c} + (\mathrm{F_s} - \mathrm{F_c}) \exp\left(- \left| \frac{\mathrm{v}}{\mathrm{V_s}} \right|^{\delta} \right) \right) \tag{3.1}$$

The first term represents the viscous friction force, and the second term equals the Stribeck effect. $\mathrm{F_s}$, $\mathrm{F_c}$, $\mathrm{V_s}$, δ and σ_2 are the static force, the Coulomb force, the Stribeck force, the shape factor and the viscous friction coefficient, respectively. this model has the discontinuity at velocity reversal which causes errors or even instability during friction compensation.

3.2.1. Non-conservative friction model

NCFM is a classical friction model. It has been used in the first works related to the control of pendulum of RSEA to estimate the friction in the joints, which based only on one type of friction coefficient [84]. The non-conservative torques due to natural damping of the pendulum of RSEAs called viscous friction torque, and it is introduced through Rayleigh's dissipation function $Ð(\theta_i)$ [85]. The non-conservative friction torque is given in equation (3.1).

$$\mathrm{F_v} = \frac{\mathrm{d}\, Ð(\theta_i)}{\mathrm{d}\theta_i} = \frac{\mathrm{d}}{\mathrm{d}\theta_i}\left(\frac{1}{2} \overline{\mathrm{C_p}} \dot{\theta}_i^{\,2} \right) = \overline{\mathrm{C_p}} \dot{\theta}_i \tag{3.2}$$

where $\overline{\mathrm{C_p}}$ is the viscous friction coefficient and $\dot{\theta}_i$ is the angular velocity of the i-th joint.

3.2.2. Linear friction model

LFM is a combination of the Viscous friction presented in the non-conservative model and another type of friction called Coulomb friction [86], the LFM, which is presented by equation (3.3).

$$F_l = F_v + F_c \tag{3.3}$$

Where F_c is the Coulomb frictions and F_v is the viscous friction torque which is proportional to the angular velocity $\dot{\theta}_i$, and given by equation (3.4). [87]

$$F_v = B_i \dot{\theta}_i \tag{3.4}$$

where B_i are the constant viscous coefficients. The Coulomb friction is proportional to the normal load force N_f which is derived as follows:

$$N_f = m\omega^2 l + mg\cos(\theta) \tag{3.5}$$

l is the distance from the pendulum of RSEA rotation center to the mass center. The pendulum parameters are given in Figure 3.1. The Coulomb frictions F_c is given by equation (3.6).

$$F_c = C_i \, sgn(\dot{\theta}_i).(ml\,\dot{\theta}_i^{\,2} + mg\cos(\theta_i)) \tag{3.6}$$

where C_i are the dynamic friction coefficients and $sgn(.)$is the signum function.

3.2.3. Non-linear friction model

The new researches in the field of friction estimation have found that the frictions in the joints can be affected by several factors such as temperature, force/torque, position, velocity and acceleration. Since friction has a complex nonlinear nature [88], the LFM becomes an oversimplified model in friction structure. The RSEA system can move in trajectories which have high and suddenly changing, position speed, acceleration and jerk. The LFM cannot cover these characteristics, especially at sudden motion reversal [89]. Therefore, the NLFM reflects a better description of the joint friction characteristics. This model can be described in the following nonlinear equation (3.7). [90]

$$\tau_f = f_o + f_c\,\mathrm{sgn}(\dot{\theta}_i) + f_v\,\dot{\theta}_i + f_a \mathrm{atan}(f_b\,\dot{\theta}_i) \tag{3.7}$$

where f_o the zero-drift error of friction torque, f_c is the Coulomb friction coefficient, f_v is the viscous friction coefficient. $f_a \mathrm{atan}(f_b\,\dot{\theta}_i)$ present the experimental friction in zero velocity behavior, which f_a and f_b are the experimental friction coefficients. $\dot{\theta}_i$ is the angular velocity, sgn(.)is the signum function and atan is the arctangent function. In fact, it appears that this nonlinear friction model is derived from the generalized friction model (equation (3.1)). The only difference between the two equations (3.1 and 3.7), the third term in equation (3.7) is modelled with the first and fourth term in equation (3.7). The reason for using the arctangent function in equation (3.7) is to overcome the discontinuity at zero velocity equation (3.1).

3.3. Torque Estimation Based on Nonlinear Friction Model

3.3.1. Nonlinear model of friction estimation

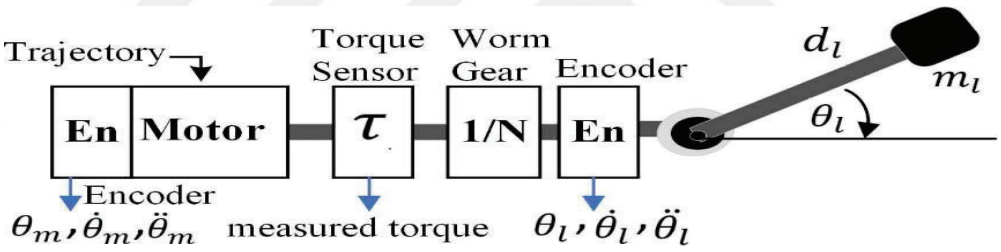

Figure 3.1. Friction estimation test system

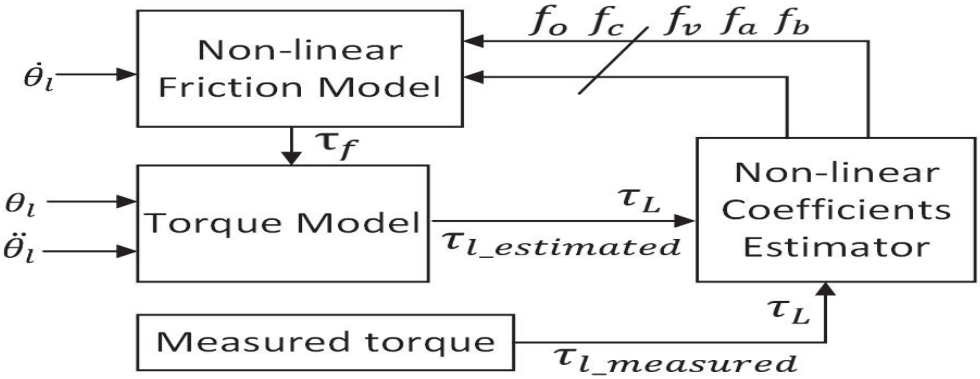

Figure 3.2. Implementation of the nonlinear model of friction estimation in Simulink RSEA model

In this part, the RSEA system torque estimation is investigated based on the nonlinear friction model. Since the worm gear has significant friction, the nonlinear

friction prediction model (NLFEM) developed in [91, 92] was employed in the structure of the friction estimator (Figure 3.2) to detect external disturbing torques in RSEA control (Figure 3.1). The estimated model of the experimental nonlinear friction was used in the proposed control system. In NLFEM, these five parameters were estimated: zero deflection error torque, viscose parameter, parameter Coulomb friction, and two experimental friction parameters [93]. The nonlinear model is the best explanation for estimating joint friction in the RSEA. The mathematical equation of nonlinear friction is defined as follows:

$$\hat{\tau}_f = f_o + f_c \,\mathrm{sgn}\left(\dot{\theta}_i\right) + f_v\left(\dot{\theta}_i\right) + f_a \mathrm{atan}\left(f_b\,\dot{\theta}_i\right) \tag{3.8}$$

f_o is zero-drift error torque, f_c is the parameter of coulomb, f_v is the parameter of viscous, f_a and f_b are two parameters of experiential friction. $\dot{\theta}_i$, $\mathrm{sgn}(.)$ and atan constitutes the angular velocity, the function of signum and the arctangent function, respectively.

$$\tau_m = K_\tau i - B_{Xm}\omega_m - J_{Xm}\frac{d\omega_m}{dt} \tag{3.9}$$

$$\tau_l = m_l d_l g\, cos(\theta_l) + \hat{\tau}_f + J_Y \frac{d\omega_l}{dt} \tag{3.10}$$

The experimental torque obtained from the torque sensor is used in the motor torque equation equation (3.9). The laws of Newton's second approach are employed to drive the torque equations (3.10). In this equation, ml is 0.3kg, and dl is 0.3m.

The actuator dynamics is defined below:

$$u_m = J_m\ddot{\theta}_m + \tau_l + \tau_f \tag{3.11}$$

Where, u_m is the torque required by the motor, θ_m is the motor position, J_m is the motor inertia, and τ_l and τ_f are the joint torques and the friction torque, respectively, and S_θ is the storage function:

$$S_\theta = \frac{1}{2}J_m\ddot{\theta}_m^2 \tag{3.12}$$

and its derivative

$$\dot{S_\theta} = \dot{\theta}_m u_m - \dot{\theta}_m\tau_l - \dot{\theta}_m\tau_f \tag{3.13}$$

The estimator dynamics is given by 21:

$$u_m = J_m\ddot{\theta}_m + \tau_l + \hat{\tau}_f \tag{3.14}$$

Where $\hat{\tau}_f$ is the estimation of the friction, and with the u_{cm} is the torque produced by the controller.

$$u_m = u_{cm} + \hat{\tau}_f \tag{3.15}$$

Since the legged robots have hybrid nonlinear dynamic behavior, their actuators are coupled with these dynamics. Therefore, linear stability methods cannot be used. Instead, the passive properties of friction compensation should be analyzed. If it turns out to be passive, the estimator can be easily incorporated into a Lyapunov stability analysis of the RSEA system with a passive controller.

$$\dot{S_\theta} = \dot{\theta}_m u_{cm} - \dot{\theta}_m \tau_l + \dot{\theta}_m(\hat{\tau}_f - \tau_f) \tag{3.16}$$

The last term can be considered as friction compensation in equation 3.16.

While the friction estimator will always provide a filtered friction signal, the absolute value of $\hat{\tau}_f$ is always smaller than the absolute value of τ_f, and the difference always has the opposed sign $\dot{\theta}_m$. Therefore, this term is always dissipative.

$$\dot{\theta}_m(\hat{\tau}_f - \tau_f) \leq 0 \tag{3.17}$$

This is dissipating energy. Due to the limited of disturbances, the compensation of friction becomes passive and convergent to the equilibrium point.

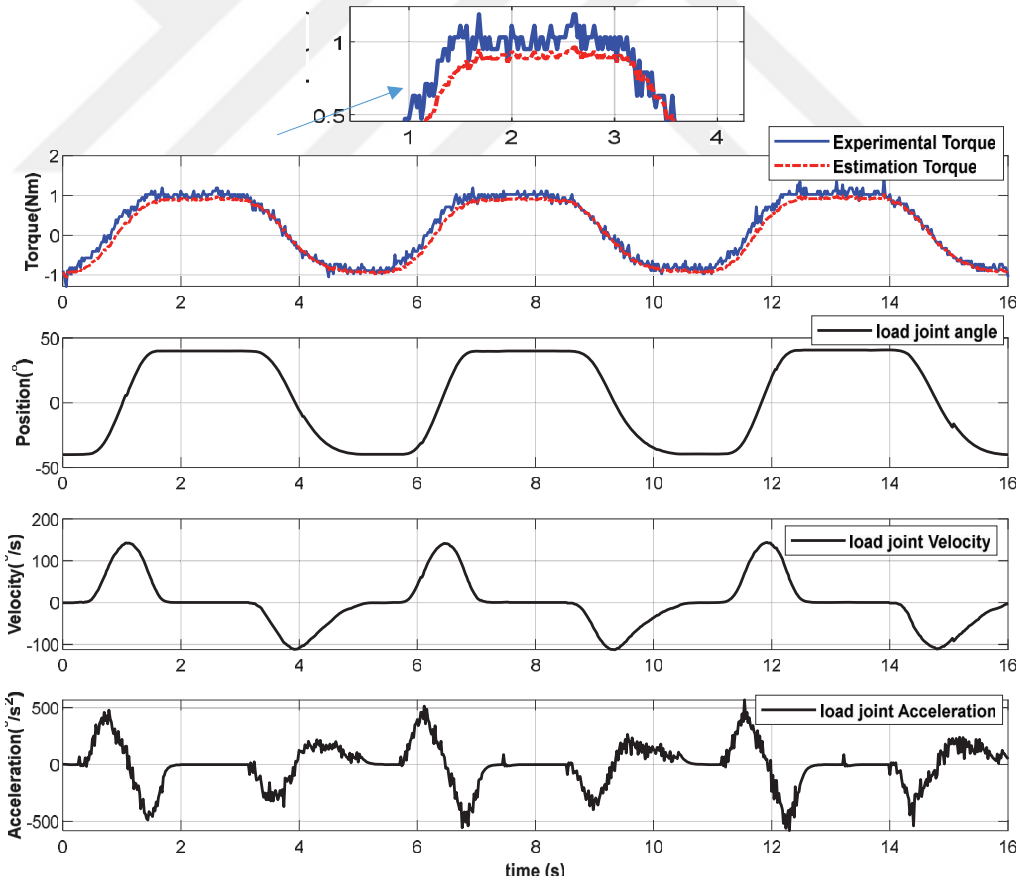

Figure 3.3. The estimated and experimental torque from the nonlinear friction model joint position, velocity, and acceleration.

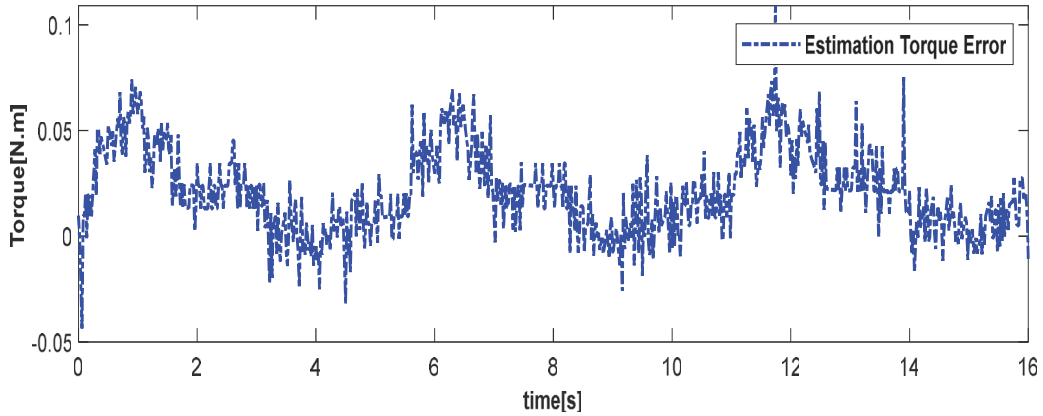

Figure 3.4. The error between the estimated torque using the NLFM and the experimental torque.

3.3.2. Experimental torque from the nonlinear friction model

The torque output is obtained by a torque sensor from the experimental system. This torque is also simulated using the mathematical model of torque with the nonlinear friction model. Inputs of the torque model are acceleration and velocity. Friction torque estimation is required to complete the torque model [94]. Figure 3.3 illustrates the friction Simulink model to estimate the torque friction. As seen in Figure 3.4, the estimated torque, which is based on the nonlinear friction model and trajectory signals (angular position, angular velocity, and angular acceleration), and the experimental torque are very similar. Figure 3.4 shows the error between torque estimated using NLFM and experimental torque.

Table 3.1. Estimation results for NLFEM

Parameters	Definition	Values	Unit
f_o	The torque of zero-drift error	1.3710e-02	$N.m$
f_c	Coefficient of Coulomb friction	6.1431e-04	$N.m$
f_v	Coefficient of viscous friction	2.910 e-02	$N.m.s/rad$
f_a	Experimental friction a coefficient	3.1413e-01	$N.m$
f_b	Experimental friction b coefficient	1.3905e-02	$N.m$

The coefficient of friction estimation results (Table 3.1) in the system load joint is based on the received error between the estimated torque using NLFEM and an experimental torque. Due to using the upright worm gear in the actuator, the coefficients of experimental friction are obtained higher than the usual power transmission mechanisms.

4. SYSTEM CONTROL AND SIMULATION RESULTS

4.1. Introduction

Rotary Series Elastic Actuator (RSEA) has been widely used for legged robots, haptics, and rehabilitation robots. SEA is often preferred for these properties: robustness, high power density, and high-bandwidth control performance, which allows the implementation of impedance control. The impedance control of Rotary Series Elastic Actuators (RSEA) has been an interesting research area in the last few years. In the literature, many novel approaches for impedance control have been developed [95]. Nowadays, the torque control approaches are classified as either Impedance Control (IC) or Hybrid Control (HC) (see Figure 4.1). The approaches classified as impedance control [96] do not attempt to explicitly control torque but control the relationship between the torque and position at the end of the ankle in contact with the environment [97]. Hence, position control leads to applied torque control. Alternatively, HC separates the robotic torque task into two subspaces, the first one is the torque control subspace, and the second one is the position control subspace [98]. Two independent controllers are required for each subspace. In [99], Anderson and Sponge developed a novel method to combine the two algorithms into a one control algorithm strategy. This approach can be called the Hybrid Impedance Controller (HIC), which combines HC and IC strategies and can be reduced to either approach. HIC can separate the task space into two subspaces, an impedance-controlled, position subspace and an explicit torque-controlled subspace [100]. The fractional-order dynamic systems and controllers have been a part of different science/engineering disciplines for many years. The fractional-order differential equations define Fractional-Order Controllers (FOC). Using the derivatives and integrals operations in fractional orders may be adjusted for the frequency response of the control system directly and continuously [101]. The controllers based on fractional-order derivatives and integrals are usually used in industrial applications and other various fields such as system identification, haptic, power electronics, robotic arms, and magnetic levitation system control [102-103]. It should be noted

that the behavior of many physical systems can be determined using FOC theory and can be controlled with FHIC even if the system has unstable or time delay behaviors. [104-106]. The FOC for a HIC extends the controller to the fractional hybrid impedance controller, in order to yield a robust and stable torque control system. Moreover, many aspects needed to be taken into account when designing these controllers. Controller parameters optimization in linear and nonlinear systems is quite difficult. There is a need for an effective and efficient global approach to optimize these parameters automatically. The optimization algorithm PSO is used to estimate the optimal parameters of the FHI controller [107-109]. PSO is an evolutionary algorithm that can be used to find the optimal solutions in a large search space. PSO algorithm is particularly used for parameter optimization in a continuous and multi-dimensional search space. The PSO technique converges faster than other optimization techniques and generates a high-quality solution in a short time [110]. Furthermore, the implementation of PSO is easily comparable to other metaheuristic optimization algorithms.

In this work, a new AFHIC approach is developed with a fractional order controller and adaptive fuzzy rules for the RSEA. The FHIC parameters are tuned with the PSO algorithm and then used in the AFHI controller [111]. This paper proposed fractional hybrid impedance control (AFHIC) for high-sensitive contact stress force tracking in uncertain environments. The main goal of such a controller is to avoid the torque overshoots in the contact stage while keeping stress force error in the high-sensitive tracking stage, where traditional control algorithms are not competent [112-114]. Moreover, the AFHIC is presented here mainly in order to cater to a sensitive fractional behavior. Its adaptability to the pressure of the sole of the foot on real environments such as grass (soft), carpet (medium), and solid floors (hard) is far superior to traditional impedance control [115]. It allows precise torque (or force) mode control. Using this control method, the design of higher-level controls for human-robot interaction can be achieved easily. The proposed control model consists of an outer concept position control loop that generates the reference acceleration to an inner torque control loop. The performance of the controllers is examined according to these parameters: RMSE of the positions and torque. Moreover,

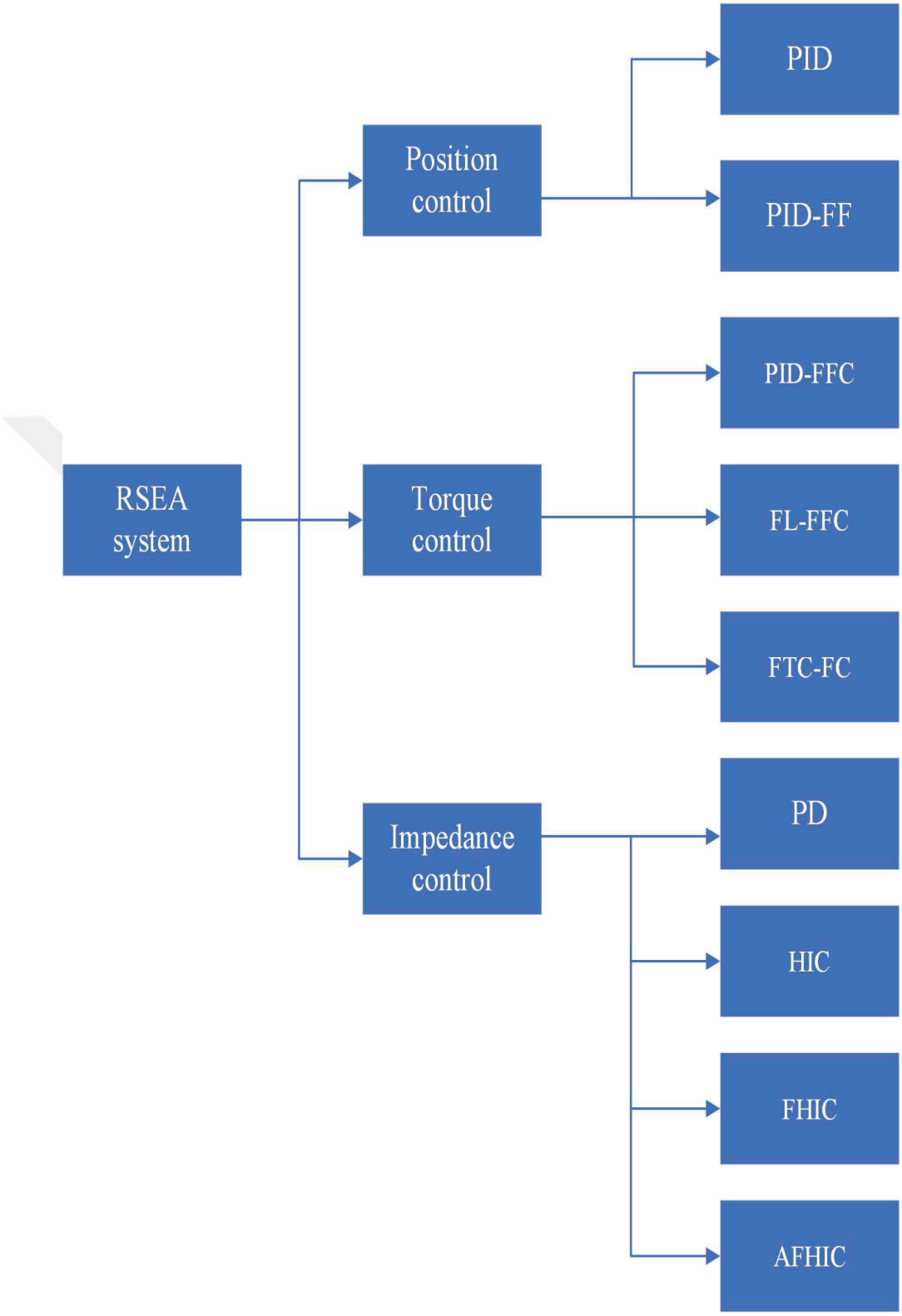

Figure 4.1. Control methods applied for the RSEA

robustness analysis of the controllers here are compared for three different cases [116]. Different simulation and an experimental setup are developed to validate the control performance of the controllers. According to the comparative study results, the responses of controllers in simulation and experimental cases are very similar.

4.2. Design of Position Controllers for the RSEA

In this section, the controller methods applied to control our RSEA are explained with details.

4.2.1. PID controller

To torque control of the RSEA in the control model of HA-SEMTAS and to control the position of joint at the desired position using the PID control approach, two PID controllers: PID controller and PID-FeedForward (PID-FF) controller have been designed for the two control loops of the system. The equations of the PID control are given as follows: [117].

$$u_{pid} = K_{pp}\, e(t) + K_{ip} \int e(t)\, dt + K_{dp} \frac{d\, e(t)}{dt} \tag{4.1}$$

$$u_{pid-f} = K_{pf}\, e(t) + K_{if} \int e(t)\, dt + K_{df} \frac{d\, e(t)}{dt} + G_{ff}\,(t) \tag{4.2}$$

Where $G_{ff}(t)$ is the feedforward equation, and $e(t)$ is the angle error of the joint link and the angle error of the horizontal link, respectively. K_{pp} , K_{ip}, K_{dp} are the PID controller parameters of the proportional, integral and derivative terms of the pendulum of RSEA link respectively. Moreover, K_{pf} , K_{if}, K_{df} are the PID-FF controller parameters of the proportional, integral and derivative terms of the link respectively. Since the dynamics of the angle of pendulum link dynamics are coupled to each other, the change in any controller parameters affects both the arm position, which makes the tuning tedious. The tuning of controller parameters is done by using trial and error methods and observing the responses of the Simulink model to be optimal (see Figure 4.2, and Figure 4.3). The tuning of controller parameters is done by minimizing the error methods using an optimization algorithm such as genetic algorithm (GA).

The parameters of the PID controller are optimized by a GA. They are given in Table 4.1. Optimization with a GA is conceptually simple and flexible. The cost function used in GA can be easily selected and reconfigured.

Table 4.1. Optimized coefficients for the PID and PID-FF controller and the genetic algorithm parameters

Gains of controller and Parameters	u_{pid} value	u_{pid-ff} value
coefficient of proportional	K_{pp} =2.31	K_{pf} =2.50
coefficient of integral	K_{ip} =1.74	K_{if} =1.32
coefficient of derivative	K_{dp} =3.89	K_{df} =3.27
generations number	100	100
population type	2 vectors	2 vectors
scaling function	Rank	Rank
selection subordinate	Stochastic uniform	Stochastic uniform
mutation subordinate	Adaptive feasible	Adaptive feasible
crossover subordinate	Scattered	Scattered

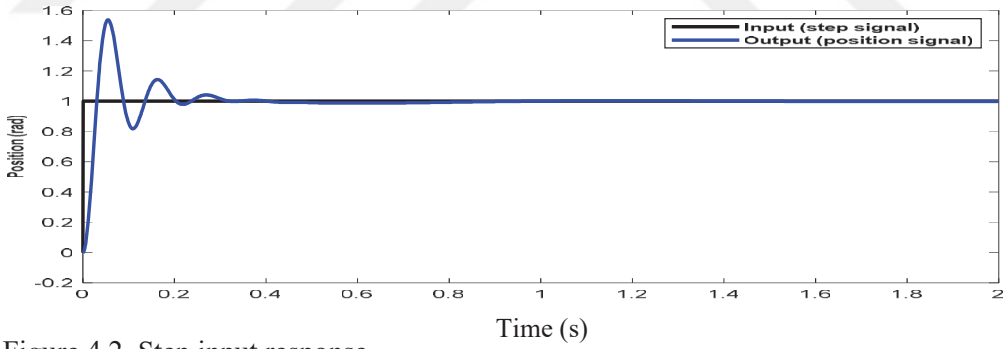

Figure 4.2. Step input response

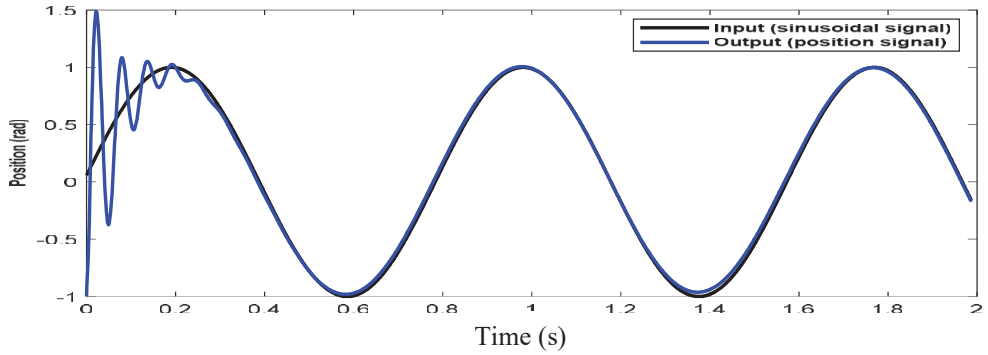

Figure 4.3. Sinusoidal input response

4.3. Design of Torque Controllers for the RSEA

4.3.1. PID-FFC design

The Feedforward technique is an ideal control scheme when there is a known or defined source of routine disturbances. Feedforward is able to key in on the source, and by modeling the range of disturbances emanating from that source feedforward Control can prepare an appropriate response [118]. The performance of the RSEA control depends on the motor response. The detailed description of the RSEA's controller with PID-FFC is considered in this part.

The impedance equation can be found as follows.

$$Z(s) = \frac{\tau_l}{\theta_l}(s) = \frac{-k_s(s^2 J_{tot} + sB_{tot})}{s^2 J_{tot} + sB_{tot} + k_s + G_c(s)} \tag{4.3}$$

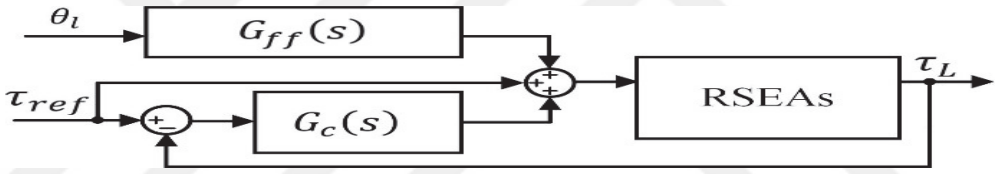

Figure 4.4. Torque feedforward controller

Figure 4.4 shows the controller G_c(s) of torque with two inputs, reference of torque, and angle of load joint. If the τ_{ref} is chosen as constant, the first and second derivatives of τ_{ref}will are equal to zero.

$$G_{ff}(s) = s^2 J_{tot} + sB_{tot} \tag{4.4}$$

$$\tau_m = \tau_{ref} + G_{ff}\theta_l \tag{4.5}$$

$G_{ff}(s)$ is the feedforward equation, and the equation of the motor torque is given in equations 4.4 and 4.5 [119].

Combining the PID controller (Equation 4.2) with FFC, a more robust control structure called PID-FFC was designed. The parameters of the PID controller are optimized by a GA. They are K_{pf} =2.16, K_{if} =1.12, K_{df} =2.59.

4.3.2. FLC structure

The FLC system shown in Figure 4.5 consists of fuzzification, inference engine and defuzzification blocks. Let $X \subset R^n$ be a universe of discourse. In Equation 4.6, the nonlinear dynamic system is modeled by the state-space equations.

$$\dot{x} = g(x) + d(x)u \tag{4.6}$$

where, $x \in X, x = [x_1 \ x_2]^T$ is a state-vector, $n \in IN^*, \dot{x} = [\dot{x_1} \ \dot{x_2}]^T$, is the derivative according to the variable of time t, $g(x) = [g_1(x) \ g_2(x)]^T$ and $d(x) = [d_1(x) \ d_2(x)]^T$ are vector functions describing process dynamics, u_c is the output signal of control. It is obtained using the defuzzification method of Centre of Gravity (COG) for FLCs Mamdani-type.

The j-th IF–THEN rule in the FLC rule-base, referred to as fuzzy rule of Mamdani [120], as follows:

The rule

$$j: \text{IF } x_j \text{ is } \widetilde{X}_{j,1} \text{ AND } .. \text{AND } x_n \text{ is } \widetilde{X}_{j,n} \text{ THEN } u_c \text{ is } \widetilde{Y}_j, j = \overline{1,r}, r \in IN, r \geq 2, \tag{4.7}$$

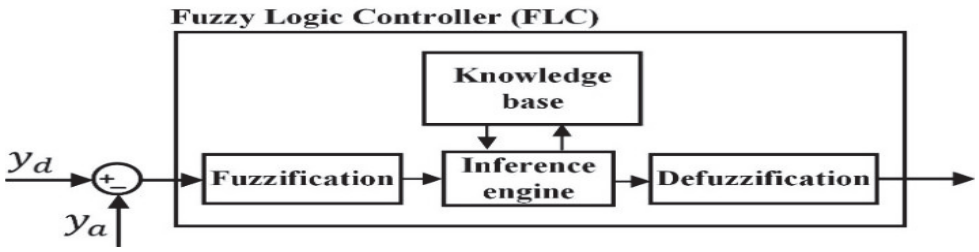

Figure 4.5. Block diagram of FLC

where $\widetilde{X}_{j1}, \widetilde{X}_{j2}$ are fuzzy sets that define the linguistics terms (LTs) of the input variables, $\widetilde{Y}_j$ describes the LTs of output variables, and r=49 is the total number of rules. Note that Y represents the domain of the output or the control signal domain and $\mu_{Y_j} \neq 0, j = \overline{1,r}$.

The activation degree of the j-th Mamdani fuzzy rule is

$$\alpha_j(x) = \min\left(\mu_{\widetilde{X}_{j,1}}(x_1), \mu_{\widetilde{X}_{j,2}}(x_2)\right) \tag{4.8}$$

It is presumed that for any x belonging to the input universe of discourse, X, there are at least one α_i amid all the rules, which is not equal to zero.

The output signal of any control rule is calculated by the COG defuzzification method applied for:

$c_j(x,y) = \min\left(\alpha_j(x), \mu_{Y_j}(y)\right)$, that is:

$$u_j(X) = \begin{cases} \dfrac{\int_Y y.\, c_j(x,y)dy}{\int_Y c_j(x,y)dy} & \text{if} \alpha_j(x) > 0 \\ 0 & \text{if} \alpha_j(x) = 0 \end{cases} \quad (4.9)$$

All rules aggregation is done in terms of applying (4.9):

$$c(x,y) = c_1(x,y) + c_2(x,y) + \cdots + c_r(x,y). \quad (4.10)$$

As a result, the signal of control fed to the process will be:

$$u = \frac{\int_Y y.\, c\, dy}{\int_Y c\, dy} = \frac{\sum_{i=1}^{r} \int_Y y.\, c\, dy}{\sum_{i=1}^{r} \int_Y c\, dy} \quad (4.11)$$

The previous structure describes this FLC as $\mathrm{COG} - \mathrm{SUM} - \mathrm{AND}$ fuzzy logic controller.

Property 1: For each $\mathrm{COG} - \mathrm{SUM} -$ AND FLC the following relationships hold

$u_{min}(x) \le u(x) \le u_{max}(x)$ for any $x \in X$, where $u_{min}(x) = \min_{i=\overline{1,r}}\left(u_i(x)\right)$,.

Proof. Let $x_0 \in X$ and $S_i = \int_Y c_i(x_0, y)dy$.

If $\alpha_i(x_0) \neq 0$ then $u_i(x_0)$ in (4.6) is bounded:

$$u_i(x_0) = \frac{\int_Y y.\, c_i(x_0,y)dy}{\int_Y c_i(x_0,y)dy} = \frac{\int_Y y.\, c_i(x_0,y)dy}{S_i}$$

And

$$u_i(x_0).S_i = \int_Y y.\, c_i(x_0,y)dy \quad (4.12)$$

Therefore:

$$u(x_0) = \frac{\int_Y y.\, c(x_0, y)dy}{\int_Y c(x_0, y)dy} = \frac{\int_Y y.\, (c_1(x_0, y) + c_2(x_0, y) + \cdots + c_r(x_0, y))dy}{\int_Y (c_1(x_0, y) + c_2(x_0, y) + \cdots + c_r(x_0, y))dy}$$

$$= \frac{u_1(x_0)S_1 + u_2(x_0)S_2 + \cdots u_r(x_0)S_r}{S_1 + S_2 + \cdots + S_r} \tag{4.13}$$

If $u_{min}(x) = \min_{i=\overline{1,r}}(u_i(x))$ and $u_{max}(x) = \max_{i=\overline{1,r}}(u_i(x))$ then it results that:

$$u(x_0) = \frac{u_1(x_0)S_1 + u_2(x_0)S_2 + \cdots u_r(x_0)S_r}{S_1 + S_2 + \cdots + S_r}$$

$$\leq \frac{u_{max}(x_0)S_1 + u_{max}(x_0)S_2 + \cdots u_{max}(x_0)S_r}{S_1 + S_2 + \cdots + S_r}$$

$$= \frac{u_{max}(x_0)(S_1 + S_2 + \cdots S_r)}{S_1 + S_2 + \cdots + S_r} = u_{max}(x_0) \tag{4.14}$$

And

$$u(x_0) = \frac{u_1(x_0)S_1 + u_2(x_0)S_2 + \cdots u_r(x_0)S_r}{S_1 + S_2 + \cdots + S_r}$$

$$\geq \frac{u_{min}(x_0)S_1 + u_{min}(x_0)S_2 + \cdots u_{min}(x_0)S_r}{S_1 + S_2 + \cdots + S_r}$$

$$= \frac{u_{min}(x_0)(A_1 + A_2 + \cdots A_r)}{S_1 + S_2 + \cdots + S_r} = u_{min}(x_0) \tag{4.15}$$

Hence, $u_{min}(x) \leq u(x) \leq u_{max}(x)$ for any $x \in X$

4.3.3. FL-FFC design

In order to design a FLC at the first step, the fuzzy rules for inputs (error and error rate) and output (motor input) are obtained to control the load of the joint [121]. It should be noted that in nonlinear systems, the FLC experimental design is preferable to the PID controller. The feedback control loop time in the real-time system is better in using industrial PC with high computation capability (good CPU and RAM). FLC is used to control RSEA torque with a 1kHz control loop. The FLC generates PWM output signals [122]. For the PWM signals, the FLC determines the appropriate duty cycle while also controlling for variations in the torque of the RSEA. FLC inputs are error and error rates. The error is determined as the difference between the RSEA measurement and the desired torque as.

$$e = y_d - y_a \tag{4.16}$$

where y_a and y_d are the actual torque and the desired torque, respectively.

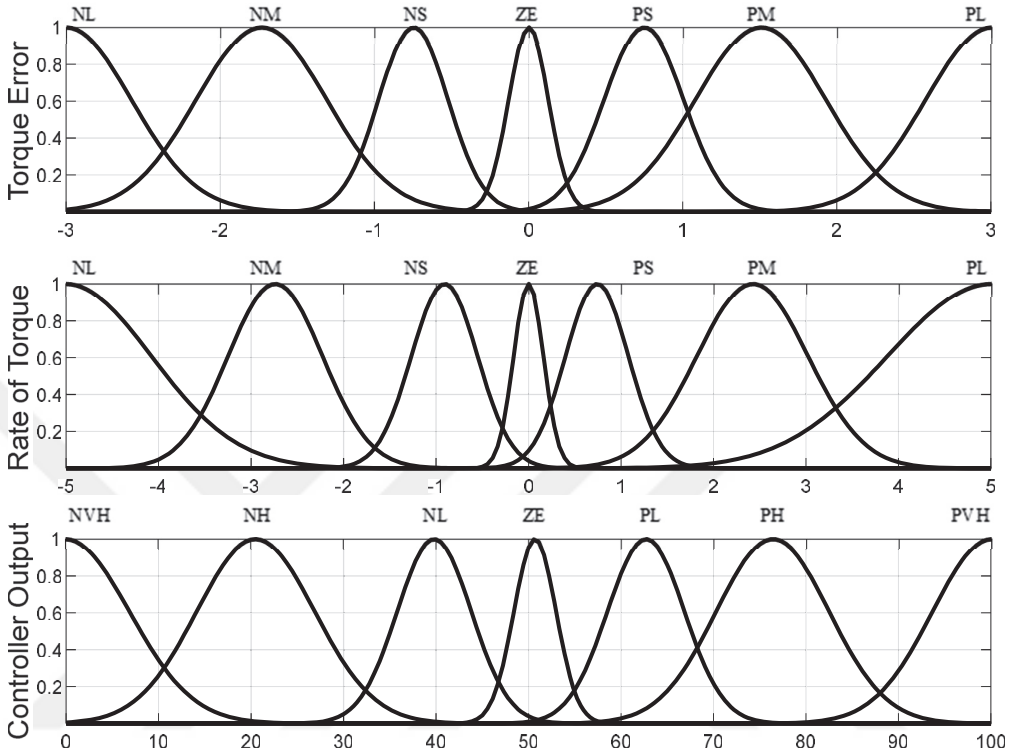

Figure 4.6 Functions of FLC membership. (a) torque error (b) rate of torque (c) control output

Figure 4.6 illustrates the FLC schematic with output and input membership functions.

In this work, the fuzzy inference of the Mamdani type is employed in FLC. The FLC has shown in table 4; 49 rules are constructed for the motor controller, three of which are illustrated below

Table 4.2. Fuzzy rules

ė \ e	NL	NM	NS	ZE	PS	PM	PL
NL	PVH	PVH	PH	PL	PL	PL	PL
NM	PVH	PH	PH	PL	PL	ZE	ZE
NS	PH	PH	PL	ZE	PL	NL	NL

Table 4.2.(Cont.) Fuzzy rules

ZE	PH	PL	ZE	ZE	ZE	NL	NH
PS	PL	ZE	ZE	NL	ZE	NH	NH
PM	ZE	NL	NL	NH	NL	NH	NVH
PL	NL	NH	NH	NVH	NH	NVH	NVH

Table 4.3. Range of the input and output variables

Ranges / Symbols	Input variables		Output variables
	Ranges of input (e)	Ranges of input (ė)	Ranges of output (U)
NL	[-5 -4 -3]	[-6 -5 -3.5]	[0 20]
NM	[-9 -6 -2]	[-4 -3 -1.5]	[0 20 40]
NS	[-3 -1.5 0]	[-2 -1 0]	[25 40 55]
ZE	[-0.75 0 0.75]	[-0.5 0 0.5]	[48 52 58]
PS	[0 -1.5 3]	[0 1 2]	[50 63 75]
PM	[2 6 9]	[1.5 3 4]	[58 78 93]
PL	[2 3 5]	[3.5 5 6]	[80 100]

where PL, PM, PS, ZE, NS, NM, and NL are linguistic values representing “low negative”, “medium negative” and so on. U is the output of the FLC, E is the error, Ec is the derivative of the error.

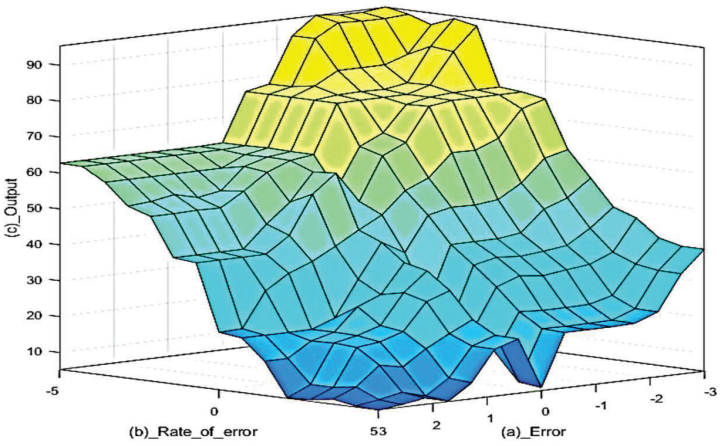

Figure 4.7. Decision surface of FLC: (a) error input (b) error rate input (c) FLC output (duty cycle)

The membership functions for the premises and results of the rules are illustrated in Figure 4.7.

4.3.4. FTC-FC design

For that to have a robust performance in the FLC method, system state variables must be able to move around the membership function flexibly. The following function is specified to provide the flexibility mentioned.

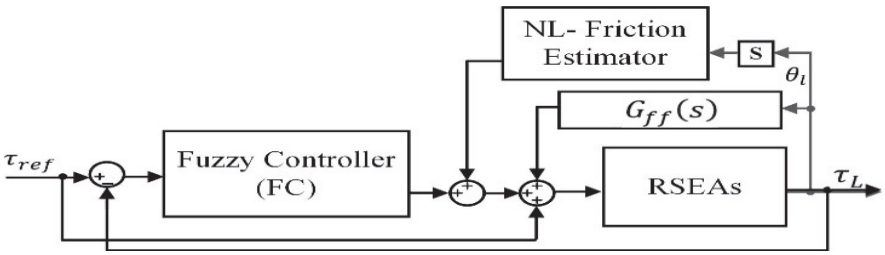

Figure 4.8. Block diagram of FL-FFC of the RSEA.

As shown in Figure 4.8, a friction estimator was added to the control block diagram in the FTC-FC to estimate nonlinear friction.

4.3.5. Stability analysis of the fuzzy controller

To determine the fuzzy stability, the fuzzy subsystem including Mamdani fuzzy rules and the system described in equation 4.6 were examined through the Lyapunov theorem. Theorem 1 demonstrates the method of stability analysis presented here. If any subsystem is stable in the Lyapunov sense with a common function of Lyapunov, it will prove that the overall system will also be stable in the Lyapunov sense [123].

Theorem 1: If P is a definite positive matrix and:

1) $V(\boldsymbol{x}) = \mathrm{x^T Px} \to \infty$ as $\|\mathrm{x}\| \to \infty, V(0) = 0,$

2) $\dot{V}(\boldsymbol{x}) \leq 0, \forall x \in X$ for all fuzzy subsystem,

3) $the\ set\ \{x \in X \,|\dot{V}(\boldsymbol{x}) = 0\}$ contains no system path except the trivial path $\boldsymbol{x}(t) = 0\ for\ t \geq 0,$

In the FLC system, the $\mathrm{COG - SUM - AND}$ and the Mamdani method defined in equation 29 is globally asymptotically stable at the origin.

Proof, the function of Lyapunov candidate $V(x) = x^T Px$ is set.

From $\dot{V}(x) = \dot{x}^T Px + x^T P\dot{x}$ and 29, the result is:

$$\begin{aligned}\dot{V}(\boldsymbol{x}) &= \big(g(x) + d(x)u(x)\big)^T Px + \boldsymbol{x}^T P\big(g(x) + d(x)u(x)\big) \\ &= g(x)^T Px + \boldsymbol{x}^T Pg(x) + \big(d(x)^T Px + \boldsymbol{x}^T Pd(x)\big)u(x) \\ &= G(x) + D(x)u(x), \end{aligned} \tag{4.13}$$

Where:

$$G(x) = \left(g(x)^T Px + \boldsymbol{x}^T P g(x)\right), \tag{4.14}$$

$$D(x) = d(x)^T Px + \boldsymbol{x}^T P d(x). \tag{4.15}$$

If $x_0 = 0 \Longrightarrow \dot{V}(\boldsymbol{x}) = 0$. According to $\dot{x}(t) = g\big(x(t)\big) + d(x(t)u\big(x(t)\big))$, it is proved that $(\dot{V})$ is negative definite. equation 43 is obtained using equation 29 under the Mamdani fuzzy rule condition:

$$\dot{V}(\boldsymbol{x}) = G(x) + D(x)u_1 < 0 \tag{4.16}$$

For any Mamdani fuzzy rule $i = \overline{1,r}$.

Now it is considered $x \neq 0$. Three possible cases should be analyzed as follows.

Case 1: $D(x)$ is strictly positive. From property 4.6, it is obtained that:

$$u_{min}(x) \leq u(x) \leq u_{max}(x)$$

$$\Longrightarrow G(x) + D(x)u_{max}(x) \leq G(x) + D(x)u(x) \leq G(x) + D(x)u_{max}(x) < 0 \tag{4.17}$$

Therefore $\dot{V}(\boldsymbol{x}) < 0$.

Case 2: $D(x)$ is strictly negative. From property 4.6 the result is 4.18:

$$u_{min}(x) \leq u(x) \leq u_{max}(x) \Longrightarrow 0 > G(x) + D(x)u_{max}(x) \geq G(x) + D(x)u(x) \geq G(x) + D(x)u_{min}(x) \tag{4.18}$$

Hence once more $\dot{V}(\boldsymbol{x}) < 0$.

Case 3: $D(x) = 0$, From (14), it results straightforward that $\dot{V}(\boldsymbol{x}) = G(x) < 0$.

According to the last three cases, it can be concluded that whatever the value of $D(x)$ is, the expected results will be obtained, $\dot{V}(\boldsymbol{x}) < 0$.

Condition 3 ensures the fulfillment of the principle of invariability of LaSalle from the theorem of LaSalle referred to in [124]. Under these conditions, the stability of the equilibrium point at the origin is global asymptotically guaranteed. This leads to convergence of the controlled system having the nonlinear friction to the equilibrium points.

In the case of nonlinear systems subject to bounded disturbances $b_{min} \leq u(x) \leq b_{max}$, Define $q = \{q_1, \dot{q_1}\}$ as the set of generalized coordinates for the system where: $q_1 = N^{-1}\theta_m$ is the angular displacement of the rotor, $\dot{q_1}$ is the angular velocity, N is the gear ratio, k_s is the flat spring stiffness, using Euler–Lagrange equations, the analytical model of the RSEA is derived a:

$$z = \begin{bmatrix} z_1 \\ z_2 \end{bmatrix} \in X = [-1,1] \times [-1,1], z_1(t) = q(t), \;\; z_2(t) = \frac{bq(t)}{dt}, \tag{4.19}$$

By substituting the defined state variables, the RSEA model is expressed with state variables, and it is obtained that:

$$\dot{z} = g(z) + d(z)u, \tag{4.20}$$

Therefore, the control method has transformed and given in equation 4.21:

$$g(z) = \begin{bmatrix} z_2 \\ \frac{1}{J_{tot}}(-B_{tot}z_2|z_1| - k_s z_1) \end{bmatrix}, d(z) = \begin{bmatrix} 0 \\ 1 \end{bmatrix}. \tag{4.21}$$

Mamdani type design $\mathrm{COG} - \mathrm{SUM} - \mathrm{AND}$ FLC will be introduced as follows. The linguistic variables z_1 and z_2 described by the membership functions in Figure 4.8 provide fuzzification settings.

The FLC operators OR, AND implemented by the max and min functions are employed in the fuzzy inference engine, respectively [125]. The set of Fuzzy rules complete the engine of inference, and the COG defuzzification method is utilized.

Let's try to prove the stability of the system by the proposed stability analysis by applying the state space (equation 29). The Lyapunov function candidate in 4.22 is given as:

$$V(\boldsymbol{z}) = \boldsymbol{z}^T \boldsymbol{P} \boldsymbol{z} = \frac{1}{2}\left(\frac{k_s}{J_{tot}} z_1^2 + z_2^2\right), \tag{4.22}$$

Where:

$$\boldsymbol{P} = \begin{bmatrix} k_s/(2J_{tot}) & 0 \\ 0 & 1/2 \end{bmatrix} \tag{4.23}$$

So, V is positive, and for $\|\boldsymbol{z}\| \to \infty$, then $V(\boldsymbol{z}) \to \infty$. It follows that $V(\boldsymbol{z}) > 0, \forall x \neq 0$

And

$$\dot{V}(\boldsymbol{z}) = \frac{1}{J_{tot}}(-B_{tot}z_1^2|z_2 + z_2 u), \tag{4.24}$$

From the rule-base of FLC (Table 4.1), it may be observed that if z_2 is Z, then u is Z too, otherwise z_2 and u are of opposite sign. Therefore, taking 4.24 into account, the derivative of V becomes $\dot{V}(\boldsymbol{z}) \leq 0$ for each FLC rule. Therefore, $\dot{V}$ is negative semi-definite.

Subsequent terms indicate that condition 3 holds in equation 4.6. A path can be assumed with:

$$z_2(t) = 0, z_1(t) \neq 0, \tag{4.25}$$

It results that:

$$\frac{bz_2(t)}{dt} = -\frac{k_s}{J_{tot}} z_1(t) \neq 0, \tag{4.26}$$

which means that $z_2(t)$ cannot remain constant. Therefore $\boldsymbol{z}(t) = 0$ is the only possible path for which $\dot{V}(\boldsymbol{z}) = 0$. So, the set $\{z \in X | \dot{V}(\boldsymbol{z}) = 0\}$ contains no path of the system except the trivial path $\boldsymbol{z}(t) = 0$ for $t \geq 0$.

According to equation 4.26, all of the FLC system defined above can be said that globally asymptotically stable at the origin.

4.4. Impedance Control of the RSEA

4.4.1. Hybrid impedance control (HIC)

Since in this work, the force of the sole of the foot is with the desired environment, so the controller brings the ankle joint to the desired position by position-based impedance control (PBIC) and contacting the environment with the impedance force-based impedance control (FBIC) without vibration (Kong et al., 2009; Lin et al., 2020; Jin et al., 2015). The desired dynamics behavior of the system is a combination of PBIC and FBIC with the switching parameter (S). The hybrid impedance control (HIC) includes both PBIC and FBIC with an S. The possible value of the S parameter can be (0,1). The HIC rule is given as follows:

$$J_{tot}(\ddot{x} - S\ddot{x_r})^{\alpha} + B_{tot}(\dot{x} - S\dot{x_r}) + K_s(x - Sx_r) - (1 - S)f_r = -f_e \tag{4.27}$$

where J_{tot}, K_s, B_{tot} are: inertia, stiffness, and damping, respectively. x_r is the angular reference position, $\dot{x_r}$ is the angular velocity and $\ddot{x_r}$ is the angular acceleration, x is the actual angular position, $\dot{x}$ is the angular velocity and $\ddot{x}$ is the angular acceleration. On the other hand, f_r is reference force, $f_e = J^{-T}\tau_e$ is the actual force exerted by the sole of the foot on the environment and measured by the wrist force sensor. The term J represents the Jacobian matrix that relates the joint velocity to the operational velocity. S is the selection vector. A fractional controller with non-integer derivation and integration parts can improve the quality and robustness of IC (Calanca and Fiorini, 2018). FHIC was developed based on HIC and using fractional parameters of $\alpha, \beta, \gamma, \delta$.

4.4.2. Fractional hybrid impedance control (FHIC)

To improve the system robustness, both parameters K_v and K_p are introduced [126]. The FHIC (see Figure 4.9) ensures compliance in the subspace of position control and accuracy force control in the subspace of force control. The output of the FHIC (u) is given in equation 4.28:

$$u = (S\ddot{x}_r)^{\alpha} + J_{tot}{}^{-1}\left[K_v B_{tot}(S\dot{x}_r - \dot{x})^{\beta} + K_p K_s(Sx_r - x)^{\gamma} + (1-S)^{\delta} f_r - f_e\right] \quad (4.28)$$

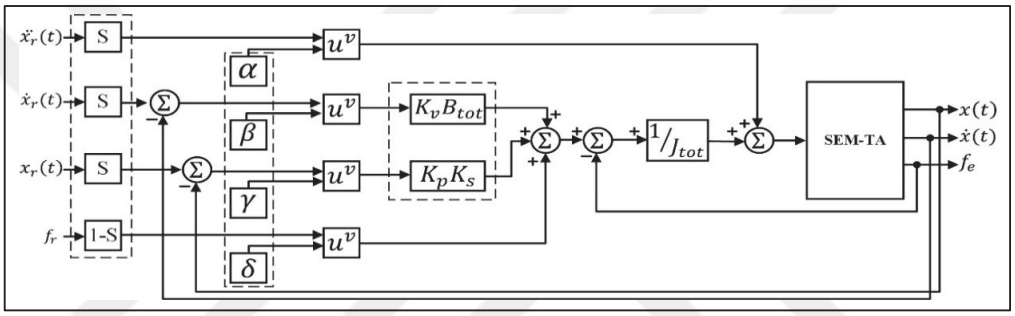

Figure 4.9. Block diagram of FHIC

Since the changes in the positive and negative values of the error can affect the controller output, the parameters of FHIC are used with the power function. The power function can conduct no precise results in the negative decimal values of error. Therefore, the negative error correction algorithm (NEC-algorithm) was developed to improve the control performance of the negative decimal values.

$x_{ri} = [\ddot{x}_r, \dot{x}_r, x_r\ ]$
$x_i = [0, \dot{x}, x\ ]$
$p_i = [\alpha, \beta, \gamma\ ]$
$Term_1 = Pow((S\ddot{x}_r), \alpha)$
$Term_2 = Pow((S\dot{x}_r - \dot{x}), \beta)$
$Term_3 = Pow((Sx_r - x), \gamma)$

before every online running the controller period Loop $(i = 1)$ Read $S, x_i, x_{ri}, and\ p_i$ Check $(Sx_{ri} - x_i) < 0$ If "yes" then Calculate $Term_i = -Pow(-(Sx_{ri} - x_i), p_i)$

Update $Term_i$ Update $i = i + 1$ Next $i <> 4$

Not: $Pow(x, y) = x^y$

4.4.3. Analysis of the steady-state error

In the free space, the actual force exerted, $f_e = 0$ results in

$$J_{tot}(\ddot{x} - \ddot{x_r}) + B_{tot}(\dot{x} - \dot{x}_r) + K_s(x - x_r) = 0 \tag{4.29}$$

so $x \to x_r$, means that there is no E_{ss} in this direction. In the constrained space, the motion of compliance must be guaranteed under the compliant motion control subspace, that is, $f_r = 0$. The accurate force control free from the stiffness parameter must be made sure. The impedance model is given as follows:

$$J_{tot}\ddot{x} + B_{tot}\dot{x} + K_s(x - x_r) = E_d \tag{4.30}$$

where $E_d = f_r - f$ is the force error. Also, the contact model is given in equation (4.31).

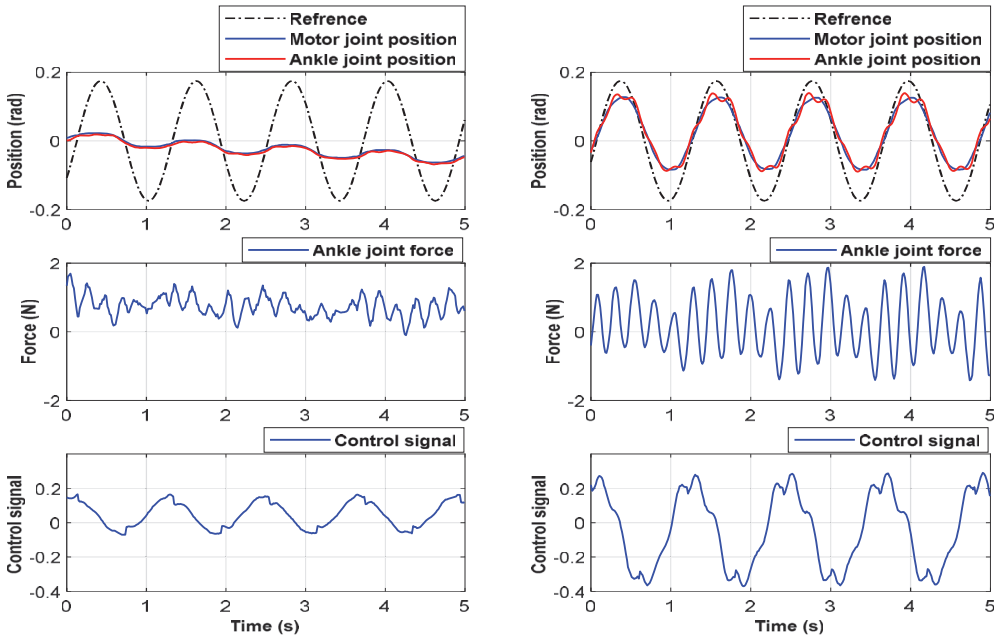

Figure 4.10. FHIC – With non-optimized parameters: $\alpha, \beta, \gamma, \delta = 0.5$ and $K_v, K_p = 5$ (a) force control mode and (b) position control mode.

$$f = \begin{cases} K_e(x - x_e), & x > x_e \\ 0, & x \leq x_e \end{cases} \quad (4.31)$$

where K_e is stiffness value, x is actual position, and x_e is the reference position. x results is given in equation (4.32)

$$x = \frac{1}{K_e} f + x_e = \frac{1}{K_e}(f_r - E_d) + x_e \quad (4.32)$$

Substitute (4.30) to (4.32), we can obtain

$$J_{tot}\ddot{E}_d + B_{tot}\dot{E}_d + E_d(K_s + K_e) = J_{tot}\ddot{F}_d + B_{tot}\dot{F}_d - K_s K_e(K_s + K_e) \quad (4.33)$$

which results in

$$e_{ss} = \begin{cases} \frac{K_s}{K_s + K_e}(f_r + K_e(x_e - x_r)) = K_{eq}\left(\frac{f_r}{K_e} + x_e - x_r\right), S = 0 \\ 0, \quad S = 1 \end{cases} \quad (4.34)$$

hence, in the subspace of the compliant motion, the following equation is satisfied

$$x_r = \frac{f_r}{K_s} + x_e \quad (4.35)$$

Accurate force control in the subspace of the compliant motion cannot be guaranteed due to incorrect prediction of the stiffness and position, while in the subspace of the contact, force control

$$f \to f_r \, , t \to \infty$$

that is to say; the E_{ss} is 0. The force control may be achieved. Figure 4.10 shows the effects of the non-optimized parameters in the FHIC, the controller parameters are selected in the middle range. The S parameter of the controller is a switch between the position control and force control. Figure 4.10 (a) shows the force control mode and in (b), the position control mod.

4.4.4. Tuning of the FHIC using PSO algorithm

In this section, the PSO algorithm is used to design and optimize the FHIC parameters in SEM-TA (Figure 4.11). The PSO technique converges faster than other optimization techniques and generates a high-quality solution in a short time.

Furthermore, the implementation of PSO is easily comparable to other metaheuristic optimization algorithms. The PSO algorithm's principal work is based on speed and acceleration changes of each particle toward its *gbest* (global best position) and the *pbest* (individual best position) at each time step. Each particle works to change the existing position and speed related to the distance between the existing position and *pbest*, and also the distance between the existing position and *gbest*. At each n step, using the *gbest* and *pbest*, the speed equation for the i^{th} particle is given in equation (4.36).

$$V_i(n) = \chi\left(V_i(n-1) + \phi_1\, r_1\big(pbest_i - P_i(n-1)\big) + \phi_2\, r_2\big(gbest - P_i(n-1)\big)\right) \quad (4.36)$$

X is defined below:

$$\chi = \frac{2}{\left|2 - \phi - \sqrt{\phi^2 - 4\phi}\right|},\ \phi = \phi_1 + \phi_2,\ \ \phi > 4 \quad (4.37)$$

The speed range is defined as $[-v_{max}, +v_{max}]$.

Changing speed with this method enables the i^{th} particle to search around its local *gbest*, and *pbest*. Based on the speed, each particle changes its position, given in equation (4.38).

$$P_i(n) = P_i(n-1) + V_i(n) \quad (4.38)$$

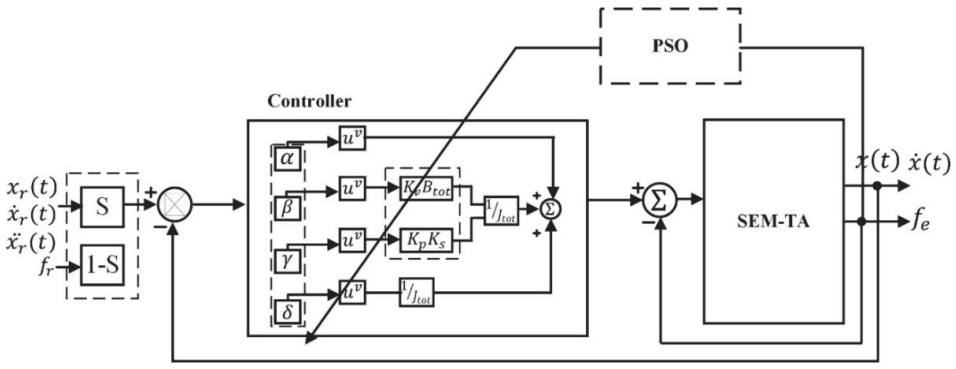

Figure 4.11. Tuning process of the FHIC controller parameters with PSO algorithm

The FHIC has six parameters to be optimized with PSO. PSO algorithm searches all parameters of the controller in AJS-RSEA. The controller parameters include six elements assigning real values. The order of parameters of FHIC is shown as the following.

$$P = [K_v, K_p, \alpha, \beta, \gamma, \delta] \quad (4.39)$$

The most critical stage in using PSO is choosing the best cost function to evaluate each particle's fitness. During the tuning process with PSO, the cost function (MRSE) is employed. These cost functions for i^{th} particle are below:

$$E_{MRSE}(k) = \frac{1}{N}\sum_{i=1}^{N}\sqrt{\left(e_1^2(i) + e_2^2(i)\right)} \quad (4.40)$$

The block diagram of the FHI controller optimizing process with PSO is illustrated in Figure 4.11. FHIC parameters are updated at every simulation time (t_f).

Table 4.4. The parameters of PSO algorithm

Parameter	Value
Population Size (P)	10
Number of particles	6
Lower bound $[\alpha, \beta, \gamma, \delta, K_v, K_p]$	[0,0,0,0,0,0]
Upper bound $[\alpha, \beta, \gamma, \delta, K_v, K_p]$	[1,1,1,1,100,100]

In this case, inspired by practical requirements and works that focus on tuning the FHIC parameters in using different systems, the characteristics of the PSO algorithm are listed in Table 4.4. According to Table 4.5, the swarm size is 10x6. The initial values of the particles are randomly generated based on the maximum values in the first generation.

Table 4.5. Tuned parameters of the designed FHI controller with PSO for the three different contact stress force (S_{PSO}: Soft PSO, M_{PSO}: Medium PSO, H_{PSO}: Hard PSO)

FHIC Parameters	$\boldsymbol{S_{PSO}}$	$\boldsymbol{M_{PSO}}$	$\boldsymbol{H_{PSO}}$
K_v	1.8403	2.4681	3.1305
K_p	10.6224	11.1753	13.0491
α	0.3821	0.4249	0.4650
β	0.7508	0.7939	0.8142
γ	0.7958	0.7944	0.7891
δ	0.6824	0.7079	0.7031

For three different constant forces, the parameters of the FHI controller tuned are summarized in Table 3. Three different forces are based on the pressure of the sole of the foot on real environments such as grass (soft), carpet (medium), and solid floors (hard).

4.4.5. Performance evaluation of the HI and FHI controllers

AJS-RSEA experimental setup was developed for evaluating the performance of the SEM-TA and the FHIC. In the experimental setup, the SEM-TA was mounted on a leg of the AJS-RSEA to drive the ankle joint in three modes of contact stress force control (soft, medium, and hard). This section consists of experimental and simulation results on the SEM-TA setup in three controller modes (Figure 4.12, 4.13, 4.14). In order to examine the performance comparison of the ankle joint controller, the experimental results are depicted in Figure 4.20.

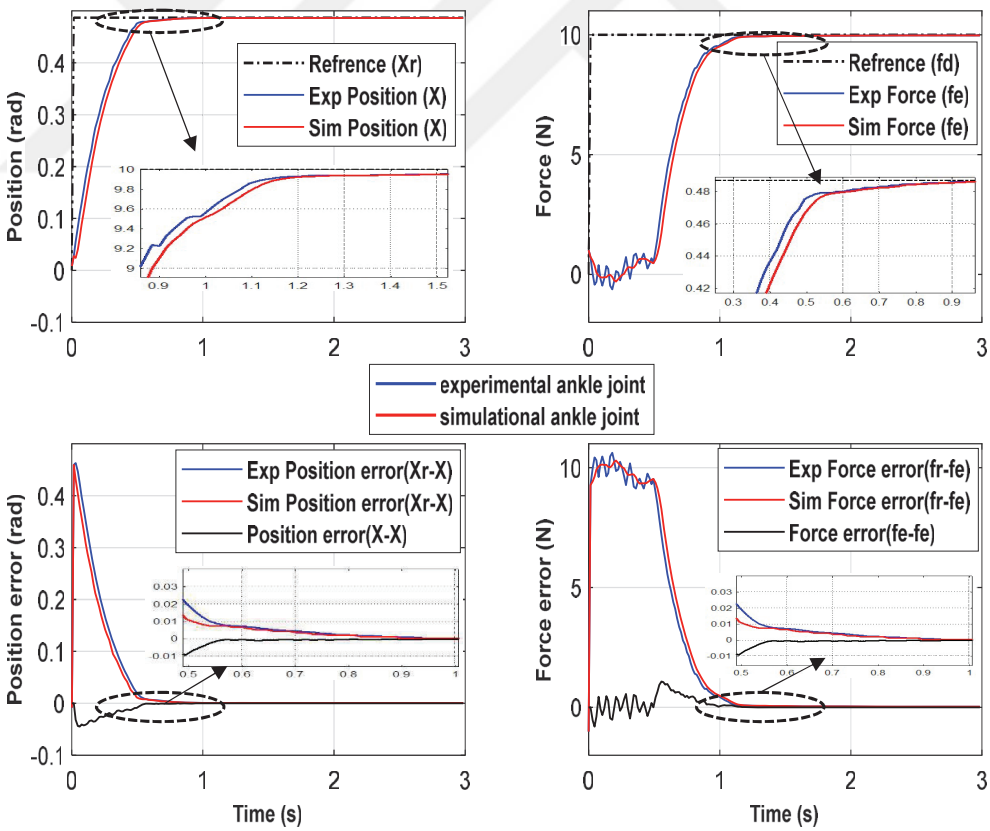

(a) (b)

Figure 4.12. SEM-TA step response affected by S_{PSO} − FHIC, (a) position reference (X_r) experiment (X) and simulation ($\hat{X}$) position output and (b) force reference (f_r) experiment (fe) and simulation ($\widehat{fe}$) force output

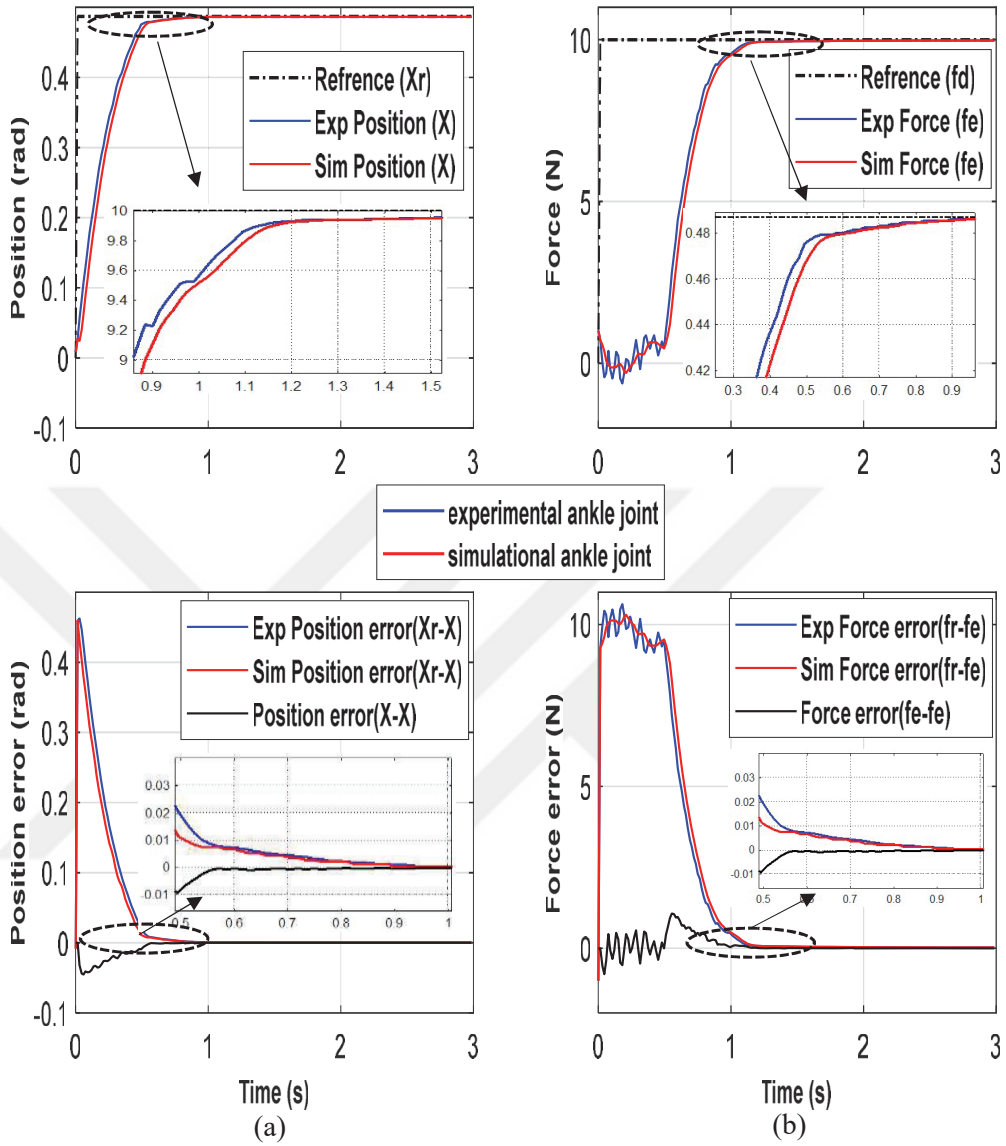

Figure 4.13. SEM-TA step response affected by M_{PSO} − FHIC, (a) position reference (X_r) experiment (X) and simulation ($\hat{X}$) position output and (b) force reference (f_r) experiment (fe) and simulation ($\widehat{fe}$) force output

According to the simulation results in Table 4.8, the S_{PSO} − FHI, the E_{ss} in position and force are 0.07 and 0.08; the T_s in position and force are 0.9 and 1.4 seconds, respectively, according to the simulation results in Table 4.8, for the M_{PSO} − FHI controller, the E_{ss} in position and force are 0.05 and 0.06; the T_s in position and force are 0.9 and 0.8 seconds, respectively, According to the simulation results in Table 4.8 the H_{PSO} − FHI controller, the E_{ss} in position and force are 0.06 and 0.07; the T_s in position and force are 0.6 and 0.8 seconds, respectively.

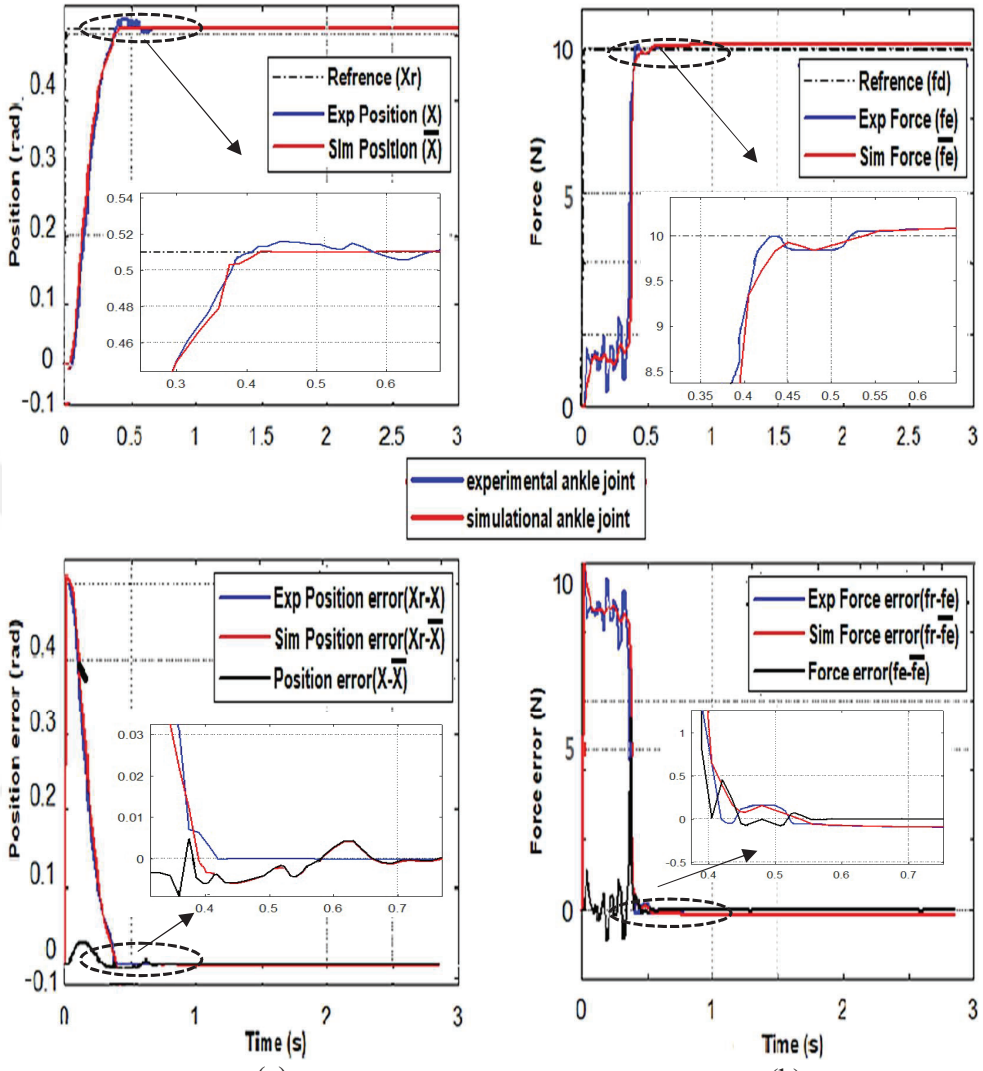

(a) (b)

Figure 4.14 SEM-TA step response affected by H_{PSO} − FHIC, (a) position reference (X_r) experiment (X) and simulation ($\hat{X}$) position output and (b) force reference (f_r) experiment (fe) and simulation ($\widehat{fe}$) force output

In order to evaluate the performance of the S_{PSO}, M_{PSO}, H_{PSO}, and HIC, the RMSEs of the position and the force (RMS-PE and RMS-FE) between the modeled reference and the measured signal from the ankle joints are computed based on the equation (4.40). The calculated RMSEs are given in Table 4.6. According to the obtained RMSEs results, the $FHIC - M_{PSO}$ controller is robust and produces better results than the and experimental controllers in terms of T_s, MO, E_{ss}, and RMSEs.

Table 4.6. Quantitative comparison of the performance of $S_{PSO} - FHIC$, $M_{PSO} - FHIC$ and $H_{PSO} - FHIC$ mode controllers

Impedance controllers	Parameters	Control	
		Position	Force
$S_{PSO} - FHIC$	T_s (s)	0.965	1.440
	MP (°)	0.247	1.247
	E_{ss} (°)	0.0647	0.0853
	RMSE (°)	0.202753	0.33931
$M_{PSO} - FHIC$	T_s (s)	0.937	0.817
	MP (°)	2.601	1.518
	E_{ss} (°)	0.0538	0.0604
	RMSE (°)	0.196358	0.32761
$H_{PSO} - FHIC$	T_s (s)	0.621	0.846
	MP (°)	1.247	5.247
	E_{ss} (°)	0.077	0.0710
	RMSE (°)	0.198633	0.33174

4.4.6. Adaptive Fractional hybrid impedance control (AFHIC)

In this section, a fuzzy logic inference system is developed to estimate the fractional coefficients in the adaptive impedance controller of the RSEA [126]. For each controller (torque and position controller) in the hybrid impedance controller, an FLC (Fuzzy Logic Controller) implemented to estimate the fractional coefficients, Figure.4.15 depicts the implementation of the FLC in the controllers of the RSEA [127]. Two inputs of FLC are the Ke and (Ke_d) derivative of Ke. The typical steps in developing the FLC system involve fuzzification, rule formation, and defuzzification is explained briefly in this section. The input variables such as Ke and Ke_d are suitably partitioned and converted into linguistic variables, as following (VLH-very low hardness, LHN-low hardness, MHN-medium hardness, HHN-high hardness, VHH-very high hardness). The output variables (fractional coefficients of the models) are partitioned and represented as fuzzy sets with linguistic terms as following (VST-very soft, SFT-soft, MDM-medium, HRD-hard, and VHD-very hard).

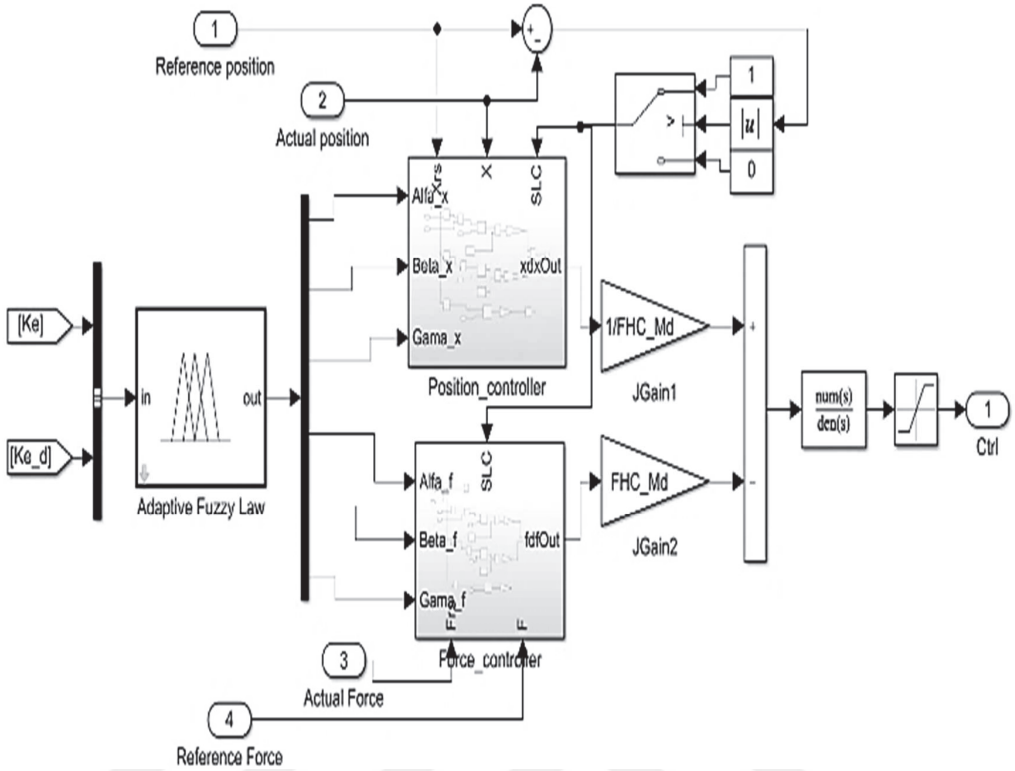

Figure 4.15. Simulink implementation of FLC of the RSEA

The maximal absolute experimental Ke and derivative of Ke of the RSEA system are 50 Nm/rad and 100 Nm.s/rad respectively. The membership functions and ranges of the input variables are obtained based on the experimental Ke and Ke_d classification. Also, the membership functions and ranges of the output variables is obtained relatively from fractional coefficients of the adaptive fractional estimation model (AFEM) given in Tables III. The fuzzy rules are the most important part of the entire method, which affect the output results crucially [128], [129]. They are set based on the experimental Ke and Ke_d classification knowledge and results obtained theoretically by the AFEM for each class. Gaussian membership functions were used for graphical inference of the input and the output variables. The membership functions of the AFHIM in RSEA are illustrated in Figure.4.15. A fuzzy rule is a standard form of expressing knowledge based on the logic of IF and Then functions. A set of rules have been constructed based on the input variables (Ke and Ke_d) and output variables (fractional coefficients) for the RSEA [130], [131]. The fuzzy rules of Alfa0 used here are given in Table 4.7. The FLC rules for AFEM were obtained based on the experimental results from torque and position in RSEA [132].

Table 4.7. FLC rules for ALFA0

$\dot{K}e$ \ Ke	VLH	LHN	MHN	HHN	VHH
VLH	VST	VST	SFT	SFT	MDM
LHN	VST	VST	SFT	SFT	MDM
MHN	VST	SFT	SFT	MDM	HRD
HHN	SFT	SFT	MDM	HRD	HRD
VHN	SFT	MDM	MDM	HRD	VHD

The defuzzification is the conversion of a fuzzy quantity to a crisp value. The centroid method was applied for defuzzification. Figure 4.16, 4.17, and 4.18 shows the FLC surface relationship between Ke, Ke_d, and fuzzy output of the fractional coefficients in AFHIM.

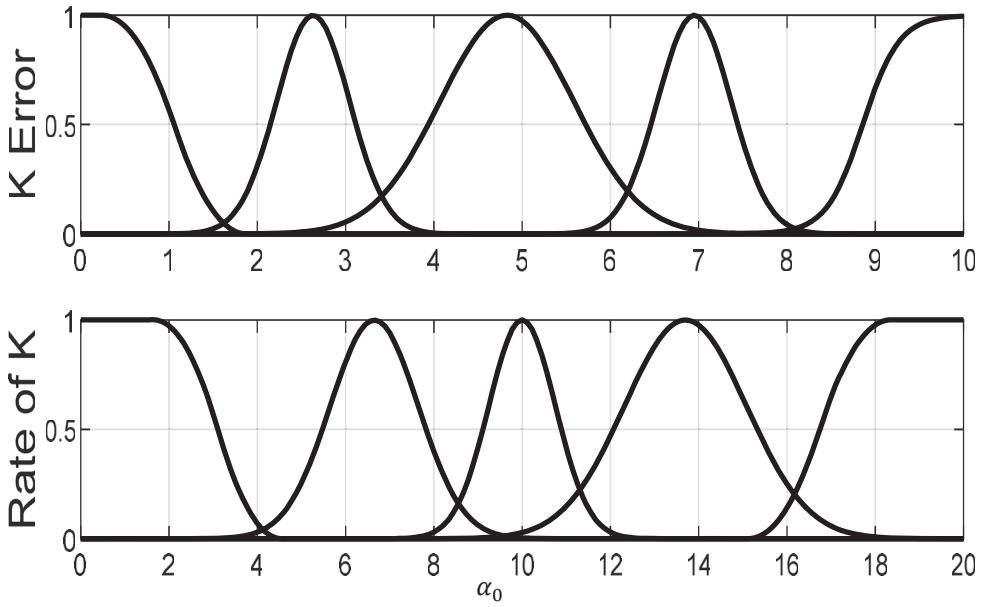

Figure 4.16. FLC membership functions of the AFHIC. Ke membership functions and Ke_d membership functions.

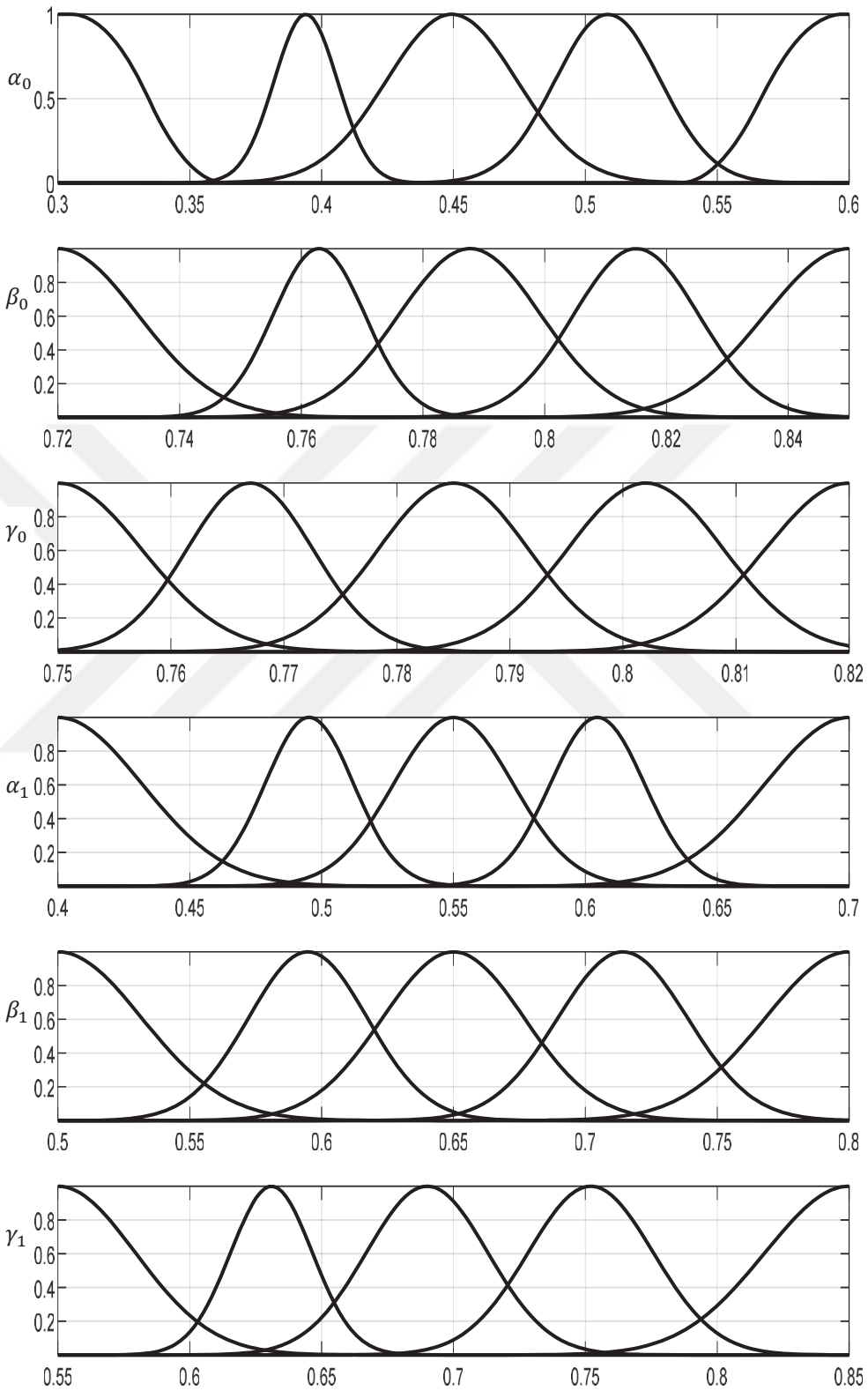

Figure 4.17. Fractional coefficient FLC membership functions of the AFHIC.

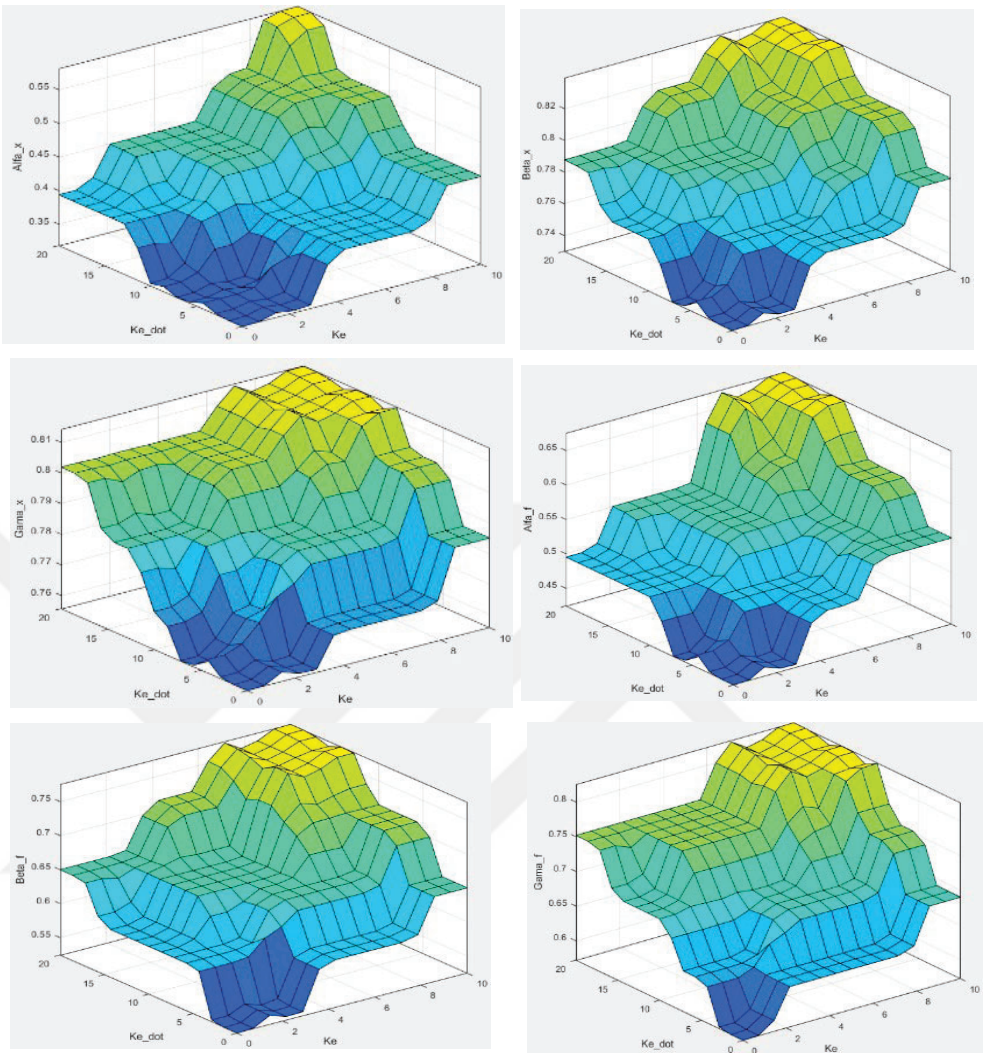

Figure 4.18. FLC surface in AFHIM for RSEA

SEM-TA experimental setup was developed for evaluating the performance of the RSEA and the AFHIC. In the experimental setup, the RSEA was mounted on a leg of the SEM-TA to drive the load joint in three modes of contact stress torque control (soft, medium, and hard). This section consists of experimental and simulation results on the RSEA setup in three controller modes. In order to examine the performance comparison of the load joint. As shown in Figure 4.18, the AFHI controller receives the position error and torque error between the position and the desired torque and the feedback position and environment torque in the direction perpendicular to the link, and then sends a control signal to the RSEA to position modify in order to maintain a constant contact force.

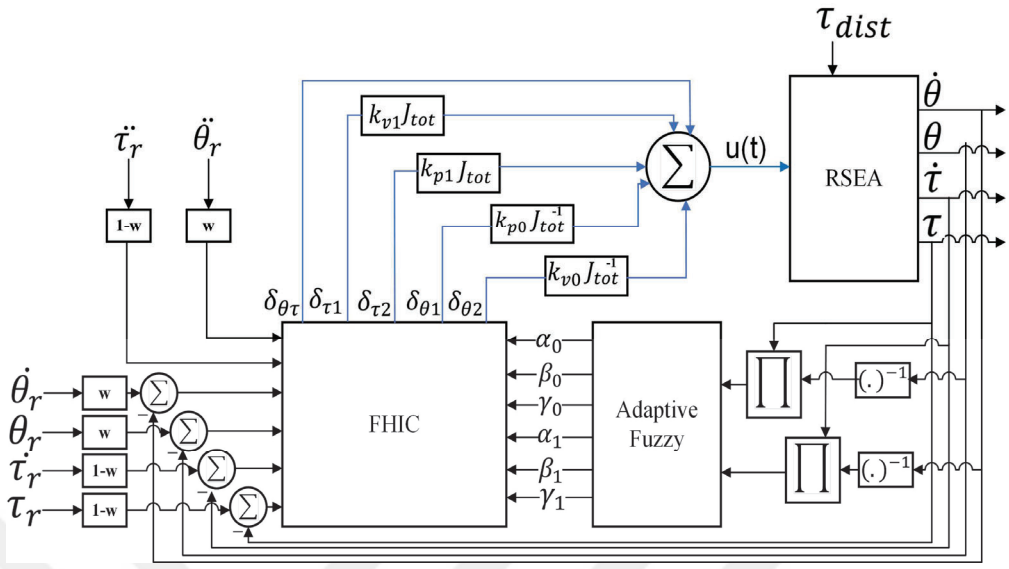

Figure 4.19. FA-FHIC (Fuzzy Adaptive Fractional Hybrid Impedance controller) block diagram.

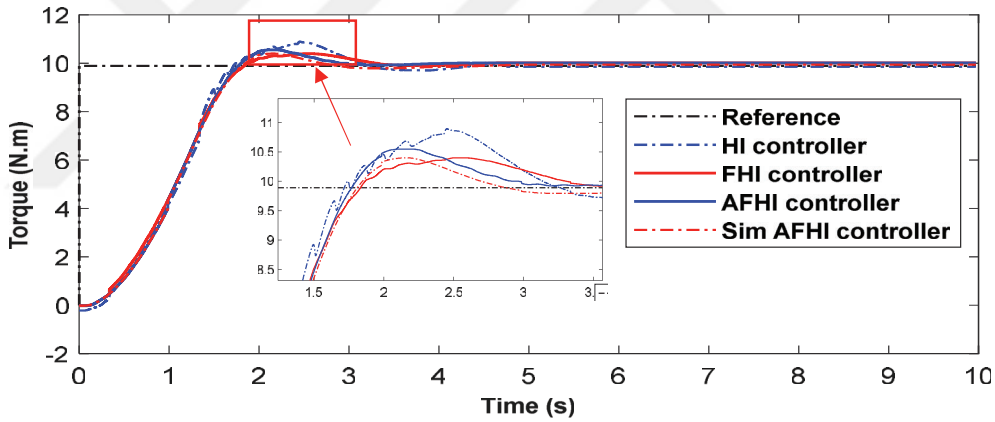

Figure 4.20. Torque tracking behaviour of AFHI control in unchangeable environment (τ_r = 10 Nm).

In this section, dynamic tracking stage, as is shown in Figure. 4.19, and Figure. 4.20, the proposed AFHI control strategy can significantly improve the dynamic torque tracking performance compared to HI and FHI controls strategy. The maximum rotatum tracking error cut down from 3.83 Nm/s to 0.59 Nm/s, and the root mean square value of torque error reduces from 1.93 Nm/s to 0.63 Nm/s. The fluctuation in the controlled torques along the environment is resulted from the roughness of the contact surface, so the fluctuation is hard to be reduced. Nevertheless, these torques are all around the setpoint, 10 Nm. The experiment results demonstrate that the AFHI control scheme can improve the dynamic torque tracking performance significantly.

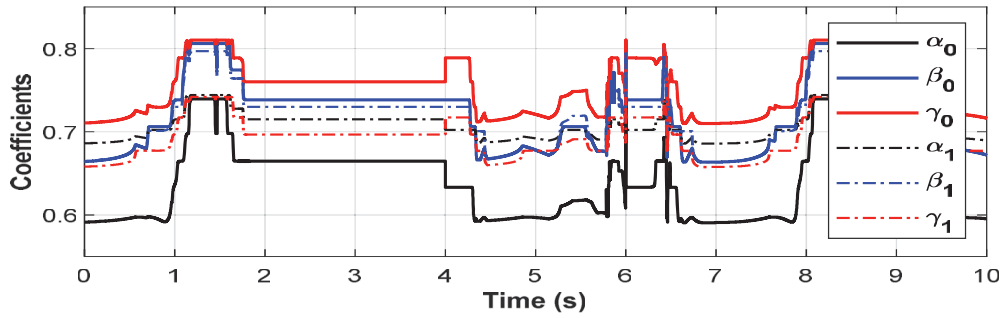

Figure 4.21. Fractional parameters ($\alpha_0, \beta_0, \gamma_0, \alpha_1, \beta_1, \gamma_1$) in simulation A-FHIC.

As shown in Figure 4.21, the proposed AFHI control strategy can perform the dynamic torque tracking strategy by dynamically controlling the fractional parameters ($\alpha_0, \beta_0, \gamma_0, \alpha_1, \beta_1, \gamma_1$) by a fuzzy controller.

5. IMPLEMENTATION OF THE REAL SYSTEM AND EXPERIMENTAL WORK

The last chapter of this thesis deals with the real prototype of the and the experimental works. All controllers investigate in the previous chapter for RSEA model, is developed and verified experimentally. At first, the mechanical structure of the system such as the DC torque motor servo system, Motor driver, encoders, spring, gearbox ..., are described with details. Secondly, PID-FFC, FL-FFC, and FTC-FC controllers are developed for the torque control problem of the real implementation of the RSEA. Furthermore, HIC, FHIC and AHIC are developed for the impedanc control of the real implementations of the RSEA. The dynamic responses of the impedance controllers were compared experimentally based on robustness analysis under external disturbances.

5.1. General Structure of the Experimental System

The actuator components include the following.

1. Frameless torque motor (50mm diameter),
2. Worm gear,
3. Torsional flat-double spiral spring (DFTFS),
4. Incremental encoders,
5. Link and Joint of the ankle load

The model of torque motor is MDS-LFTM-50, which consists of a 2048 ppr (pulses per revolution) encoder. The rotational motion of the torque motor is transmitted to the other rotary axes using a worm gear. The DFTFS connects the worm gear mechanism to the joint of the load case and conveys the movement to the carriage in which DFTFS is located. The transmission ratio between the worm gear system and the motor is 1/60. The stiffness of DFTFS is 64.251 Nm/rad. The proposed experimental setup and significant parameters of the RSEA is illustrated in Figure5.1.

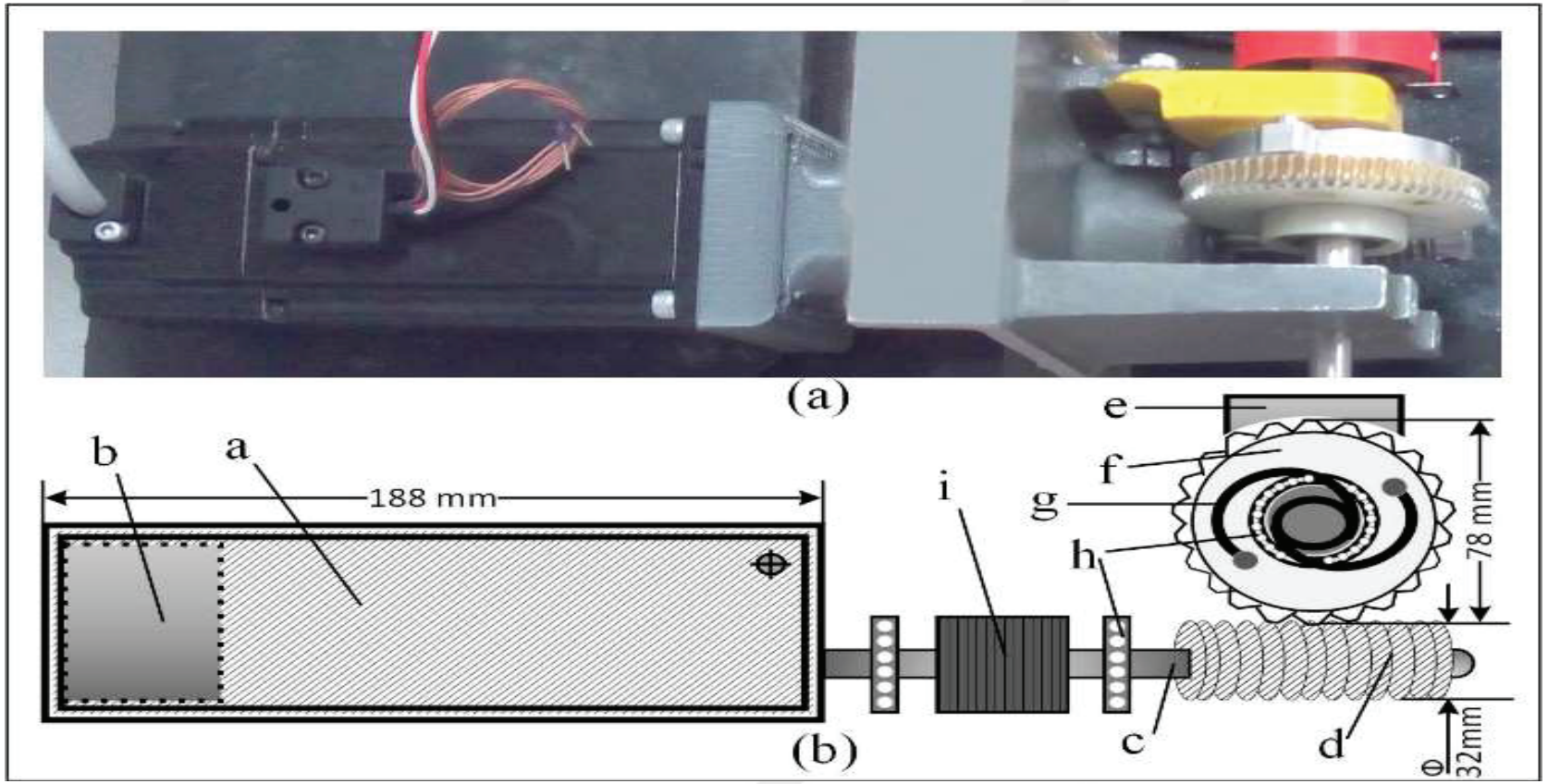

Figure 5.1. (a) Rotary SEA system and (b) cross sectional view of the actuator indicates parts including a=frameless 50mm diameter of the torque motor with a body, b=motor joint encoder, c=shaft, d=worm, e=load joint encoder with bearing, f=worm wheel, g=spring, h=ball bearing, and i=coupling

5.1.1. Brushless DC torque servo-motor

The system is driven by a direct drive brushless DC torque servo-motor (Type: LFTM-50-50-N, ± 48V) in joint of the link (θ_l). τ is the torque applied at the horizontal link produced by the torque servo-motor, it is given in the equation (5.1).

$$\tau = \frac{\eta_m K_t (V_m - K_m \dot{\theta})}{R_m} \tag{5.1}$$

Where the motor efficiency coefficient $\eta_m = 0.73$. Motor constant $K_m = 0.063$. The armature resistance $R_m = 3.78$. V_m is the input voltage. The datasheet of the servo-motor is given in Table 5.1. Figure 5.2 shows the direct drive brushless DC torque servo-motor (Type: LFTM-050, ± 10V). [133]

Table 5.1. Datasheet of the direct drive brushless DC torque servo-motor (Type: LFTM-50-50-N, ± 48V)

Motor Parameters	Symbols	Units	LFTM-50-50-N
Rated Torque	T_r	Nm	0.535
Peak Torque	T_{peak}	Nm	1.84
Rated Speed	N_r	rpm	1280
No-Load Speed	$N_{no-load}$	rpm	1480
Torque Constant	K_t	Nm/A	0.38
Voltage Constant	K_v	V/rpm	0.032
Max. Cogging Torque	T_{cog}	Nm	0.008
Torque Ripple	T_{ripple}	%	0.24
Number of Pole	2n	--	8
Rated Current	I_r	Arms	1.41
Peak Current	I_{peak}	Arms	4.95
Line Resistance	R_{LL}@20°	Ohm	3.78
Line Inductance	L_{LL}	mh	4.56

Table 5.1.(Cont.) Datasheet of the direct drive brushless DC torque servo-motor (Type: LFTM-50-50-N, ± 48V)

Stator Weight	W_s	kg	0.43
Rotor Weight	W_r	kg	0.18
Total Weight	W_{total}	kg	0.61
Meh. Time Constant	K_{mech}	ms	0.025
Thermal Resistance (2)	R_{th}	°C/W	5.60
Inertia	J	$Kg.m^2$	0.000017
Motor Constant	K_m	Nm/W	0.063
Rotor ID	mm		9.55
Stator OD	mm		49.18

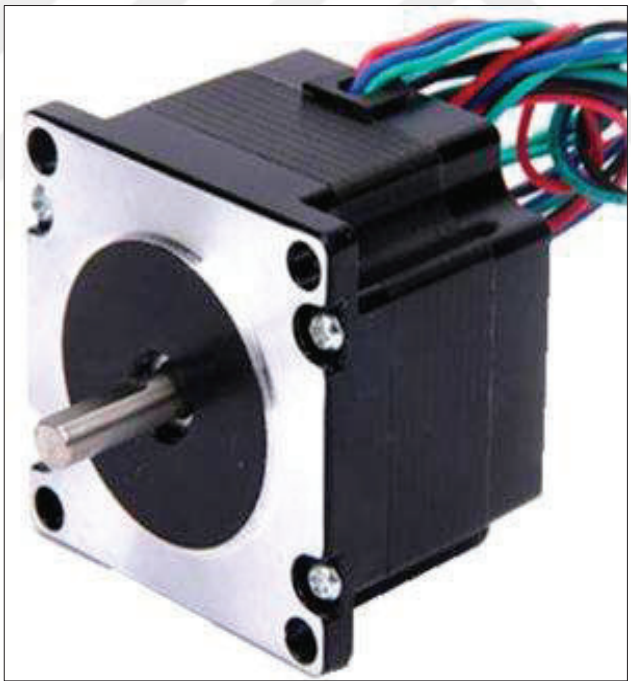

Figure 5.2. Brushless DC torque servo-motor Type: LFTM-50-50-N, ± 48V

5.1.2. Driver motor

The brushless DC torque servo-motor (Type: LFTM-50-50-N, ± 48V) is driven by a driver motor (Model: Lenze, Type: Inverter Drives 8400 TopLine) [134]. This driver

is used in order to easily achieve high dynamic performance and precision in the first link of the TLRIP. The power of the driver is 0.75Kw, which supply a single phase 200/240v. This driver is particularly suitable for handling and positioning systems such as the control of the RSEA. Figure 5.3 shown the driver motor used in our system (Model: Lenze, Type: Inverter Drives 8400 TopLine).

5.1.3. Encoders

The joints' angles are measured with three encoders having a resolution of 2048 pulses per revolution (Model: Fenac, Type: 2048 PPR sin cosine accurate speed information) [135]. The encoder is an electro-mechanical device that converts the angular position of the shaft to digital output signals. Figure 5.4 shown an example of the encoder model used in joints for the system.

Figure 5.3. Driver motor (Model: Lenze, Type: 8400 TopLine, 2.2Kw)

Figure 5.4. Encoder (Model: Fenac, Type: 2048 PPR sin cosine accurate speed information)

5.1.4. Worm gear

There are various methodologies to satisfy the conditions for the differential mechanism, and thus to realize the series elasticity.

Table 5.2. Characteristics of gearboxes used robotic

Type of gearbox	Reduction ratio	Torque capacity	Size	Efficiency (%)	Precision (arcmin)
Simple planetary	1/4 – 1/10	low	small	>95	>3
Two-stage planetary	1/10 – 1/50	low	small	<90	>3
Harmonic	1/30 – 1/60	mid	mid	60 - 80	1 – 3
Simple cycloid	1/5 – 1/20	high	big	>95	<1
Two-stage cycloid	1/30 – 1/300	high	big	<90	<1
Plantery + cycloid	1/30 – 1/200	high	big	<90	<1
Worm gear	1/5 – 1/60	high	mid	60 - 90	1 – 3

Table 5.2. summarizes the characteristics of various speed reducers installed in robot joints. As a simple planetary gear reducer cannot have a large reduction ratio, it is often connected through a plurality of stages. In general, the compound planetary

gearboxes have advantages of the compact structure and a large reduction ratio [136]. However, this efficiency decreases according to the increase in the reduction ratio [137]. On the other hand, harmonic gear reducers are lightweight, compact, and have a large reduction ratio with high precision but low efficiency. Cycloid gear reducers deliver high torque capacity with both high accuracy and high efficiency. Mechanical paradox gearboxes usually have low-efficiency characteristics between 70% and 75% (see Figure 5.5). Hori proposed efficiency improvement of the mechanical paradox gearbox in [138]. He achieved up to 80–85% efficiency. In general, there are several tradeoffs among the power transmission efficiency, reduction ratio, allowable torque, size, and backlash of the speed reducer [139]. More specifically, reducing the reduction ratio increases the permissible torque, whereas reducing the size or backlash of the reducer decreases the power transmission efficiency. In fact, reverse driving by a small speed reducer with a reduction ratio of ∼1/100 is difficult to achieve in conventional robot applications.

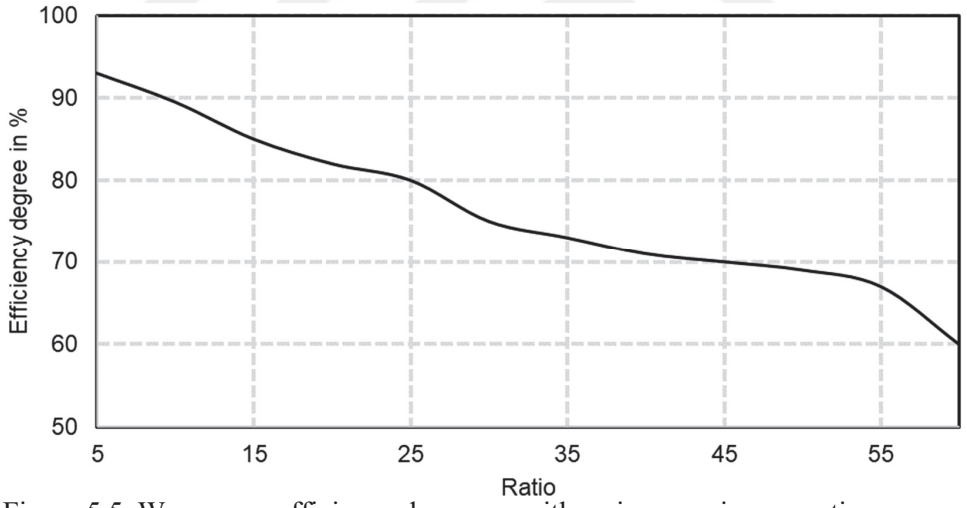

Figure 5.5. Worm gear efficiency decreases with an increase in gear ratio

The efficiency of a worm gearbox is based on the ratio and it drops sharply as the ratio increases. This because of the constant sliding action between worm and worm wheel reduces the overall efficiency of the worm gearbox since the usable power is converted to heat. These heat friction issues cause vast inefficiencies ranging up to 50%. One of most widely used structure as the differential mechanism is a warm gear, The worm gear transmission is generally composed of a worm screw and worm wheel. Notice that this type of worm gear set is so called the Nonparallel and

Nonintersecting Axes gear, A gearbox designed using a worm and worm-wheel is considerably smaller than one made from plain spur gears, and has its drive axes at 90° to each other. With a single start worm, for each 360° turn of the worm, the worm-wheel advances only one tooth of the gear wheel. Therefore, regardless of the worm's size (sensible engineering limits notwithstanding), the gear ratio is the "size of the worm wheel - to - 1". Given a single start worm, a 60-tooth worm wheel reduces the speed by the ratio of 60:1. Unlike with ordinary gear trains, the direction of transmission (input shaft vs output shaft) is not reversible when using large reduction ratios. This is due to the greater friction involved between the worm and worm-wheel, and is especially prevalent when a single start (one spiral) worm is used. This can be an advantage when it is desired to eliminate any possibility of the output driving the input.

Worm gear configurations in which the gear cannot drive the worm are called self-locking. Whether a worm and gear is self-locking depends on the lead angle, the pressure angle, and the coefficient of friction. The gearbox transmits power from the motor shaft to the load shaft. The worm gear used reduces the speed and increases the power. The use of high reduction gearbox ratios in the motor is particularly preferred (see Figure 5.6). Hence, the effective joint mass is typically higher. The transmission ratio between the worm gear system and the motor is 1/60.

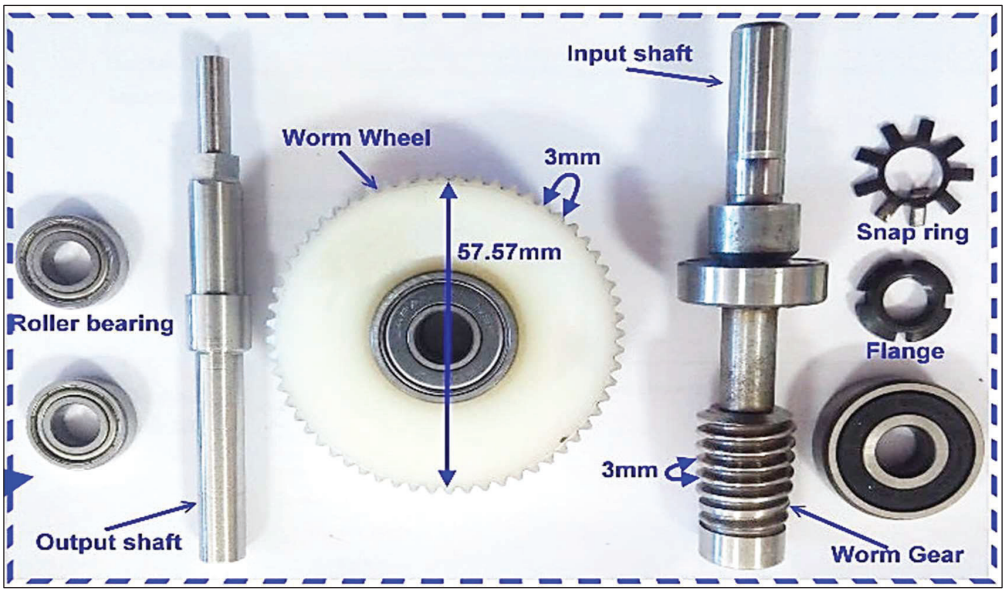

Figure 5.6. Worm gear (Model: KTK, Type: LT03 Series)

5.1.5. Controller board

A dSPACE-DS1103 controller board is used to treat the received signals from the encoders. At present dSPACE DS1103 is the famous hardware and real-time software tools which operate through Matlab/Simulink interface programming for rapid control prototyping [140]. However, it has different various ADC and DAC ports, internal memory and a different number of input/output ports etc. Figure 5.7 shown an example of a dSPACE controller board.

Figure 5.7. An example of a dSPACE controller board

5.2 Torque Control for a Real Experimental Implementation of the RSEA

The tree torque controllers (PID-FFC, FL-FFC, and FTC-FC) developed in the Simulink environment in the last chapter, will be verified experimentally in this section. The RSEA consists of a 50mm diameter of the torque motor (48V of the supply voltage, 1280rpm of the nominal speed) with a worm gear ratio of 1/60, used to apply rotational force (see Figure 5.8). The motor driver type is (10A-EC). Position sensors of rotary encoders (FNCC 10bit - 40EF) are used in the system. The

angular position signal of motor and load joints are given to the unit of control by the sensors of the rotary encoder [141]. At the output load joint, a torque sensor (TRS600 50Nm FUTEK) is mounted to measure the torque of output. A pendulum is mounted in the system output, which can be a robot leg model. The experimental system control block comprises a card of PWM pulse generator (ATMEGA128 microcontroller) an industrial PC (motion controller GT_800 series - GoogolThech) with a 1kHz control frequency, which is responsible for filtering and controlling RSEA outputs and inputs (see Figure 5.9).

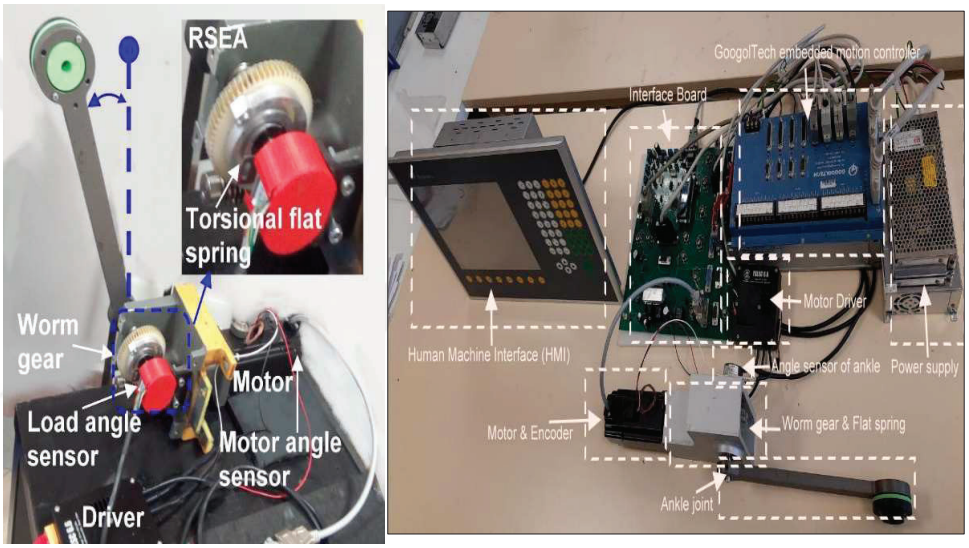

Figure 5.8. Real experimental implementation of the RSEA for torque control

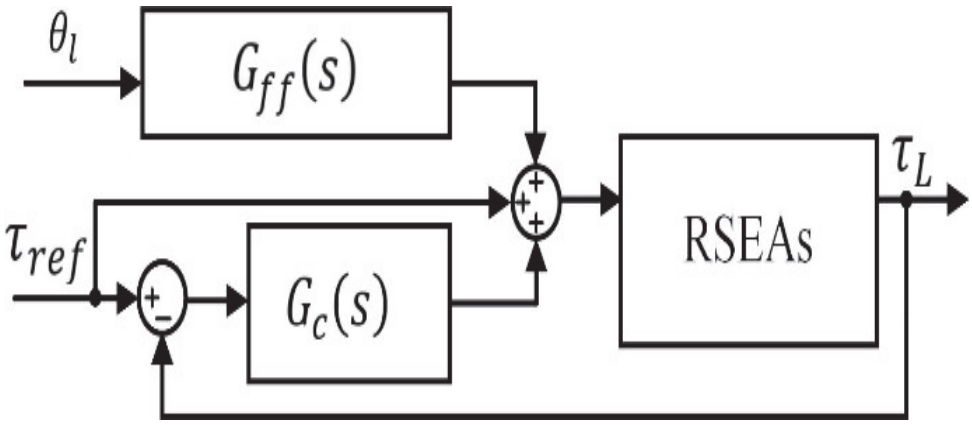

(a)

Figure 5.9. dSPACE models of the torque controllers in Matlab/Simulink: (a) FL-FFC (b) FTC-FC

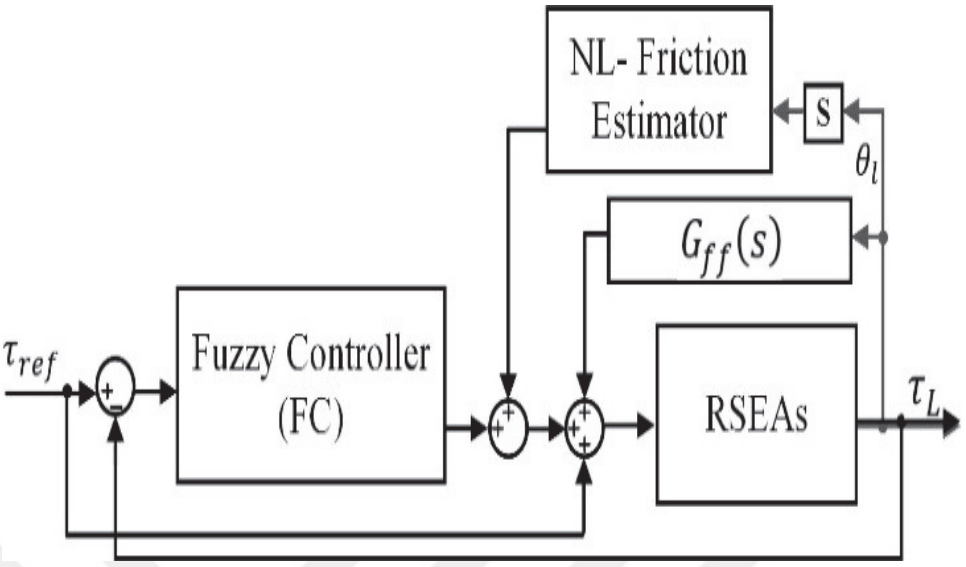

(b)

Figure 5.9.(Cont.) dSPACE models of the torque controllers in Matlab/Simulink: (a) FL-FFC (b) FTC-FC

5.2.1. Performance evaluation of the torque PID-FFC, FL-FFC, and FTC-FC controllers

A sinusoidal signal with 1Hz of frequency is applied as an input trajectory function to examine the performance of the controllers in the RSEA system. As seen in Figures 5.10 and 5.11, FTC-FC yields a good tracking trend with the minimum tracking error. The performance of controllers is presented in Table 5.2. In the first step, improved 11.84% system response by adding a fuzzy controller to the system. and the second step Improved a 4.75% system response by adding nonlinear friction compensation to the system. The best performance is uniformly obtained by the fuzzy controller using the nonlinear friction estimator.

Table 5.3. RMSEs of the control and output signals in PID-FFC, FL-FFC, and FFTC-FF

Controller Type	Controller effect	RMSE
PID-FFC	1.500847	0.101952
FL-FFC	1.388514	0.089924
FTC-FC	1.136346	0.085806

RMSE: root mean square error; PID-FFC: PID Feedforward Controller; FL-FFC: fuzzy Logic Feedforward Controller; FTC-FC: Fuzzy Torque Controller with Friction Compensation.

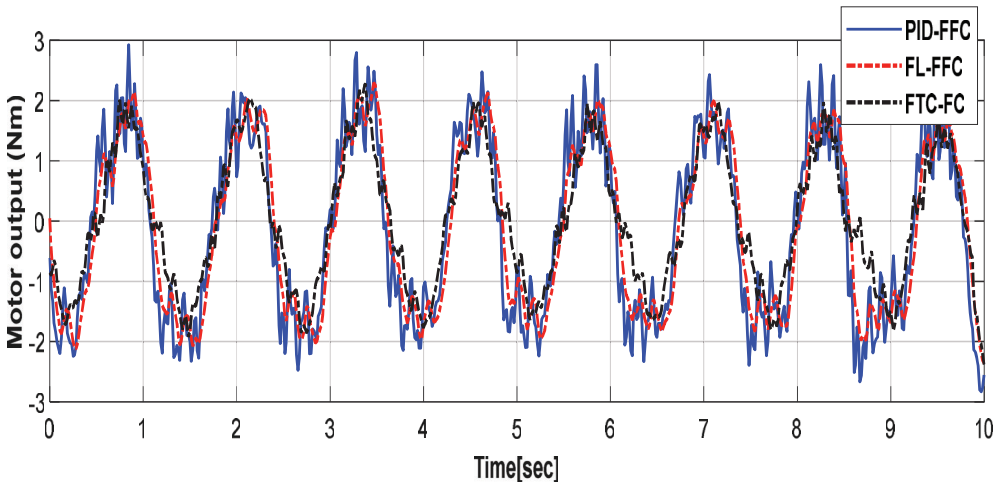

Figure 5.10. Controller effect in experimental results of the PID-FFC, FL-FFC, and FTC-FC

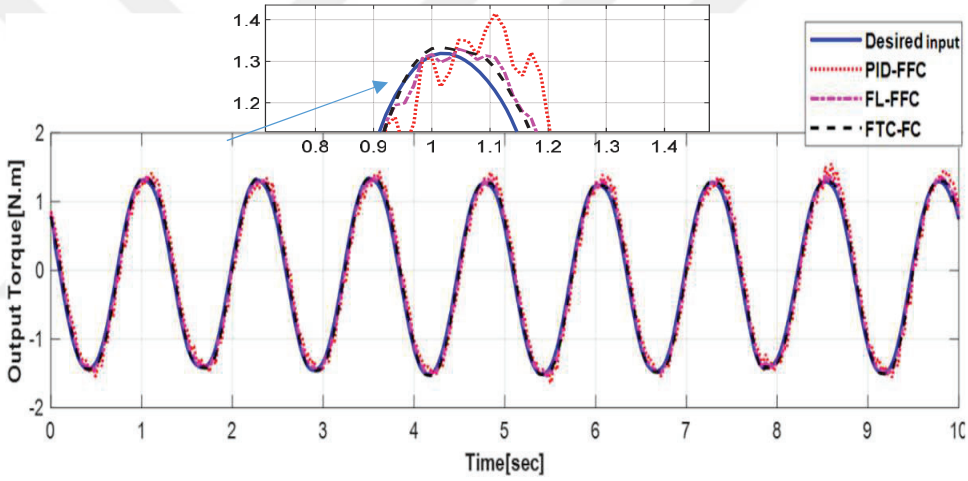

Figure 5.11. The experimental results of torque for the PID-FFC, FL-FFC, and FTC-FC

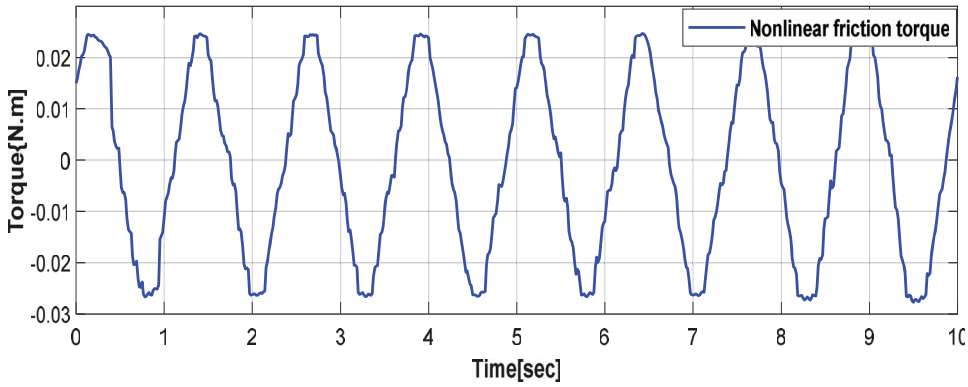

Figure 5.12. Real-time nonlinear friction torque estimation in torque tracking control with FTC-FC

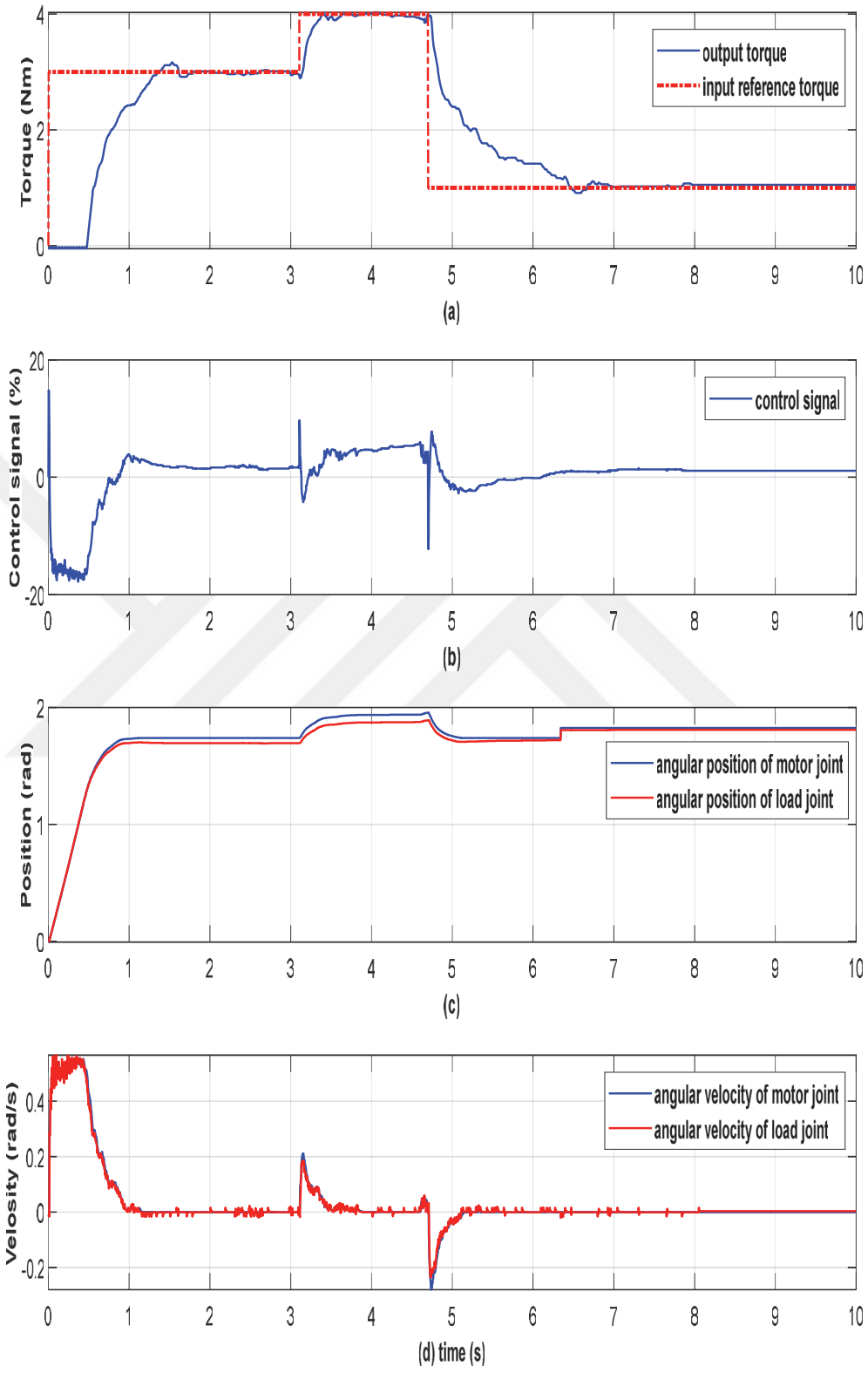

Figure 5.13. The experimental results in trajectory tracking torque control signal – control signal -joint position and velocity- of RSEA with FTC-FC.

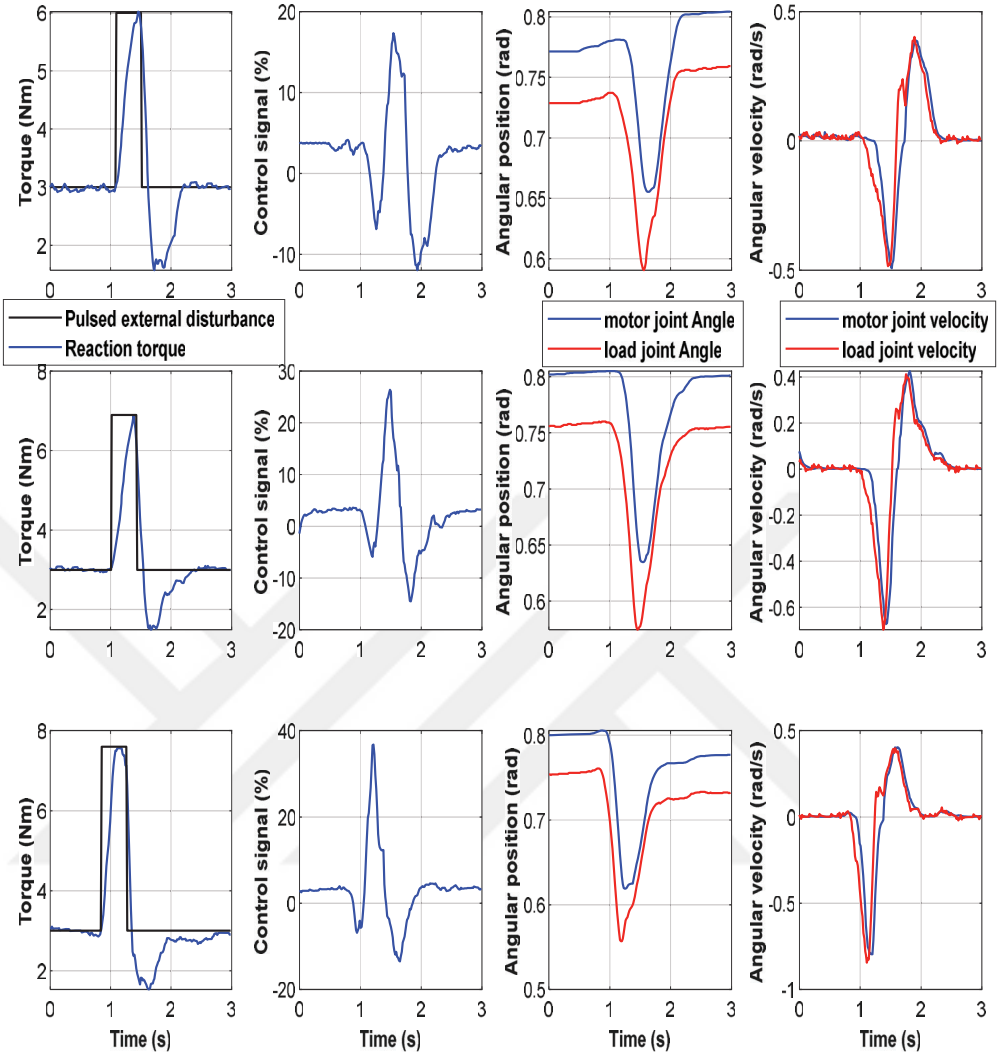

Figure 5.14 Torque disturbance control at three maximum set points such as 6, 7, and 7.5 Nm. Reaction torque (τ_l) and pulsed external disturbance, the control signal, the angular position and velocity of the motor joint and load joint.

The real-time estimations of nonlinear friction internal state in torque tracking control are illustrated in Figure 5.12. The FTC-FC controller response and the NLFEM parameter are also much better than their variations in the other controller, as shown in the figures. Experimental results show that the designed FTC-FC is able to track the trajectory of any dynamic reference torque control signal with reasonable spring reaction time in a friction composition manner, and a decrease in system impedance is observed, as shown in Figure 5.13. In order to evaluate the controller performance in case of external disturbances, the system has been tested three maximum set points such as 6, 7, and 7.5 Nm. The response of the system and the control signal is illustrated in Figure 5.14.

5.3. impedance Control for a Real Experimental Implementation of the RSEA

Three controllers HIC, FHIC and AFHIC developed in the Simulink environment will be verified experimentally in this section. The impedance control is performed by the system parameters of K_s = 63.665 Nm/rad, k_t = 2.391 Nm/A, J_m = 0.00032 kg/m^2, All output variables of the RSEA need to be stabilized at the reference point by all impedance controllers. The real experimental implementation of the RSEA is shown in Figure 5.15. The dSPACE models of the impedance controllers (HIC, FHIC and AFHIC) in Matlab/Simulink are depicted in Figure 5.16. As can be seen from Figure 5.16, the arm and the joint links were controlled at the reference position and torque with minimum vibrations.

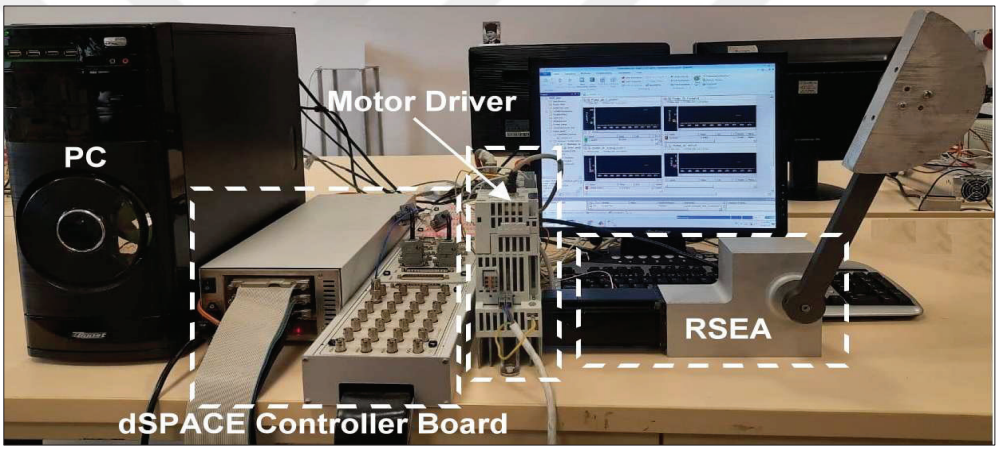

Figure 5.15. Real experimental implementation of the RSEA for impedance control

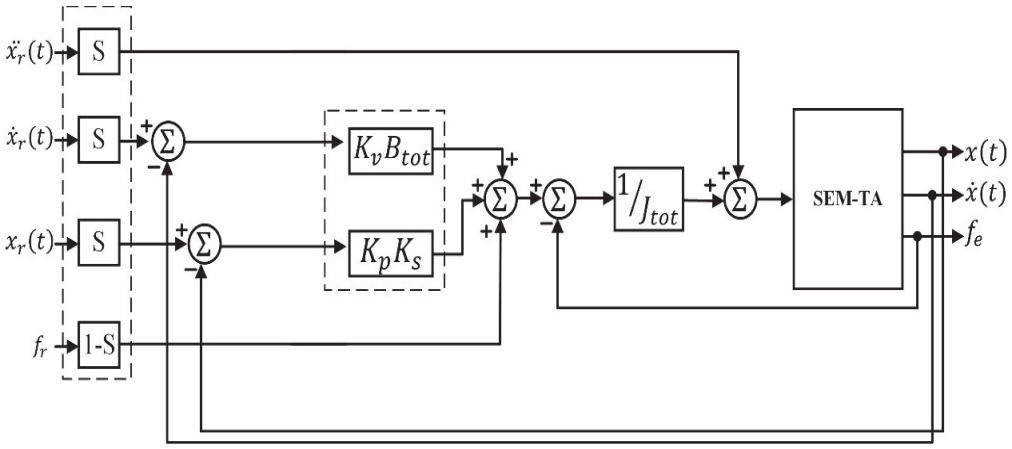

(a)

Figure 5.16. dSPACE models of the controllers in Matlab/Simulink: (a) HIC, (b) FHIC and (c) AFHIC

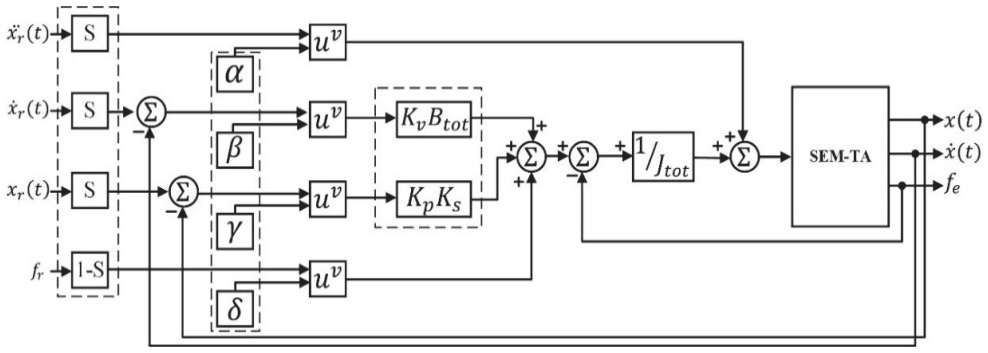

(b)

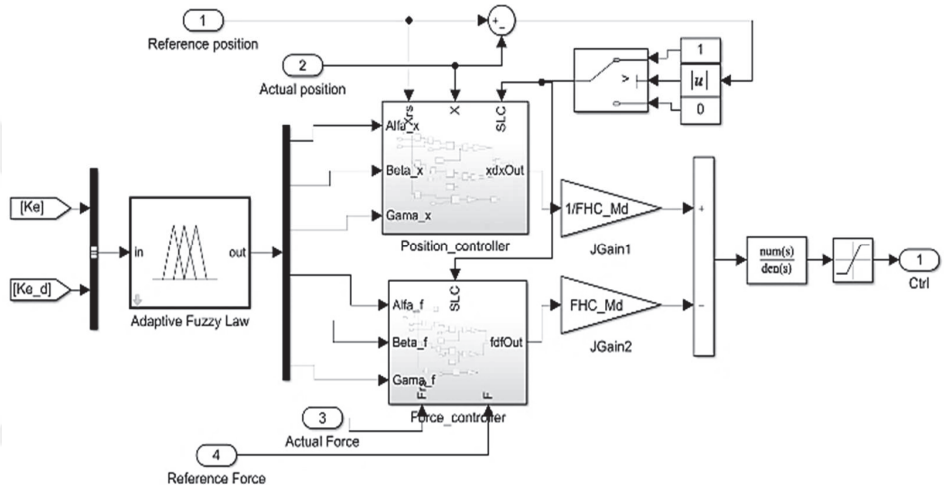

(c)

Figure 5.16.(Cont.) dSPACE models of the controllers in Matlab/Simulink: (a) HIC, (b) FHIC and (c) AFHIC

5.3.1. Performance evaluation of the HIC, FHIC and AFHIC controllers

Figure 5.17 shows a comparison between the position and force signals with impedance controllers of the RSEA in experiment case. According to the obtained results, all controllers have effectively maintained the impedance control of the RSEA with minimum vibration. The FHI controller is developed in order to give the best results in terms of T_s, MP, E_{ss} and the RMSEs than the FHI and HI controllers. Table 5.3 , 5.4 and 5.5 shows the comparison of $S_{PSO}-$ FHIC, $S_{PSO}-$ FHIC and $S_{PSO}-$ FHIC impednace controllers in terms of T_s, MP, E_{ss} and the RMSEs in the experiment. To verify the AFHIC performance compared with other impednace controllers; the improvement percentages of all parameters are calculated and given in Table 5.6.

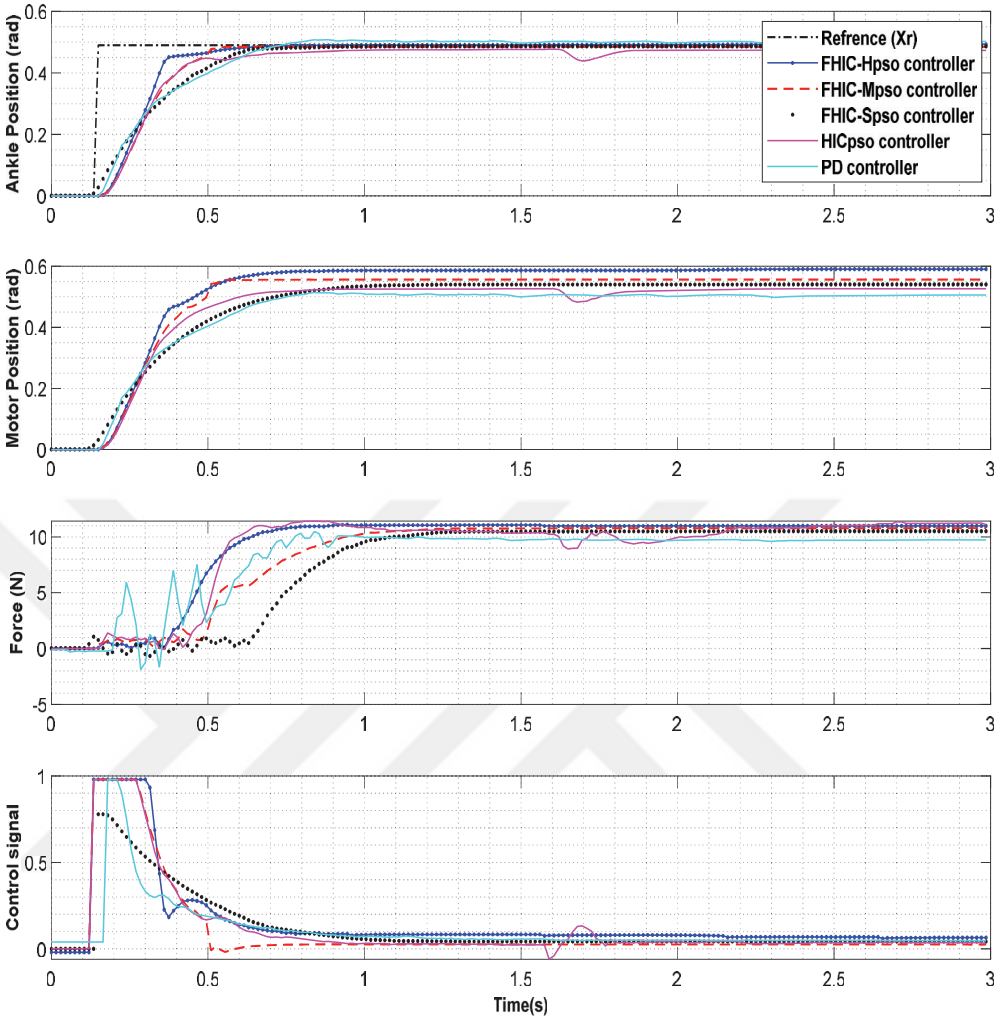

Figure 5.17. FHIC results with different optimum PSO parameters (S_{PSO}, M_{PSO}, and H_{PSO}) and HIC, PD controllers

Table 5.4. Comparison of performance results for S_{PSO} mode controller (MO: maximum overshoot (%), T_s: settling time, e_{ss}: steady state error)

Controller	Position			Force		
	$MO(\%)$	T_s	E_{ss}	$MO(\%)$	T_s	e_{ss}
Experiment S_{PSO} − FHIC	4.521	0.971	0.0735	3.521	1.465	0.0881
Simulation S_{PSO} − FHIC	0.247	0.965	0.0647	1.247	1.440	0.0853

According to the experimental and simulation results in Table 5.3, the S_{PSO} − FHI, the E_{ss} in position and force are 0.07 and 0.08; the T_s in position and force are 0.9 and 1.4 seconds, respectively.

Table 5.5. Comparison of performance results for M_{PSO} mode controller (MO: maximum overshoot (%), T_s: settling time, e_{ss}: steady state error)

Controller	Position			Force		
	$MO(\%)$	T_s	E_{ss}	$MO(\%)$	T_s	e_{ss}
Experiment M_{PSO} − FHIC	12.835	0.941	0.0551	4.370	0.825	0.0611
Simulation M_{PSO} − FHIC	2.601	0.937	0.0538	1.518	0.817	0.0604

According to the experimental and simulation results in Table 5.4, for the M_{PSO} − FHI controller, the E_{ss} in position and force are 0.05 and 0.06; the T_s in position and force are 0.9 and 0.8 seconds, respectively.

Table 5.6. Comparison of performance results for H_{PSO} mode controller (MO: maximum overshoot (%), T_s: settling time, e_{ss}: steady-state error)

Controller	Position			Force		
	$MO(\%)$	T_s	E_{ss}	$MO(\%)$	T_s	e_{ss}
Experiment H_{PSO} − FHIC	3.521	0.681	0.065	8.521	0.920	0.0731
Simulation H_{PSO} − FHIC	1.247	0.621	0.077	5.247	0.846	0.0710

According to the experimental and simulation results in Table 5.5 the $\mathrm{H_{PSO}}-$ FHI controller, the E_{ss} in position and force are 0.06 and 0.07; the T_s in position and force are 0.6 and 0.8 seconds, respectively

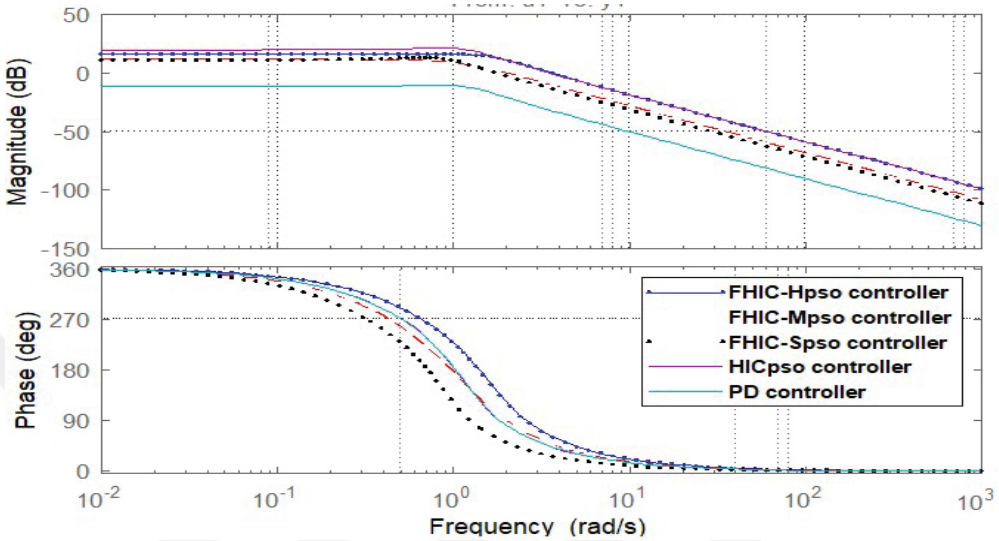

Figure 5.18. Frequency responses of SEM-TA

Using the parameters optimized by the PSO algorithm in $M_{\mathrm{PSO}}-$ FHI controller at a frequency of 1 Hz, the system response to a sinusoidal signal with an error of less than 2% and the system response to the square signal with an error of less than 5% can be seen in Figure 5.18. As shown in Figure 5.19, and Figure 5.20, the operational bandwidth of FHI controllers is robust and broader than PD and HI controllers.

Table 5.7. RMSEs between experiment and simulation result of the FHI controller with the three different PSO contact stress force

Controller Type	RMS-PE	RMS-FE
$FHIC - S_{PSO}$	0.202753	0.33931
$FHIC - M_{PSO}$	0.196358	0.32761
$FHIC - H_{PSO}$	0.198633	0.33174
HIC_{PSO}	0.224021	0.39471
PD	0.225524	0.41920

In order to evaluate the performance of the S_{PSO}, M_{PSO}, H_{PSO}, and HIC, the RMSEs of the position and the force (RMS-PE and RMS-FE) between the modeled reference and the measured signal from the ankle joints are computed based on the equation (4.6). The calculated RMSEs are given in Table 5.6. According to the obtained RMSEs results, the $FHIC - M_{PSO}$ controller is robust and produces better results than the and experimental controllers in terms of T_s, MO, E_{ss}, and RMSEs.

Table 5.8. Comparison of the controllers based on improvement percentage of RMSE

Controller Type	RMS-PE rate	RMS-FE rate
$FHIC - S_{PSO}$ versus HIC_{PSO}	10.48%	16.32%
$FHIC - S_{PSO}$ versus PD	11.23%	23.54%
$FHIC - M_{PSO}$ versus HIC_{PSO}	14.08%	20.48%
$FHIC - M_{PSO}$ versus PD	14.85%	27.95%
$FHIC - H_{PSO}$ versus HIC_{PSO}	11.33%	18.98%
$FHIC - H_{PSO}$ versus PD	13.53%	26.36%

According to the calculated rate of improvement percentages in Table 5.7, the $FHIC - S_{PSO}$ returned more accurately than HIC_{PSO} and PD for the impedance control of the SEM-TA. The RMS-PE improvement percentages are 10.48% for the HIC_{PSO} controller, 11.23% for the PD controller. The RMS-FE improvement percentages are 16.32% for the HIC_{PSO} controller, 23.54% for the PD controller. According to the calculated rate of improvement percentages in Table 8, the $FHIC - M_{PSO}$ returned more accurately than HIC_{PSO} and PD for the impedance control of the SEM-TA. The RMS-PE improvement percentages are 14.08% for the HIC_{PSO} controller, 14.85% for the PD controller. The RMS-FE improvement percentages are 20.48% for the HIC_{PSO} controller, 27.95% for the PD controller. According to the calculated rate of improvement percentages in Table 8, the $FHIC - H_{PSO}$ returned more accurately than HIC_{PSO} and PD for the impedance control of the SEM-TA. The RMS-PE improvement percentages are 11.33% for the HIC_{PSO} controller, 13.53%

for the PD controller. The RMS-FE improvement percentages are 18.98% for the HIC_{PSO} controller, 26.36% for the PD controller.

Table 5.9. Gain margin (G_m) and phase margin (P_m) of the controllers

Controller Type	G_m (dB)	frequency (rad/s)	P_m (deg)	frequency (rad/s)
$FHIC - S_{PSO}$	2.02	1.14	58.1	1.76
$FHIC - M_{PSO}$	2.8	0.978	48.4	2.01
$FHIC - H_{PSO}$	4.1	0.72	59.2	3.58
HIC_{PSO}	8.5	1.02	65.7	3.49
PD	10.6	1.01	inf	-

According to Table 5.9, FHI controllers are robust controllers in terms of phase margin. The range of gain and phase margins of the developed FHI controllers in Table 5.8 are between 2-5 and 30°-60°, respectively. As was expected, the parameters of the FHI controllers were found optimally.

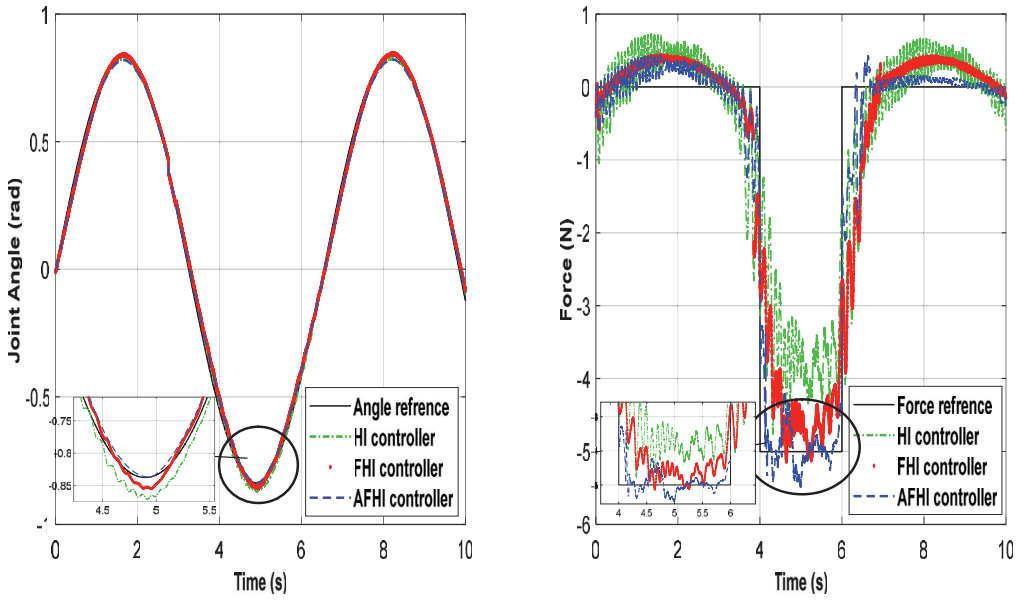

Figure 5.19. The dynamic position-torque trajectory tracking performance of HI, FHI, and AFHI are compared, (a) position tracking (b) Torque tracking.

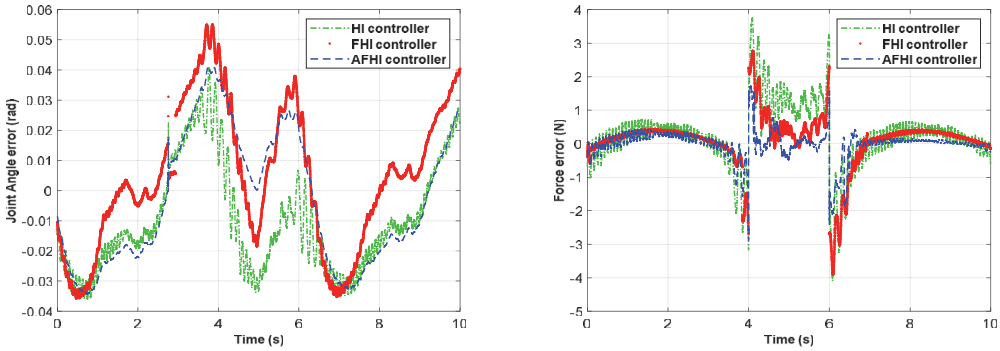

Figure 5.20. Experimental error results during tarjectory tracking

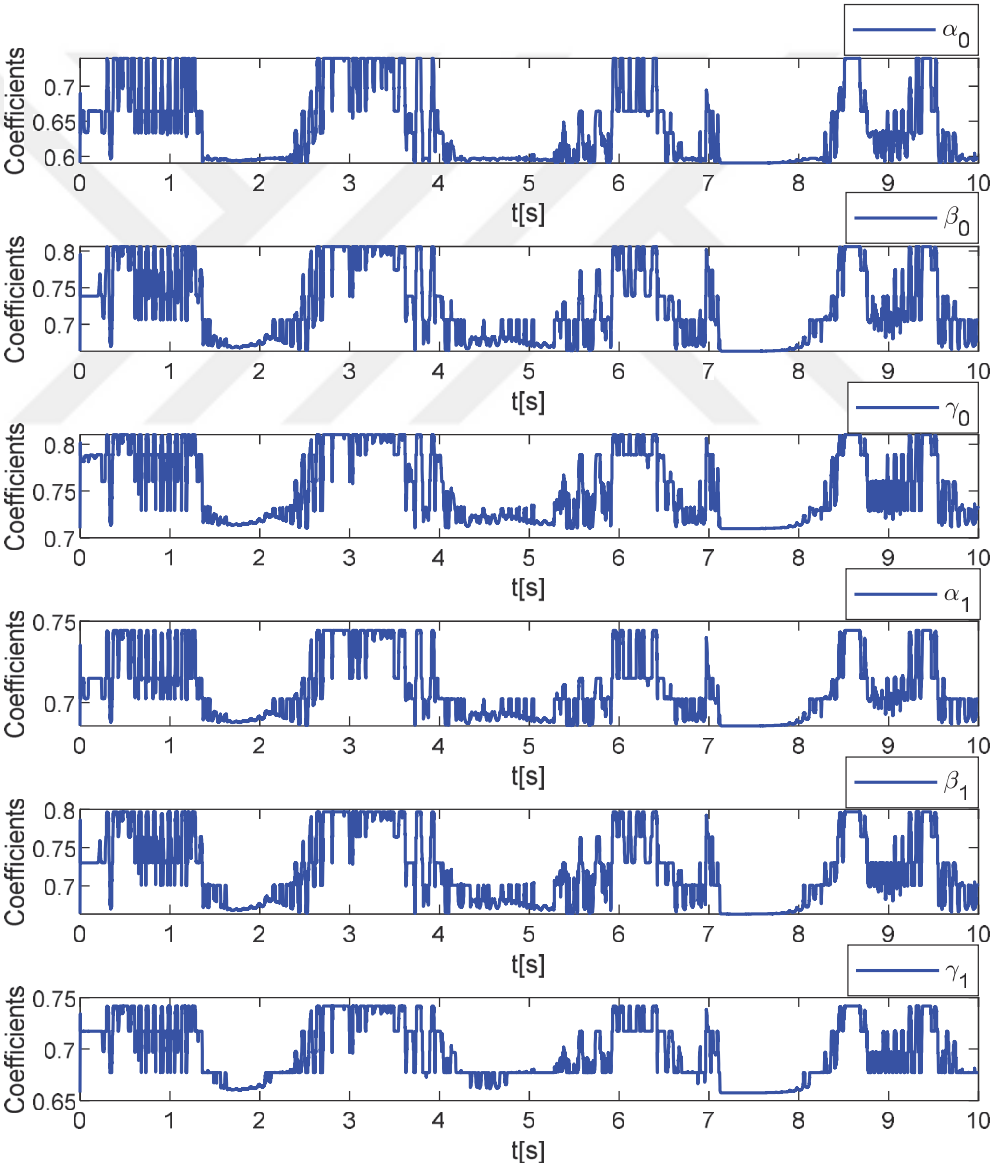

Figure 5.21. Fractional parameters ($\alpha_0, \beta_0, \gamma_0, \alpha_1, \beta_1, \gamma_1$) in experimental A-FHIC

Figure.5.21 illustrates the fractional parameters obtained by the adaptive fuzzy model for the FHIC of the SEM-TA System. At a distance of seconds, the fuzzy controller is in the medium-mode and at the point of high-stress torque is in the hard-mode, and at a distance of seconds when the torque enters the steady-state it is soft-mode and again at the point of 6 seconds at medium and hard modes and then goes to soft-mode.

Table 5.10. The experimental results in terms of RMSEs

Controller Type	$RMSE_P$ (rad)	$RMSE_T$ (N)
$HI\ controller$	0.23821	0.58727
$FHI - SFT_{PSO}\ controller$	0.19264	0.42793
$FHI - MDM_{PSO}\ \ controller$	0.20486	0.54835
$FHI - HRD_{PSO}\ controller$	0.23715	0.58321
$AFHI\ controller$	0.18417	0.37423

In order to evaluate the performance of the $FHI - SFT_{PSO}$, $FHI - MDM_{PSO}$, $FHI - HRD_{PSO}$ controllers, HI controller, and $AFHI\ controller$ the RMSEs of the position and the torque ($RMSE_P$ and $RMSE_F$) between the reference signal and the measured signal from the load joints are computed based on the equation (4.6). The calculated RMSEs are given in Table 5.9. According to the obtained RMSEs results, the $AFHI\ controller$ is robust and produces better results than the and experimental controllers in RMSEs.

Table 5.11. Comparison of the controllers based on improvement percentage of RMSE

Controller Type	$RMSE_P$ rate	$RMSE_F$ rate
$AFHI$ versus HI	11.38%	18.15%

Table 5.10.(Cont.) Comparison of the controllers based on improvement percentage of RMSE

$AFHI$ versus $FHI - S_{PSO}$	6.84%	12.37%
$AFHI$ versus $FHI - M_{PSO}$	6.03%	9.26%
$AFHI$ versus $FHI - H_{PSO}$	7.55%	15.54%
$FHI - M_{PSO}$ versus HI	8.46%	13.51%
$FHI - M_{PSO}$ versus $FHI - S_{PSO}$	6.17%	10.80%
$FHI - M_{PSO}$versus $FHI - H_{PSO}$	7.25%	12.72%

According to the calculated rate of improvement percentages in Table 5.10, the $AFHI$ returned more accurately than HI and $FHIs$ for the impedance control of the RSEA. The $RMSE_P$ improvement percentages are 11.38% for the HI controller, 6.84% for the $FHI - S_{PSO}$ controller, 6.03% for the $FHI - S_{PSO}$ controller, 7.55% for the $FHI - H_{PSO}$ controller. The $RMSE_F$ improvement percentages are 18.15% for the HI controller, 12.37% for the $FHI - S_{PSO}$ controller, 9.26% for the $FHI - MDM_{PSO}$ controller, 15.54% for the $FHI - H_{PSO}$ controller. According to the calculated rate of improvement percentages in Table 5.10, the $FHI - M_{PSO}$ returned more accurately than HI and $FHIs$ for the impedance control of the RSEA. The $RMSE_P$ improvement percentages are 8.46% for the HI controller, 6.17% for the $FHI - S_{PSO}$ controller, 7.25% for the $FHI - H_{PSO}$ controller. The $RMSE_F$ improvement percentages are 13.51% for the HI controller, 10.80% for the $FHI - SFT_{PSO}$ controller, 12.72% for the $FHI - H_{PSO}$ controller.

5.3. Experimental result of the FHIC

To evaluate the FHIC in order to optimize its parameters, the controller has been used in different modes and the results have been plotted. By connecting a 2 kg weight to the system, we apply a force equivalent to 19.6 N to the system. By changing the controller parameters according to Table 5.12, different outputs are plotted as results, indicating a change in each parameter in that position. Figures 5.22, 5.23, 5.24, 5.25, 5.26, 5.27, 5.28, 5.29, 5.30, and 5.31 respectively show the results of the system output with constant parameters ($K_p = 2.175, K_v = 0.251$) and

variable parameters $(\alpha, \beta, \gamma, \delta)$ and, Figures 5.32, 5.33, 5.34, 5.35, 5.36, 5.37, 5.38, 5.39, 5.40, and 5.41 respectively show the results of the system output with constant parameters ($K_p = 2.280, K_v = 0.345$) and variable parameters $(\alpha, \beta, \gamma, \delta)$.

Table 5.12. FHIC parameters

Experiment case	SEL	K_p	K_v	α	β	γ	δ
1	0	0	0	0	0	0	0
2	0.5	2.175	0.251	0.5	0.5	0.5	0.5
3	0.5	2.175	0.251	1	1	1	0.5
4	0.5	2.175	0.251	0	1	1	0.5
5	0.5	2.175	0.251	0	1	0	0.5
6	0.5	2.175	0.251	0	1	1	0
7	0.5	2.175	0.251	0	1	1	1
8	0	2.175	0.251	0	1	1	1
9	0	2.175	0.251	0.5	0.5	0.5	0.5
10	0.5	2.175	0.251	0.5	1	1	1
11	0.5	2.280	0.345	1	1	1	1
12	0.5	2.280	0.345	0	1	1	1
13	0.5	2.280	0.345	0	0	1	1
14	0.5	2.280	0.345	0	0	0	1
15	0.5	2.280	0.345	0	0	0	0
16	1	2.280	0.345	0	0	0	0
17	1	2.280	0.345	0	1	0	0
18	1	2.280	0.345	0	1	1	0
19	1	2.280	0.345	0	1	0	1
20	1	2.280	0.345	0	1	0	1

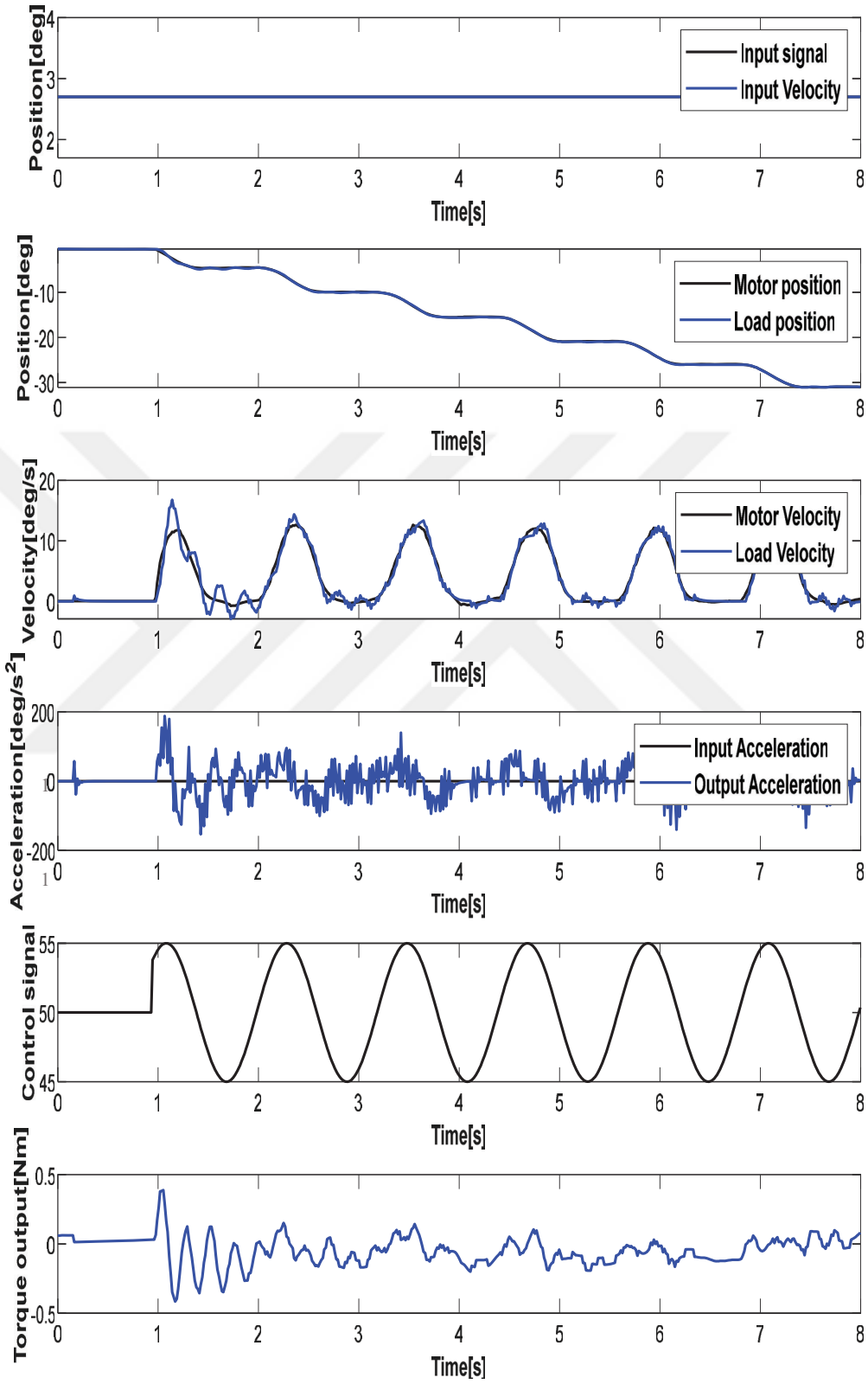

Figure 5.22. FHIC experimental results with case 1 parameters

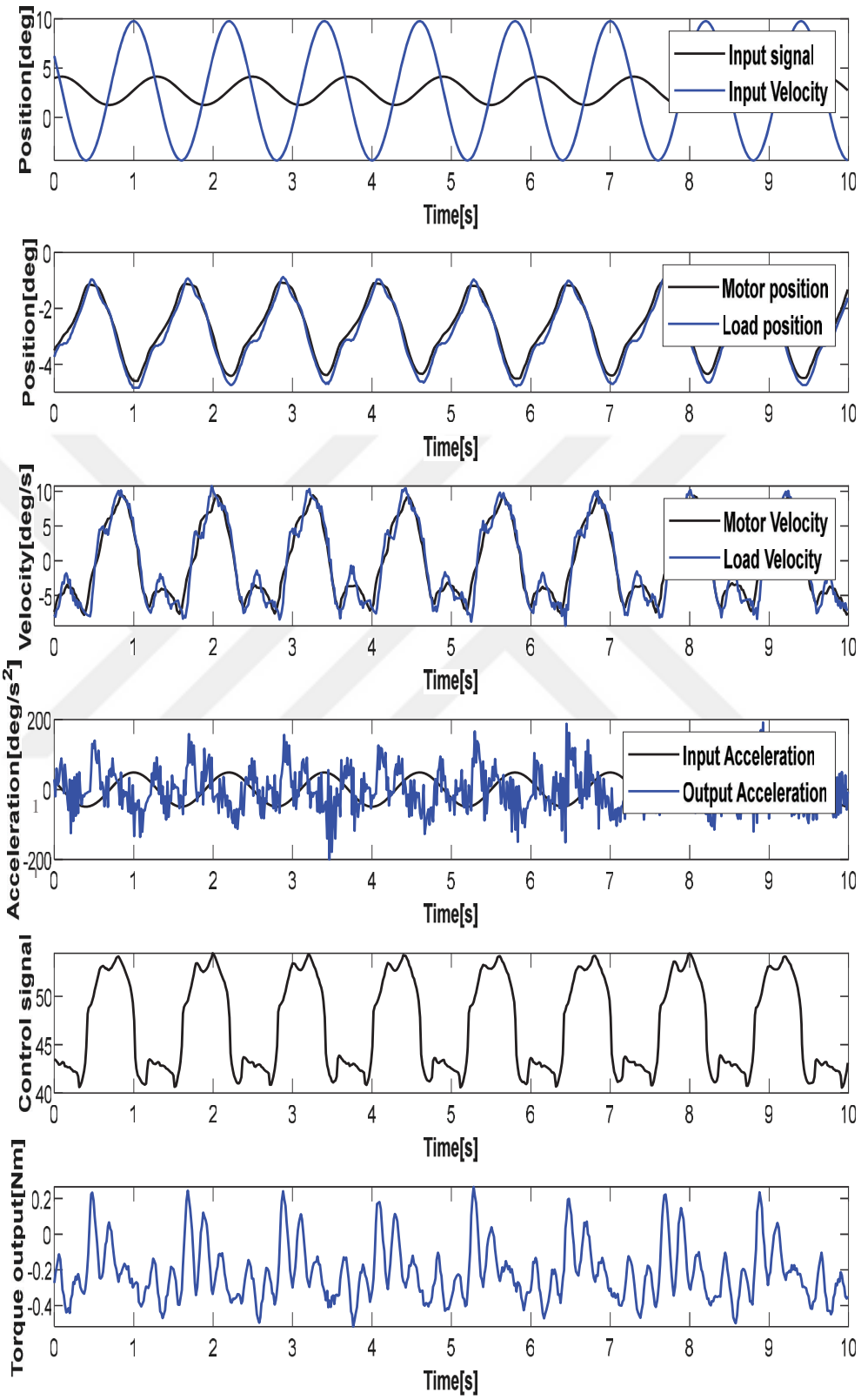

Figure 5.23. FHIC experimental results with case 2 parameters

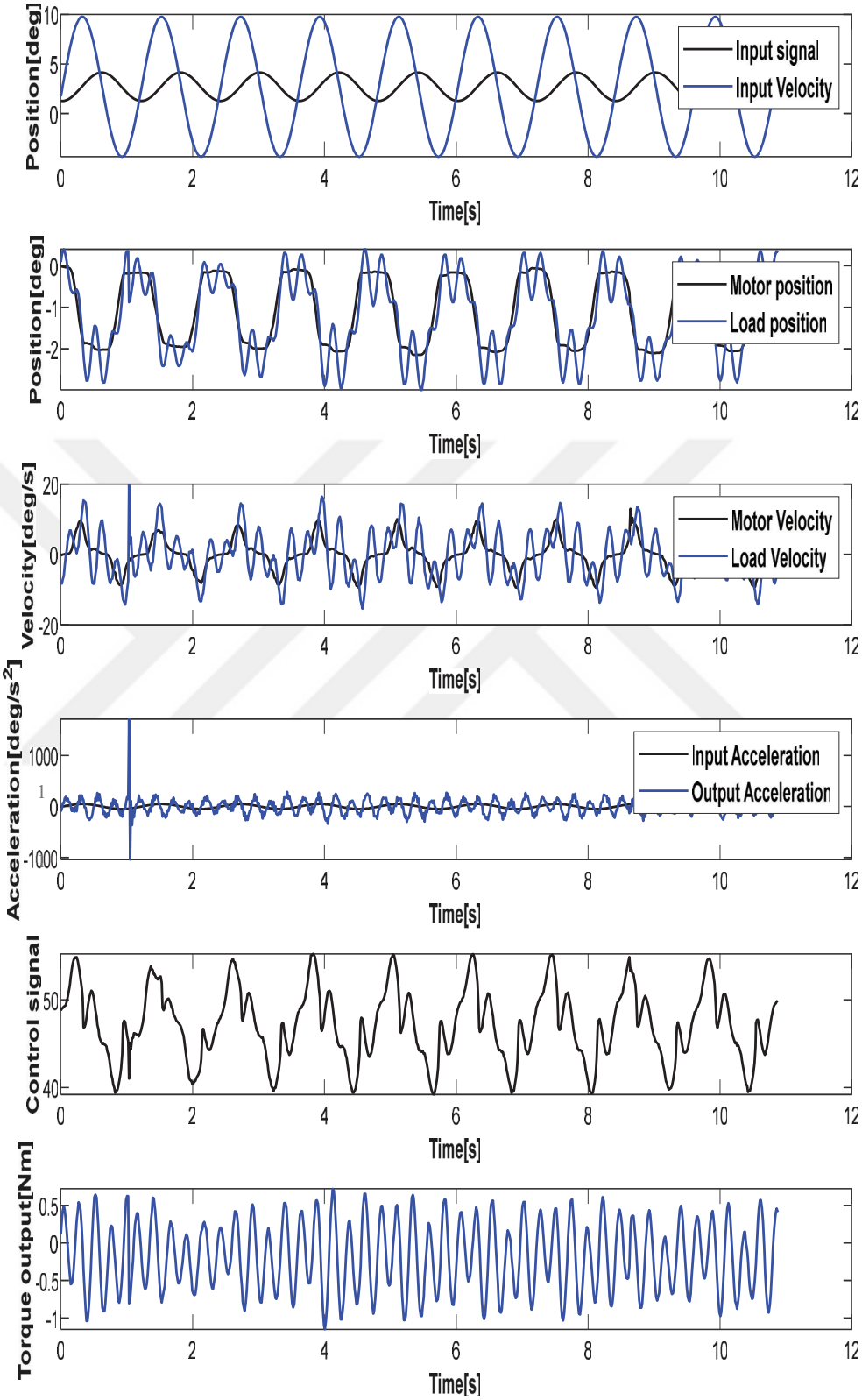

Figure 5.24. FHIC experimental results with case 3 parameters

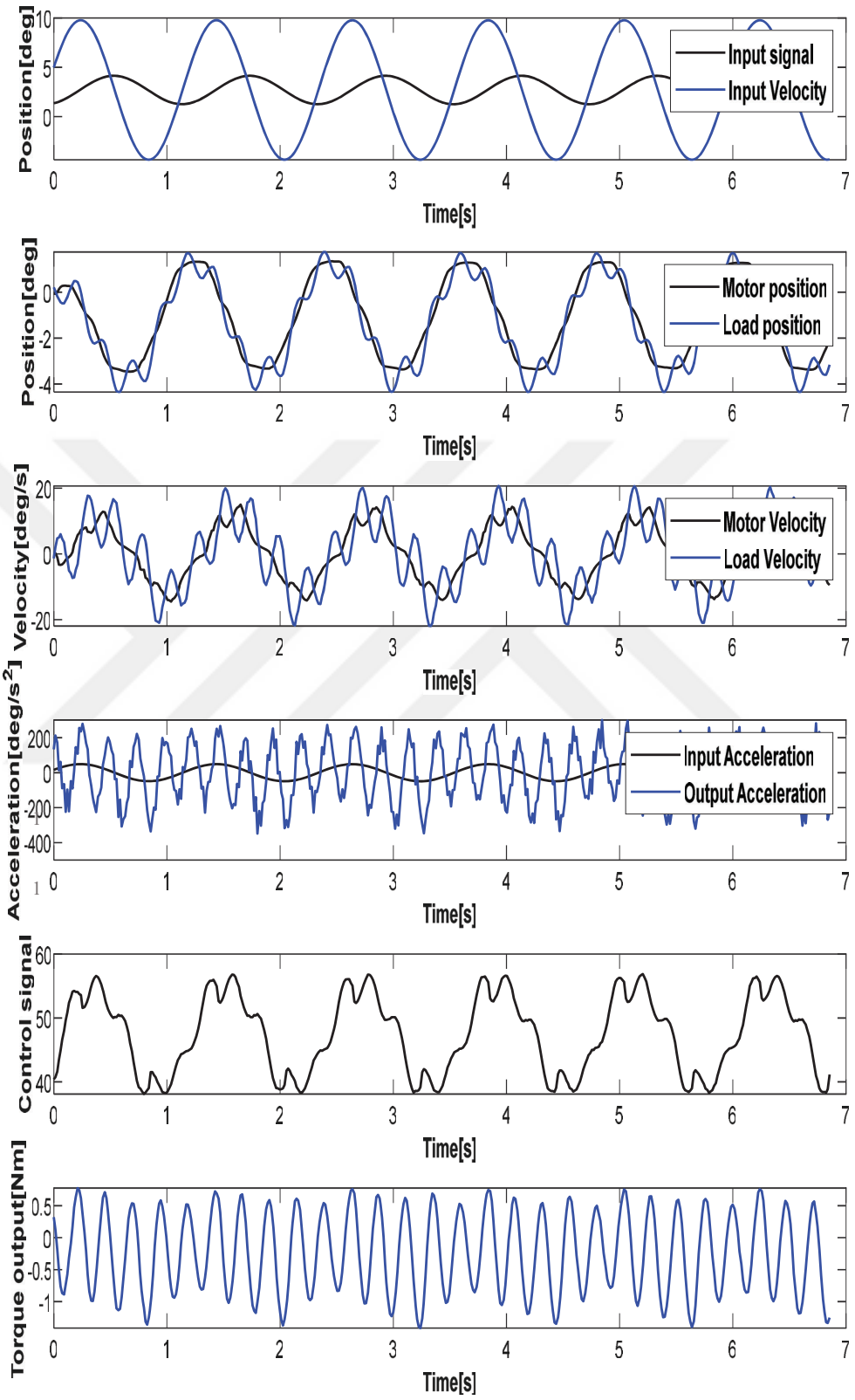

Figure 5.25. FHIC experimental results with case 4 parameters

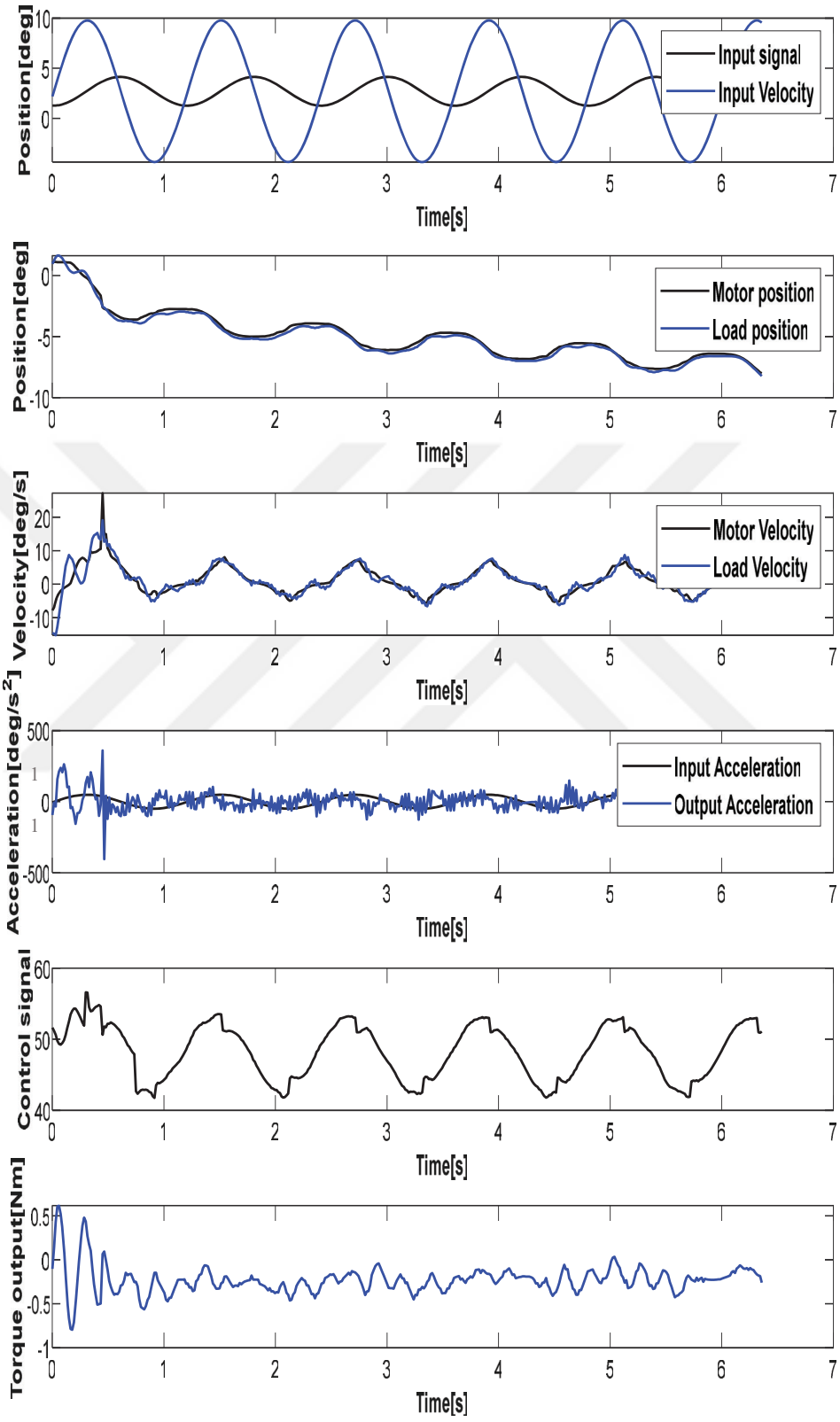

Figure 5.26. FHIC experimental results with case 5 parameters

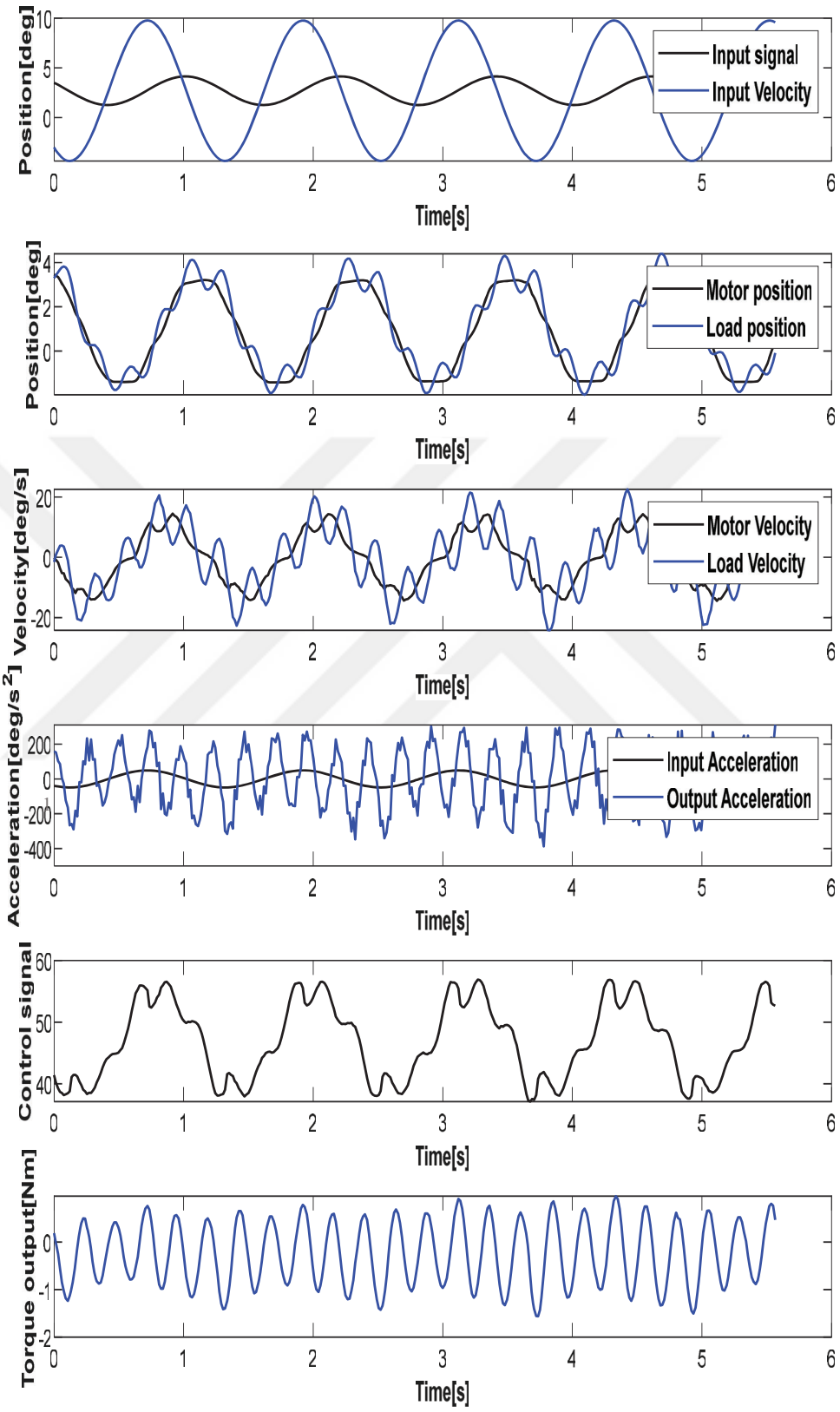

Figure 5.27. FHIC experimental results with case 6 parameters

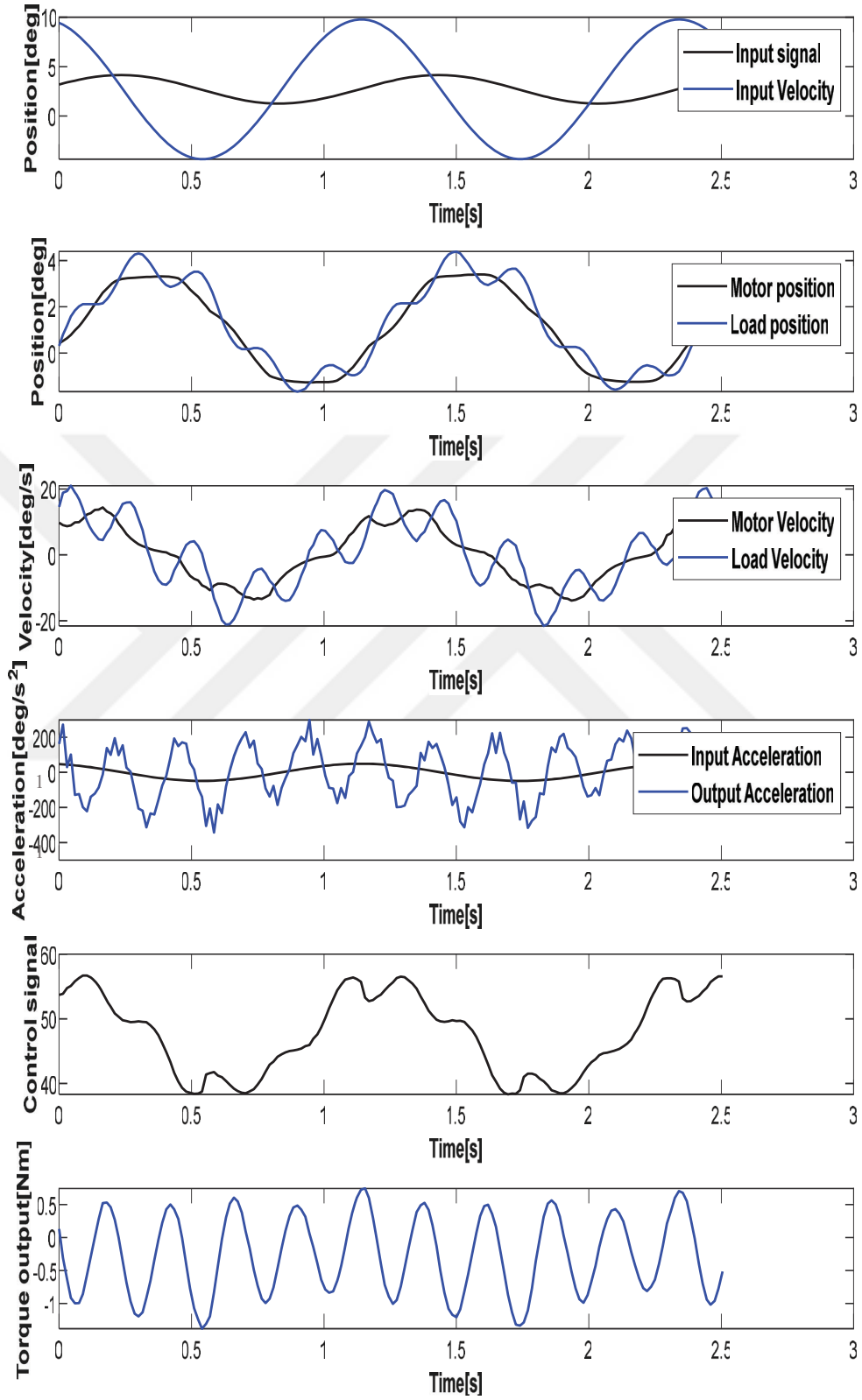

Figure 5.28. FHIC experimental results with case 7 parameters

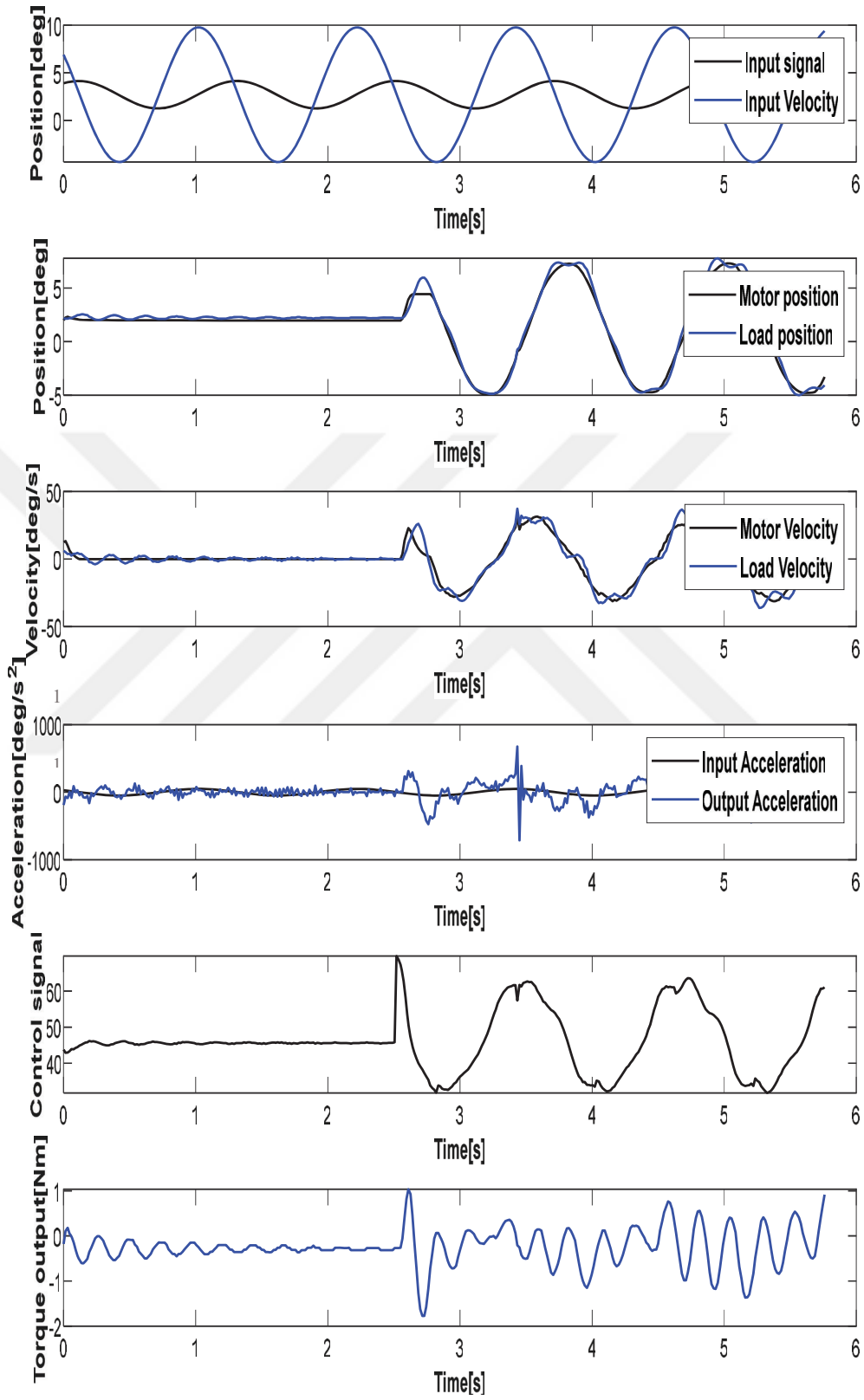

Figure 5.29. FHIC experimental results with case 8 parameters

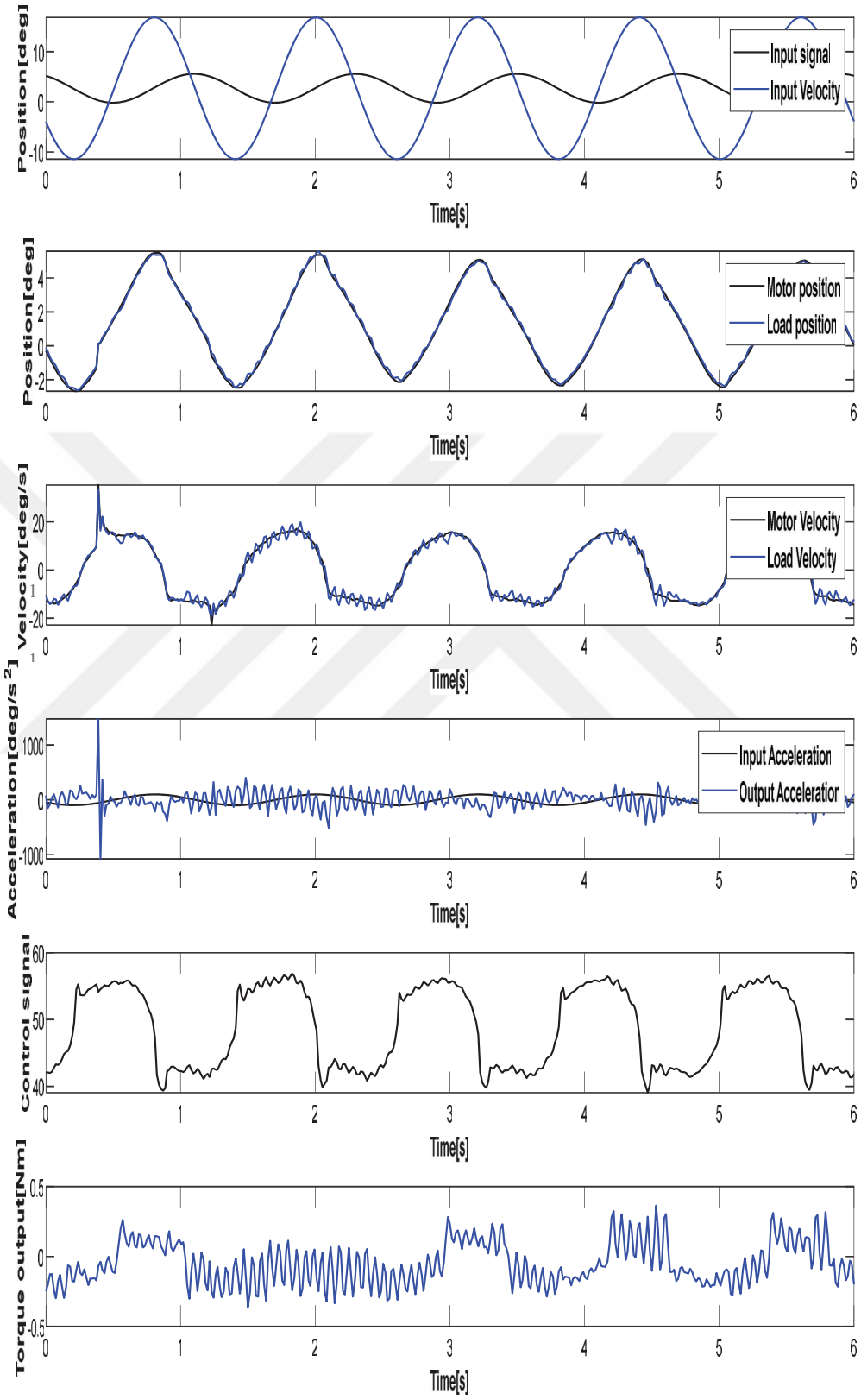

Figure 5.30. FHIC experimental results with case 9 parameters

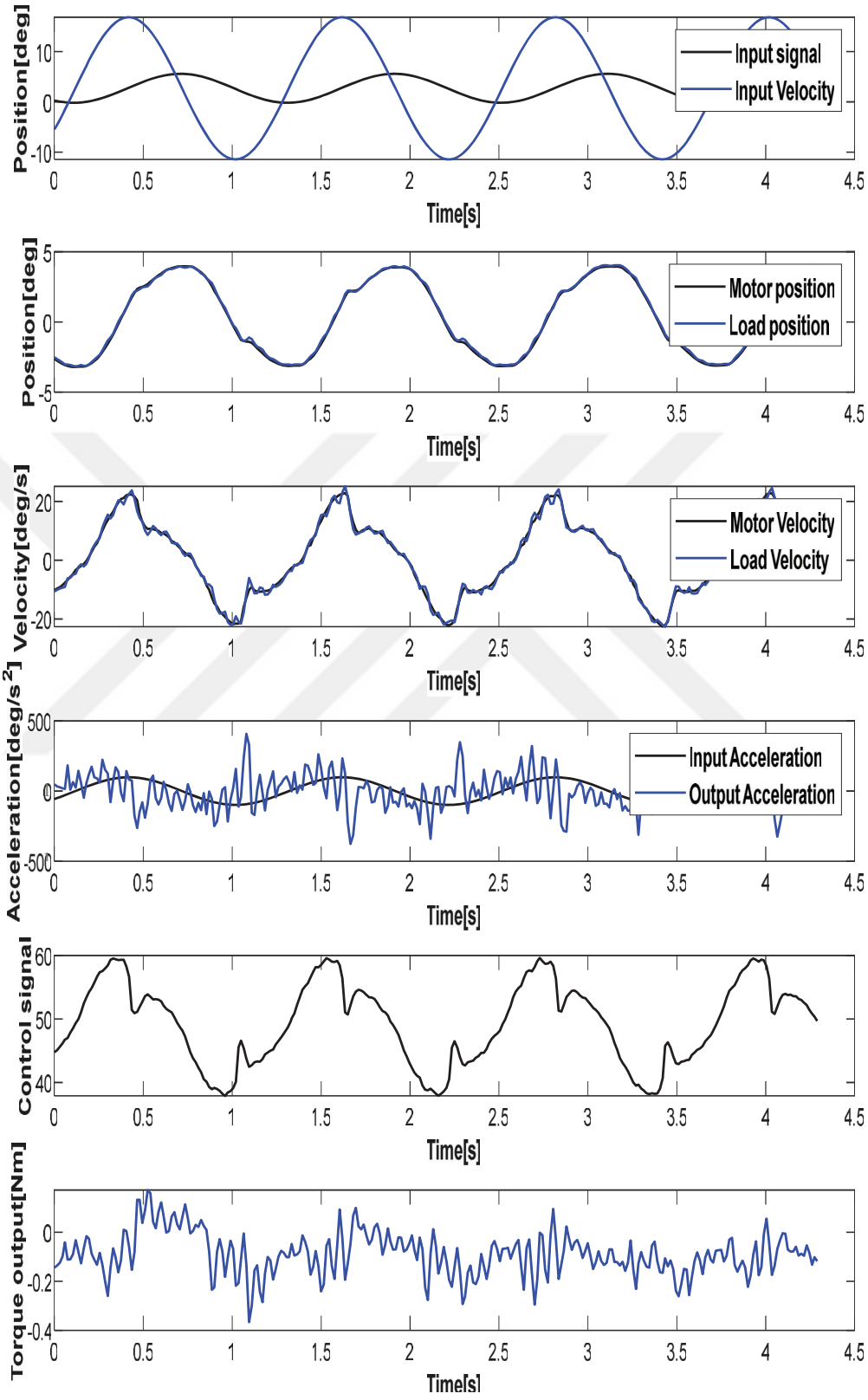

Figure 5.31. FHIC experimental results with case 10 parameters

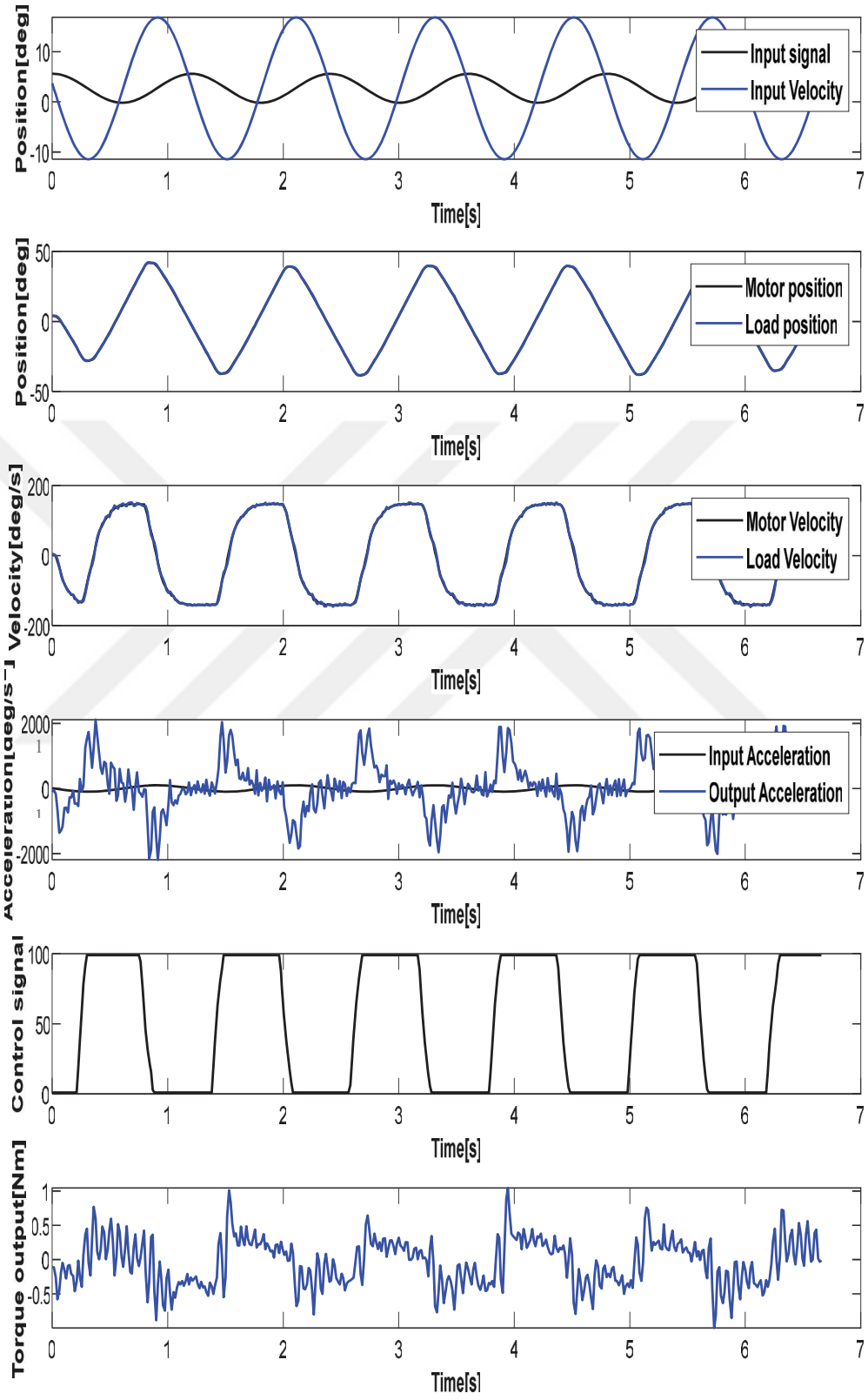

Figure 5.32. FHIC experimental results with case 11 parameters

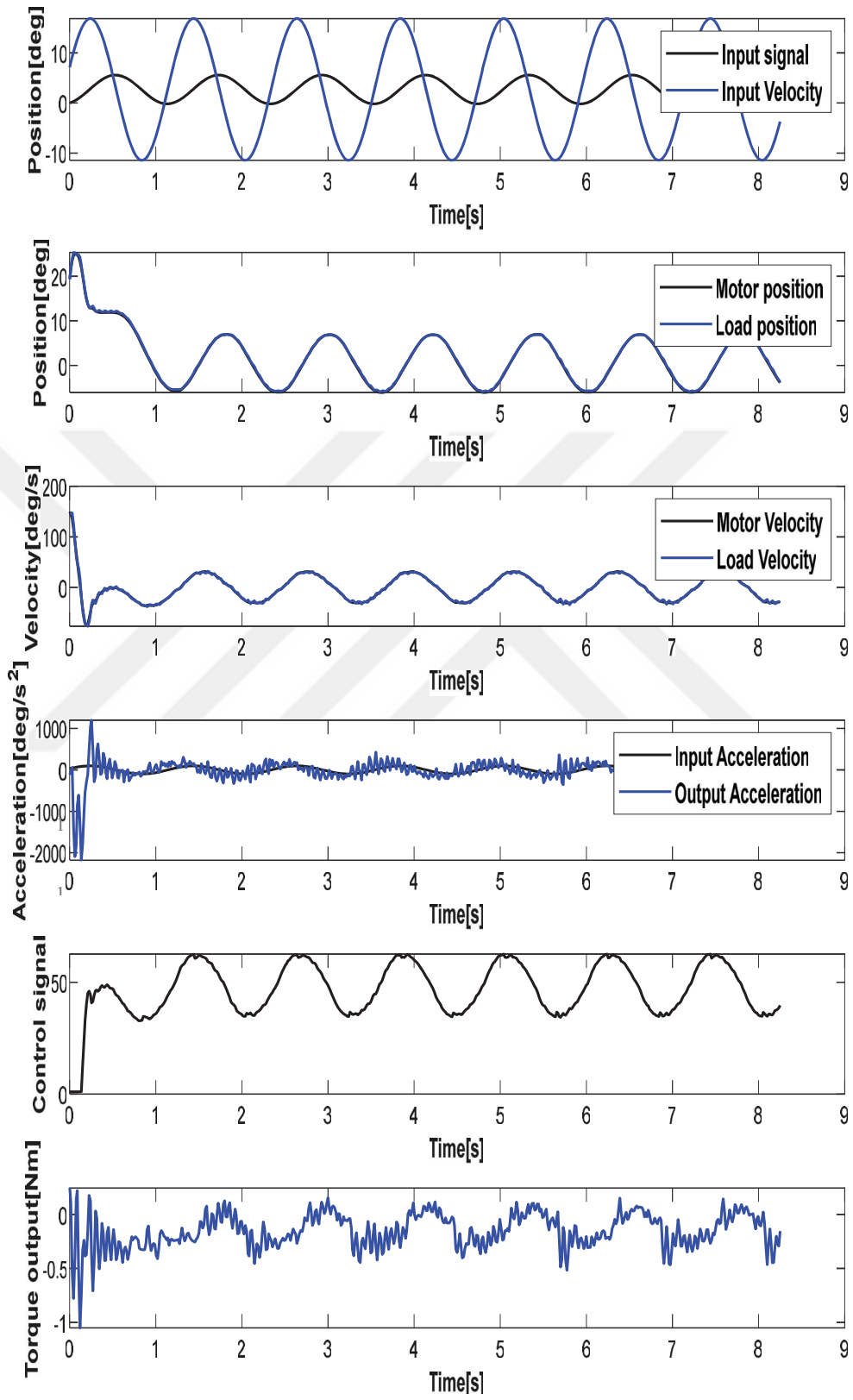

Figure 5.33. FHIC experimental results with case 12 parameters

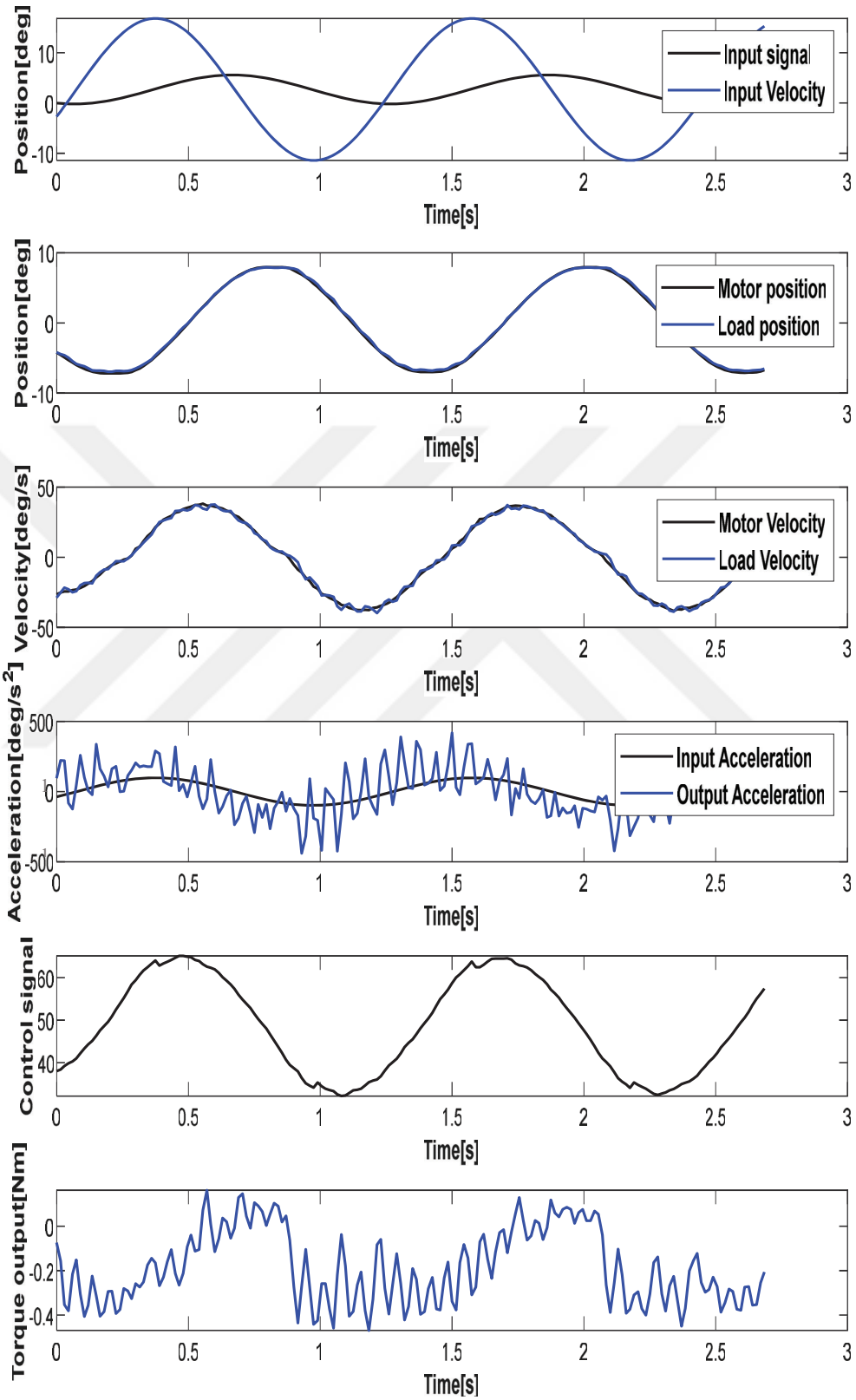

Figure 5.34. FHIC experimental results with case 13 parameters

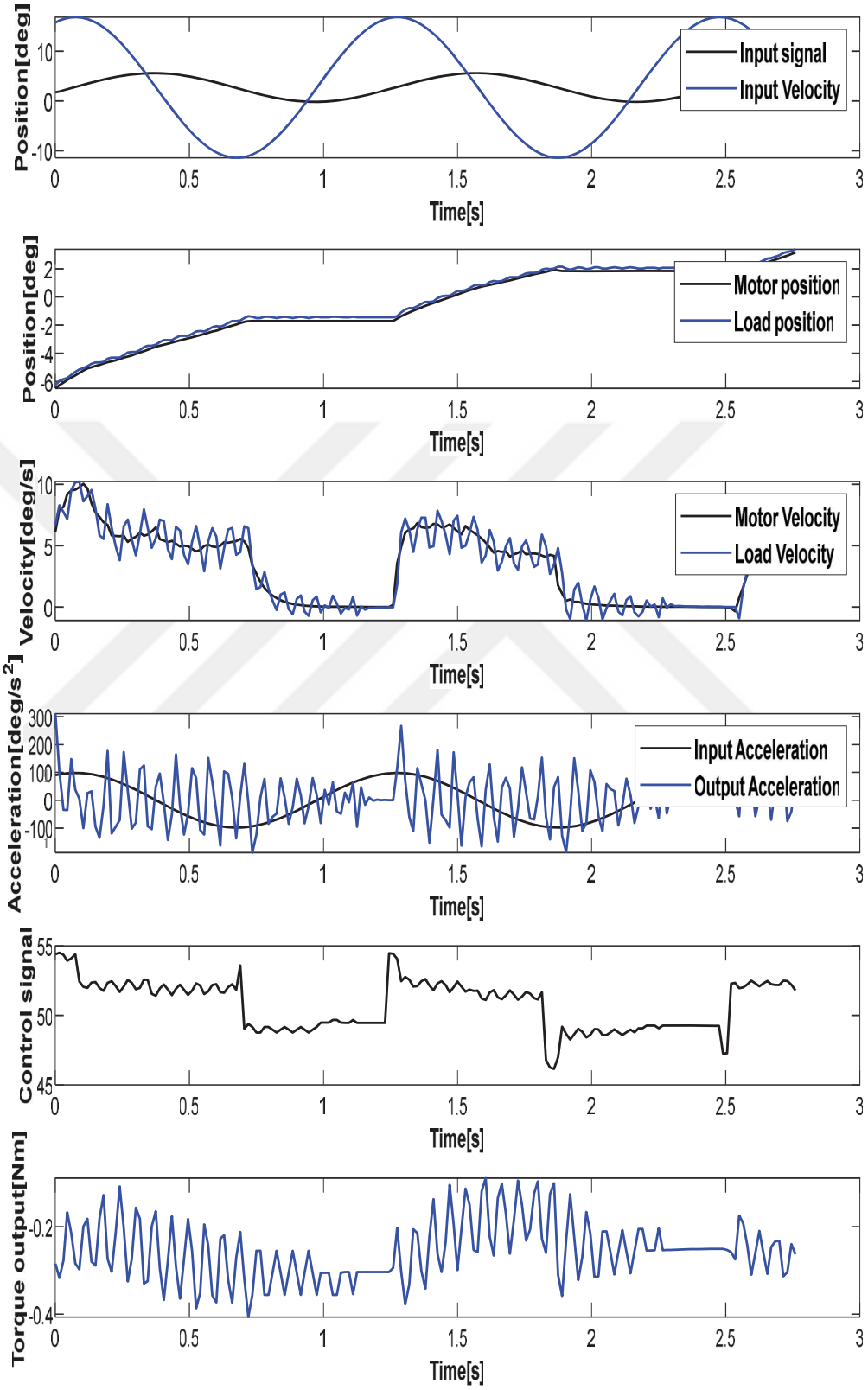

Figure 5.35. FHIC experimental results with case 14 parameters

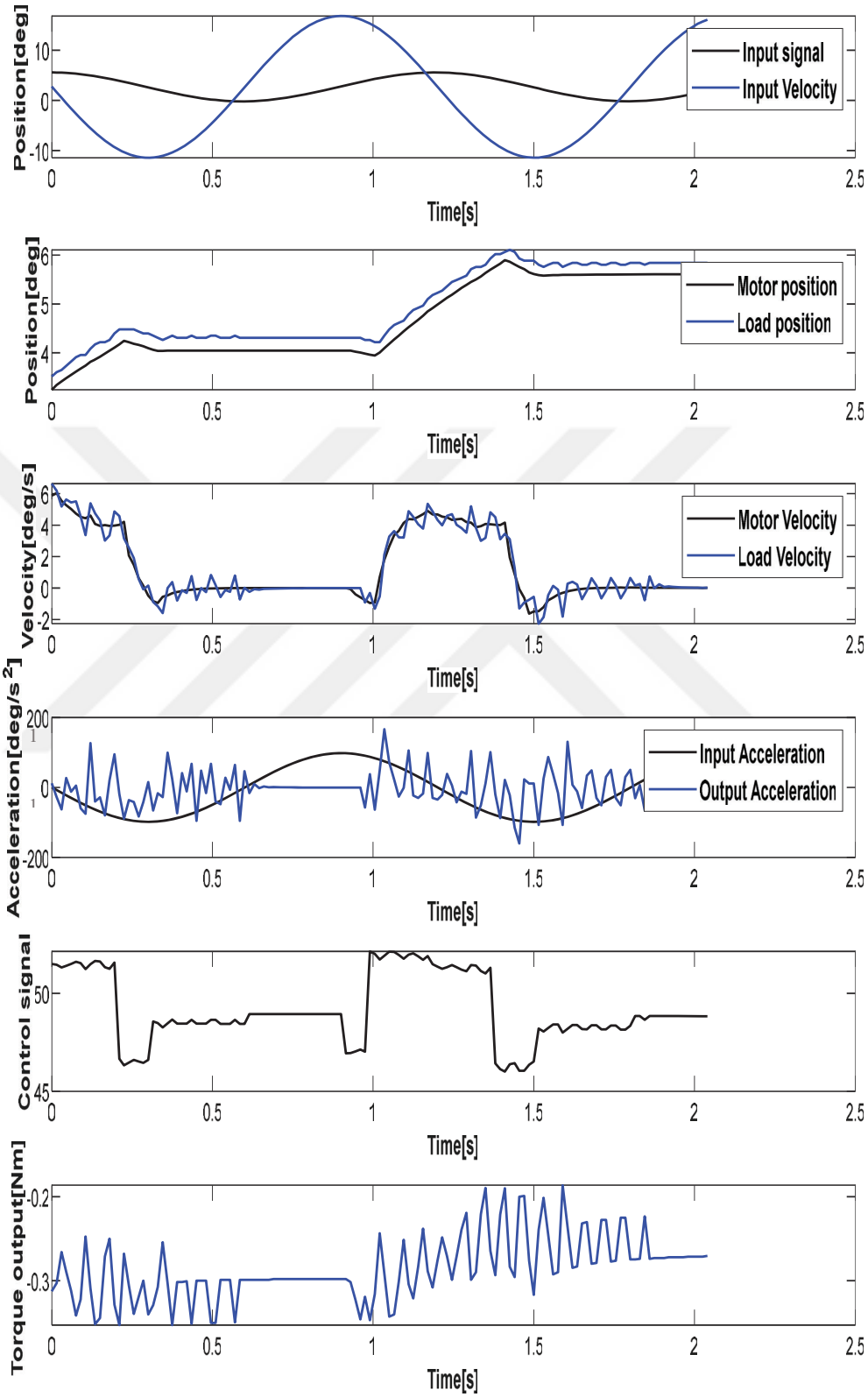

Figure 5.36. FHIC experimental results with case 15 parameters

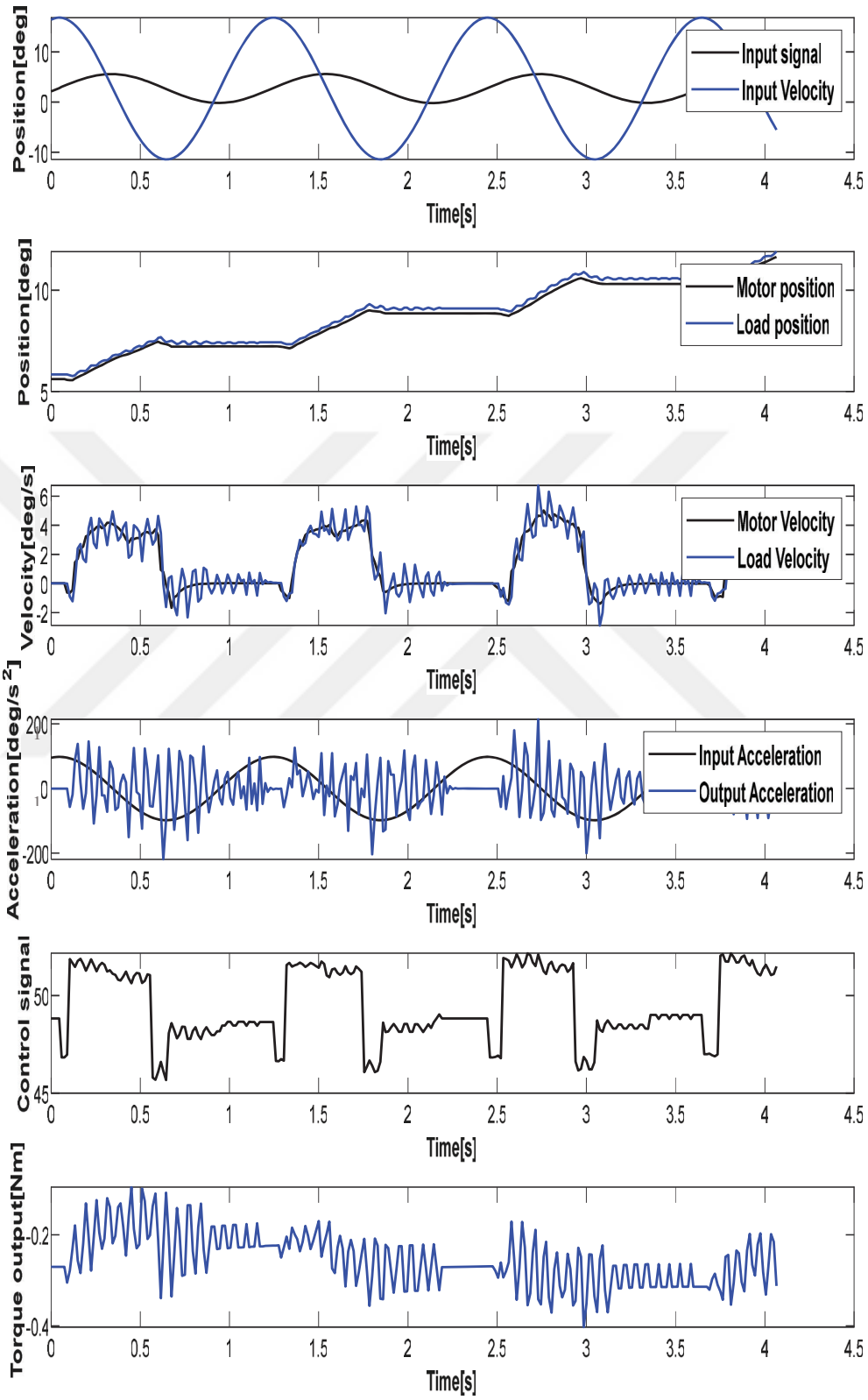

Figure 5.37. FHIC experimental results with case 16 parameters

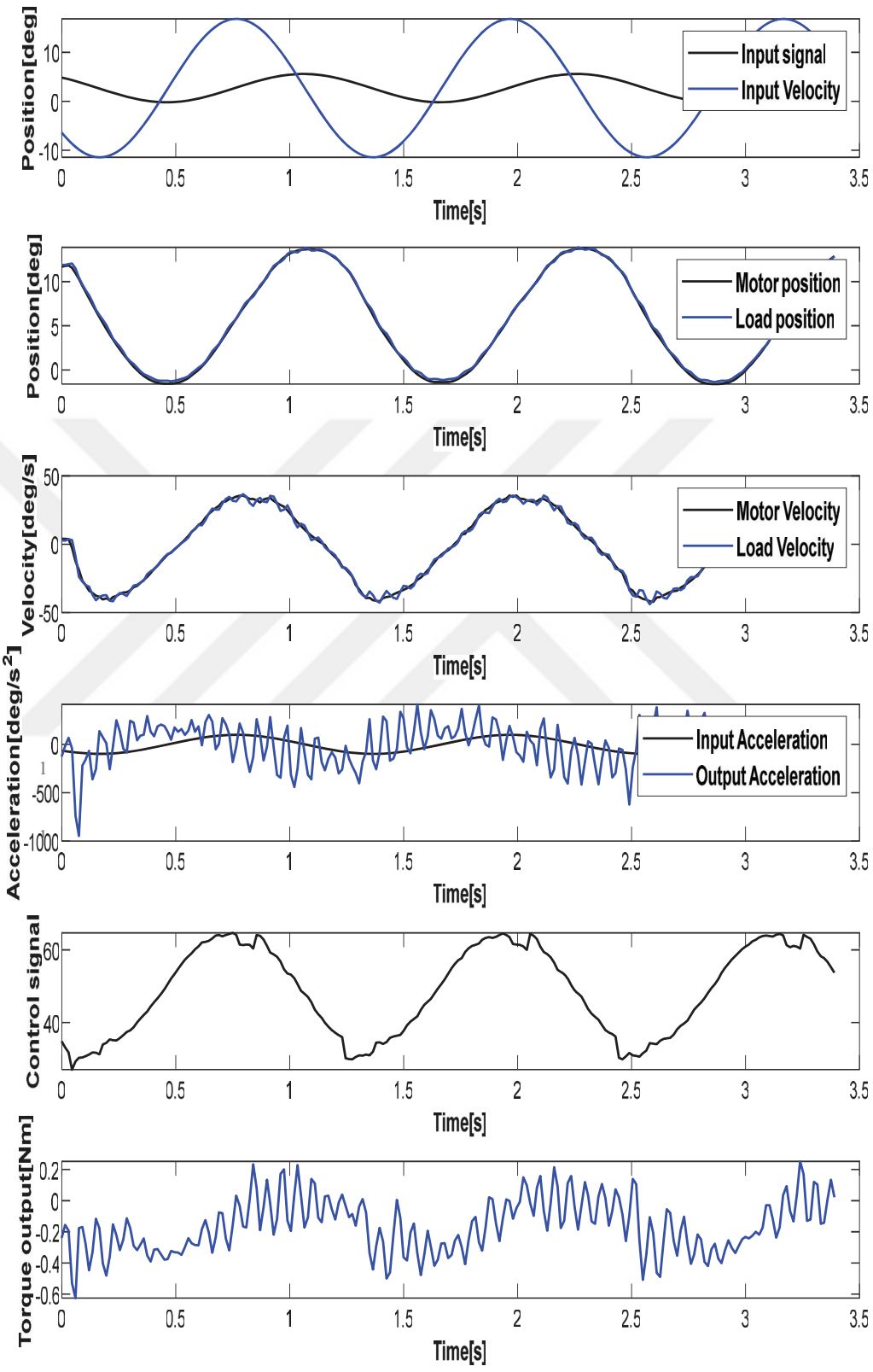

Figure 5.38. FHIC experimental results with case 17 parameters

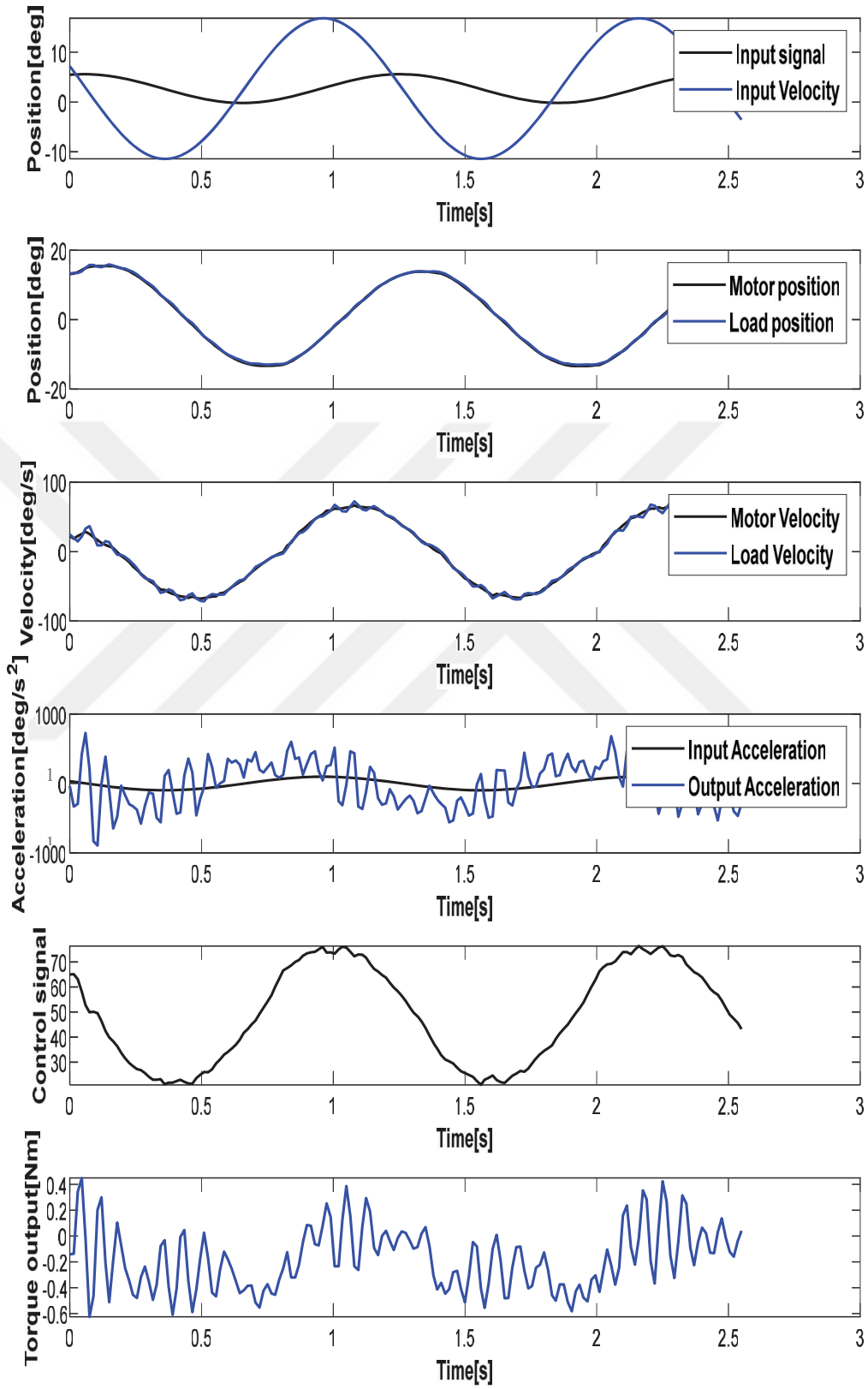

Figure 5.39. FHIC experimental results with case 18 parameters

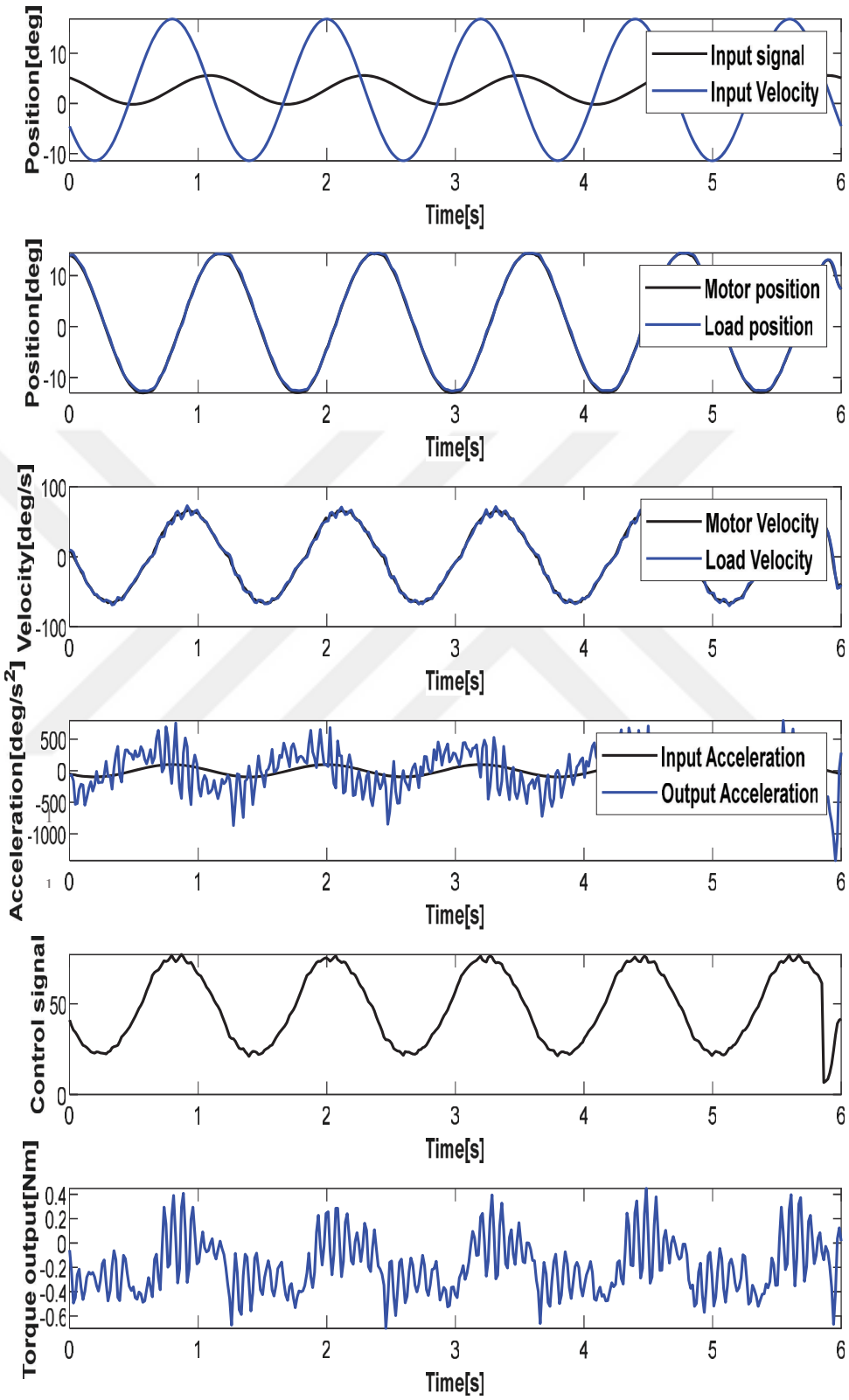

Figure 5.40. FHIC experimental results with case 19 parameters

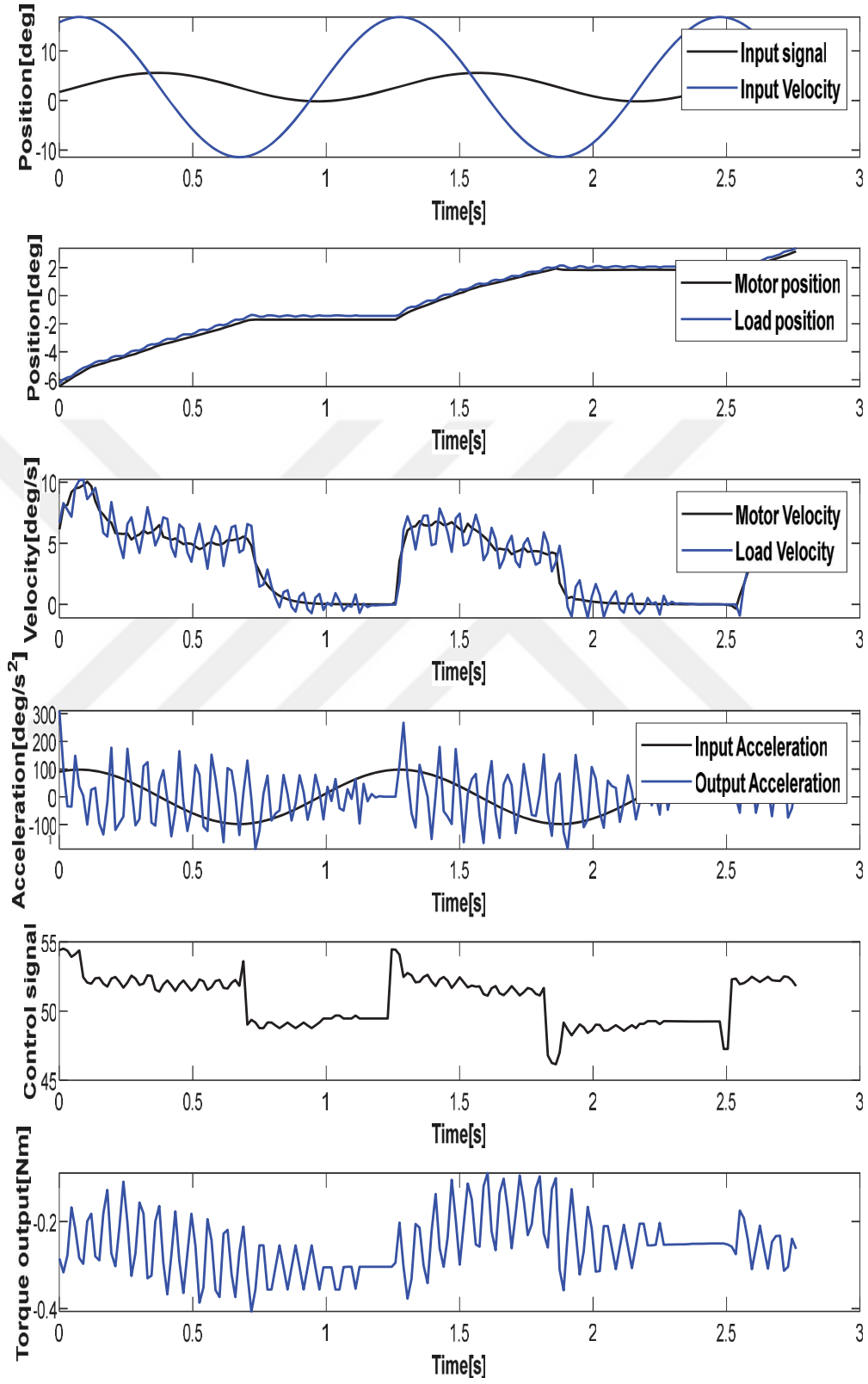

Figure 5.41. FHIC experimental results with case 20 parameters

6. CONCLUSIONS AND RECOMMENDATIONS

In this thesis, a novel design of a rotary series elastic actuator (RSEA) system is developed to be controlled. This system presents an important challenging problem in the area of linear and nonlinear control engineering applications. The contribution of this thesis consisted of the development of novel friction estimation models which take into consideration positions, velocities, and accelerations of the joints of links. Furthermore, more sophisticated nonlinear controllers such as FL-FFC, FTC-FC, and FHIC are developed for the torque and control problems. The novel nonlinear controllers take into consideration the complex inputs-outputs and nonlinear function approximation of the system.

In this research, joint frictions of the RSEA are examined based on its experimental and simulation dynamic responses. Three different friction estimation models such as NCFM, LFM and NLFM are compared to estimate the joint frictions of the RSEA developed in our laboratory. In order to determine the estimation performance of the friction models, RMSEs between position simulation results obtained from each joint friction model and encoders in the experimental setup are computed. According to the comparative experimental friction analysis, the joint frictions of the RSEA are estimated more effectively using an NLFM which yields better improvement percentage from 11.56% to 94.55%. The aim of this study is to obtain joint friction models which depend on both velocity and acceleration in a large range of motion trajectory that involves difficult and sudden large changes. In order to determine the estimation performance of the friction models, the RMSEs of position in all joints are computed. The NLFMs produce better estimation results than the LFMs. Among NLFMs, the NLFM gives the best results which provide the best improvement percentage from 11.56% and 94.55%. In this research, the friction study has three important contributions to the literature: Firstly, all friction models in the literature depend only on velocity; however, the friction model developed here depends on both velocity and acceleration. This approach has enabled us to obtain a two-dimensional friction model. Secondly, the coefficients of all friction models in the

literature were constant when the physical quantities change. On the other hand, the coefficients of the friction models in this work vary depending on the state of the velocity and acceleration. Hence, this friction model allows for better estimation of the effects of friction in different velocity and acceleration conditions. Thirdly, much of existing researches in the literature have studied only the frictions of the linear motion which depends on linear velocity and force. This work examines frictions on the joints which have hard rotational motions.

The torque and impedance control problems of the system are studied for the RSEA, respectively. To determine the control performance of all controllers, different control parameters are computed such as T_s, PO, E_{ss}, MP and the RMSEs of the joint positions. PID-FFC, FL-FFC, and FTC-FC controllers are developed for the torque control problem of the RSEA. The controllers are compared under external disturbance. The robustness results indicate that the FTC-FC controller under external disturbances was effective. The RMSEs improvement percentages between FL-FFC versus PID-FFC are from 24.28% to 75,28%. Moreover, according to the incremental calculated percentages of RMSEs of the control signals, the FL-FFC returned more effort than PID-FFC with 42.95 % under external disturbance. Furthermore, nonlinear HIC and FHIC controllers are developed for the impedance control of the RSEA systems. The aim of this work is to study dynamic performance analysis of both FTC-FC and FHIC controllers and to compare them with the classical PID and PID-FFC controllers, respectively. The developed controllers were tested under internal and external disturbances to determine the robustness performance of the controllers. According to the obtained simulation results, the nonlinear FTC-FC and FHIC controllers are robust and produce better results than the PID and PID-FFC controllers. Based on to the obtained results of the torque control of the RSEA, In this work, a robust real-time FTC-FC of RSEA is developed using an industrial PC for the legged robots. The real-time torque was estimated based on the nonlinear friction model by the measured and empirical torques. In order to examine the robustness of the controller, the proposed controller was tested with friction forces, external disturbances, and parameter uncertainty. The different control methods, such as PID-FFC, FL-FFC, and FTC-FC have been compared in the RSEA under external and internal disturbances. Comparing the control performance

of all controllers, the FTC-FC method is a novel robust control structure for the torque tracking control of the uncertain nonlinear RSEA system. The tracking performance and stability of the RSEA control were enhanced using nonlinear friction estimation. Moreover, a sagacious choice of the fuzzy functions in the fuzzy controller improved the rejected disturbance and reduced torque tracking error. The improvement percentage of FTC-FC under external disturbances is 15.83% and 4.57% better than PID-FFC and FL-FFC, respectively. The results obtained here indicate that the FTC-FC controller with the nonlinear friction model performs well for high and sudden disturbances. This study investigated the impedance controller design and performance characterization of SEM-TA by incorporating different contact stress forces (soft-medium-hard). In particular, we proposed a fractional hybrid impedance control (FHIC) method of the SEM-TA control structure. The main contribution of this research is designing a novel optimum FHIC based on RSEA in uncertain environments. A DFTFS was installed in the SEM-TA between a human joint and a motor as the energy buffer. The force was precisely generated via the flat spring deflection by controlling the motor part with an impedance control method. In this study, three different types of contact force models (S_{PSO}, $M_{PSO}$and H_{PSO}) were defined to evaluate the performance of SEM-TA. It was shown that the proposed control methods meet the desired performances: the SEM-TA precisely generated the force as desired, and its impedance error has been decreased significantly. The real-time torque controller for AJS-RSEA was embedded in the Motion Controller Series model: GoogolThech GT-800. The FHIC parameters in the controller tuned by using the PSO algorithm. The FHI controller with SEM-TA enhances the stability and control performance of the AJS-RSEA. According to the obtained simulation and experimental results, the M_{PSO} controller is robust and produces better results than the S_{PSO} and H_{PSO} controllers in terms of T_s, MO, E_{SS}, and RMSEs. The RMS-PE of $FHIC - M_{PSO}$ improvement percentages is 14.08% and 14.85% better than HIC_{PSO} and PD, respectively. On the other hand, The RMS-FE of $FHIC - M_{PSO}$ improvement percentages is 20.48% and 27.95% better than HIC_{PSO} and PD, respectively. The proposed controller responds to a sinusoidal signal and square signal with an error of less than 2% and 5%. The SEM-TA and its control methods proposed in this paper can provide a good solution for actuation approaches in human-robot interaction applications. Based on selecting one of the H_{PSO}, the

M_{PSO}, and the S_{PSO}, the force's maximum rate can vary between 0.9727 N/s and 1.6443 N/s for this actuator structure. Since the control method does not require any physical properties of the human body, the design of controllers do not necessarily need to be customized for every individual. It allows precise force (or torque) mode control. The design of higher-level controls for human-robot interaction can be achieved easily by using this control method.

REFERENCES

[1] Richard Dorf C., Bishop R.H., Modern Control Systems, 12th ed, Pearson, 1998.

[2] Winter David A., *Biomechanics and motor control of human gait: normal, 2nd ed, elderly and pathological*, 1991.

[3] Korn G.A., *Interactive Dynamic-System Simulation*. Crc Press, 1998.

[4] Williamson Matthew M., Series elastic actuators, MIT library, 1524, 1-83, 1995.

[5] Robinson David W., Jerry E. Pratt, Daniel J. Paluska, and Gill A. Pratt, Series elastic actuator development for a biomimetic walking robot, *Advanced Intelligent Mechatronics Conference, IEEE*, 561-568, 1999.

[6] Cummings J.P., Ruiken D., Wilkinson, E.L., Lanighan, M.W., Grupen, R.A. and Sup, F.C., A compact, modular series elastic actuator. *Journal of Mechanisms and Robotics*, 2016, *8*(4).

[7] Kong K., Bae J. and Tomizuka M., A compact rotary series elastic actuator for human assistive systems. *IEEE/ASME transactions on mechatronics*, 2011, 17(2), 288-297.

[8] Oh S., Kong K., High-precision robust force control of a series elastic actuator. *IEEE/ASME Transactions on mechatronics*, 2016, 22(1), 71-80.

[9] dos Santos W.M., Caurin G.A. and Siqueira A.A., Design and control of an active knee orthosis driven by a rotary series elastic actuator. *Control Engineering Practice*, 2017, *58*, 307-318.

[10] Krafes S., Chalh Z., Saka A., A Review on the Control of Second Order Underactuated Mechanical Systems, *Complexity*, Sep 2018.

[11] Sensinger J.W. and Weir R.F., Design and analysis of a non-backdrivable series elastic actuator, 9th International Conference on Rehabilitation Robotics (ICORR), *IEEE*, 390-393, 2005.

[12] Chen X. Yu R., Huang K., Zhen S., Sun H., Shao K., Linear Motor Driven Double Inverted Pendulum: A Novel Mechanical Design as a Testbed for Control Algorithms, *Simulation Modelling Practice and Theory*, 2018, 81, 31-50.

[13] Winter D., The Biomechanics and Motor Control of Human Gait: Normal, Elderly and Pathological, 2nd ed. Waterloo, ON: Univ. Waterloo Press, 1991.

[14] Naghmehm B., Hooshiar A., Masoudrazban J., chun-Yi Su., Stabilization of Double Inverted Pendulum On Cart: LQR Approach, *International Journal of Mechanical and Production Engineering,* 2017*, 4*(10), 84-89 2.

[15] Matteo Laffranchi, Adaptive Modular Architectures for Rich Motor Skills, AMARSi project Marh 2011.

[16] Eltohamy K.G., Kuo C.Y., Nonlinear Optimal Control of a Triple Link Inverted Pendulum with Single Control Input, *International Journal of Control*, 1998, 69(2), 239-56.

[17] Pratt J., Krupp B., and Chris Morse, Series elastic actuators for high fidelity force control, *Ind. Robot. Int. J.*, 29, 234–241, 2002.

[18] Sehgal S., Tiwari S., LQR Control for Stabilizing Triple Link Inverted Pendulum System, *International Conference on Power*, *Control and Embedded Systems*, *IEEE,* 1-5, 17 Dec 2012.

[19] Šetka V., Čečil R., Schlegel M., Triple Inverted Pendulum System Implementation Using a New ARM/FPGA Control Platform, *18th International Carpathian Control Conference (ICCC), IEEE*, 321-326, 28 May 2017.

[20] Santos D., Wilian M., Caurin G. A., and Siqueira A. A., Design and control of an active knee orthosis driven by a rotary series elastic actuator, *Control Eng. Prac.*, 58, 307–318, 2017.

[21] Franco E., Astolfi A., Baena FR y., Robust Balancing Control of Flexible Inverted-Pendulum Systems, *Mechanism and Machine Theory*, 2018, 130, 539-51.

[22] Gandhi P.S., Borja P., Ortega R., Energy Shaping Control of an Inverted Flexible Pendulum Fixed to a Cart, *Control Engineering Practice*, 2016, 56, 27-36.

[23] Lagoda C., Design of an electric series elastic actuated joint for robotic gait rehabilitation training, in *Proc. 3rd IEEE RAS EMBS Int. Conf. Biomed. Robot. Biomechatronics*, 2010, 21–26.

[24] Saranlı U., Arslan Ö., Ankaralı MM, Morgül Ö., Approximate Analytic Solutions To Non-Symmetric Stance Trajectories of the Passive Spring-Loaded Inverted Pendulum With Damping, *Nonlinear Dynamics*, 2010, 62(4), 729-42.

[25] Blickhan R., The Spring-Mass Model for Running and Hopping, *Journal of biomechanics*,1989, 22(11-12), 1217-27.

[26] Luo Q., Chevallereau C., Aoustin Y., Walking Stability of a Variable Length Inverted Pendulum Controlled with Virtual Constraints, *International Journal of Humanoid Robotics*, 2019, 1950040.

[27] Carpino G., A novel compact torsional spring for series elastic actuators for assistive wearable robots, *J. Mech. Des.*, vol. 134.12, 2012, Art, 121002.

[28] Lee C., Generalization of Series elastic actuator configurations and dynamic behavior comparison, Actuators, vol. 6.3, p. 26, 2017.

[29] Xing L., Chen Y., Wu X., A Novel Parallel-Type Double Inverted Pendulum Control Method, *International Conference on Intelligent Computing and Intelligent Systems*, *IEEE*, Vol. 1, 880-887, 29 Oct 2010.

[30] Riener R., M. Rabuffetti, and C. Frigo, Joint powers in stair climbing at different slopes, in Proc. 1st Joint BMES/EMBS Conf., 1999, 1, 530.

[31] Deng M., Inoue A., Henmi T., Ueki N., Analysis and Experiment on Simultaneous Swing‐Up of a Parallel Cart Type Double Inverted Pendulum, *Asian Journal of Control*, 2008, **10**(1), 121-8.

[32] https://www.mathworks.com/products/connections/product_detail/feedback-instruments-digital-pendulum.html (Last Visited: 06. December.2020).

[33] Akhtaruzzaman M., Shafie A.A., Modeling and Control of a Rotary Inverted Pendulum Using Various Methods, Comparative Assessment and Result Analysis, *International Conference on Mechatronics and Automation*, *IEEE,* 1342-1347, 4 aug 2010.

[34] Dwivedi P., Pandey S., Junghare A. S., Stabilization of Unstable Equilibrium Point of Rotary Inverted Pendulum Using Fractional Controller, *Journal of the Franklin Institute*, 2017, 354(17), 7732-7766.

[35] Ramírez-Neria M., Sira-Ramírez H., Garrido-Moctezuma R., Luviano-Juarez A., Linear Active Disturbance Rejection Control of Underactuated Systems: The Case of the Furuta Pendulum, *ISA transactions*, 2014, 53(4), 920-8.

[36] https://www.quanser.com/products/rotary-inverted-pendulum/ (Last Visited: 06 Dec 2020).

[37] Ruderman M. and Bertram T., 2012. Modeling and observation of hysteresis lost motion in elastic robot joints. *IFAC Proceedings Volumes*, *45*(22), 13-18.

[38] Awtar S., King N., Allen T., Bang I., Hagan M., Skidmore D., Craig K., Inverted Pendulum Systems: Rotary and Arm-Driven-a Mechatronic System Design Case Study, *Mechatronics*, 2002, 12(2), 357-70.

[39] Jadlovska S., Sarnovsky J., Modelling of Classical and Rotary Inverted Pendulum Systems a Generalized Approach, *Journal of Electrical Engineering*, 2013, 64(1), 12–19.

[40] https://www.quanser.com/products/rotary-double-inverted-pendulum/ (Last Visited: 06 Dec 2020).

[41] Ruderman M., Aranovskii S.V., Bobtsov A.A. and Bertram T., 2012. Nonlinear dynamics of drives with elasticities and friction. *Automation and Remote Control*, *73*(10), 1604-1615.

[42] Alex S. Shafer and Mehrdad R. Kermani, Development of High Performance Intrinsically Safe 3-DOF Robot, *International Conference on Robotics & Automation (ICRA), IEEE, 2014*.

[43] https://www.quanser.com/blog/common-and-not-so-common-pendulum-configurations/attachment/pendubot/ (Last Visited: 06. December.2020).

[44] http://coecsl.ece.illinois.edu/pages/pendubot.html (Last Visited: 06. December.2020).

[45] Tedrake R., Underactuated Robotics: Learning, Planning, And Control for Efficient and Agile Machines Course Notes for MIT 6.832, *Working Draft Edition*, 3, 2009.

[46] Spong M.W., The Swing Up Control Problem for The Acrobot, *IEEE Control Systems Magazine*, 1995, 15(1), 49-55.

[47] Bortoff S.A., Spong M.W., Pseudolinearization of the Acrobot Using Spline Functions, *Proceedings of the 31st Conference on Decision and Control*, *IEEE,* 593-598, 16 Dec1992.

[48] Peyman Yadmellat., Design and Development of a Safe Robot Manipulator Using a New Actuation Concept, *International Conference on Robotics and Automation (ICRA) Karlsruhe, IEEE, May 6-10, 2013*.

[49] Montoya O.D., Gil-González W., Nonlinear Analysis and Control of a Reaction Wheel Pendulum: Lyapunov-Based Approach, *International Journal of Engineering Science and Technology*, 2020, 23(1), 21-9.

[50] Krishna B., Chandran D., George VI., Thirunavukkarasu I., Modeling and Performance Comparison of Triple PID and LQR Controllers for Parallel Rotary Double Inverted Pendulum, *Int. J. Emerg. Trends Electr. Electron*, 2015, 11(2), 145-50.

[51] Hamza M.F., Yap H.J., Choudhury I.A., Isa A.I., Zimit A.Y., Kumbasar T., Current Development on Using Rotary Inverted Pendulum as a Benchmark for Testing Linear and Nonlinear Control Algorithms, *Mechanical Systems and Signal Processing*, 2019, 116, 347-69.

[52] https://jglobal.jst.go.jp/detail?JGLOBAL_ID=201402212594922165 (Last Visited: 06 Dec 2020) .

[53] Horvath R., Flowers G.T., and Overfelt, R.A., Stability Investigation of a Two-Link 3DOF Rotational Pendulum, *International Design Engineering Technical Conferences and Computers and Information in Engineering Conference*, vol.37033, 903-912, 1 Jan 2003.

[54] David J. Braun, Matthew Howard., Exploiting Variable Stiffness in Explosive Movement Tasks, *Robotics Science and systems (R:SS 2011) USA*.

[55] Gianluca Palli., Design of a Variable Stiffness Actuator Based on Flexures, *DEIS – DIEM – Universita ` di Bologna, Viale Risorgimento 2,40136 Bologna, Italy - Journal of Mechanisms and Robotics AUGUST 2011*.

[56] https://www.solutions4u-asia.com/PDT/GT/LAB/R-PlanarInvPen.html (Last Visited: 06 Dec 2020)

[57] Gupta N., Dewan L., Modeling and Simulation of Rotary-Rotary Planer Inverted Pendulum, *Journal of Physics, Conference Series*, Vol. 1240.1, 012089, Jul 2019.

[58] Nawawi S.W., Ahmad M.N., Osman J.H., Real-Time Control Of A Two-Wheeled Inverted Pendulum Mobile Robot, *World Academy of Science, Engineering and Technology*, 39,214-20, May 2008.

[59] Jeong S., Takahashi T., Wheeled Inverted Pendulum Type Assistant Robot: Design Concept and Mobile Control, *Intelligent Service Robotics*, 2008,**1**(4), 313-20.

[60] Chowdhary P., Gupta V., Gupta D., Jadhav A., Mishra V., Design of Two Wheel Self Balancing Robot Using PID Controller, *International Journal of Engineering Research & Technology (IJERT)*, volume 5, issue 01, 2017.

[61] Jonathan P., Cumming S., A Compact, Modular Series Elastic Actuator, *Journal of Mechanisms and Robotics, AUGUST 2016*.

[62] Jin S., Ou Y., A Wheeled Inverted Pendulum Learning Stable and Accurate Control from Demonstrations, *Applied Sciences*, 2019, 9(24), 5279.

[63] Zhang C., Hu H., Gu D., Wang J., Cascaded Control for Balancing an Inverted Pendulum on a Flying Quadrotor, *Robotica*, 2017, 35(6), 1263-79.

[64] Hehn M., D'Andrea R., A flying inverted pendulum, *International Conference on Robotics and Automation*, *IEEE*, 763-770, 9 May 2011.

[65] Spong M.W., Block D.J., The Pendubot: A Mechatronic System for Control Research and Education, *34th Conference on Decision and Control*, *IEEE*, Vol. 1, 555-556, 13 Dec 1995.

[66] Wang L.X., Stable Adaptive Fuzzy Controllers with Application to Inverted Pendulum Tracking, *IEEE Transactions on Systems, Man, and Cybernetics, Part B (Cybernetics)*, 1996, **26**(5), 677-91.9.

[67] Cheng F., Zhong G., Li Y., Xu Z., Fuzzy Control of a Double-Inverted Pendulum, *Fuzzy Sets and Systems*, 1996, **79**(3), 315-21.

[68] Aracil J., Gordillo F., Acosta J.A., Stabilization of Oscillations in The Inverted Pendulum, *IFAC Proceedings Volumes*, 2002, **35**(1),79-84.

[69] Guus V., Initialization of the Series Elastic Actuators of TUlip Predoctoral Assignment June 2011 Report nr. 011CE2011 Control Engineering EE-Math-CS University of Twente.

[70] Kizir S., Bingül Z., Oysu C., Fuzzy Control of a Real Time Inverted Pendulum System, *Journal of Intelligent and Fuzzy Systems*, 2010, 21(1, 2), 121-33.

[71] Zhang J.L., Zhang W., LQR Self-Adjusting Based Control for the Planar Double Inverted Pendulum, *Physics Procedia*, 2012, 24,1669-76.

[72] Li B., Rotational Double Inverted Pendulum, *Doctoral dissertation, University of Dayton*, 2013.

[73] Furuta K., Yamakita M., Kobayashi S., Swing-Up Control of Inverted Pendulum Using Pseudo-State Feedback, *Proceedings of the Institution of Mechanical Engineers, Part I: Journal of Systems and Control Engineering*, 1992, 206(4), 263-9.

[74] Yamakita M., Nonaka K., Furuta K., Swing Up Control of a Double Pendulum, *American Control Conference, IEEE*, 2229-2233, 2 Jun 1993.

[75] Yamakita M Iwashiro M. Sugahara Y., Furuta K., Robust Swing Up Control of Double Pendulum, *Proceedings of American Control Conference (ACC*), *IEEE*, vol.1, 290-295, 21 Jun 1995.

[76] Yasunobu S., Mori M., Swing Up Fuzzy Controller for Inverted Pendulum Based on a Human Control Strategy, *Proceedings of International Fuzzy Systems Conference*, *IEEE*, vol.3, 1621-1625, 5 Jul 1997.

[77] Åström K.J., Furuta K., Swinging Up a Pendulum by Energy Control, *Automatica*, 2000, 36(2), 287-95.

[78] Åström K.J., Furuta, K., Swinging Up a Pendulum by Energy Control, *IFAC Proceedings Volumes*, 1996, 29(1), 1919-1924.

[79] Rubı J., Rubio A., Avello A., Swing-Up Control Problem for a Self-Erecting Double Inverted Pendulum, *IEE Proceedings-Control Theory and Applications*, 2002, 149(2), 169-75.

[80] Graichen K., Treuer M., Zeitz M., Swing-Up of the Double Pendulum on a Cart by Feedforward and Feedback Control with Experimental Validation, *Automatica*, 2007, 43(1), 63-71.

[81] Jaiwat P., Ohtsuka T., Real-Time Swing-Up of Double Inverted Pendulum by Nonlinear Model Predictive Control, *International Symposium on Advanced Control of Industrial Processes*, 290-295, 28 May 2014.

[82] Agarwal P. and Deshpande A.D., Series elastic actuators for small-scale robotic applications, Journal of Mechanisms and Robotics, 2017, 9(3), 031016.

[83] A. Calanca, L. Capisani, and P. Fiorini, Robust Force Control of Series Elastic Actuators, Actuators, Spec. Issue Soft Actuators, vol. 3.3, 182-204, 2014.

[84] Chang C.Y., Adaptive Fuzzy Controller of the Overhead Cranes with Nonlinear Disturbance, *IEEE Transactions on Industrial Informatics*, 2007, **3**(2),164-72.

[85] Solihin M.I., Wahyudi, Legowo A., Fuzzy-tuned PID Anti-swing Control of Automatic Gantry Crane, *Journal of Vibration and Control,* 2010, **16**(1),127-45.

[86] Zhang Z., Wu Y., Huang J., Differential-Flatness-Based Finite-Time Anti-Swing Control of Underactuated Crane Systems, *Nonlinear Dynamics*, 2017, **87**(3), 1749-61.

[87] Küçük S., Bingül Z., Inverse Kinematics Solutions for Industrial Robot Manipulators with Offset Wrists, *Applied Mathematical Modelling*, **38**(7-8), 1983-99.

[88] Küçük S., Bingül Z., Robot Kinematics: Forward and Inverse Kinematics, *INTECH Open Access Publisher*,1 Dec 2006.

[89] Bingül Z., Küçük S., Robot Dinamiği ve Kontrolü. *Birsen Yayınevi*, 2008.

[90] Vallery H., Veneman J., Van E. H. F., Asseldonk R. Ekkelenkamp, M. Buss, and H. van Der Kooij, Compliant actuation of rehabilitation robots, IEEE Robot. Autom. Mag., vol. 15.3, 60-69, Sep. 2008.

[91] Furuta K., Yamakita M., Kobayashi S., Nishimura M., A New Inverted Pendulum Apparatus for Education, *Advances in Control Education*, 1992, 133-138, Pergamon.

[92] Hazem Z.B., Fotuhi M.J., Bingül Z., A Comparative Study of the Joint Neuro-Fuzzy Friction Models for a Triple Link Rotary Inverted Pendulum, *IEEE Access*, 2020, **8**, 49066-78.

[93] Park D., Chwa D., Hong S.K., An Estimation and Compensation of the Friction in an Inverted Pendulum, *SICE-ICASE International Joint Conference, IEEE*, 779-783, 18 Oct 2006.

[94] Calanca A., Muradore R., and Fiorini P., A Review of Algorithms for Compliant Control of Stiff and Fixed Compliance Robots. Accepted to IEEE Transaction on Mechatronics, 2015.

[95] Gäfvert M., Svensson J., Astrom K.J., Friction and Friction Compensation in the Furuta Pendulum, *European Control Conference (ECC)*, 3154-3159, *IEEE*, Aug1999.

[96] Hazem Z.B., Fotuhi M.J., Bingül Z., A Comparative Study of the Friction Models with Adaptive Coefficients for a Rotary Triple Inverted Pendulum,

6th International Conference on Control Engineering and Information Technology (CEIT), *IEEE*, 1-6, 25 Oct 2018.

[97] Dupont P.E., Friction Modeling in Dynamic Robot Simulation, *Proceedings, International Conference on Robotics and Automation*, *IEEE*, 1370-1376, 13 May 1990.

[98] Acosta J.A., Furuta's Pendulum: A Conservative Nonlinear Model for Theory and Practice, *Mathematical Problems in Engineering*, Mar 2010.

[99] Fotuhi M.J., Hazem Z.B., Bingül Z., Comparison of Joint Friction Estimation Models for Laboratory 2 DOF Double Dual Twin Rotor Aero-Dynamical System, *Conference of the Industrial Electronics Society* (*IECON)*, *IEEE*, 2231-2236, 21 Oct 2018.

[100] Hu C., Wan F., Parameter Identification of a Model with Coulomb Friction for a Real Inverted Pendulum System, *Chinese Control and Decision Conference*, 2869-2874, 17 Jun 2009.

[101] Guida D., Nilvetti F., Pappalardo C.M., Dry Friction Influence on Inverted Pendulum Control, *Proceedings of the International Conference on Applied Mathematics, Simulation, Modelling, Vouliagmeni Beach*, 29-31, Athens, Greece, 29 Dec 2009.

[102] Hu C., Wan F., Parameter Identification of a Model with Coulomb Friction for a Real Inverted Pendulum System, *Chinese Control and Decision Conference*, *IEEE*, 2869-2874, 17 Jun 2009.

[103] Bittencourt A.C., Wernholt E., Sander-Tavallaey S., Brogårdh T., An Extended Friction Model to Capture Load and Temperature Effects in Robot Joints, *International Conference on Intelligent Robots and Systems (RSJ)*, *IEEE*, 6161-6167, 18 Oct 2010.

[104] Ding L., Li X., Li Q., Chao Y., Nonlinear Friction and Dynamical Identification for a Robot Manipulator with Improved Cuckoo Search Algorithm, *Journal of Robotics*, 2018.

[105] Dupont P.E., The Effect of Friction on the Forward Dynamics Problem, *International Journal of Robotics Research*, 1993, 12(2), 164-79.

[106] Al-Bender F., Symens W., Characterization of frictional hysteresis in ball-bearing guideways, *Wear*, 2005, 258(11-12),1630-42.

[107] Lampaert V., Swevers J., Al-Bender F., Experimental Comparison of Different Friction Models for Accurate Low-Velocity Tracking, *Proceedings of the Mediterranean Conference on Control and Automation (MED'02)*, 9 Jul 2002.

[108] Fotuhi M.J., Hazem Z.B., Bingül Z., Adaptive Joint Friction Estimation Model for Laboratory 2 DOF Double Dual Twin Rotor Aerodynamical

Helicopter System, *International Conference on Control Engineering and Information Technology (CEIT)*, *IEEE*, 1-6, 25 Oct 2018.

[109] Al-Sumait J.S., Al-Othman A.K., Sykulski J.K., Application of Pattern Search Method to Power System Valve-Point Economic Load Dispatch, *International Journal of Electrical Power and Energy Systems*, 2007, 29(10), 720-30.

[110] Yu H., Xie T., Paszczynski S., Wilamowski B.M., Advantages of Radial Basis Function Networks for Dynamic System Design, *IEEE Transactions on Industrial Electronics*, 2011, 58(12), 5438-50.

[111] Zemouri R., Racoceanu D., Zerhouni N., Recurrent Radial Basis Function Network for Time-Series Prediction, *Engineering Applications of Artificial Intelligence*, 2003, 16(5-6), 453-63.

[112] Gençay R., Qi M., Pricing and Hedging Derivative Securities with Neural Networks: Bayesian Regularization, Early Stopping, and Bagging, *IEEE Transactions on Neural Networks*, 2001, 12(4), 726-34.

[113] Ekekwe N., Etienne-Cummings R., Kazanzides P., Incremental Encoder Based Position and Velocity Measurements VLSI Chip with Serial Peripheral Interface, *International Symposium on Circuits and Systems*, *IEEE*, 3558-3561, 2007.

[114] Baumann W., Rugh W., Feedback Control of Nonlinear Systems by Extended Linearization, *IEEE Transactions on Automatic Control*, 1986, 31(1), 40-6.

[115] El-Hawwary M.I., Elshafei A.L., Emara H.M., Fattah H.A., Adaptive Fuzzy Control of the Inverted Pendulum Problem, *IEEE Transactions on Control Systems Technology*, 2006, 14(6), 1135-44.

[116] Prasad L.B., Tyagi B., Gupta H.O., Optimal Control of Nonlinear Inverted Pendulum System Using PID Controller and LQR: Performance Analysis Without and with Disturbance Input, *International Journal of Automation and Computing*, 2014, 11(6), 661-70.

[117] Yi J., Yubazaki N., Hirota K., Upswing and Stabilization Control of Inverted Pendulum System Based on the Sirms Dynamically Connected Fuzzy Inference Model, *Fuzzy Sets and Systems*, 2001, 122(1), 139-52.

[118] Tao C.W., Taur J.S., Hsieh T.W., Tsai C.L., Design of A Fuzzy Controller with Fuzzy Swing-Up and Parallel Distributed Pole Assignment Schemes for an Inverted Pendulum and Cart System, *IEEE Transactions on Control Systems Technology*, 2008, 16(6), 1277-88.

[119] Tao C.W., Taur J.S., Chen Y.C., Design of a Parallel Distributed Fuzzy LQR Controller for the Twin Rotor Multi-Input Multi-Output System, *Fuzzy Sets and Systems*, 2010, 161(15), 2081-103.

[120] Adeli M., Zarabadipour H., Zarabadi S.H., Shoorehdeli M.A., Anti-swing Control for a Double-Pendulum-Type Overhead Crane Via Parallel Distributed Fuzzy LQR Controller Combined with Genetic Fuzzy Rule Set Selection, *International Conference on Control System*, *Computing and Engineering*, *IEEE*, 306-311, 25 Nov 2011.

[121] Tsagarakis N.G., Laffranchi M., Vanderborght B. and Caldwell D.G., A compact soft actuator unit for small scale human friendly robots, International conference on robotics and automation, *IEEE*, 4356-4362, 23 May 2009.

[122] Harifi S., Khalilian M., Mohammadzadeh J., Ebrahimnejad S., Optimizing A Neuro-Fuzzy System Based on Nature Inspired Emperor Penguins Colony Optimization Algorithm, *IEEE Transactions on Fuzzy Systems*, 2 Apr 2020.

[123] Precup R.E., Filip H.I., Rădac M.B., Petriu E.M., Preitl S., Dragoş C.A., Online Identification of Evolving Takagi–Sugeno–Kang Fuzzy Models for Crane Systems, *Applied Soft Computing*, 2014, 24, 1155-63.

[124] Baojiang Z., Shiyong L., Ant Colony Optimization Algorithm and Its Application to Neuro-Fuzzy Controller Design, *Journal of Systems Engineering and Electronics*, 2007, 18(3), 603-10.

[125] Vallery H., Veneman J., E. H. F. van Asseldonk, R. Ekkelenkamp, M. Buss, and H. van Der Kooij, Compliant actuation of rehabilitation robots, IEEE Robot. Autom. Mag., vol. 15,3, 60-69, Sep. 2008.

[133] https://www.mdsmotor.com/?lang=en&content=default (Last Visited: 06 Dec 2020).

[134] https://www.lenze.com/en-tr/products/inverters/control-cabinet-installation/8400-topline-frequency-inverters/ (Last Visited: 06 Dec 2020).

[135] https://www.fenac.com.tr/img/pdf/fnc-sc2048-series-pdf-61092.pdf (Last Visited: 06 Dec 2020).

[136] Manglik V.K., *Elements of Mechanical Engineering*, PHI Learning Pvt. Ltd 2013.

[137] Faulhaber F., A second look at Gearbox efficiencies. *Machine design*, *74*(12), 82-83, 2002.

[138] Hori K., Toshiba Corp, *Differential planet gear unit*. U.S. Patent 4,942,781, 1990.

[139] Wang A. and Kim S., Directional efficiency in geared transmissions: Characterization of backdrivability towards improved proprioceptive control. In *2015 IEEE International Conference on Robotics and Automation (ICRA)* (1055-1062). IEEE, 2015.

[140] https://www.dspace.com/en/pub/home/support/pli/elas/elashw/elads1103.cfm Last Visited: 06 Dec 2020).

[141] https://media.futek.com/content/futek/files/pdf/productdrawings/trs600.pdf (Last Visited: 08 Dec 2020).

APPENDIX

Appendix-A

The VC++ .CPP codes used to calculate the control models of the RSEA is given in this section. Only the variables of each model must take into consideration for the codes.

```
// SEA_mv2Dlg.cpp : implementation file

#include "stdafx.h"

#include "SEA_mv2.h"

#include "SEA_mv2Dlg.h"

#include "gts.h"

#include "math.h"

#include "stdio.h"

#include "stdlib.h"


#ifdef _DEBUG

#define new DEBUG_NEW

#undef THIS_FILE

static char THIS_FILE[] = __FILE__;

#endif


#define TIME_OP  0.016

#define M_PI     3.14159265358979323846264338327 95

#define PI       3.1412

#define SIN_GAIN 100

#define EN_RAD   0.0007669903939428206
```

```
#define EN_DEG   0.043945312500000

#define EN_PPR   8192

#define GR_CON   60.033

#define TRQ_COF  1.150


#define Xr1  110

#define Xr2  630

#define Yr1  10

#define Yr2  280

#define Yr3  Yr1+((Yr2/3)/2)

#define Yr4  Yr1+(Yr2/6)*3

#define Yr5  Yr1+(Yr2/6)*5



FILE *fp;


int radio_b=1,cntrl=0;

int
graf_x=0,graf_y=0,graf_y_eski=0,graf_y2=0,graf_y2_eski,graf_y3=0,graf_y3_eski=0,graf_y4=0,graf
_y4_eski=0;

double
Enc_1_ACT=0,Enc_1_old=0,Enc_2_old=0,EncVel_1_old=0,EncVel_2_old=0,EncVel_1_old_old=0,
EncVel_2_old_old=0,EncVel_1=0,EncVel_2=0,TorkVel=0,Tork_old=0,CurentVel=0,Curent_old=0;

int timr_clk=0,timr_const=0,run_system=0;
```

```
double
sl1=0,sl2=0,sin_d=0,enc1_org=0,enc2_org=0,EncAcc_1=0,EncAcc_2=0,pos1_ofs=0,pos1_cal=0,out_
pwm=50,sin_pls=0;

double
encs_er=0,encs_int=0,encs_drv=0,pid_p=0,pid_i=0,pid_d=0,enc1_er=0,enc1_int=0,enc1_drv=0,enc2
_er=0,enc2_int=0,enc2_drv=0,setp1=0,setp2=0;

double
enc_org_v1=0,enc_org_v2=0,enc1v_er=0,enc1v_int=0,EncAcc_1_old_old=0,EncAcc_1_old=0,lod_tr
q_er=0,lod_trq_int=0,sin_gain=100,lod_imp_er=0,lod_imp_int=0;


float
FHIC_OUT=0,FHIC_Xr=0,FHIC_Xr_d=0,FHIC_Xr_dd=0,FHIC_X=0,FHIC_X_d=0,FHIC_X_dd=0,
FHIC_alfa=1,FHIC_beta=1,FHIC_gama=1,FHIC_zeta=1,FHIC_SEL=1,FHIC_Jtot=1,FHIC_Btot=1,F
HIC_Ks=0,FHIC_Kp=0,FHIC_Kv=0,FHIC_fr=0,FHIC_fe=0,ic_stpnt_vel_old=0,ic_stpnt_old=0;

float trm1=0,trm2=0,trm3=0,trm4=0;

//@@@@@@@@@@@@@@@@@@@@@@@@@@@@@@@@@@@@@Functions

double saturate(double in_sgnl,double min_lim,double max_lim);

double pid_con(double p,double i,double d,double p_gain,double i_gain,double d_gain);

int sgn_z(int say);

int sgn_wz(int sgn_num);

double out_to_pwm(double out_data);


//**********************color for graf

static DWORD dwColor[9]={RGB(0,0,0),        //black
                         RGB(255,0,0),      //red
                         RGB(0,255,0),      //green
                         RGB(0,0,255),      //blue
```

```
                RGB(255,255,0),     //yellow
                RGB(255,0,255),     //magenta
                RGB(0,255,255),     //cyan
                RGB(127,127,127),   //gray
                RGB(255,255,255)     //white
};
                  CPen pen_blk(PS_SOLID,2,dwColor[0]);
                  CPen pen_red(PS_SOLID,2,dwColor[1]);
                  CPen pen_grn(PS_SOLID,2,dwColor[2]);
                  CPen pen_blu(PS_SOLID,2,dwColor[3]);
                  CPen pen_ylw(PS_SOLID,2,dwColor[4]);
                  CPen pen_mgt(PS_SOLID,2,dwColor[5]);
                  CPen pen_cyn(PS_SOLID,2,dwColor[6]);
                  CPen pen_gry(PS_SOLID,2,dwColor[7]);
                  CPen pen_wit(PS_SOLID,2,dwColor[8]);

//////////////////////////////////////////////////////////////////////////////

// CAboutDlg dialog used for App About


class CAboutDlg : public CDialog

{

public:

        CAboutDlg();
```

```
// Dialog Data
        //{{AFX_DATA(CAboutDlg)
        enum { IDD = IDD_ABOUTBOX };
        //}}AFX_DATA

        // ClassWizard generated virtual function overrides
        //{{AFX_VIRTUAL(CAboutDlg)
        protected:
        virtual void DoDataExchange(CDataExchange* pDX);    // DDX/DDV support
        //}}AFX_VIRTUAL

// Implementation
protected:
        //{{AFX_MSG(CAboutDlg)
        //}}AFX_MSG
        DECLARE_MESSAGE_MAP()
};

CAboutDlg::CAboutDlg() : CDialog(CAboutDlg::IDD)
{
        //{{AFX_DATA_INIT(CAboutDlg)
        //}}AFX_DATA_INIT
}
```

```
void CAboutDlg::DoDataExchange(CDataExchange* pDX)
{
	CDialog::DoDataExchange(pDX);
	//{{AFX_DATA_MAP(CAboutDlg)
	//}}AFX_DATA_MAP
}

BEGIN_MESSAGE_MAP(CAboutDlg, CDialog)
	//{{AFX_MSG_MAP(CAboutDlg)
		// No message handlers
	//}}AFX_MSG_MAP
END_MESSAGE_MAP()

/////////////////////////////////////////////////////////////////////////////
// CSEA_mv2Dlg dialog

CSEA_mv2Dlg::CSEA_mv2Dlg(CWnd* pParent /*=NULL*/)
	: CDialog(CSEA_mv2Dlg::IDD, pParent)
{
	//{{AFX_DATA_INIT(CSEA_mv2Dlg)
	ch_imp = TRUE;//FALSE;
	ch_trq = TRUE;
	ch_spd = TRUE;
	m_ic_stpnt = 0.0;
```

m_ic_d = 0.251;

m_ic_i = 0.0;

m_ic_p = 2.175;

m_l_motr = 0.0;

m_lod_angl = 0.0;

m_lod_en = 0.0;

m_lod_impdnc = 0.0;

m_lod_trq = 0.0;

m_lod_vlcty = 0.0;

m_motr_en = 0.0;

m_motr_pwm = 0.0;

m_r_motr = 0.0;

m_tc_p =0.5;//0.1234;//alfa

m_tc_i = 0.5;//0.3834;//beta

m_tc_d = 0.5;//0.7644;//gama

m_sc_p = 0.5;//0.5079;//zeta

m_sc_i = 0.5;//0.9157;//sel

m_sc_d = 0;

m_sc_stpnt = 0;

m_sprng_en = 0.0;

m_tc_stpnt = 1.0;

m_cs_out = 0.0;

m_sl_pwm = 0;

```
	m_pwm_frq = 1.0;
	m_pc_lstpnt = 0.0;
	m_pc_mstpnt = 0.0;
	m_sl_amp = 0;
	//}}AFX_DATA_INIT
	// Note that LoadIcon does not require a subsequent DestroyIcon in Win32
	m_hIcon = AfxGetApp()->LoadIcon(IDR_MAINFRAME);
}

void CSEA_mv2Dlg::DoDataExchange(CDataExchange* pDX)
{
	CDialog::DoDataExchange(pDX);
	//{{AFX_DATA_MAP(CSEA_mv2Dlg)
	DDX_Check(pDX, IDC_CHECK_IMP, ch_imp);
	DDX_Check(pDX, IDC_CHECK_TRQ, ch_trq);
	DDX_Check(pDX, IDC_CHECK_SPD, ch_spd);
	DDX_Text(pDX, IDC_EDIT_IC_STPNT, m_ic_stpnt);
	DDX_Text(pDX, IDC_EDIT_IC_D, m_ic_d);
	DDX_Text(pDX, IDC_EDIT_IC_I, m_ic_i);
	DDX_Text(pDX, IDC_EDIT_IC_P, m_ic_p);
	DDX_Text(pDX, IDC_EDIT_L_MOTR, m_l_motr);
	DDX_Text(pDX, IDC_EDIT_LOD_ANGL, m_lod_angl);
	DDX_Text(pDX, IDC_EDIT_LOD_EN, m_lod_en);
	DDX_Text(pDX, IDC_EDIT_LOD_IMPDNC, m_lod_impdnc);
```

```
	DDX_Text(pDX, IDC_EDIT_LOD_TRQ, m_lod_trq);
	DDX_Text(pDX, IDC_EDIT_LOD_VLCTY, m_lod_vlcty);
	DDX_Text(pDX, IDC_EDIT_MOTR_EN, m_motr_en);
	DDX_Text(pDX, IDC_EDIT_MOTR_PWM, m_motr_pwm);
	DDX_Text(pDX, IDC_EDIT_R_MOTR, m_r_motr);
	DDX_Text(pDX, IDC_EDIT_SC_D, m_sc_d);
	DDX_Text(pDX, IDC_EDIT_SC_I, m_sc_i);
	DDX_Text(pDX, IDC_EDIT_SC_P, m_sc_p);
	DDX_Text(pDX, IDC_EDIT_SC_STPNT, m_sc_stpnt);
	DDX_Text(pDX, IDC_EDIT_SPRNG_EN, m_sprng_en);
	DDX_Text(pDX, IDC_EDIT_TC_D, m_tc_d);
	DDX_Text(pDX, IDC_EDIT_TC_I, m_tc_i);
	DDX_Text(pDX, IDC_EDIT_TC_P, m_tc_p);
	DDX_Text(pDX, IDC_EDIT_TC_STPNT, m_tc_stpnt);
	DDX_Text(pDX, IDC_EDIT_CS_OUT, m_cs_out);
	DDX_Slider(pDX, IDC_SLIDER1, m_sl_pwm);
	DDX_Text(pDX, IDC_EDIT_PWM_FRQ, m_pwm_frq);
	DDX_Text(pDX, IDC_EDIT_PC_LSTPNT, m_pc_lstpnt);
	DDX_Text(pDX, IDC_EDIT_PC_MSTPNT, m_pc_mstpnt);
	DDX_Slider(pDX, IDC_SLIDER2, m_sl_amp);
	//}}AFX_DATA_MAP
}

BEGIN_MESSAGE_MAP(CSEA_mv2Dlg, CDialog)
```

```
	//{{AFX_MSG_MAP(CSEA_mv2Dlg)
	ON_WM_SYSCOMMAND()
	ON_WM_PAINT()
	ON_WM_QUERYDRAGICON()
	ON_BN_CLICKED(IDC_BUTTON3, On_Impedance)
	ON_BN_CLICKED(IDC_BUTTON4, On_torque)
	ON_BN_CLICKED(IDC_BUTTON5, On_speed)
	ON_COMMAND(ID_EDIT_CONTROLCAPTURE, OnEditControlcapture)
	ON_NOTIFY(NM_CUSTOMDRAW, IDC_SLIDER1, OnCustomdrawSlider1)
	ON_BN_CLICKED(IDC_RADIO_NORMAL, OnRadioNormal)
	ON_BN_CLICKED(IDC_RADIO_SQUARE, OnRadioSquare)
	ON_BN_CLICKED(IDC_RADIO_SINUSOID, OnRadioSinusoid)
	ON_WM_TIMER()
	ON_BN_CLICKED(IDC_BUTTON_RUN_TIMER, OnButtonRunTimer)
	ON_BN_CLICKED(IDC_BUTTON_CNTRL, OnButtonCntrl)
	ON_BN_CLICKED(IDC_BUTTON2, OnStop)
	ON_NOTIFY(NM_CUSTOMDRAW, IDC_SLIDER2, OnCustomdrawSlider2)
	//}}AFX_MSG_MAP
END_MESSAGE_MAP()

/////////////////////////////////////////////////////////////////////////////
// CSEA_mv2Dlg message handlers

BOOL CSEA_mv2Dlg::OnInitDialog()
```

```
{
	CDialog::OnInitDialog();

	// Add "About..." menu item to system menu.

	// IDM_ABOUTBOX must be in the system command range.
	ASSERT((IDM_ABOUTBOX & 0xFFF0) == IDM_ABOUTBOX);
	ASSERT(IDM_ABOUTBOX < 0xF000);

	CMenu* pSysMenu = GetSystemMenu(FALSE);
	if (pSysMenu != NULL)
	{
		CString strAboutMenu;
		strAboutMenu.LoadString(IDS_ABOUTBOX);
		if (!strAboutMenu.IsEmpty())
		{
			pSysMenu->AppendMenu(MF_SEPARATOR);
			pSysMenu->AppendMenu(MF_STRING, IDM_ABOUTBOX,
strAboutMenu);
		}
	}

	// Set the icon for this dialog.  The framework does this automatically
	//  when the application's main window is not a dialog
```

```
	SetIcon(m_hIcon, TRUE);			// Set big icon
	SetIcon(m_hIcon, FALSE);		// Set small icon

	// TODO: Add extra initialization here

	return TRUE;  // return TRUE  unless you set the focus to a control
}

void CSEA_mv2Dlg::OnSysCommand(UINT nID, LPARAM lParam)
{
	if ((nID & 0xFFF0) == IDM_ABOUTBOX)
	{
		CAboutDlg dlgAbout;
		dlgAbout.DoModal();
	}
	else
	{
		CDialog::OnSysCommand(nID, lParam);
	}
}

// If you add a minimize button to your dialog, you will need the code below
//  to draw the icon.  For MFC applications using the document/view model,
//  this is automatically done for you by the framework.
```

```
void CSEA_mv2Dlg::OnPaint()
{
	if (IsIconic())
	{
		CPaintDC dc(this); // device context for painting

		SendMessage(WM_ICONERASEBKGND, (WPARAM) dc.GetSafeHdc(), 0);

		// Center icon in client rectangle
		int cxIcon = GetSystemMetrics(SM_CXICON);
		int cyIcon = GetSystemMetrics(SM_CYICON);
		CRect rect;
		GetClientRect(&rect);
		int x = (rect.Width() - cxIcon + 1) / 2;
		int y = (rect.Height() - cyIcon + 1) / 2;

		// Draw the icon
		dc.DrawIcon(x, y, m_hIcon);
	}
	else
	{
		CDialog::OnPaint();
	}
```

```
}

// The system calls this to obtain the cursor to display while the user drags
//  the minimized window.
HCURSOR CSEA_mv2Dlg::OnQueryDragIcon()
{
	return (HCURSOR) m_hIcon;
}

void CSEA_mv2Dlg::On_Impedance()
{

	if(ch_imp==0) ch_imp=1;
	else ch_imp=0;

	UpdateData(false);
}

void CSEA_mv2Dlg::On_torque()
{
	if(ch_trq==0) ch_trq=1;
	else ch_trq=0;
```

```
        UpdateData(false);

}

void CSEA_mv2Dlg::On_speed()
{
        if(ch_spd==0) ch_spd=1;
        else ch_spd=0;

        UpdateData(false);

}

void CSEA_mv2Dlg::OnEditControlcapture()
{
        graf_x=10;

        CDC *p=GetDC();
        p->Rectangle(Xr1,Yr1,Xr2,Yr2);
        p->MoveTo(Xr1,Yr1+(Yr2/3));
        p->LineTo(Xr2,Yr1+(Yr2/3));
        p->MoveTo(Xr1,Yr1+(Yr2/3)*2);
        p->LineTo(Xr2,Yr1+(Yr2/3)*2);
   p->SelectObject(&pen_gry);
```

```
p->MoveTo(Xr1,Yr3);

p->LineTo(Xr2-10,Yr3);

p->MoveTo(Xr1,Yr4);

p->LineTo(Xr2-10,Yr4);

p->MoveTo(Xr1,Yr5);

p->LineTo(Xr2-10,Yr5);


fp=fopen("c:/RSEA_Data.csv","wt");

fputs("Time",fp); //^^^^^^^^^^^^^^^^1

fputc(',',fp);

fputs("Motor Angle",fp);//^^^^^^^^^^2

fputc(',',fp);

fputs("Motor Velocity",fp);//^^^^^^^3

fputc(',',fp);

fputs("FHIC_X",fp);//^^^^^^^^^^4

fputc(',',fp);

fputs("FHIC_X_d",fp);//^^^^^^^^5

fputc(',',fp);

fputs("FHIC_X_dd",fp);//^^^^^^^^5_2

fputc(',',fp);

fputs("Error Angle",fp);//^^^^^^^^^^6

fputc(',',fp);

fputs("FHIC_Xr",fp);//^^^7

fputc(',',fp);
```

```
fputs("FHIC_Xr_d",fp);//^^^7_2
fputc(',',fp);
fputs("FHIC_Xr_dd",fp);//^^^7_3
fputc(',',fp);
fputs("FHIC_fr",fp);//^^^^^^8
fputc(',',fp);
fputs("FHIC_fe",fp);//^^^^^^^9
fputc(',',fp);
fputs("FHIC_Kp",fp);//^^10
fputc(',',fp);
fputs("FHIC_Kv",fp);//^^11
fputc(',',fp);
fputs("FHIC_alfa",fp);//^^11_2
fputc(',',fp);
fputs("FHIC_beta",fp);//^^11_3
fputc(',',fp);
fputs("FHIC_gama",fp);//^^11_4
fputc(',',fp);
fputs("FHIC_zeta",fp);//^^11_5
fputc(',',fp);
fputs("FHIC_SEL",fp);//^^11_6
fputc(',',fp);
fputs("Speed controller out",fp);//12
fputc(',',fp);
```

```
		fputs("PWM out",fp);//^^^^^^^^^^^^^^13
		fputc(',',fp);
		fputs("Frequncy",fp);//^^^^^^^^^^^^14
		fputc(',',fp);
		fputs("Load torque",fp);//^^^^^^^^^^15
		fputc('\n',fp);

	 //timr_const=timr_clk;
}

void CSEA_mv2Dlg::OnCustomdrawSlider1(NMHDR* pNMHDR, LRESULT* pResult)
{

		UpdateData(true);
  // pos1_ofs=m_smalmotor;
		double tp1=0;
		short pval=0;
		short rtn;
		rtn=GT_Open();

		if(radio_b==1)
		{
			tp1=(m_sl_pwm);
			pval=31767*(tp1/100);
```

```
                GT_SetDac(1,&pval,1);
                m_l_motr=sgn_z(tp1-50)*(tp1-50);
                m_r_motr=sgn_z(50-tp1)*(50-tp1);
                m_motr_pwm=tp1;//100*pow(tp1/10000,sin_gain/10000);
        }
        else if((radio_b==2)||(radio_b==3))
        {
                sl2=sl1;
                sl1=m_sl_pwm;
                m_pwm_frq=m_pwm_frq+((sl1-sl2)/100);
        }

        if(run_system==0)
         m_motr_pwm=50;

   pval=31767*(m_motr_pwm/100);
        GT_SetDac(1,&pval,1);

        UpdateData(false);
        *pResult = 0;
}

void CSEA_mv2Dlg::OnCustomdrawSlider2(NMHDR* pNMHDR, LRESULT* pResult)
{
```

```
            // TODO: Add your control notification handler code here
            UpdateData(true);
    sin_gain=100-m_sl_amp;
    m_pc_mstpnt=sin_gain;
             UpdateData(false);
            *pResult = 0;
}

void CSEA_mv2Dlg::OnRadioNormal()
{ radio_b=1;  UpdateData(false); }

void CSEA_mv2Dlg::OnRadioSquare()
{ radio_b=2;  UpdateData(false); }

void CSEA_mv2Dlg::OnRadioSinusoid()
{ radio_b=3;  UpdateData(false); }

void CSEA_mv2Dlg::OnStop()
{
            UpdateData(true);
            double tp1=0;
            short pval=0;
            short rtn;
            rtn=GT_Open();
```

```
		radio_b=1;
		sin_pls=0;
		run_system=1;
		cntrl=0;
		m_motr_pwm=50;

	pval=31767*(m_motr_pwm/100);
		GT_SetDac(1,&pval,1);

		UpdateData(false);
}

void CSEA_mv2Dlg::OnButtonRunTimer()//*************************Timer *************
{
		SetTimer(1,1,NULL);

		run_system=1;
	short pval=0;
		short rtn;
		rtn=GT_Open();
	rtn=GT_ZeroPos(1);// Restart Encoder1
		rtn=GT_ZeroPos(2);// Restart Encoder2
```

```
		out_pwm=50;
		m_motr_en=0;
		m_lod_en=0;
		m_lod_angl = 0.0;
		m_lod_en = 0.0;
		m_lod_impdnc = 0.0;
		m_lod_trq = 0.0;
		m_lod_vlcty = 0.0;
	pval=31767*(out_pwm/100);
	GT_SetDac(1,&pval,1);
	rtn=GT_Close();
		UpdateData(false);
}
void CSEA_mv2Dlg::OnTimer(UINT nIDEvent)
{
		UpdateData(true);
		double enc_pos=0,enc_vel=0;
//*****GoogolTech Open Port**********
		short SRTN;
		double tp1=0;
		short pval=0;
		unsigned long sclk;
		SRTN=GT_Open();
//*****************************Time******************
```

```
  GT_GetClock(&sclk);
        timr_clk++;
//@@@@@@@@@@@@@@@@@@@@@@@@@@@@ Encoder1
        Enc_1_old=m_motr_en;
        GT_GetEncPos(1,&enc_pos,1);
        enc1_org=enc_pos;
        m_motr_en=(enc1_org/-GR_CON)*EN_DEG;

        EncVel_1_old_old=EncVel_1_old;
        EncVel_1_old=EncVel_1;
        EncVel_1=((m_motr_en-Enc_1_old)/TIME_OP);
        enc_org_v1=EncVel_1;
        EncVel_1=(EncVel_1+EncVel_1_old+EncVel_1_old_old)/3;//Moving avrage filter (3)



        EncAcc_1_old_old=EncAcc_1_old;
        EncAcc_1_old=EncAcc_1;
  EncAcc_1=((EncVel_1-EncVel_1_old)/TIME_OP);
        EncAcc_1=(EncAcc_1+EncAcc_1_old+EncAcc_1_old_old)/3;//Moving avrage filter (3)

//@@@@@@@@@@@@@@@@@@@@@@@@@@@@ Encoder 2
        Enc_2_old=m_lod_en;
        GT_GetEncPos(2,&enc_pos,1);
        enc2_org=enc_pos;
```

```
       m_lod_en=enc2_org*EN_DEG;


       EncVel_2_old_old=EncVel_2_old;

       EncVel_2_old=EncVel_2;

       EncVel_2=((m_lod_en-Enc_2_old)/TIME_OP);

       enc_org_v2=EncVel_2;

       EncVel_2=(EncVel_2+EncVel_2_old+EncVel_2_old_old)/3;//Moving avrage filter (3)

  m_lod_vlcty=EncVel_2;


       EncAcc_2=((EncVel_2-EncVel_2_old)/TIME_OP);

//_-_-_-_-_-_-_-_-_-_-_-_-_-_-_-_-_-_-_-_-_-_-_-_-_-_-_-_-_-_-_-_-_-_-_-_-_-_-_-_-_-_-_-_-_-_-_

  encs_er=m_motr_en-m_lod_en;

       m_sprng_en=encs_er;

       enc1_er=m_pc_mstpnt-m_motr_en;

       enc2_er=m_pc_lstpnt-m_lod_en;


       //m_ic_stpnt=m_lod_en-m_motr_en;//gratity

       m_lod_impdnc=m_lod_en;

       lod_imp_er=m_ic_stpnt-m_lod_impdnc;


       m_lod_trq=encs_er*TRQ_COF;

       lod_trq_er=m_tc_stpnt-m_lod_trq;


       //*****************************************FHIC****************
```

```
        FHIC_Xr=(m_ic_stpnt);
FHIC_Xr_d=((m_ic_stpnt-ic_stpnt_old)/TIME_OP);
        ic_stpnt_old=m_ic_stpnt;

        FHIC_Xr_dd=((FHIC_Xr_d-ic_stpnt_vel_old)/TIME_OP);
        ic_stpnt_vel_old=FHIC_Xr_d;

FHIC_X=m_lod_en;
        FHIC_X_d=EncVel_2;
FHIC_X_dd=EncAcc_2;

        FHIC_alfa=m_tc_p;
        FHIC_beta=m_tc_i;
        FHIC_gama=m_tc_d;
        FHIC_zeta=m_sc_p;

        FHIC_SEL=m_sc_i;
        FHIC_Jtot=1;
        FHIC_Btot=1;
        FHIC_Ks=TRQ_COF;

        FHIC_Kp=m_ic_p;
        FHIC_Kv=m_ic_d;
```

```
        FHIC_fr=m_tc_stpnt;

        FHIC_fe=m_lod_trq*4;

//****************************************** Integral

        encs_int+=(encs_er*TIME_OP);//**Integre encs***


        enc1_int+=(enc1_er*TIME_OP);//**Integre enc1***


        enc2_int+=(enc2_er*TIME_OP);//**Integre enc2***


        lod_trq_int+=(lod_trq_er*TIME_OP);//**Integre load torq***


        lod_imp_int+=(lod_imp_er*TIME_OP);//**Integre load imp***

//@@@@@@@@@@@@@@@@@@@@Radio button

        if(radio_b==1)

        {

         //sin_pls=m_sl_pwm;

        }

        if((radio_b==2)||(radio_b==3))

        {

          sin_pls = sin_gain*(sin((PI*(m_pwm_frq*200))*timr_clk));

          if (radio_b==2) sin_pls=sgn_wz(sin_pls)*(sin_gain-1);//Sqr pulse


//**********************SQR-Sinus Pulse*********************

        if(cntrl==0)
```

```
        {
        if(sin_pls>=0)
        {
        m_l_motr=(sin_pls/2);
        m_r_motr=0;
        m_motr_pwm=50+(sin_pls/2);
        }
        if(sin_pls<0)
        {
        m_l_motr=0;
   m_r_motr=(-sin_pls/2);
        m_motr_pwm=50-(-sin_pls/2);
        }
        }
                }
//*****************************Controller ********************
        if(cntrl==1)
        {
    if((radio_b==2)||(radio_b==3))
                    if (ch_imp==1)
                        m_ic_stpnt=sin_pls;
                    else if(ch_trq==1)
                  m_tc_stpnt=sin_pls;
                    else if(ch_spd==1)
```

```
                    m_sc_stpnt=sin_pls;


    /*if(ch_imp==1)
                {
                if((encs_er>0.1)||(encs_er<-0.1))
                {
m_sc_stpnt=pid_con(-encs_er,encs_int,enc2_drv,10,0,0);
                }

   else if ((encs_er<=0.1)&&(encs_er>=-0.1))
m_sc_stpnt=0;

    }*/
    //***Fractinal Hybrid Impedance Control****
                if(ch_imp==1)// FHIC
     {
 if((FHIC_SEL*FHIC_Xr_dd)<0)
                        trm1=-1*pow((FHIC_SEL*FHIC_Xr_dd)*-1,FHIC_alfa);
 else
                        trm1=pow((FHIC_SEL*FHIC_Xr_dd),FHIC_alfa);


                       if((FHIC_SEL*FHIC_Xr_d-FHIC_X_d)<0)
                trm2=-1*pow((FHIC_SEL*FHIC_Xr_d-FHIC_X_d)*-1,FHIC_beta);
 else
```

```
                trm2=pow((FHIC_SEL*FHIC_Xr_d-FHIC_X_d),FHIC_beta);


                if((FHIC_SEL*FHIC_Xr-FHIC_X)<0)
                 trm3=-1*pow((FHIC_SEL*FHIC_Xr-FHIC_X)*-1,FHIC_gama);
                else
                 trm3=pow((FHIC_SEL*FHIC_Xr-FHIC_X),FHIC_gama);


                if((1-FHIC_SEL)<0)
                 trm4=-1*pow((1-FHIC_SEL)*-1,FHIC_zeta);
                else
                 trm4=pow((1-FHIC_SEL),FHIC_zeta);


        FHIC_OUT=trm1+(1/FHIC_Jtot)*(FHIC_Kv*FHIC_Btot*trm2+FHIC_Kp*FHIC_Ks*trm3-
trm4*FHIC_fr-FHIC_fe);
                  //m_tc_stpnt=FHIC_OUT;
                  //m_sc_stpnt=m_tc_stpnt;
                }

/*
                if(ch_imp==1)
          {
      m_tc_stpnt=pid_con(lod_imp_er,lod_imp_int,enc2_drv,m_ic_p,-m_ic_i,m_ic_d);
          }
```

```
                if(ch_trq==1)
            {
        m_sc_stpnt=pid_con(lod_trq_er,lod_trq_int,enc2_drv,m_tc_p,m_tc_i,m_tc_d);
            }
                if(ch_spd==1)
            {
             enc1v_er=(m_sc_stpnt-EncVel_1);
                enc1v_int+=(enc1v_er*TIME_OP);//**Integre enc1 velocity ***
       m_cs_out=pid_con(enc1v_er,enc1v_int,EncAcc_1,m_sc_p,m_sc_i,m_sc_d);
            }
*/

      m_motr_pwm=out_to_pwm(FHIC_OUT);
          }

  m_motr_pwm=saturate(m_motr_pwm,1,99);
  pval=31767*(m_motr_pwm/100);
  GT_SetDac(1,&pval,1);

//@@@@@@@@@@@@@@@@@@@@@@@@@@@@@@@@@@@@ Graf
          graf_y=m_motr_en*0.5;
   graf_y2=m_lod_en*0.5;
          graf_y3=(encs_er)*20;
   graf_y4=(m_motr_pwm-50);
```

```
        //graf_y5=(m_sin_pls/3);


        CDC *p=GetDC();


p->SelectObject(&pen_blu);//*********Position en1
        p->MoveTo(graf_x++,Yr3-graf_y_eski);
        p->LineTo(graf_x,(Yr3-graf_y));
        graf_y_eski=graf_y;


--graf_x;
p->SelectObject(&pen_red);//******** Position en2
        p->MoveTo(graf_x++,Yr3-graf_y2_eski);
        p->LineTo(graf_x,(Yr3-graf_y2));
        graf_y2_eski=graf_y2;


--graf_x;
p->SelectObject(&pen_grn);//******** Position Error
        p->MoveTo(graf_x++,Yr4-graf_y3_eski);
        p->LineTo(graf_x,(Yr4-graf_y3));
        graf_y3_eski=graf_y3;


--graf_x;
p->SelectObject(&pen_mgt);//******** PWM out
        p->MoveTo(graf_x++,Yr5-graf_y4_eski);
```

```
            p->LineTo(graf_x,(Yr5-graf_y4));
            graf_y4_eski=graf_y4;

if(graf_x>(Xr2-10)) // Graf backgrand
{
            graf_x=Xr1;

            CDC *p=GetDC();
            p->Rectangle(Xr1,Yr1,Xr2,Yr2);
            p->MoveTo(Xr1,Yr1+(Yr2/3));
            p->LineTo(Xr2,Yr1+(Yr2/3));
            p->MoveTo(Xr1,Yr1+(Yr2/3)*2);
            p->LineTo(Xr2,Yr1+(Yr2/3)*2);
   p->SelectObject(&pen_gry);
            p->MoveTo(Xr1,Yr3);
            p->LineTo(Xr2-10,Yr3);
            p->MoveTo(Xr1,Yr4);
            p->LineTo(Xr2-10,Yr4);
            p->MoveTo(Xr1,Yr5);
            p->LineTo(Xr2-10,Yr5);
}//_-_-_-_-_-_-_-_-_-_-_-_-_-_-_-_-_-_-_-_-_

//@@@@@@@@@@@@@@@@@@@@@@@@ Save Data
```

```
fprintf(fp,"%i",(sclk));//^1

fputc(',',fp);

fprintf(fp,"%f",m_motr_en);//^^^^^^^^^^2

fputc(',',fp);

fprintf(fp,"%f",EncVel_1);//^^^^^^^^^^3

fputc(',',fp);

fprintf(fp,"%f",FHIC_X);//^^^^^^^^^^4

fputc(',',fp);

fprintf(fp,"%f",FHIC_X_d);//^^^^^^^^^^5

fputc(',',fp);

fprintf(fp,"%f",FHIC_X_dd);//^^^^^^^^^^5_2

fputc(',',fp);

fprintf(fp,"%f",encs_er);//^^^^^^^^^^6

fputc(',',fp);

fprintf(fp,"%f",FHIC_Xr);//^^^^^^^^7

fputc(',',fp);

fprintf(fp,"%f",FHIC_Xr_d);//^^^^^^^^7_2

fputc(',',fp);

fprintf(fp,"%f",FHIC_Xr_dd);//^^^^^^^^7_3

fputc(',',fp);

fprintf(fp,"%f",FHIC_fr);//^^^^^^^^8

fputc(',',fp);

fprintf(fp,"%f",FHIC_fe);//^^^^^^^^9

fputc(',',fp);
```

```
fprintf(fp,"%f",FHIC_Kp);//^^^^^^10
fputc(',',fp);
fprintf(fp,"%f",FHIC_Kv);//^^^^^^11
fputc(',',fp);
fprintf(fp,"%f",FHIC_alfa);//^^^^^^11_2
fputc(',',fp);
fprintf(fp,"%f",FHIC_beta);//^^^^^^11_3
fputc(',',fp);
fprintf(fp,"%f",FHIC_gama);//^^^^^^11_4
fputc(',',fp);
fprintf(fp,"%f",FHIC_zeta);//^^^^^^11_5
fputc(',',fp);
fprintf(fp,"%f",FHIC_SEL);//^^^^^^11_6
fputc(',',fp);
fprintf(fp,"%f",m_cs_out);//^^^^^^^^12
fputc(',',fp);
fprintf(fp,"%f",m_motr_pwm);//^^^^^^^13
fputc(',',fp);
fprintf(fp,"%f",m_pwm_frq);//^^^^^^^14
fputc(',',fp);
fprintf(fp,"%f",m_lod_trq);//^^^^^^^15
fputc('\n',fp);

//@@@@@@@@@@@@@@@@@@@@@@@@@@
```

```
    UpdateData(false);
            CDialog::OnTimer(nIDEvent);
}

void CSEA_mv2Dlg::OnButtonCntrl()
{

  if (cntrl==0) cntrl=1;
  else
              cntrl=0;
}
//@@@@@@@@@@@@@@@@@@@@@@@@@@ MJF Functions

//@@@@@@@@@@@@@@@@@@@@@@@@@@@@ SGN Function
int sgn_wz(int sgn_num)
{
              if(sgn_num>=0)  return 1;
 else if(sgn_num<0)  return -1;
}

int sgn_z(int z_num)
{
            if(z_num>0)  return 1;
```

```
        if(z_num<=0)  return 0;
}
//@@@@@@@@@@@@@@@@@@@@@@ Saturation Function
double saturate(double in_sgnl,double min_lim,double max_lim)
{
        if (in_sgnl<min_lim)
                return min_lim;
        else if(in_sgnl>max_lim)
                return max_lim;
        else return in_sgnl;
}
//@@@@@@@@@@@@@@@@@@@@@@ PID Controller
double pid_con(double p,double i,double d,double p_gain,double i_gain,double d_gain)
{
        return ((p_gain*p)+(d_gain*d)+(i_gain*i));
}
//@@@@@@@@@@@@@@@@@@@@@@ PWM MOTOR out
double out_to_pwm(double out_data)
{
        return (50+out_data);
}
```

Appendix-B

The Matlab .m codes used to the FHIC of the RSEA is given in this section.

```
close all; clear; clc;
%%%-------------------------------------
rsea.shaftRadii      = 1;  % cm
rsea.pinionShaft     = 7.5; % cm
fuz2=readfis("fuz2");
% load('data_body(tim_hip_knee_anle).mat')
% tim=data_body(:,1);
% hip=data_body(:,2);
% knee=data_body(:,3);
% ankle=data_body(:,4);
% ****data****************
% tim=sin_data(:,1);
% f_pls=sin_data(:,2);
% f_HIC=sin_data(:,3);
% f_FHIC=sin_data(:,4);
% f_AFHIC=sin_data(:,5);
% p_pls=sin_data(:,6);
% p_HIC=sin_data(:,7);
% p_FHIC=sin_data(:,8);
% p_AFHIC=sin_data(:,9);
%.............................
FHC_S=1;
FHC_Alfa_x=0.21;
FHC_Beta_x=0.2;
FHC_Gama_x=0.51;
FHC_Alfa_f=0.21;
FHC_Beta_f=0.20;
FHC_Gama_f=0.51;

FHC_Fd=1;
FHC_Md=1;
FHC_Kd=1;
FHC_Bd=1;
FHC_I=1;

FHC_Kpp=0.4403;
FHC_Kvp=0.1524;
FHC_Kpf=0.4403;
FHC_Kvf=0.1524;

% FHC_S=0.5;
% FHC_Alfa=0.3234;
% FHC_Beta=0.3834;
% FHC_Gama=0.5644;
% FHC_Zeta=0.1079;
% FHC_Fd=79.2302;
% FHC_Md=93.8535;
% FHC_Kd= 64.6219;
% FHC_Bd=19.6451;
% FHC_I=15.224
%%%-------------------------------------
```

```
%>>>>>>>>>>>>>>>>>>RSEA parameter >>>>>>>>>>>>
Ks =64.251;
N=60.333;
Jxm=0.000017;  Jxw=0.000623;   Jx=Jxm+Jxw;
Jys=0.00002;   Jyw=0.000032;   Jy=Jys+Jyw;
%Jtot=Jy+N^2*Jx;

Bxm=0.00005;  Bx=Bxm;
Byw=0.012;  By=Byw;
Btot=By+N^2*Bx;

Jtot=2.3208;
%Btot=0.183;

BJ=Btot/Jtot;
KJ=Ks/Jtot;
KJ2=Ks/Jtot^2;

Cff = 0.28;

%.............................

tim=data1(:,1);
pwm=data1(:,2);
teta=data1(:,3);
vel=data1(:,4);
trqm=data1(:,5);
trq=data1(:,6);

clc
close all
clear all
%% ACO paramters
n_iter=30; %number of iteration
NA=10; % Number of Ants
alpha=0.8; % alpha
beta=0.2; % beta
roh=0.7; % Evaporation rate
n_param=3; % Number of paramters
LB=(0.01).*ones(1,27); % lower bound
UB=30.*ones(1,27); % upper bound
n_node=10000; % number of nodes for each param
cost_best_prev=inf;
%% Generating Nodes
T=ones(n_node,n_param).*eps; % Phormone Matrix
dT=zeros(n_node,n_param); % Change of Phormone
for i=1:n_param
    Nodes(:,i) =linspace(LB(i),UB(i),n_node); % Node generation at
equal spaced points
end
%% Iteration loop
for iter=1:n_iter

    for tour_i=1:n_param
        prob(:,tour_i)=            (T(:,tour_i).^alpha)            .*
((1./Nodes(:,tour_i)).^beta);
        prob(:,tour_i)=prob(:,tour_i)./sum(prob(:,tour_i));
    end

    for A=1:NA
```

```
        for tour_i=1:n_param
            node_sel=rand;
            node_ind=1;
            prob_sum=0;
            for j=1:n_node
                prob_sum=prob_sum+prob(j,tour_i);
                if prob_sum>=node_sel
                    node_ind=j;
                    break
                end
            end
            ant(A,tour_i)=node_ind;
        end
        cost(A)=cost_func(Nodes(ant(A,:)),0);
        clc
        disp(['Ant number: ' num2str(A)])
        disp(['Ant Cost: ' num2str(cost(A))])
        disp(['Ant Paramters: ' num2str(Nodes(ant(A,:)))])
        if iter~=1
        disp(['iteration: ' num2str(iter)])
        disp('_________________')
        disp(['Best cost: ' num2str(cost_best)])
        disp(['Best                    paramters:                    '
num2str(Nodes(ant(cost_best_ind,:)))])
        end


    end
    [cost_best,cost_best_ind]=min(cost);

    % Elitsem
    if (cost_best>cost_best_prev) && (iter~=1)
        [cost_worst,cost_worst_ind]=max(cost);
        ant(cost_worst_ind,:)=best_prev_ant;
        cost_best=cost_best_prev;
        cost_best_ind=cost_worst_ind;
    else
        cost_best_prev=cost_best;
        best_prev_ant=ant(cost_best_ind,:)
    end



    dT=zeros(n_node,n_param); % Change of Phormone
    for tour_i=1:n_param
        for A=1:NA

dT(ant(A,tour_i),tour_i)=dT(ant(A,tour_i),tour_i)+cost_best/cost(A);
        end
    end

    T= roh.*T + dT;




    %% Plots , this section will not effect the algorithem
    % you can remove it to speed up the run
   cost_mat(iter)=cost_best;
```

```
    figure(1)
    plot(cost_mat)
    figure(2)
    cost_func(Nodes(ant(cost_best_ind,:)),1);

    param_mat(iter,:)=Nodes(ant(cost_best_ind,:));
    save('ACO_data.mat','cost_mat','param_mat')
    drawnow
end

function cost_value=cost_func(k,plotfig)

assignin('base', 'P',k(1))
assignin('base', 'I',k(2))
assignin('base', 'D',k(3))

sim('RSEA_model_control.slx')

err=reference-output;
[n,~]=size(err);
cost_value=0;
for i=1:n
%  cost_value=cost_value+(err(i))^2 ;  % ISE
%   cost_value=cost_value+abs(err(i));  % IAE
  cost_value=cost_value+t(i)*abs(err(i));  % ITAE
%   cost_value=cost_value+t(i)*(err(i))^2;  % MSE
end
%   cost_value=cost_value/t(n);  % MSE

if plotfig
    figure(3)
    plot(t,reference,t,output)
    end
end
```

PUBLICATIONS

[1] **Fotuhi M.J.,** and Bingul Z., Fuzzy torque trajectory control of a rotary series elastic actuator with nonlinear friction compensation, *ISA Transactions*, 2021, 115, 206-217.

[2] **Fotuhi M.J.,** and Bingul Z., Novel fractional hybrid impedance control of series elastic muscle-tendon actuator. *Industrial Robot, the international journal of robotics research and application*, 2021, 48(4), 532-543.

[3] **Fotuhi M.J.,** Yılmaz O., and Bingul Z., Human postural ankle torque control model during standing posture with a series elastic muscle-tendon actuator. *SN Applied Sciences*, 2020, *2*(2), 1-8.

[4] **Fotuhi M.J.,** Hazem Z.B., and Bingül, Z., Adaptive Joint Friction Estimation Model for Laboratory 2 DOF Double Dual Twin Rotor Aerodynamical Helicopter System, *6th International Conference on Control Engineering and Information Technology (CEIT)*, *IEEE*, 1-6, 2018.

[5] **Fotuhi M.J.,** Hazem Z.B., and Bingül, Z., Comparison of Joint Friction Estimation Models for Laboratory 2 DOF Double Dual Twin Rotor Aero-Dynamical System, *Conference of the Industrial Electronics Society (IECON)*, *IEEE*, 2231-2236, 2018.

[6] **Fotuhi M.J.,** Hazem Z.B., and Bingül, Z., Modelling and Torque Control of an Non-Linear Friction Inverted Pendulum Driven with A Rotary Series Elastic Actuator, *International Symposium on Multidisciplinary Studies and Innovative Technologies (ISMSIT)*, *IEEE*, 1-6, 2019.

[7] Hazem Z.B., **Fotuhi M.J.,** and Bingül, Z., Comparison of Friction Estimation Models for Rotary Triple Inverted Pendulum, *International Journal of Mechanical Engineering and Robotics Research,* 2019, 8(1).

[8] Hazem Z.B., **Fotuhi M.J.,** and Bingül, Z., A Comparative Study of the Friction Models with Adaptive Coefficients for a Rotary Triple Inverted Pendulum, *6th International Conference on Control Engineering and Information Technology (CEIT)*, *IEEE*, 1-6, 2018.

[9] Hazem Z.B., **Fotuhi M.J.,** and Bingül, Z., A Comparative Study of the Joint Neuro-Fuzzy Friction Models for a Triple Link Rotary Inverted Pendulum, *IEEE Access,* 2020, 8, 49066-49078.

[10] Hazem Z.B., **Fotuhi M.J.,** and Bingül, Z., Development of a Fuzzy-LQR and Fuzzy-LQG Stability Control for a Double Link Rotary Inverted Pendulum, *Journal of the Franklin Institute*, 2020, 357(15), 10529-10556.

CURRICULUM VITAE

Mohammad Javad Fotuhi is a PhD candidate at Kocaeli University in Mechatronics engineering department. Received his B.S degree in computer hardware engineering in 2007. received his M.S in Mechatronics engineering in 2011. His research interests include Intelligent Control of Mechatronic and Robotic Systems, Fuzzy Control Systems, and MEMS. He dedicated his thesis to Series Elastic Actuator in robotics.